‘Ultra-High Strength Steels for Roll Formed Automotive Body in White Applications’

By

Dane William Hardwicke

Submitted to Swansea University in fulfilment of the requirements for the Degree of Doctor of Engineering

College of Engineering

Swansea University

2023

Declarations

This work has not previously been accepted in substance for any degree and is not being concurrently submitted in candidature for any degree.

Signed [redacted]

Date 02/06/2023

This thesis is the result of my own investigations, except where otherwise stated. Other sources are acknowledged by footnotes giving explicit references. A bibliography is appended.

Signed [redacted]

Date 02/06/2023

I hereby give consent for my thesis, if accepted, to be available for photocopying and for inter-library loan, and for the title and summary to be made available to outside organisations.

Signed [redacted]

Date 02/06/2023

The University's ethical procedures have been followed and, where appropriate, that ethical approval has been granted.

Signed [redacted]

Date 02/06/2023

Acknowledgments

I want to express my gratitude to all the individuals and organisations who have contributed to the research reported in this thesis. It is my pleasure to thank my sponsoring company TATA Steel UK and the funders, which include Welsh European Funding Office (WEFO), EPSRC, and the M2A, for their invaluable support and funding throughout the work involved in this thesis. This work would not have been possible without their generous support and funding. I also extend a special thanks to the M2A for allowing me to refine my thermodynamic modelling expertise by sending me on a ThermoCalc training course in Sweden. The knowledge gained from this training course was essential in designing the alloys within this thesis. Furthermore, I am grateful for the support of my academic supervisor, Dr Elizabeth Sackett, whose guidance was crucial in the final stages of writing this thesis. Additionally, I would like to thank my industrial supervisors, Mr Peter Evans and Dr Richard Underhill, and the Tata Steel Strip Products UK team, including Geraint Gladwyn, Andrew Brown, and Lee Jones, for their assistance in processing my Q&P alloys. I would also like to acknowledge TATA Steel Ijmuiden for providing me with 50kg casts of each of my designed alloys for the initial ingot casting. Thanks also to Peter Davies, James Russel, and Michael Shakib for their assistance in using the AIM facility's scanning electron microscope. Lastly, I want to express my gratitude to my partner Natalie Brown, who has been supportive throughout my four-year journey of researching and analysing steels. I am proud of the work accomplished in this thesis and believe that my results have demonstrated the viability of quenching and partitioning steels in an industrial setting.

Abstract

One of the more recent steel developments is the quenching and partitioning process, first proposed by Speer et al. in 2003 on developing 3rd generation advanced high-strength steel (AHSS). The quenching and partitioning (Q&P) process set a new way of producing martensitic steels with enhanced austenite levels, realised through controlled thermal treatments. The main objective of the so-called 3rd generation steels was to realise comparable properties to the 2nd generation but without high alloying additions. Generally, Q&P steels have remained within lab-scale environments, with only a small number of Q&P steels produced industrially. Q&P steels are produced either by a one-step or two-step process, and the re-heating mechanism for the two-step adds additional complexities when heat treating the material industrially. The Q&P steels developed and tested throughout this thesis have been designed to achieve the desired microstructural evolution whilst fitting in with Tata's continuous annealing processing line (CAPL) capabilities. The CALPHAD approach using a combination of thermodynamics, kinetics, and phase transformation theory with software packages ThermoCalc and JMatPro has been successfully deployed to find novel Q&P steels. The research undertaken throughout this thesis has led to two novel Q&P steels, which can be produced on CAPL without making any infrastructure changes to the line. The two novel Q&P steels show an apparent reduction in hardness mismatch, illustrated visually and numerically after nano-indentation experiments. The properties realised after Q&P heat treatments on the C-Mn-Si alloy with 0.2 Wt.% C and the C-Mn-Si alloy with the small Cr addition is superior to the commercially available QP980/1180 steels by BaoSteel. Both novel alloys had comparable levels of elongation and hole expansion ratio to QP1180 but are substantially stronger with a > 320MPa increase in tensile stress. The heat treatment is also less complex as there is no requirement to heat the steel back up after quenching due to one-step quenching and partitioning being employed on the novel alloys.

Contents

List of Figures

List of Tables

Nomenclature

AHSS	Advanced High Strength Steel
A_r^1	Austenite Decomposition Temperature
A_r^3	Austenite Transformation Temperature
AUST.SS	Austenitic Stainless Steel
BCC	Body Centre Cubic
BiW	Body in White
B_s	Bainite Start Temperature
CALPHAD	Calculation of Phase Diagrams
CAPL	Continuous Annealing Processing Line
CCT	Continuous Cooling Transformation Diagram
CGJC	Conventional Gas Jet Cooling
CP	Complex Phase
DP	Dual Phase
EDM	Electrical Discharge Machining
FCC	Face Centre Cubic
FSV	Future Steel Vehicle
GPa	Giga Pascals
HDAS	Hot Dip Annealing Simulator
HER	Hole Expansion Ratio

HGJC	High Gas Jet Cooling
HSLA	High Strength Low Alloy
HT1	Heat Treatment One
HT2	Heat Treatment Two
Hv	Vickers Hardness
K&M	Koistinen Marburger Relationship
kN	Kilo Newton
$M_{50\%}$	Martensite 50% Transformed Temperature
MART	Martensitic
$M_f/M_{90\%}$	Martensite Finish Temperature / Martensite 90% Transformed Temperature
MPa	Mega Pascals
M_s	Martensite Start Temperature
PSE	Product of Stress Elongation
Q&P	Quenching and Partitioning
QPT	Quench Partitioned Tempered
ReX	Recrystallization Temperature
T_m	Melting Point
TRIP	Transformation Induced Plasticity
TTA	Time Temperature Austenisation Diagram
TTP	Time Temperature Precipitation Diagram
TTT	Time Temperature Transformation Diagram
TWIP	Twinning Induced Plasticity
UFG	Ultra Fine Grain
ULSAB	Ultra-Light Steel Auto Body
UHSS	Ultra-High Strength Steel

UTS	Ultimate Tensile Stress
VIM	Vacuum Induction Melting

Chapter 1

Introduction

1. Introduction

The automotive industry is a sector that is trying to improve its impact by lightweighting automobile parts to improve fuel economy and emissions. Push for light weighting is seen through increasing demands via legislators worldwide passing vehicle emissions regulations through 2020 and beyond. These regulations have led the steel industry to develop advanced high-strength steels (AHSS), which have superior strength and formability properties compared to conventional steels and high-strength low alloy steels. Looking at the development of these new grades of steel, in 1994, 35 sheet steel producers initiated the Ultra-Light Steel Auto Body (ULSAB) to develop a lightweight steel auto body structure. The body-in-white (BiW) was unveiled in 1998, meeting an extensive range of performance and safety measures and demonstrating that ULSAB is lightweight, affordable, structurally robust and executable. This program was the first onset of AHSS, which had unique microstructures and could go through complex deformation and phase transformation processes to realise superior combinations of strength and ductility never seen before [1]. From the success of the ULSAB project, WorldAutoSteel [2] in 2008 began the FutureSteelVehicle program (FSV), where steel members further developed new AHSS grades, pushing for better combinations of strength and ductility properties. AHSSs with Giga Pascal strength were realised and designed for reduced life cycle emissions. The FSV could achieve a 39% mass reduction in body structure whilst improving crass worthiness, fuel emissions and consumption [3]. Using steel for weight reduction in vehicles has advantages over materials such as aluminium due to its lower overall impact during production. The production of aluminium produces 6-7 times more emissions than AHSS. Work done by world auto steel on life cycle assessment has shown it takes 12 years of use phase for aluminium to recover its greenhouse gas (GHG) production and be at the same level as an intensive AHSS body structured automobile [3]. Figure 1 shows the difference between AHSS and aluminium cumulative GHG production over time [1].

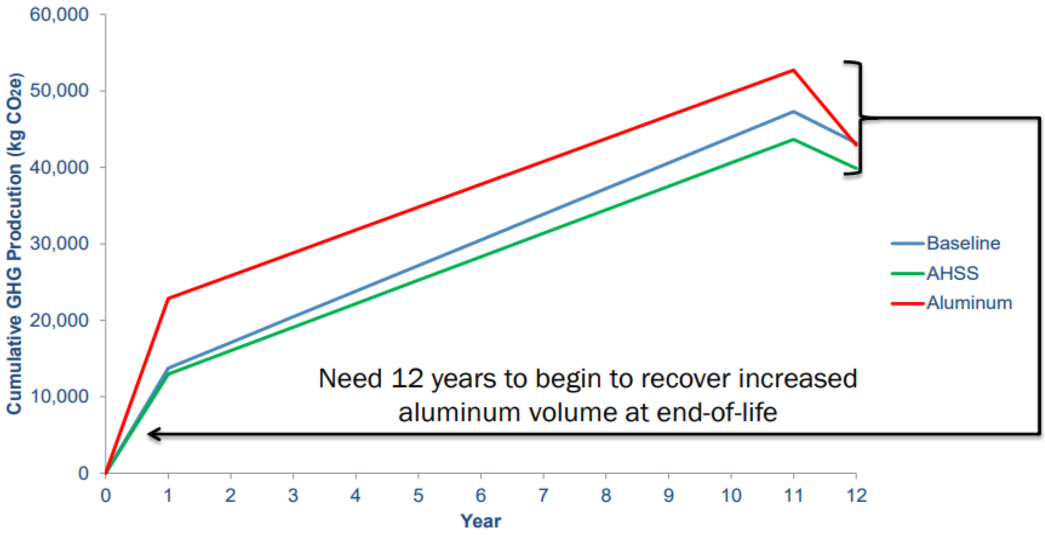

Figure 1: Difference between AHSS and aluminium over time [1].

More recently, in 2021, the UK government presented a net zero strategy termed 'Build Back Greener' and set a target to reach net zero by 2050. Throughout the legislation, it sets proposals to de-carbonise all sectors within the UK. Steel as an industry is responsible for 7% of global CO2 emissions, and for the UK government to reach net zero, the steel industry will need to significantly reduce its emissions [4]. Several strategies establish how the steel industry can achieve these goals.

- Increase the use of electric arc furnaces with recycled steel scrap.
- Direct reduced iron using green hydrogen.
- Carbon capture utilisation and storage.
- Using less steel to make products.

This project will focus on the last point, emphasising reducing the weight of BiW (body in white) components. The so-called 3rd generation steels realise their superior combination in properties through more specialised heat treatments. Heat treatment of steel is one of the most powerful tools we use to improve and tailor the properties substantially. Of all metallic systems, steel is by far the most used; Mridha et al. estimate that steel accounts for 80% of all metallic materials used in 2016 [5]. The high use of steel is due to the allotropic nature of iron, meaning it can exist in more than one crystalline form [6]. This iron property is responsible for achieving different microstructures and properties during heating and cooling. Steel is composed of iron with up to 2 Wt.% carbon. The carbon atom is 1/30th the size of the iron atom, and this phenomenon sets the underlying principles that facilitate the improvements possible during heat treatment [7].

This thesis will describe and discuss the design process employed for designing quenching and partitioning (Q&P) alloys using a combination of thermodynamic and kinetics software (ThermoCalc and JMatPro). Quenching and partitioning (Q&P) steels as a new class of advanced high-strength steels emerged in the early 2000s and has opened new avenues for producing ultra-high strength and formable steel grades [8]. The promising properties of Q&P steels demonstrated in the laboratory have led to extensive research efforts to understand their microstructure and properties [9]–[11]. However, industrial-scale adoption of Q&P steels has been relatively slow, owing to several factors.

1. One such factor is the iterative process of development and optimisation. Refining Q&P steel alloy compositions, processing parameters, and heat treatment techniques requires time and effort. This has resulted in a prolonged research and development phase, which has limited the availability of Q&P steels for industrial applications.
2. Another significant challenge is the complexity of scaling up production from the laboratory to the industrial level. Manufacturers must invest in equipment and modify existing processes to accommodate the specific requirements of Q&P steels. This necessitates significant capital investments and rigorous testing, which poses a significant barrier to adoption.
3. Cost considerations also play a crucial role in the adoption of Q&P steels. Production costs can be higher than conventional steels due to the complex and precise heat treatment process and the required alloying elements. This limits their adoption in price-sensitive industries.
4. Finally, market demand and awareness of the benefits of Q&P steels are essential drivers of adoption. Manufacturers require additional data on long-term performance and reliability to assess potential applications. Market education and awareness are, therefore, vital for driving adoption.

Despite these challenges, the industrial adoption of Q&P steels has been gradually increasing [12]. However, further research, development, and industry collaboration are required to refine production processes, optimise costs, and enhance the recognition of their benefits. This could drive increased industrial-scale implementation of Q&P steels. One way to reduce the complexity of the heat treatment process is using the 1-step Q&P cycle, and this will be the focus of this thesis and will be used to produce the Q&P steels. Throughout this thesis the processing of the novel Q&P alloys, covering VIM casting, cogging, transfer bar sectioning, and hot/cold rolling, will be described and discussed in detail. Also, the mechanical response of the alloys after hot rolling and cold rolling and annealing will be described and compared to show the substantial improvements in properties achieved after Q&P heat treatments. The characterisation of alloys will be covered using scanning electron microscopy and x-ray diffraction to confirm the phase proportions. Finally, the reduction in hardness mismatch will be shown with nano-indentation accelerated property mapping, and the feasibility of scaling up will be shown by running the heat treatments on a hot-dip annealing simulator.

Project Goals

- Design formable ultra-high strength steel.
- Design the steel with industry settings in mind, as it will need to be heat treated on Tata Port Talbot’s CAPL line (continuous annealing processing line).
- Realise superior properties whilst keeping alloying additions below 4.5 Wt.%.
- Below 700MPa after hot rolling to ensure the alloys will not exceed the rolling load limit at Tata.
- Design alloys to have a superior combination of properties. With tensile stress > 1200MPa and total elongation > 12%.
- Achieve a high hole expansion ratio with clear evidence of a reduction in hardness mismatch between the phases.

Chapter 2

Literature Review

2. Literature Review

2.1 Steel Processing and Manufacturing

This section will go through the stages in producing advanced high-strength steel strips, including continuous casting, hot rolling, cold rolling, continuous annealing, and roll forming.

2.1.1 Continuous Casting

Continuous casting provides the link between steelmaking and rolling. Where 95% of all steel produced is via a continuous casting route (Figure 2), this supersedes the previous ingot-cast steel method [13], where it was in the 1960s that continuous casting became the dominant steelmaking process. In continuous casting, liquid steel transfers in a ladle to the caster. Once started, the nozzle opens at the bottom of the ladle. Allowing the steel to flow into the tundish and then through a submerged entry nozzle into a water-cooled oscillating copper mould, with further cooling provided by water sprays as it exits the mould. The solidification event starts at the metal/mould interface, where the thickness of the solidified shell increases as it is drawn through the mould. The secondary cooling event occurs when the water sprays as it exits the mould. Several parameters need controlling to ensure a good surface and internal quality. These are casting speed, steel chemistry, liquid steel temperature, mould level/powder/oscillation, secondary cooling (water jets) and parameters affecting the mould flow [14]. During a solidification event, it is inevitable for inclusions and precipitates to form and for micro and macro-segregation patterns to appear. Because of this, the composition of the slab is heterogeneous throughout its thickness. Continuous casting is susceptible to centre-line segregation of lower solubility alloying elements, such as; carbon, phosphorus, sulphur and manganese [13]–[15].

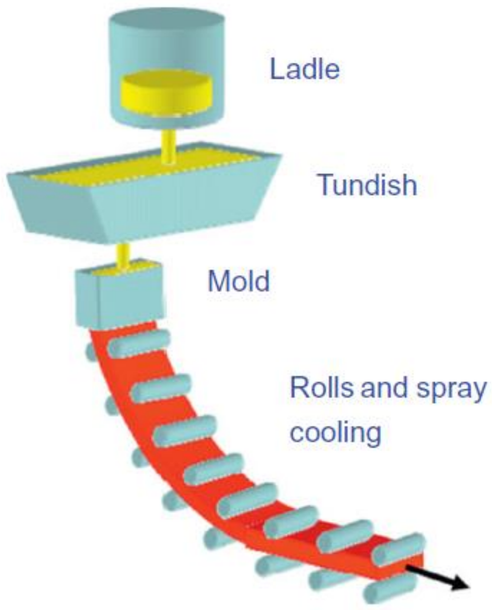

Figure 2: Continuous casting schematic [13].

2.1.2 Micro and Macro-Segregation

Micro-segregation results from the solute redistribution during solidification at the level of dendrites. Where during the solidification of the melt, dendrite arms will grow, and due to the lower solubility of solutes, they will secrete out ahead of the solidification front. Hypothetically if the diffusion were infinite during solidification, the concentration of solidus when the melt has solidified would be homogeneous and have the same composition as the nominal. However, this is not the case as diffusion is not infinite, so concentration gradients will exist at the solid-liquid interface for substitutional elements as the diffusion of substitutional elements is slow compared to interstitial elements. The level of micro-segregation for solute will increase as the solute's partition coefficient and the solid's diffusion coefficient decrease [14]. Different cooling rates affect the level of micro-segregation. A high cooling rate leads to a smaller dendrite arm spacing reducing the segregation, but the high rate will reduce the time for diffusion, leading to higher segregation. As a result, the micro-segregation of solutes leads to a local change in chemistry, deviating from the nominal composition at a micro level. Further working of the material, hot/cold rolling and annealing can help to reduce micro-segregation [14], [16].

Macro-segregation at the central plain of a cast, the chemical heterogeneity is 10-100 times higher than the dendritic structure. This is called macro-segregation. The movement of micro-segregated areas over macroscopic distances from several millimetres to meters [17]. This fluid flow and solid movement can be caused by the following;

- Contraction of the solid and liquid during cooling.
- Flow due to thermal and solute gradients in the liquid.
- Forced flows due to pouring, stirring, vibration, gas bubbles, and others.
- Movement of small grains or solid fragments heterogeneously nucleated in the melt melted off dendrites or separated from the mould wall.
- Deformations from thermal, shrinkage stresses or external forces to the solid network.

Where this variation in composition harms the processing ability and properties of the cast material and, in some cases, can lead to cast rejection. Positive segregation is a region high in solute content, and negative segregation is low in solute content. To reduce and even prevent macro-segregation, the fluid flow and movement of the solid need controlling. One way of controlling the flow is to use an electromagnetic stirrer which promotes the formation of equiaxed grains suppressing the centreline segregation. Another example is to adjust the alloy composition or thermal gradients to include a stable density stratification in the liquid [18].

2.1.3 Hot Rolling

After continuous casting, the slabs are hot rolled and depending on the alloy composition and hot rolling schedule, the strain hardening and dynamic recrystallisation will differ at each pass of the roughing and finishing mill. As the alloying content increases, so will the hot deformation resistance due to the influence of carbon, silicon, manganese, and micro-alloying elements. A higher rolling force is needed to achieve the same hot rolling reduction rate as steels with low alloying content. It is crucial to optimise hot rolling schedules to achieve the desired microstructure evolution. Parameters that need to be optimised are; temperature, reduction per pass, stand roll profiles and speed [16], [19], [20]. Even though cold rolling and continuous annealing follow hot rolling, the temperature and reduction in hot rolling still play a big part in the desired final microstructure. As the name suggests, hot rolling is at elevated temperatures in the austenitic region. Austenite is a face-centred cubic (FCC) phase, which has 12 slip systems. An FCC structure has increased formability due to additional slip systems. Typically, this solution heat treatment will be done in the temperature range of 1100-1250°C before hot rolling commences. The higher the rolling temperature, the higher the driving force for recrystallisation [16], [20].

2.1.4 Cold Rolling

The purpose of cold rolling is to achieve a strip product with a thinner gauge and high dimensional accuracy. As the hardness of higher alloyed grades increases, the cold rolling schedule needs to be optimised, for example, the reduction rate at each rolling stand. A cold rolling setup uses backing rolls, which prevent the work rolls from bowing or losing pressure in the centre section. These rolls are essential to produce flat, dimensionally accurate strip products (Figure 3) [21].

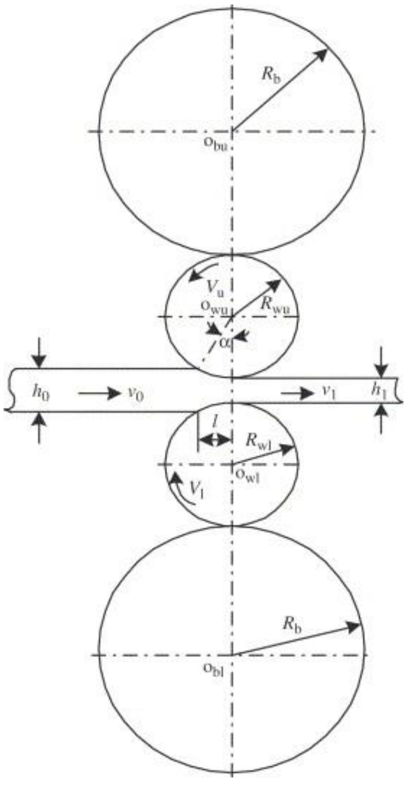

Figure 3: 4-High rolling mill schematic [21].

When a strip gets cold rolled, it is said to be anisotropic, as the properties in the rolling direction will be different to that in the 45° and 90° directions. Cold rolling enhances strength due to work hardening and is generally more robust than hot-rolled strip products. Difficulties that can arise from cold rolling are the possibility of defects at the strip edges, surface, or bulk. These defects can result from heterogeneities inherited from previous production steps, resulting in an increased likelihood of strip fracture during cold reduction. The strengthening mechanism from cold rolling is the build-up of high internal stresses and the build-up dislocations storing more energy in the strip, which inherently reduces the total elongation. The build-up of stored energy is for the recrystallisation of the microstructure in subsequent annealing processes [16]. Pavel Kusakin et al. [22] discuss the microstructural evolution and strengthening mechanisms of Fe-23Mn-0.3C-1.5Al TWIP steel during cold rolling. The main conclusions were;

- After a 20% cold reduction, the microstructure has a high dislocation density and frequent deformation twins within the initial grains. The deformations of twins increased with rolling reduction up to a plateau of 40% reduction. The further reduction did lead to the reduced distance between twins but did not reduce the thickness of the twins.
- When the reduction exceeds 40%, there is a development of shear bands. At 80%, the microstructure evolution was twinned crystallites divided by shear bands.
- By increasing the reduction from 20% to 80%, the yield increased from 690MPa to 1400MPa but reduced total elongation from 36% to 4%.

2.1.5 Continuous Annealing

The history of continuous annealing was first introduced in 1936 by Armco steel corporation as a process step in producing hot dip galvanised steel. This first onset of continuous annealing was not without issues, as the strip had poor cold-forming characteristics and ageing. These poor cold-forming characteristics were due to the high cooling rates of the carbon solute staying in supersaturation. To mitigate these issues, the Japanese (Nippon Steel) incorporated an overage section in the 1970s, which improved the properties of the strip [23]. Nowadays, continuous annealing is the most common method, superseding the batch annealing process. The annealing mechanism works by heating the steel to a temperature above its recrystallisation temperature (ReX) and then holding it at this temperature (soak) before it is cooled. Annealing works in 3 stages; recovery (stress relief), recrystallisation and grain growth. The recovery stage is the removal of dislocations and internal stresses, which results in softening of the steel. Once the temperature reaches 0.4Tm (40% of the melting point), recrystallisation will begin, where strain-free grain grains begin to nucleate and grow to replace grains deformed by internal stresses. In the final stage, the grains will continue to grow, leading to a coarse microstructure impacting their strength negatively. It is not always desirable to have excessive grain growth, so control at this stage is needed to balance strength and ductility: Figure 4, a-b recrystallisation and c-d grain growth [24].

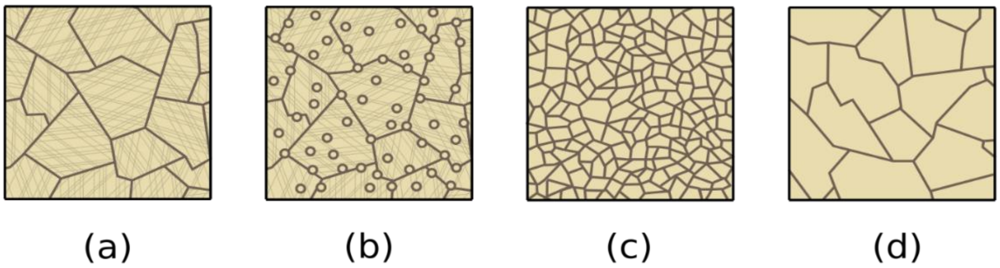

Figure 4: a-b recrystallisation and c-d Grain Growth [24].

The process steps in continuous annealing (Figure 5) are;

1. Strip steel coil placed on a decoiler.
2. The head end of coil joined (welded) to tail end of previous coil.
3. Strip steel is fed into accumulators to allow time for the joining operation, one before the heating section and one after (this allows for the continuous movement of strip through the heating section).
4. Strip fed from accumulators into the heating section.
5. Held at this temperature to produce an austenitic microstructure or austenite and ferrite if at an intercritical temperature.
6. Slow cooling section.
7. Rapid cooling section.
8. Overage section.
9. Secondary and final cooling sections.

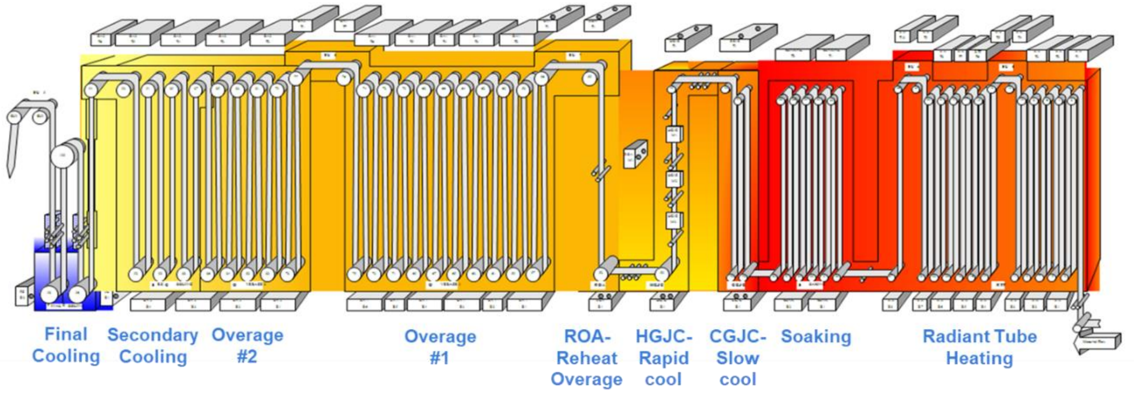

Figure 5: Continuous Annealing Schematic.

2.1.6 Roll Forming

In roll forming, the material feeds through multiple sets of rolling dies which incrementally deforms the metal substrate into the final desired profile. The resulting sections get cut into specified lengths for the final part. Roll forming is typically a high-volume process but can tailor for shorter runs. Manufacturing sectors utilising roll forming are construction, automotive, aircraft, and white goods. Feedstock for roll forming can be either pre-cut to a pre-determined length or post-cut after the roll forming operation to a specified length. A common defect in roll forming is springback, a geometric change that can occur to the part at the end of the forming process once the part releases from the forces of the roll forming tool. The part exhibits elastic and plastic deformation during the forming operation, and once the forces are removed, the elastic part will return to its original shape, causing a dimensional inaccuracy [25]. When a strip is roll-formed, it is subject to transversal bending, but this also induces redundant deformations into the strip. Redundant deformations include; transversal elongation/shrinkage, shear in the plane and direction of the strip of metal's thickness, longitudinal bending/bending back and longitudinal elongation/shrinkage [26]. Other common defects in roll forming are twist and end flare. Weiss et al. [27] looked at the effect of coil set on shape defects in roll forming and found end flare and twist defects change depending on the position the coil feeds into the roll forming line. For a convex upwards feed, the twist and end flare at the back section after cut-off was higher, but at the front section, the end flare was lower than a convex downward feed. Figure 6 illustrates a convex upwards and downwards feed configuration [27].

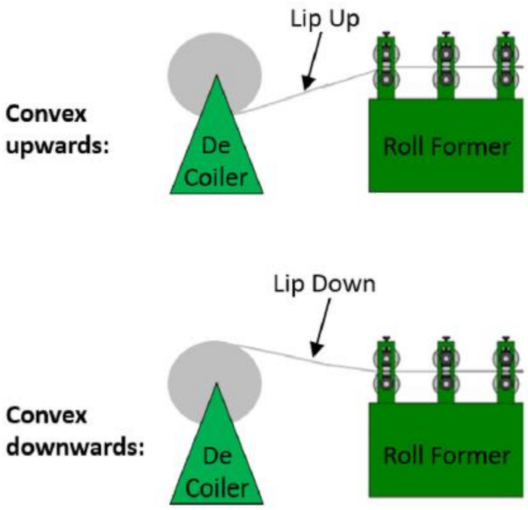

Figure 6: Schematic of convex upwards (top) and downwards feed (bottom) [27].

Another defect in roll-formed products is bowing, which is caused by excessive longitudinal strain exceeding the buckling limit. Bidabadi [28] et al. investigated the bowing defects in a cold roll-formed U-channel section experimentally and numerically. The study investigated the effects of distance between stands, strip gauge, forming angle increment, bend radii and flange width on bowing defects in a symmetrical roll-formed part. Forming angle increment was shown to have the most significant effect on bowing defects, so a solution to this is to incorporate more stands to reduce the bending angle at each stand. Increasing flange width reduces sectional bowing as it reduces longitudinal strains at the strip edge, and reducing strip gauge was shown to have a negligible effect on reducing bowing, whereas the other factors have minimal impact on reducing bowing defects [29]. Optimising the design process is key to reducing product defects. Wiebenga et al. [30] looked at optimising the roll-forming process of a V-section profile and found that optimising the process settings of the adjustable rolls at the final stand improved the dimensional accuracy of said V-section profile. From the numerical and experimental studies, longitudinal bow and springback were shown to be compensated by reducing the roll gap at the final stand. Previous process steps can have an influence on the defects in a roll-formed part. Abvadi et al. [31] studied the influence of residual stress on a roll-formed part and found thickness reduction rolling before roll forming, introducing residual stress at the strip's surface and compressive residual stress at the mid-plane of the strip. The residual stress/compression resulted in increased springback and end flare in the roll-formed part but a reduction in the bow. In the design process, the material to be roll formed first has to have a proper stand sequence (Figure 7) and a flower pattern design (Figure 8) [30].

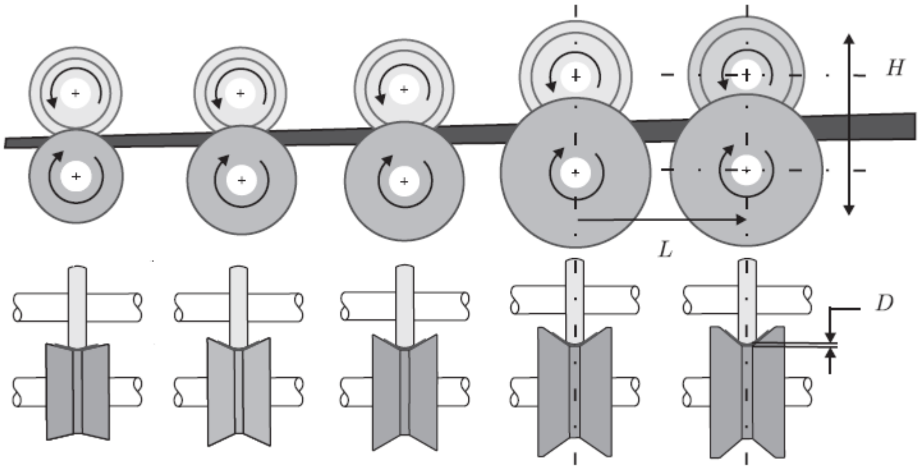

Figure 7: Roll forming setup schematic [30].

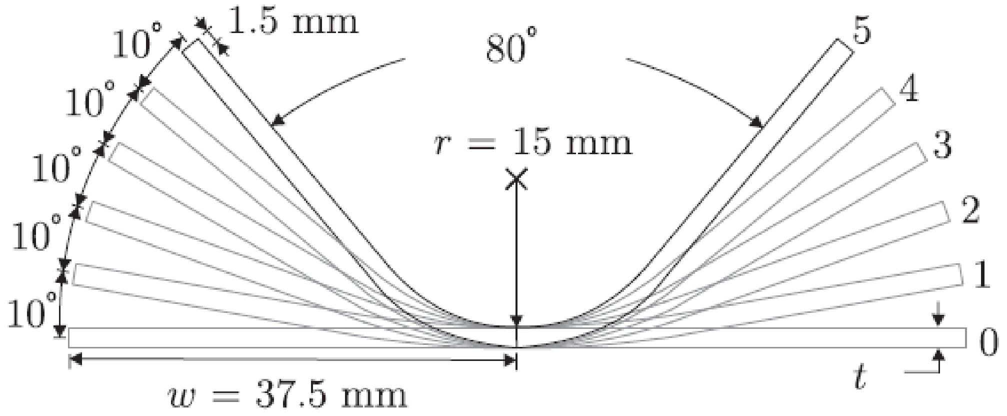

Figure 8: Flower pattern schematic [30].

The material used accounts for 65-95% of the total manufacturing cost in roll forming. So, selecting suitable material for the job is of utmost importance. Halmos [26] discusses how, when choosing a material to be roll formed, the following factors must be considered during the design process;

“1. Mechanical properties

2. Manufacturability (formability)

3. Appearance

4. Price

5. Availability of material

6. Equipment and tool capacity

7. Weight of the product

8. Customer’s specification

9. Supplier’s or other specifications

10. Corrosion resistance (application, environment, storage, discolouration, cathodic resistance)

11. Heat and wear resistance

12. Weldability, acceptance of coatings

13. Susceptibility of surface (scratch, mar)

14. Market acceptance

15. Electrical, magnetic, or other properties.’’

As a result, considering all these factors will lead to a more efficient and economic roll forming process. In roll forming, the material plastically deforms to realise its final shape. Because of this, the roll forming force needs to be above the materials yield strength but not as high as the UTS, as this can cause cracking of the strip. Materials with a large window between their yield and UTS are most suited for roll forming [26]. Xiaoli Lui et al. investigated the forming parameter effects on springback considering a variable young's modulus. They concluded that increasing the flange width, sidewall height, roll gap, and distance increased the springback and strip thickness and web width reduced the springback [32]. Buddhika Abeyrathna et al. looked at 'the effect of process and geometric parameters on longitudinal edge strain and product defects in cold roll forming. The work looked at three different materials, DP600, DP1000 and MS900, in two different gauges, 1.5 and 2mm and found; that the peak longitudinal edge strain increases with increasing yield strength. MS900 had a higher bow than DP1000 due to DP1000 having a higher level of strain hardening. The longitudinal bow is affected by yield and material hardening. Springback increases with increasing yield and flange width and decreases with increasing interstation distance [33]. In recent literature, Efthymiads et al. [34] looked at the mechanical and microstructural performance of DP, CP and MART steels during tensile, forming and flanging operations. This literature concludes that DP steels show higher levels of elongation, but CP steel would perform better during a bending operation due to less of a hardness mismatch between the phases of martensite and bainite compared to martensite and ferrite. The CP steels achieved a tighter bending radius, less springback and no signs of local failure at a microstructural level compared to the DP steels. The hardness mismatch in DP steels between ferrite and martensite causes microvoids and small cracks in individual grains, whereas the CP steels behave like a single-phase alloy. The tests on the martensitic steel showed any presence of inclusions is detrimental, as, at these inclusion sites, excessive void growth led to microcrack formation towards the neighbouring matrix [34].

2.2 Advanced High Strength Steel (AHSS)

The development of AHSSs can be categorised into the following: 1st generation AHSSs, 2nd generation AHSSs and in the current research area, 3rd generation AHSSs. The global formability diagram (Figure 9) shows the areas where these different generations of AHSSs sit relative to strength and elongation [35].

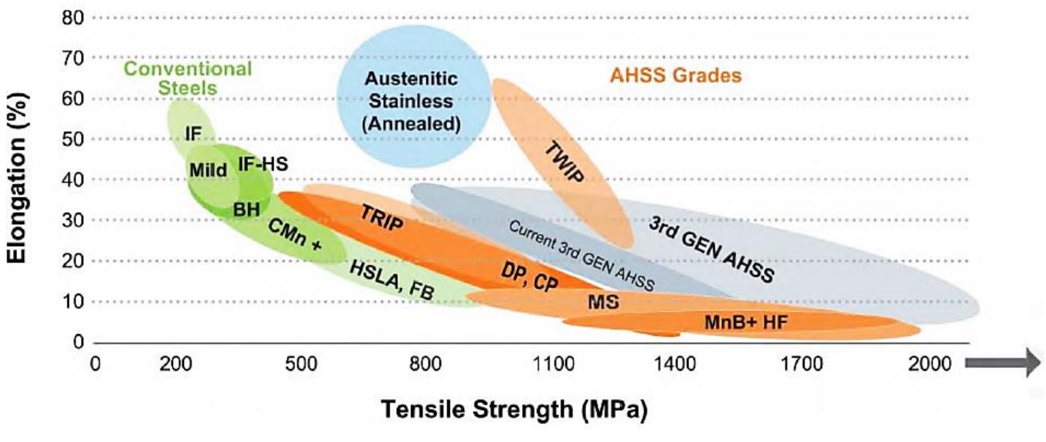

Figure 9: Global formability diagram for today's AHSS grades [35].

2.2.1 1st Generation Advanced High Strength Steel

The automotive industry is trying to improve its global impact by lightweighting automobile parts to improve fuel economy and emissions. Legislators around the world are increasingly pushing for lighter-weight vehicles with reduced emissions. This is reflected in the passing of vehicle emissions regulations through 2020 and the recent net-zero legislation known as 'Build Back Greener' for 2030-2050 [4]. The goal is to reduce emissions by 45% by 2030 and reach net zero by 2050. One aspect where the steel industry will help is in the lightweighting of parts, starting with the development of advanced high-strength steels (AHSS), which have superior strength and formability properties compared to conventional steels and high-strength low alloy steels. Looking at the development of these new steel grades, in 1994, 35 sheet steel producers initiated the Ultra-Light Steel Auto Body (ULSAB) to develop a lightweight steel auto body structure (Figure 10). The body-in-white (BiW) was unveiled in 1998, meeting an extensive range of performance and safety measures and demonstrating that ULSAB is lightweight, affordable, structurally robust and executable [1], [36].

Figure 10: ULSAB body structure [36].

This program was the first onset of AHSS, which had unique microstructures and could go through complex deformation and phase transformation processes to realise superior combinations of strength and ductility. 1st generation steels comprise Dual Phase (DP), Transformation Induced Plasticity (TRIP), Complex Phase (CP) and Martensitic (MART) steels which have moderate combinations of strength and ductility [1].

2.2.2 Dual Phase (DP)

Dual-phase steels have a microstructure consisting of a soft ferrite matrix and between 10-40% hard martensite or martensite-austenite islands. DP steels typically have an ultimate tensile strength (UTS) range of 500-1200MPa, controlled by the phase fraction of martensitic islands. The soft ferrite matrix and the size and distribution of martensite controls the ductility [37]. The production route for DP steels is either controlled cooling from the austenite phase for hot-rolled products or continuously annealed cold-rolled products; it is a controlled cooling from the two-phase ferrite plus austenite field to transform some of the austenite to ferrite before rapid cooling to transform any remaining austenite to martensite. Depending on the rate of cooling and alloy additions, it is possible for some amount of bainite or retained austenite to be present in the final microstructure. Figure 11 shows a micrograph of DP steel; dark constituents are the martensitic islands, and the light-coloured phase is the surrounding ferrite matrix [38].

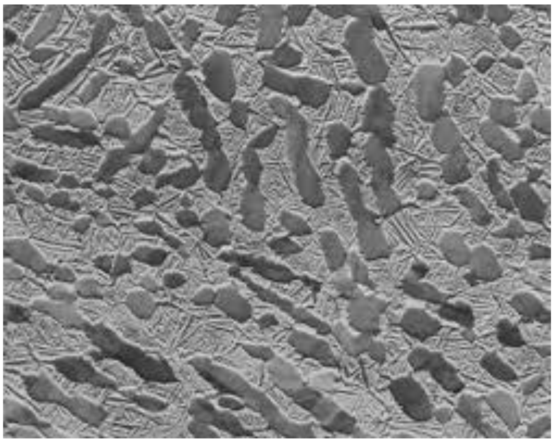

Figure 11: DP steel micrograph [38].

In DP steel, the ferrite phase is usually continuous, providing excellent ductility properties to these steels. During deformation events, the strain is concentrated in the lower-strength ferrite phase, providing a high initial work hardening rate (n-value) compared to high-strength low alloy steels. In general, the tensile strength of DP steels is a linear relationship with the volume fraction of martensite increasing, but there is a critical volume fraction of martensite and once surpassed, this trend will differ [39]–[41]. Grain refinement of the microstructure is another way to increase the strength of DP steels. Literature has shown that grain refinement increases strength without negatively impacting strain hardenability or elongation. Papa Rao et al. produced through an intercritical annealing route ultra-fine grain (UFG) DP steel, showing a superior combination of strength 1295MPa and uniform elongation of 13%. The steel composition had microalloying elements V and Nb, which are powerful carbide/nitride-forming elements. These promote the precipitation of nanoscale carbonitride precipitates, which suppress the recovery process of dislocations and their substructure, increasing tensile strength. These precipitates also prevent grain growth and help to stabilise the UFG microstructure [42]. The elemental composition of DP steel is a low C-Mn-Si system, where the carbon acts as an austenite stabiliser, determines the phase distribution and variation of mechanical properties and strengthens the martensite. Typically, the carbon content will range between 0.06-0.15 Wt.% for DP steels. Manganese is an austenite stabiliser with a range between 1.5-2.5wt%; this also acts as a ferrite solid solution strengthener and retards ferrite formation. The silicon promotes ferritic transformations. Most DP steels will have other alloying elements, such as molybdenum, chromium, niobium, and vanadium, to improve their mechanical properties, alter the microstructure and stabilise the austenite. The weight per cent of molybdenum and chromium does not usually surpass 0.4 Wt.%, and this helps to retard the formation of bainite and pearlite [43]. Precipitation strengthening refines the microstructure, and vanadium and niobium are used for this purpose, with their contents not surpassing 0.06 Wt.% and the latter 0.04wt%. Niobium also has other features; reduction of martensite transformation temperature and promotes ferrite transformation from non-recrystallised austenite. It is essential to correctly balance these alloy additions to get not just an improvement in mechanical properties but also not hinder the material's ability to be welded. Another feature with DP steels is that there are no apparent yield points as it exhibits dis-continuous yielding caused by internal stresses that allow dislocation mobility [43]–[45].

2.2.3 Complex Phase (CP)

Complex-phase steel has a microstructure consisting of a ferrite/bainite matrix with small amounts of martensite, retained austenite and pearlite (Figure 12) [46].

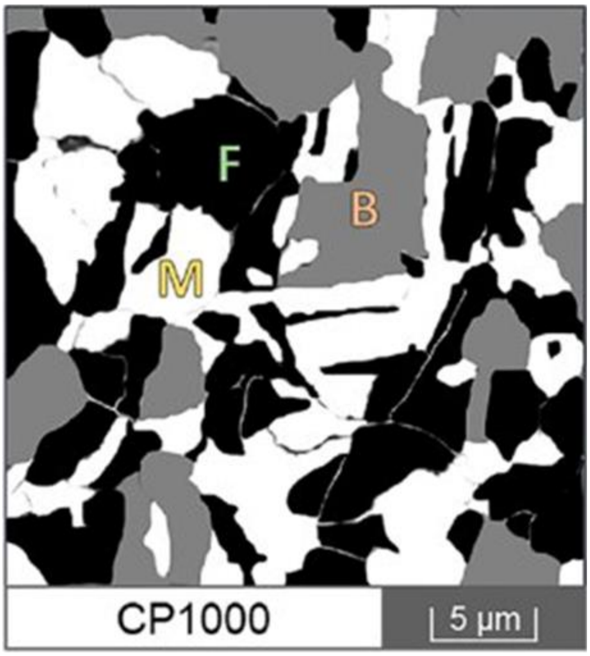

Figure 12: CP steel microstructure schematic [46].

Strengthening mechanisms in CP steels are achieved by solid solution strengthening, grain refinement, precipitation strengthening and phase transformations. The carbon content in these steels is usually less than 0.15 Wt.%, with alloying elements used similarly to that of DP steels. Additions of micro-alloying elements titanium, niobium and vanadium combine with carbon and nitrogen to form fine precipitates, which enhance the tensile strength. These precipitates also help to achieve grain refinement, and another method of grain refinement is retarded recrystallisation. The UTS of a CP steel can vary from 800-1200MPa, but this has a negative trend on ductility, going from 13% down to 3%. The mechanical properties of CP steel are directly related to the volume fraction of phases present, and these vary depending on the cooling rate employed from the austenitic region [43], [47]. Depending on the cooling rates used, it will influence the formation of ferrite, bainite and tempered martensite. Suppression of ferrite and promotion of martensite happens with high cooling rates. Karelova et al. [48] investigated the hole expansion of dual-phase and complex-phase steels with different edge conditions. The investigation found that for all edge conditions, CP steel showed a higher hole expansion ratio than DP steel, even though the CP grade has lower overall elongation properties (Figure 13). It shows that hole expansion is related to microstructural phases, the strength of the matrix and the difference in hardness between phases. For example, the difference in hardness in a DP grade between its soft ferrite matrix and martensite islands is significant. Comparing this to a CP grade with a bainitic matrix and martensitic islands, there is much less of a difference. Also, CP grades have a higher ratio between yield and ultimate tensile strength, which is another reason CP grades show a higher hole expansion ratio [48].

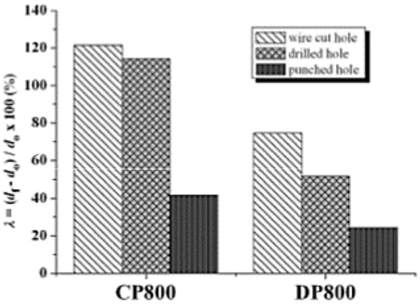

Figure 13: Hole expansion ratio comparison between CP and DP AHSSs [48].

2.2.4 Martensitic (MART)

Martensitic steels have an ultimate tensile strength of over 800MPa and a microstructure consisting of a martensitic matrix with small amounts of ferrite and bainite. In the production of martensitic steels, the austenitic structure that exists during annealing or hot rolling is transformed to martensite once quenched in the cooling section of the continuous annealing line or on the run-out table. Of all the steel grades amongst the first-generation AHSSs, martensitic grades show the highest levels of strength, but this is also attributed to them having a lower ductility, especially with ultra-high-strength MART grades. The transformation from austenite to martensite is a shear type of transformation, meaning its diffusion-less as there is no interchange between neighbouring atoms. A diffusion-based transformation will happen if the cooling rate is slow, so the cooling rate needs to be high, so these diffusion-based mechanisms cannot suppress the formation of ferrite, pearlite and bainite. On a continuous cooling diagram, the martensite start (Ms) and martensite finish (Mf) are shown by horizontal lines, indicating that time is not critical for the transformation. Figure 14 illustrates a TTT diagram for a eutectoid (0.76 Wt.% C) steel, where austenite will begin to transform to martensite once cooled below the Ms, and the transformation completes once cooled to the martensite finishing temperature Mf / M90 [24].

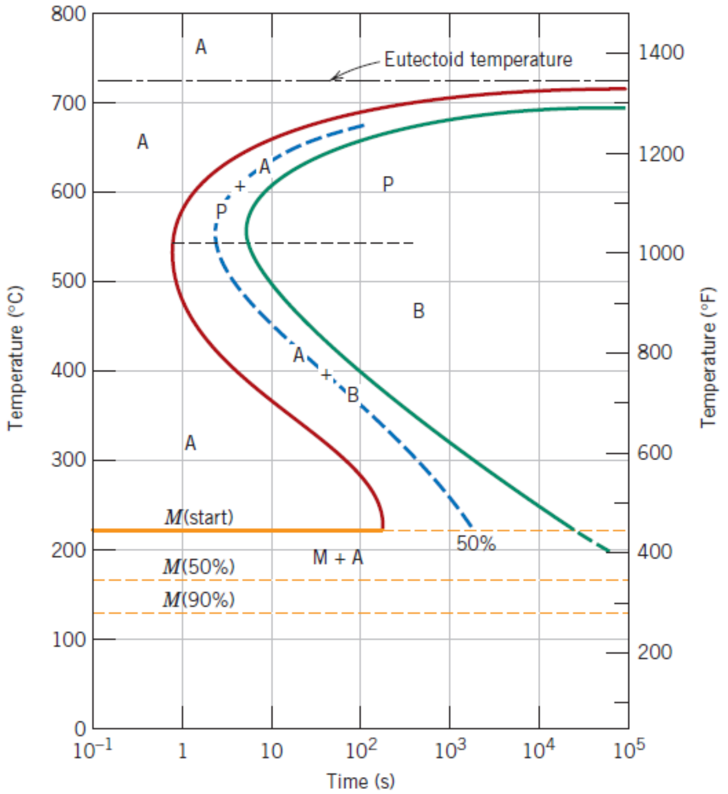

Figure 14: TTT diagram [24].

Temperature controls the fraction of martensite transformed from austenite, where it is zero at Ms and increases in fraction, leading to completion at Mf. To improve ductility, tempering heat treatments can be employed on martensitic steels. Tempering helps to enhance the formability of MART steels, with these steels typically being roll formed as they have a single-phase structure. Tempering is in 3 stages, dependent on the tempering temperature. In the first stage of tempering, there is a precipitation of transition carbides eta (η) and epsilon carbide (ε) in the martensitic crystals when the temperature is between 100-200°C. Once the tempering temperature is between 200-300°C, residual austenite transforms into a mixture of ferrite and cementite, and this is stage 2. For tempering higher than 300°C, transition carbides are replaced by cementite, and this is the mechanism for stage 3. Yan-jun Zhao et al. looked at the effect of tempering on the microstructure and mechanical properties of 3Mn-Si-Ni martensitic steel at temperatures ranging from 180 to 650°C. In that work, a tempering temperature of 230°C showed the ideal balance of properties, strength 1550MPa and toughness 91.5J, which was caused by a higher dislocation density in the fine martensitic lathes, short rod-like ε-carbides and the absence of cementite [49].

2.2.5 Transformation Induced Plasticity (TRIP)

Transformation-induced plasticity steels are composed of a multiphase microstructure consisting of a continuous ferrite matrix (0.50-0.55 volume fraction), bainite (0.30-0.35 volume fraction), possible martensite (0.01-0.05 volume fraction) and metastable retained austenite (0.05-0.20 volume fraction), (Figure 15) [47],[35].

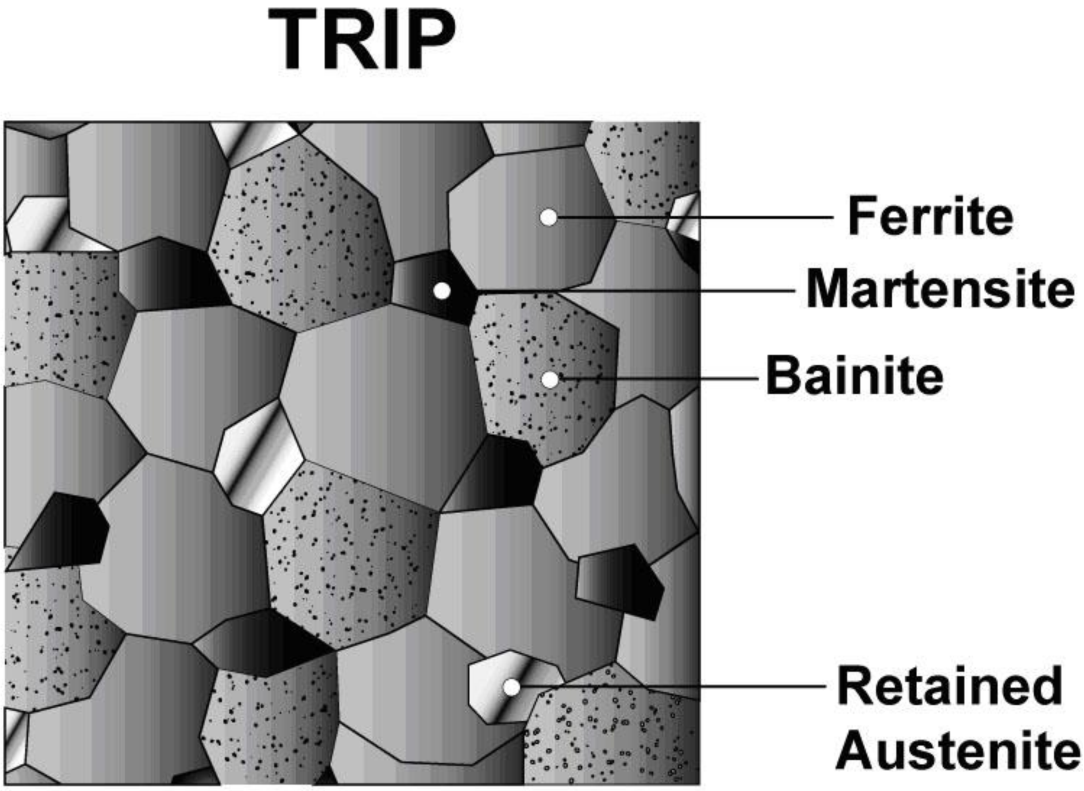

Figure 15: Trip microstructure schematic [47].

Due to their multiphase structure, they are well suited for light weighting car parts because of their excellent combination of properties in strength and high formability, and they provide extra crashworthiness due to the TRIP effect. During an impact event, the retained austenite in the structure will transform to martensite, hardening the steel. This TRIP effect allows for superior crash energy absorption compared to DP or HSLA steels as it has a high work hardening rate during a crash event [50]–[52]. The stability of retained austenite directly affects the TRIP effect, where the higher the stability, the more delayed the austenite to martensite transformation will be during deformation. Due to these facts, the fraction of retained austenite and stability needs controlling to ensure a good balance of strength and ductility properties. Typically, TRIP steels are characterised by having a low alloy content, approximately 3.5 Wt.% [37]. To process TRIP steels requires two-stage heat treatment, firstly intercritical annealing in the two-phase ferrite + austenite region where a controlled fraction of ferrite forms, then austempering in the bainitic temperature region where the partial transformation of austenite to bainite leads to the stabilisation of austenite and quenching to room temperature (Figure 16) [53].

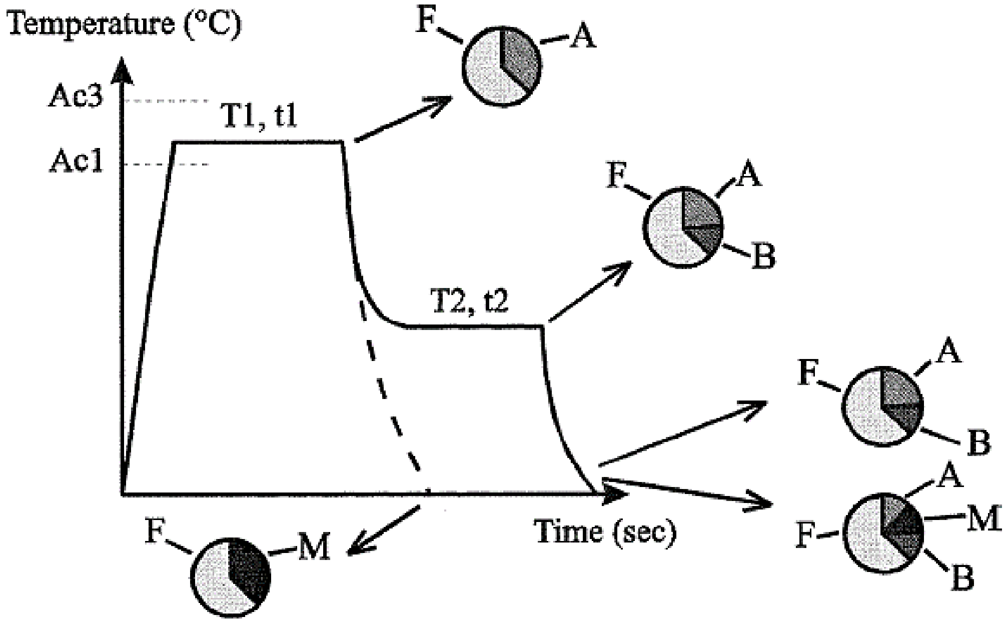

Figure 16: TRIP heat treatment cycle [53].

Retention of austenite at room temperature is of great importance in TRIP steels, so the martensite start temperature (Ms) needs to be below room temperature. To reduce the Ms temperature, austenite stabilising elements such as carbon, manganese, or others are used. Another purpose of the process route is to enrich the austenite grains with carbon to help stabilise them at room temperature. The enrichment of austenite with carbon first happens during the intercritical annealing, followed by a carbon redistribution from bainite to residual austenite during the austempering stage. Other elements added to TRIP steels are silicon or aluminium, or both, as these help to suppress the formation of cementite during the bainitic holding, which subsequently promotes the formation of carbon-supersaturated austenite [53].

2.2.6 2nd Generation Advanced High Strength Steel

The first generation of AHSSs realised good combinations of strength and ductility properties, but the need for further lightweighting of car parts led to development of the second generation of AHSSs. The second generation includes twinning-induced plasticity steels (TWIP) and austenitic stainless steels (AUST.SS). The mechanical properties are superior to the first-generation steels as they have high alloy additions. They are required to have stabilised austenite at room temperature, so they have high levels of elements such as; manganese, chromium and nickel. Due to these additions, TWIP and AUST.SS steels are expensive to produce and can also have difficulties where welding applications need to be applied. TWIP steels have a very high manganese content which is prone to a delayed cracking phenomenon [54]–[59].

2.2.7 Twinning Induced Plasticity (TWIP)

TWIP steels are characterised in having high manganese contents in the range 18-25 Wt.%, this allows the steel to be fully austenitic at room temperature (Figure 17) [38].

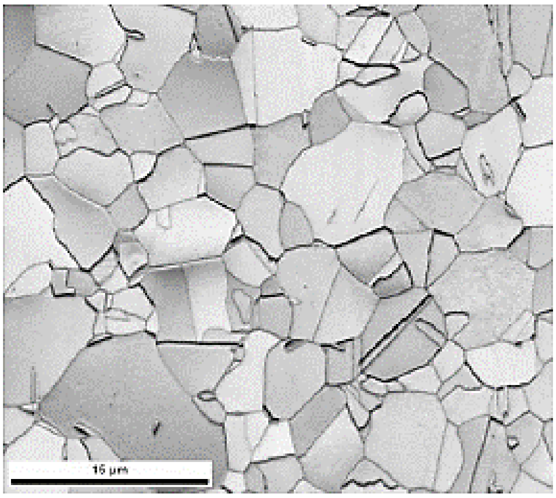

Figure 17: As annealed TWIP photomicrograph [38].

Manganese acts as an austenite stabiliser and will also have some strengthening effects. Additions of other elements such as carbon, aluminium, and silicon to obtain higher strength and ductility properties. Carbon also acts as an austenite stabiliser and significantly affects the strengthening of the steel, with its typical range being 0.5-1.0 Wt.%. It is beneficial to avoid martensite formation in TWIP steels, adding 0.6 Wt.% carbon suppresses the formation of carbides in the austenite microstructure. The higher the stability of austenite, the more pronounced the TWIP effect. They have a high rate of work hardening from forming deformation twins in the microstructure. The high work hardening rate leads TWIP steels to have excellent combinations of tensile strength and ductility. The twinning in the structure leads to a high instantaneous hardening rate (n-value) as the microstructure refines. A large part of the deformation is driven by the formation of these twins, where these twin boundaries strengthen the steel and act as grain boundaries, as these will restrict the movement of dislocations. The formation of twins happens when two crystals share some of the same crystal lattice points symmetrically. As mentioned previously, TWIP steels are susceptible to a delayed cracking phenomenon, with several reports on this matter [55], [56], [59], [60]. Delayed cracking or hydrogen embrittlement can happen if residual stresses build up in the formed part. Due to the high manganese content, it causes the formation of MnS inclusions, which act as an initiation site for small, elongated cracks to start. In the presence of hydrogen, the crack will enlarge due to hydrogen atoms gathering in the crack forming hydrogen gas, which can form hydrides and increase cracks' internal pressure. Hong et al. [55] looked at the 'effects of inclusions on delayed fracture properties of three TWIP steels' and found additions of 1.6 Wt.% and 1.9 Wt.% aluminium showed improved resistance to delayed cracking in comparison to a 0.6C-16Mn TWIP steel. Park et al. [60] and Bai et al. [59] looked at the effects of grain refinement on resistance to hydrogen embrittlement, with both reports finding grain refinement as a helpful mechanism in the resistance to hydrogen embrittlement by suppressing the transition of fracture mode from ductile to brittle.

2.2.8 Austenitic Stainless Steel (AUST.SS)

AUST.SS have superior mechanical properties compared to the 1st generation of AHSS, and as it is stainless steel, it also has exceptional corrosion resistance. It is crucial in AUST.SS to have enough quantities of austenitic stabilising elements so that the austenite structure can persist at room temperature. The face centre cubic structure of austenite, which has more slip systems than a body centre cubic structure, provides the steel with good toughness, strength, and ductility combinations. AUST.SS is a highly alloyed steel with between 16-26 Wt.% chromium additions and other elements such as manganese, carbon, and silicon. Some AUST.SS will also contain nickel, titanium, molybdenum, copper, niobium and others [43].

2.2.9 3rd Generation Advanced High Strength Steel

Because of the higher costs with the 2nd generation AHSS, development of the 3rd generation was needed, where the goal is to achieve similar properties to the 2nd generation but without the higher costs and alloy additions. 3rd generation AHSS steels are produced through more complex thermomechanical simulations to manipulate the microstructure evolution and achieve superior properties without substantial costs from high alloy additions. There are several thermomechanical heat treatments for 3rd generation AHSSs. Two are quenching and partitioning (Q&P) and quenching-partitioning-tempering (Q-P-T) treatments. Quenching and partitioning treatment aims to achieve a microstructure consisting of carbon-depleted martensite and carbon-enriched austenite via a controlled thermal treatment process. A schematic of Q&P heat treatment in Figure 18 [61].

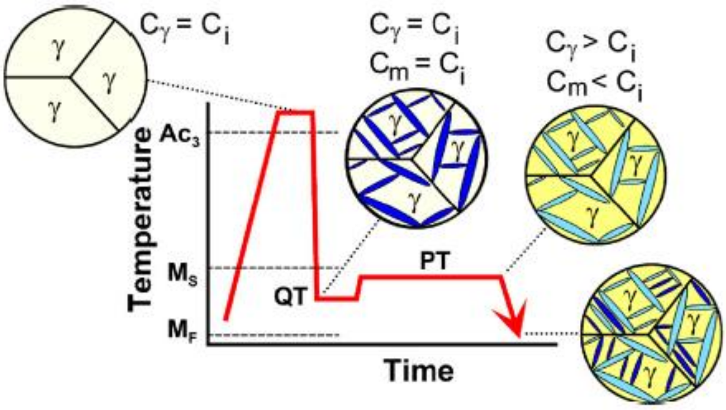

Figure 18: Q&P process schematic [61].

Q&P is a 3-stage thermal treatment which involves:

- Full austenisation of the steel above the A_r^3 temperature.
- Rapid cooling to a specified temperature, to create a controlled volume fraction of martensite.
- Partitioning treatment at the partitioning temperature allows for the carbon depletion of martensite and carbon transport to enrich the austenite.

Partitioning helps to stabilise the austenite and allows the enriched austenite to be present at room temperature once the steel has had its final quench [43]. Modifying the Q&P process led to the development of the Q-P-T process. It is achieved by adding carbide-forming elements molybdenum and niobium to the treated steels. To avoid the formation of cementite, the carbon content needs to be less than 0.5 Wt.%, as the formation could cause quench and temper embrittlement. The Q-P-T is a four-stage treatment which involves.

- Full austenisation of the steel above the A_r^3 temperature.
- Rapid cooling to a quenching temperature between the M_s and M_f to gain the maximum fraction of retained austenite.
- Partitioning treatment at the partitioning temperature allows carbon atoms to partition from supersaturated martensite into austenite and nanoprecipitation from the martensitic matrix.
- During the tempering stage, fine carbides precipitate to dig out the effect of precipitation strengthening in the AHSS and further carbon enrichment in the untransformed austenite.

This process has achieved excellent strength and formability properties compared to 1st generation and Q&P steels. Zhong et al [62] achieved a good combination of tensile strength at 1500MPa and elongation at 15%. Showing this treatment is suitable for creating ultra-high strength steels with adequate ductility.

The first industrial production of Q&P steels was done by BaoSteel in 2009 and by 2012 their cold rolled Q&P steel was commercially available. The Q&P steel was called QP980, with a tensile strength of 980MPa [8]. This steel is already being utilised within automotive BiW; typical components are shown in Figure 19.

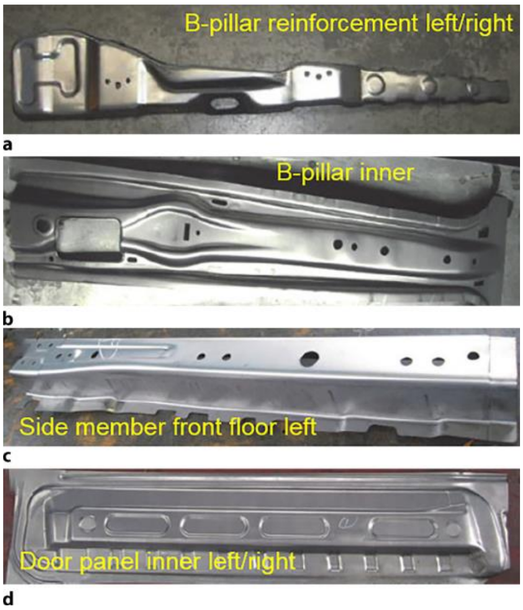

Figure 19: Automotive components using QP980: a. B-pillar reinforcement, b. B-pillar inner, c. Side member front floor left, and d. Door panel inner [8].

2.2.10 Alloying Amounts from Previous Studies and Industrially Processed QP Steels

To get an idea about the amount of alloying needed to produce Q&P steels, a selection of studied and industrially produced steels have been tabulated to compare the total alloying additions (Table 1). The industrially produced Q&P steels are marked with an asterisk, whereas the rest are produced at laboratory scale. Generally, the carbon additions are high, with them all being over 0.19 Wt.% and up to a maximum of 0.43 Wt.%. When carbon is above 0.25 Wt.%, it can cause problems during welding. Within the HAZ (heat-affected zone), high carbon martensite can form during cooling, which is extremely hard and brittle. It is common for high-carbon steels to need post-weld heat treatment. It will be interesting to target steels with between 0.15-0.2 Wt.% C, as a high proportion of Q&P steels, have C above 0.2 Wt.%. Total alloying additions in Table 1 vary from 3.19 Wt.% up to 7.69 Wt.%. To keep the additions and costs down, 4.5 Wt.% will be the maximum addition for the studied Q&P steels in this thesis.

Table 1: Alloying amounts of five industrially produced and lab scale Q&P steels.

Alloy	Reference	Composition	Total Alloying Content (Wt.%)
QP980 (*)	[63]	0.201C-1.93Mn-1.62Si	3.75
QP1180 (*)	[63]	0.204C-2.26Mn-1.74	4.20
DOCOL 600DH (*)	[64]	0.15C-0.8Si-2.5Mn-1AL-0.15Nb+Ti-1.4Cr+Mo-0.005B-0.2Cu	6.21
DOCOL 800DH (*)	[65]	0.18C-0.8Si-2.5Mn-1AL-0.15Nb+Ti-1.4Cr+Mo-0.005B-0.2Cu	6.24
DOCOL 1000DH (*)	[66]	0.23C-1.8Si-2.9Mn-1Al-0.15Nb+Ti-1.4Cr+Mo-0.005B-0.2Cu	7.69
0.2C-3Mn-1.6Si	[67]	0.2C-3Mn-1.6Si-0.06Al	4.86
H1	[68]	0.43C-0.59Mn-2.6Si-0.008Al-0.03Mo-1.33Cr	4.99
H2	[68]	0.43C-1.17Mn-2.6Si-0.008Al-0.03Mo-1.33Cr	5.57
CMnSi	[69]	0.2C-1.63Mn-1.63Si	3.46
CMnSi	[69]	0.24C-1.61Mn-1.45Si-0.3Al	3.99
HiSi	[70]	0.195C-3.5Mn-1.54Si-0.006Al	5.24
LSi	[71]	0.198C-3.5Mn-0.45Si-0.22Al	4.37
De Knijf et al.	[72], [73]	0.25C-3Mn-1.5Si	4.75
Seo et al.	[74]	0.21C-4Mn-1.6Si-1Cr	6.81
Arlazarov et al.	[75]	0.29C-3Mn-1.4Si	4.69
LCLNi	[74]	0.22C-2.42Mn-2.49Si-0.49Mo-0.72Cr	6.34
HCHNi	[74], [76]	0.39C-2.39Mn-2.64Si-0.5Mo-0.78Cr	6.7
LCHNi	[74], [76]	0.28C-2.37Mn-3Si-0.6Mo-0.71Cr	6.96
Cheng et al.	[77]	0.19C-1.53Mn-1.55Si-0.025Al-0.45Mo-1.01Cr-1.01Cu	5.77
40SiMnNiCr	[78]	0.41C-1.30Mn-1.27Si-1.01Ni-0.56Cr	4.55
Chen et al.	[79]	0.19C-1.26Si-2.82Mn-0.92Ni	5.19
Liu et al.	[80]	0.3C-3Mn-1.5Si	4.8
Seo et al.	[81]	0.41C-4Mn-1.6Si-1Cr	7.01
Xiong et al.	[82]	0.3C-2.5Mn-1.5Si0.8Cr	5.1
42SiCr	[83]	0.43C-0.59Mn-2.03Si-1.33Cr-0.07Ni-0.008Al-0.03Nb-0.03Mo	4.52
42SiMn	[83]	0.43C-0.59Mn-2.03Si-0.07Ni-0.008Al-0.03Nb-0.03Mo	3.19

2.3 CALculation of PHAse Diagrams (CALPHAD)

2.3.1 Introduction

Before the onset of software packages, such as ThermoCalc, JMatPro and others, new steels and other materials were designed using analytical methods to model and predict their performance. This approach is timely and expensive as it would follow a trial-and-error design process to develop the new steels or alloys. CALculation of PHAse Diagrams (CALPHAD) was a methodology introduced by Larry Kaufman in 1970.

Larry Kaufman and a group of international scientists in the 1970s started working on the computer calculation of phase diagrams, using the basis of experimental phase boundary and thermodynamic data [84]. Computers were in their infancy and classed as feeding computers which used punched cards and paper tape. To start, they were performing simple phase diagram calculations, where the results of this early work were first reported in London in 1971 and Munster, Germany, in 1972. Before computers, binary phase diagrams were derived using common tangents to hand-calculate Gibbs energy curves with a ruler. Common tangent construction is time-consuming, as multiple calculations are needed to construct one single diagram. This process of doing it by hand is termed phase diagram construction. This method would only work effectively for systems with just two components, and it is no longer viable once into the multi-component alloy space. This, in part, is why CALPHAD was born [85], [86].

2.3.2 Thermodynamic and Kinetic Modelling

Multiple software packages utilise the CALPHAD method to model thermodynamic data. For this thesis, the use of software packages ThermoCalc and JMatPro have been employed to design new quenching and partitioning steels. As materials are generally never in their equilibrium state, almost always metastable by nature, kinetics considerations and non-equilibrium simulations using Scheil solidification models are needed. These data sets can predict the alloy’s microstructure, behaviour, and underlying properties more accurately. When performing diffusion-based kinetic simulations, equilibrium data such as phase formation against a stepping temperature can find suitable temperatures to run subsequent kinetic simulations. For example, if the formation of a desirable precipitate is wanted, secondary heat treatment to an alloy can be run, and the step-in temperature calculation would show the temperature they start to form. Simulating this temperature can show how the precipitate will evolve and where it will start to nucleate. JMatPro as standard considers both thermodynamic and kinetics, whereas ThermoCalc is purely thermodynamics unless additional modules DICTRA and PRISMA are added to the licence [85], [87].

2.3.3 Modelling Software Utilised for Thesis

A) ThermoCalc by ThermoCalc Software with (TCFE7 – Steel and Iron alloy database)

ThermoCalc is a software tool that enables the simulation and modelling of various thermodynamic quantities and material properties. This tool provides a powerful way to gain insights into the behaviour and properties of materials under different conditions, which is critical for designing new materials with specific properties for various applications. Using ThermoCalc, materials scientists can simulate thermodynamic quantities such as the amounts and compositions of phases, transformation temperatures, solubility limits, driving forces for phase formation, activities, chemical potentials, and phase diagrams. This information is invaluable in understanding the fundamental principles that govern the behaviour of materials and in designing new materials with specific properties. In addition to simulating thermodynamic quantities, ThermoCalc can also model a wide range of material properties, including mechanical properties such as yield strength and hardness, and how these properties change with temperature and compositional variations. Other thermophysical properties, such as enthalpy, entropy, specific heat, latent heat of melting/freezing, thermal expansions, and thermal and electrical quantities, can also be modelled using ThermoCalc. ThermoCalc can also simulate equilibrium and non-equilibrium solidification processes, including freezing ranges, liquidus, solidus, solidification paths, fraction solid curves, micro segregation, shrinkage, and tearing. These simulations are essential in understanding and predicting the behaviour and properties of materials under different conditions and in designing new materials with specific properties for various applications.

Overall, ThermoCalc is a powerful tool that enables the ability to gain insights into the behaviour and properties of materials, which is essential for developing new materials with improved properties and performance for a wide range of applications [88].

B) DICTRA by ThermoCalc software with (MOBFE2 – Steel and Iron mobility database)

DICTRA is a software module that is used in combination with ThermoCalc to simulate multicomponent diffusion-based transformations. It utilises the CALPHAD method and numerical solutions of multicomponent diffusion equations to calculate a range of phenomena encountered in materials. One of the key features of DICTRA is its ability to determine how heating/cooling rates affect the amount of phases transformed. This information can be used to design materials with specific properties. DICTRA can also calculate the length of annealing time required to dissolve precipitates and the soak time and temperature necessary to homogenise an as-cast structure. These calculations provide essential insights for developing new materials. DICTRA can also simulate other phenomena such as homogenisation, growth, and dissolution of secondary phases, interdiffusion for coated materials or dissimilar joints, micro segregation, phase transformations, sintering, and coarsening of precipitate phases. These simulations help to better understand materials' behaviour under different conditions.

DICTRA is a valuable tool for simulating diffusion-based questions and phenomena in materials science. It allows the ability to gain insights into the behaviour of materials and to design new materials with specific properties and performance [89].

C) TC-PRISMA by ThermoCalc software (MOBFE2 – Steel and Iron mobility database)

TC-PRISMA is a valuable add-on module to ThermoCalc, which extends the software's capabilities to include precipitation-based calculations. Utilising the Langer-Schwartz theory and Kampmann-Wagner numerical approach [90], [91], TC-PRISMA can simulate nucleation, growth/dissolution, and coarsening under various heat treatment conditions for multicomponent and multiphase systems [92], [93]. The module enables the simulation of a wide range of precipitation-based questions, including the sequence of precipitation, the time required for precipitates to form, the yield strength/hardness of the material following specific heat treatments, and how the size distribution of precipitates varies with heat treatment [94]. It is also possible to explore how precipitates affect grain growth and how different alloying elements influence precipitation kinetics. TC-PRISMA in addition, provides the ability to estimate yield strength, hardness, and their contributions, such as grain boundary strengthening/hardening and precipitation strengthening/hardening, and study how these properties vary with temperature and the formation of precipitates. Moreover, TC-PRISMA allows concurrent simulation of nucleation, growth/dissolution, and coarsening of precipitates. It enables the calculation of nucleation and coarsening rates, volume fractions and composition of precipitates, mean radius, and particle size distribution. Additionally, using TC-PRISMA, it can simulate the time-temperature-precipitation (TTP) diagrams and continuous-cooling-transformation (CCT) diagrams, which can help predict materials' behaviour under different heat treatment conditions. Lastly, the module also provides an estimation of interfacial energy.

In summary, TC-PRISMA is an excellent tool to simulate precipitation-based phenomena in metallurgy. It offers a wide range of capabilities that help gain insights into the behaviour of materials under different heat treatment conditions and design new materials with specific properties and performance.

D) JMatPro by Sente Software (General Steels module, Version 10.2)

JMatPro is a comprehensive software package providing a range of tools for analysing and predicting the properties and behaviour of materials. With JMatPro, users can explore the mechanical properties of materials, including tensile strength, yield strength, and hardness, as well as high-temperature strength and property contributions per phase. The software also enables users to calculate solidification using Scheil-Gulliver solidification, including modifications to include C or N as fast diffusing elements in steels and thermo-physical properties during solidification. In addition, JMatPro supports the analysis of stable and metastable phase equilibria using concentration/temperature stepping calculations. It allows users to study microstructural evolution and resulting properties during heating, cooling, and isothermal holding, generate TTT/CCT/TTA/TTP diagrams and simulate precipitation kinetics. JMatPro also includes tools for analysing diffusion-controlled transformations such as martensite tempering for steels, carburization, homogenisation, and coarsening. With its wide range of capabilities, JMatPro is a valuable resource for designing new metallic materials [95][96].

i. Time-Temperature-Transformation (TTT) and Continuous-Cooling-Transformation (CCT) Diagrams, Concept and Benefits

The transformation of austenite into different microstructures during cooling involves a complex process of diffusion of atoms and nucleation and growth of new phases. The kinetics of transformation depends on factors such as temperature, time, and cooling rate. TTT diagrams provide information on the transformation kinetics at a constant temperature, showing the time required for a particular microstructure to form. In contrast, CCT diagrams show the relationship between the cooling rate and the time required for a particular microstructure to form under a range of cooling rates. By considering both TTT and CCT diagrams, users can develop new steel compositions with desired microstructures and properties and predict the microstructure and properties of steels under specific heat treatment or cooling conditions.

Furthermore, these diagrams can be used to investigate the effect of various processing variables on the microstructure and properties of steels, leading to the development of new processing techniques that improve the performance of existing steels or create new steels with unique microstructures and properties. These diagrams can also be used in conjunction with computational modelling software such as ThermoCalc to optimise the composition and processing conditions of new steel compositions with high accuracy and efficiency. In conclusion, TTT and CCT diagrams are crucial tools for developing new steel compositions with desired microstructures and properties and improving the performance of existing steels [97].

2.3.4 CALPHAD Theory

The CALPHAD method, in simplistic terms, is all about minimising a system's free energy to define universal equilibrium. Many formulas are utilised within the CALPHAD method, and a selection will be described throughout this section.

A) Spontaneous Processes

Chemistry states that a spontaneous process occurs without the addition of external energy. It can take place quickly or slowly, as spontaneity does not relate to the reaction rate or kinetics. These reactions can be endothermic or exothermic, meaning spontaneity is not necessarily related to the change in enthalpy of a process. The second law of thermodynamics determines if a process will occur spontaneously. A spontaneous process must increase the entropy in the universe and is expressed in the following equation [98].

$$\Delta S_{universe} = \Delta S_{system} + \Delta S_{surroundings} > 0 \; For\ a\ spontaneous\ process \qquad Eq.\ 1$$

When this occurs at constant pressure and temperature, the second law of thermodynamics rearranges, and a new quantity is defined. This quantity is termed Gibbs free energy of a system and will be described in the following section.

B) Gibbs free energy of a system

The second law of thermodynamics plays a vital part in any reaction, such as a chemical process or phase transformation in metallic systems. Heat/work/energy involved in reactions is considered in the first law of thermodynamics. These considerations are insufficient to determine whether a reaction will proceed, but the free energy of the reaction will. It is the change in free energy which determines if a process will occur [86].

$$\Delta G = \Delta U + p\Delta v - T\Delta S \qquad \text{Eq. 2}$$

Where;

ΔG = Free energy change.

ΔU = Change in internal energy.

p = Pressure.

Δv = Change in volume.

T = Temperature in Kelvin.

ΔS = Change in entropy.

The reaction will only proceed if $\Delta G < 0$ and if the system is at constant pressure and temperature Eq. (2) can be modified [99].

$$\Delta G = \Delta H - T\Delta S \qquad \text{Eq. 3}$$

Now a change in enthalpy term has been added to the equation. It is possible to calculate the change in Gibbs free energy using the change in enthalpy term and the entropy change of the system. Depending if ΔG is positive, negative or equal to zero will indicate if the reaction is spontaneous in the forward direction, backward direction or if the reaction is at equilibrium [100].

$\Delta G < 0$ - Exergonic process and will proceed spontaneously in the forward direction.

$\Delta G > 0$ - Endergonic process and is spontaneous in the reverse direction.

$\Delta G = 0$ - Equilibrium system, concentrations of the products and reactants remain constant.

2.3.5 CALPHAD Method

As mentioned previously, CALPHAD is all about minimizing free energy, namely Gibbs free energy of a system. Rule of mixtures can calculate this quantity [101].

$$G = \sum_i n_i \bar{G}_i \qquad \textit{Eq. 4}$$

Where

n_i = Amount of component i.

$\bar{G}_i$ = Chemical potential of component i.

$\bar{G}_i -$ is calculated using the following equation.

$$\bar{G}_i = \bar{G}_i^0 + RT \ln a_i \qquad \textit{Eq. 5}$$

$\bar{G}_i^0$ = Standard chemical potential.

R = Gas constant = 8.3144598 J. mol^{-1}. K^{-1}.

T = Temperature in Kelvin.

a_i = Activity of species i.

The next equation is for standard mass balance.

$$\sum_i a_{ij} x_i = n_j \ \ (j = 1,2 \ldots m) \qquad \textit{Eq. 6}$$

Where

a_{ij} = Number of atoms of element j in species i.

x_i = Number of moles in species i.

n_j = Total number of moles of j in the system.

Following the simple rule of mixtures, Dantzig et al in 1957 developed the linear programming approach and presented the following equation [102].

$$\frac{G}{RT} = \sum_{i} x_i \left(\frac{\bar{G}_i^0}{RT}\right) + x_{total} \sum \left(\frac{x_i}{x_{total}}\right) ln \left(\frac{x_i}{x_{total}}\right) \qquad \textit{Eq. 7}$$

Where

$x_{total} = \sum_i x_i$

Other variables are the same as previous equations. This equation and model are one of the most important used within the CALPHAD method and are the basis for the software packages used within this thesis.

2.3.6 ThermoCalc - Types of Calculations

This section will describe the different calculations used within ThermoCalc.

A) Equilibrium Calculator

ThermoCalc provides an equilibrium calculator that allows for equilibrium-based calculations to be performed. The calculator can be created from set templates or added to the system definer — the configuration window inputs settings for conditions, functions, and options. The conditions tab defines conditions for the stepping or mapping axis variables. The advanced mode is available for complex calculations. For example, if the A_r^3 temperature is required in steels, the BCC phase can be fixed to zero moles. The calculation will then show the temperature where BCC is at 0 moles. Functions and quantities can be defined for calculations and plots in the functions tab. In the options tab, numerical settings that determine how equilibria are calculated can be changed. The equilibrium calculator is used for single-point equilibrium, one-axis, grid, and phase diagram calculations. For single-point equilibrium, the equilibrium is calculated at a single point with no axes. The results can be viewed in the event log or a table renderer. One-axis calculation varies either temperature or elemental amount of one element on the X-axis. In grid calculations, equilibrium is calculated for each single grid point, which is varied by a two-dimensional grid. Finally, two or more independent mapping variables usually construct the phase diagram within a specific space. ThermoCalc equilibrium calculator is a powerful tool offering a wide range of options for equilibrium-based calculations.

B) Scheil-Gulliver Calculator

Scheil-Gulliver calculations are a type of non-equilibrium transformation used in ThermoCalc and JMatPro. This model was first formulated by Gulliver in 1913, as a qualitative description of solute redistribution during solidification [103]. It has two main assumptions; no diffusion takes place in the solid phase, and solid redistribution in the liquid phase is infinitely fast [104]. In 1942 Scheil presented the following differential equation (8) and its analytical solution (9) [105].

$$(C_L - S_S)\delta f_S = (1 - f_s)\delta C_L \qquad \textit{Eq. 8}$$

$$C_S = kC_0(1 - f_S)^{k-1} \qquad \textit{Eq. 9}$$

Where

C_S = The local composition of the solid.

C_L = The local composition of the liquid.

k = C_s/C_L, which is the partition coefficient.

C_0 = The base composition.

f_s = Fraction of solid.

In ThermoCalc, there are several options for Scheil-Gulliver simulations. These are classic Scheil with or without fast diffusing elements, such as carbon or nitrogen, Scheil with back diffusion in the primary phase and Scheil with solute trapping for faster solidification speeds seen in additive manufacturing applications. For this thesis, classic Scheil with and without fast diffusion and Scheil with back diffusion in the primary phase have been used and described in further detail in the following section.

.i Classic Scheil (with or without fast diffusion)

When using classic Scheil, the following assumptions are set:

- Diffusion in the solid phase is assumed to be zero.
- In the liquid phase, diffusion is assumed to be infinitely fast.
- The interface between liquid/solid is in thermodynamic equilibrium.

Starting at either the liquidus or a selected temperature, it will then decrease step by step for a classic Scheil simulation. As the temperature drops below the liquidus, the equilibrium amount and composition of the solid-liquid phase are calculated. At the next temperature step, removal of the solid phase from the system, with the remaining liquid phase used for the following calculation. This process repeats until the liquid phase disappears, indicating the solidus temperature and overall freezing range. This calculation uses the assumptions above, but for alloy systems with interstitial elements, such as steels, the assumption of no solid diffusion is incorrect as interstitial elements have rapid diffusion rates. For this reason, the model is modified, allowing the user to set fast diffusing elements [106], [107].

.ii Scheil with Back Diffusion in the Primary Phase

This model uses the thermodynamic and mobility databases to consider the actual back diffusion of all elements in the primary solid phase. For back diffusion, a fast-cooling rate would provide a similar result to classic Scheil as there is less time for back diffusion. A slow cooling rate would allow time for almost complete back diffusion, with the solidification simulation closer to an equilibrium calculation. The solidification domain is also required, which usually corresponds to the secondary dendrite arm spacing. An empirical model used in ThermoCalc calculates the secondary arm spacing, dependent on the cooling rate used. As with other Scheil models, there are several assumptions: Diffusion of all elements in the primary solid phase is calculated using mobility data, domain size and cooling rate [108].

- Infinitely fast diffusion of all elements in the liquid phase.
- The interface between liquid/solid is in thermodynamic equilibrium.

2.4 Literature Conclusion

- Each step in producing steel influences the microstructural evolution and resulting properties. Each step must be carefully controlled. For example, hot rolling reductions help to break the cast structure and form new equiaxed grains, which can lead to a finer grain structure. During each rolling pass, strain is imparted, increasing the dislocation density and the materials' work hardening ability.

- More advanced thermomechanical heat treatments can achieve comparable properties to the highly alloyed 2nd generation AHSS.
- Quenching and partitioning heat treatments produce steels with excellent strength/elongation properties.
- Vital elements for Q&P steels are carbon, manganese, and silicon.
- BAO Steels QP980/1180 are already being utilised for automotive BiW, which shows that Q&P steels are suitable for these applications.
- Most Q&P steels have only been produced on the laboratory scale. There is only a minimal number available commercially.
- In industrial settings the complexity of heating the steel back up after quenching for the partitioning stage, shows the need to find suitable one-step Q&P steels.
- A lot of the researched Q&P steels have high carbon contents of > 0.2 Wt.%. Carbon contents will be kept between 0.15-0.2 Wt.% to improve weldability. Medium carbon steels (0.3-0.6 Wt.%) are known to be prone to cracking during welding applications.
- CALPHAD approach using a combination of ThermoCalc and JMatPro can be utilised to find suitable Q&P compositions.

Chapter 3

Experimental

3. Experimental

This section delves into the modelling techniques employed in this thesis for Tata tubes 3827 and 3832 and the creation of novel Q&P steels. The design of heat treatment and the usage of advanced software packages ThermoCalc and JMatPro, which rely on thermodynamics and kinetics, are described. Secondly, the processing of the novel Q&P alloys, followed by a the Gleeble 3500 heat treatment procedure. Finally, a detailed methodology encompassing the mechanical testing and characterization of the alloys will be covered.

3.1 Modelling Utilised in Thesis

In the upcoming sections, the complexities of heat treatment design will be examined for all the alloys that have been thoroughly studied. Additionally, the domain of thermodynamic and kinetics-based simulations will be discussed.

3.2 Tata Tubes 3827 and 3832

Both 3827 and 3832 are low alloyed Tata tube materials, where the objective was to see if modifying the heat treatment regime could improve the properties. Ultimately the purpose of studying these steels was to lay the foundations to develop the new Q&P steels designed throughout this thesis. These steel grades are very lean, with the main additions being C, Mn, and Si, and from being able to drastically improve the properties through cleverly designed heat treatments to induce desired microstructural evolution it has set the groundwork by.

- Using JMatPro to design the heat treatments from simulating TTT and CCT diagrams.
- Using ThermoCalc to calculate transformation temperatures and how varying the elemental amount affects these temperatures.
- Set the starting point of elements (C, Mn, and Si) to develop new Q&P steels.

Table 2 below illustrates the composition of each grade. The following section will cover the heat treatment design using JMatPro to simulate TTT and CCT diagrams and ThermoCalc to study elemental effects on transformation temperatures.

Table 2: 3827 & 3832 composition (Wt.%).

Grade	Gauge (mm)	C	Mn	Si	Cr	Ni	P	S	Nb
3827	1.5	0.147	1.421	0.186	0.025	0.022	0.016	0.009	-
3832	1.5	0.141	1.377	0.185	0.02	0.023	0.016	0.005	0.033

3.2.1 JMatPro

Transformation information from simulated CCT and TTT (continuous cooling transformation diagrams and time-temperature transformation diagrams) diagrams in JMatPro software (version 10.2) was used to create the heat treatments. First input the steel composition and using the formula, predict the austenitic grain size, and then simulate the CCT and TTT diagrams. TTT diagrams provide transformation temperatures and times, for example, A_r^1, A_r^3, M_s, $M_{50\%}$, and $M_{90\%}$. The CCT shows the predicted formation phases, tensile, Yield and hardness for different cooling rates. Also, the heat treatments must follow the heating and cooling sections on Tata's CAPL line. Using Tata's in-house CAPL mimic (see section 3.3.4 for further information on CAPL Mimic) ensures that the heat treatments accurately align with each section of CAPL. The line speed dictates the time spent in each section of the annealing process. Tata's continuous annealing process line incorporates these stages; ramp 1, ramp 2, soak start, soak hold, CGJC start, CGJC hold, HGJC start, HGJC hold, Overage, second cooling and final cooling (Figure 5, section 2.1.5). Heat treatments for 3827 and 3832 had the line speed fixed at 90mpm, with the only variables being the CGJC and HGJC temperatures. For all the heat treatments, a fixed soak temperature of 840°C (40°C below the maximum CAPL temperature and 20°C above the A_r^3), overage end temperature of 280°C, second cooling down to 190°C and final cooling to 40°C [109]. The variable CGJC temperatures were 700°C, 660°C and 620°; and as these temperatures reduce, it promotes the formation of pro eutectoid ferrite; For the HGJC, 420°C promotes bainite formation, which cools through the lower temperature bainite region, 390°C is between M_s and $M_{50\%}$, which increases the amount of martensite formation and 360°C is below the $M_{50\%}$ and promotes a more significant proportion of martensite. Figure 20 illustrates a schematic for the different temperatures. There were nine different heat treatment schedules for 3827 and 3832. Figure 21 is a graph showing the different heat treatment routes.

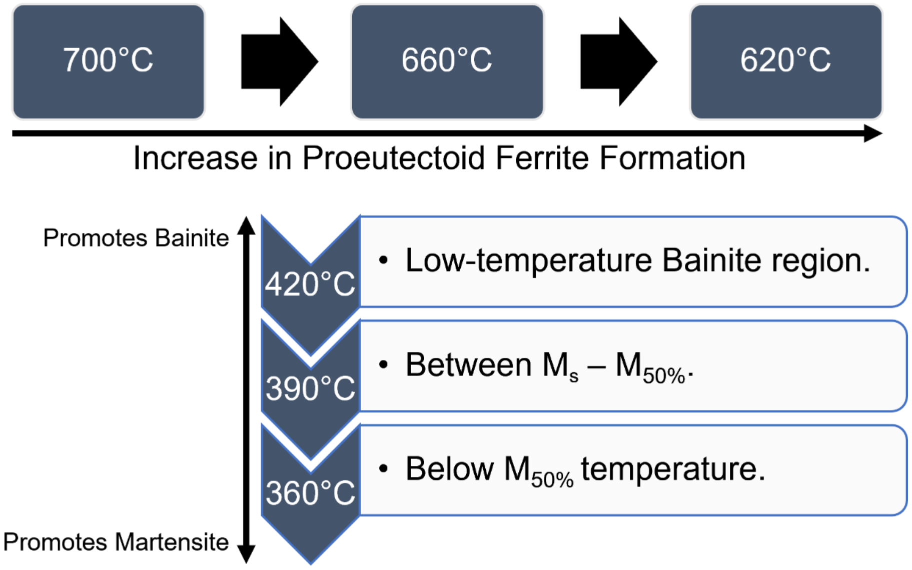

Figure 20: Phases in relation to different CGJC and HGJC temperatures.

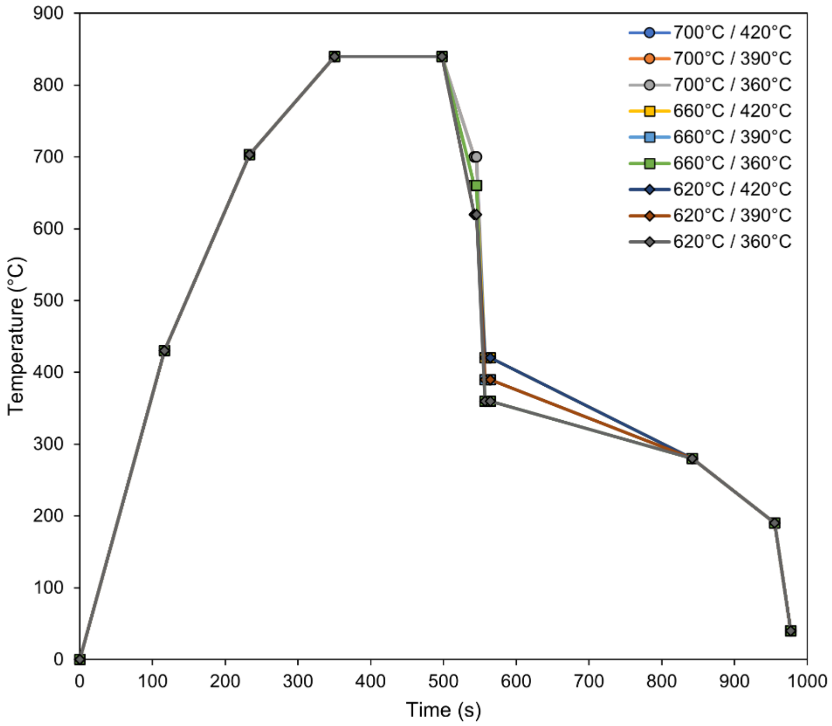

Figure 21: 3827 & 3832 annealing cycles.

3.2.2 ThermoCalc

For validation, a simulation was run in ThermoCalc to directly compare against the A_r^1 and A_r^3 temperatures calculated using JMatPro.

A) ThermoCalc A_r^3 and A_r^1 Calculation Setup

First, select the graphical mode in ThermoCalc (version 2020a) and both the thermodynamic and mobility databases (TCFE7 and MOBFE2). Select single-point equilibrium; this opens a project tree composed of a system definer, equilibrium calculator and a table renderer. On the system definer, input the steel composition in the element tab and to reduce simulation time, remove any phases on the phase and phase constitution tab, such as graphite and diamond, as these will not form in real-life conditions. On the equilibrium calculator, use the pre-inputted amounts for temperature, pressure and system size and perform the simulation. Create a new successor termed equilibrium calculator 2. The system will already be defined, so it is just the configuration of simulation settings. On equilibrium calculator 2, using the advanced mode, un-tick the temperature condition and add a new condition as fix phase – BCC_A2 – 0.0 moles. In the functions tab set the quantity definition to Q1 = Temperature in Celsius and function definitions to A3 = Q1. On table renderer 2, change the drop down to function – A3 – Q1 and perform the simulation. The results tab will show the A_r^3 temperature, system calculations, and stable and fixed phase information. Similarly, for A_r^1 temperature, instead of fixing BCC_A2 to 0.0 moles, fix Cementite to 0.0 moles and set the function to A1 = Q1 instead.

B) ThermoCalc Elemental Effects on the Ar^3 Temperature

Use the same TCU file (ThermoCalc file extension) from the previous calculation (3.2.2 A) and complete the following steps to calculate the effects of carbon, manganese, and silicon on the A_r^3 temperature. Create a new successor off equilibrium calculator 2 and use the same configuration previously used in advanced mode but with the addition of a one-axis simulation. For the one-axis simulation, select either C, Mn or Si with the composition varied between a minimum and maximum. Next, set the functions tab to A3 = Q1, and create a new successor called plot renderer. On the plot renderer tab, set the X-axis to axis variable – composition – C, Mn, or Si – mass per cent and axis type – linear. For the Y-axis, set the axis variable to – function – A3 – Q1 and axis type – linearly, and perform the simulation. The simulation was run once for each element, with the resulting graphs showing how each element affects the A_r^3 transformation temperature.

3.3 Quenching and Partitioning Steels

This section covers how the Q&P steels were designed, what factors were used and the limitations of CAPL.

3.3.1 Alloy Design

This section will go through the design procedure for two C-Mn-Si, one C-Mn-Si-Cr, and one C-Mn-Si-Mo alloys. Experiments were designed in excel with levels set for each element to be progressively analysed. Important transformation information such as A_r^1, A_r^3, M_s, $M_{50\%}$, $M_{90\%}$, and transformation times was tabulated and analysed to find which elements fit best with the processing windows of Tata's CAPL line. JMatPro software was utilised via the simulation of TTT and CCT diagrams. The aim was to find compositions which can achieve a microstructure composed of bainite, martensite, and retained austenite or M-A constituent through 3rd generation heat treatments, namely quenching and partitioning. One of the requirements of these types of steel is to ensure that cementite formation is suppressed, as shown in literature when Si additions are >= 1.4 Wt.% [37], [110]–[113], cementite formation supressed. By suppressing the formation of cementite, there is more free carbon in the system to diffuse from either martensite or bainite to austenite during the isothermal hold section. When austenite is sufficiently saturated with carbon, the austenite phase field extends to room temperature stabilising the austenite phase[38], [114]–[117].

3.3.2 Element Selection

Before designing the steels, the elements of interest need to be decided. Elements have different effects on the microstructure evolution during thermomechanical processes. The elements need to be balanced to produce a Q&P whilst fitting in with the processing windows of CAPL.

Carbon

- The amount of carbon controls the hardness and strength of the steel and response to heat treatment (hardenability).

- The kinetics of ferritic transformation is significantly affected by carbon. Carbon slows down diffusion, lowers the A_r^3 temperature, and shifts the entire ferrite area in a CCT diagram to the right.

Silicon

- Suppresses cementite formation when alloying is >= 1.4 Wt.%.
- Ferrite stabilising element.

Manganese

- Provides hardenability and lowers the A_r^3 temperature.
- The amount of manganese affects the kinetics of ferrite transformation.

Chromium

- Chromium provides further hardenability and delays the bainitic and pearlitic transformations.

Molybdenum

- Provides hardenability and has been shown in the literature to achieve more significant austenite fractions, and sensitivity to partitioning time is reduced. Mo also retards bainite formation and reduces the critical cooling rate needed for martensite formation [61].

A) C-Mn-Si

Silicon is added to these compositions to ensure cementite suppression is achieved. Si is a ferrite stabilizing element. It increases the A_r^1 temperature, so enough Mn and C are added to ensure the A_r^1 is below 700°C [118], [119]. A DOE procedure was used to identify suitable compositions for C-Mn-Si. CCTs and TTTs were generated for many different combinations of C-Mn-Si, with the transformation temperatures/times and property information tabulated to analyse. Additionally, a secondary step of quench property simulation was completed to narrow down to the two chosen compositions for lab casting.

B) C-Mn-Si-Cr

Chromium is added to these compositions as it provides further hardenability and delays the bainitic and pearlitic transformations, making these compositions suitable for 1-step Q&P processing [83], [120]. A DOE procedure was used to identify suitable compositions for C-Mn-Si-Cr alloys. CCT's and TTTs were generated for a large number of C-Mn-Si-Cr compositions, with transformation temperatures/times and property information tabulated to analyse. Additionally, a secondary step of quench property simulation was completed to narrow down to the two chosen compositions for lab casting.

C) C-Mn-Si-Mo

Molybdenum also provides hardenability and has been shown in the literature to achieve more significant austenite fractions, reducing sensitivity to partitioning time [61]. Mo also retards bainite formation and reduces the critical cooling rate needed for martensite formation [121]. To identify a suitable composition for C-Mn-Si-Mo, a DOE procedure was used. CCTs and TTTs were generated for many different C-Mn-Si-Mo compositions, with transformation temperatures/times and property information tabulated to analyse. Additionally, a secondary step of quench property simulation was completed to narrow down to the two chosen compositions for lab casting.

3.3.3 Tata Continuous Annealing Process Line (CAPL) Capabilities

Within the scope of the project, these steels need to be able to be produced on Tata's CAPL line without having to make any changes to the existing infrastructure. Figure 22 illustrates a schematic of the CAPL line at Port Talbot.

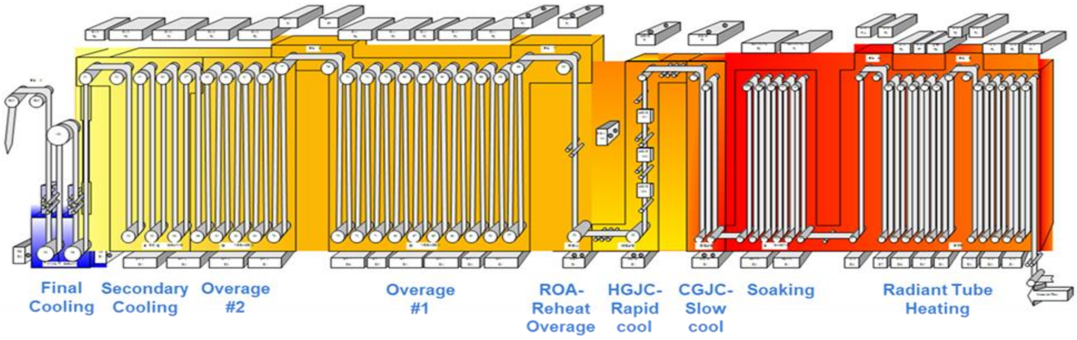

Figure 22: CAPL Schematic.

With Q&P steels, the microstructure must be fully austenitic before rapid cooling down to the calculated quenching temperature. The maximum soak temperature on CAPL is 880°C, so the A_r^3 needs to be less than 840°C to ensure a fully austenitic microstructure. Additionally, the CAPL line requires a slow cool section after soaking.

The maximum slow cool temperature is 700°C, so the time for ferrite transformation must be longer than the slow cool section to ensure no ferrite formation. The most critical stage of Q&P steel is the partitioning step, where carbon diffuses away from the martensitic phase enriching the austenitic phase and stabilising the phase to room temperature. This requires the optimum quenching temperature to be isothermally held throughout the overage section, which is possible on Tata's CAPL line. Tata no longer has a reheating overage section, so the 1-step Q&P heat treatment will be the focus. From Figure 23, it is possible to see that the annealing line is broken down into several sections. The time the strip steel will travel through each section is determined by the line speed. Due to this, accurate annealing cycles can be designed which can be reproduced on CAPL. To ensure the heat treatments are accurately designed Tata's inhouse CAPL MIMIC will be used and described in section 3.3.4. Notably, Tata no longer have a re-heating overage section, which is why only one-step Q&P steels will be explored throughout this thesis. Figure 23 demonstrates a typical annealing cycle including the names for each section.

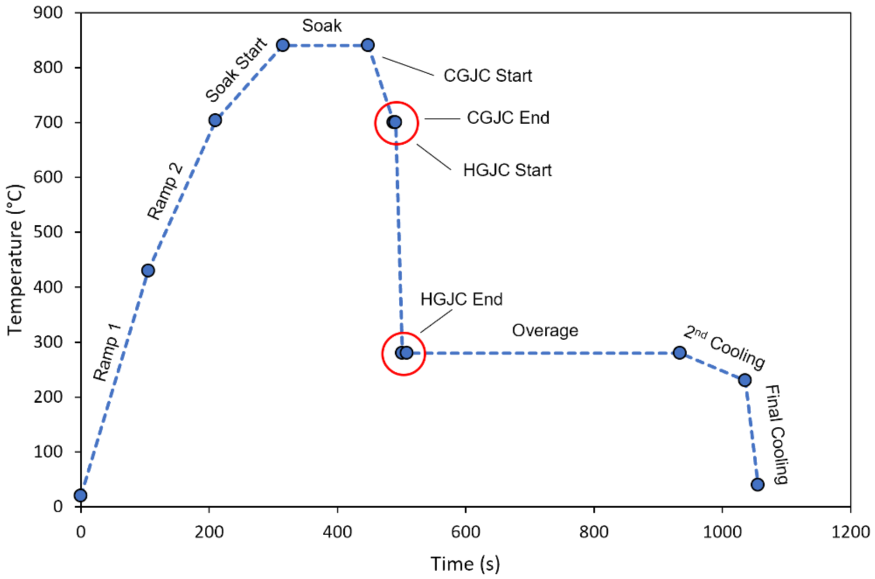

Figure 23: CAPL annealing cycle.

3.3.4 CAPL MIMIC

Tata uses a specialised spreadsheet called CAPL MIMIC to ensure precise heat treatment simulations for strip steel passing through each section of CAPL (Figure 22). By Tata accurately calculating the distances of each section, the spreadsheet can determine the time it takes for the strip steel to pass through each section based on the line speed. To generate an exact annealing cycle representative of CAPL, the following inputs are required:

- Line speed
- Soak
- CGJC
- HGJC
- OA
- 2nd cooling temperature

These inputs will generate a CAPL cycle which can be programmed into laboratory-based annealing simulators such as a Gleeble, HDAS or other thermo-mechanical simulators. This allows for precise and effective heat treatment simulations in the laboratory.

3.3.5 Design Factors

When heat-treating Q&P steels, they must be fully austenitic before quenching but remain below the maximum operating soak temperature for CAPL. The CAPL line includes a slow cool section after soaking, during which ferrite formation needs to be suppressed (CGJC). The line speed determines the duration of the slow cool section, and for a line speed of 100mpm, the total time spent through the CGJC, including cooling, and holding, is 42.5s. The gauge of the material is one factor that dictates realistic line speeds. However, the chosen speed of 100mpm is justified as it relates to the maximum possible cooling rate achievable on the Gleeble 3500. Furthermore, current TATA grades such as DP1000 and CP1000 are processed at line speeds between 90-150mpm, and since they are comparable in terms of strength and processing, reinforces using 100mpm as the line speed for heat treating the novel Q&P steels designed throughout this thesis.

Factor 1: $A_r^3 < 840°C$

Factor 2: $A_r^1 <= 700°C$ or Ferrite transformation times sufficiently suppressed

Factor 3: 1% Ferrite transformation time > 20s

Factor 4: Hot rolled tensile stress < 700MPa

Factor 5: Ultimate tensile stress >1300MPa

Factor 6: Total elongation > 12%

Factor 7: Alloying additions < 4.5 Wt.%

Factor 8: Vickers hardness > 400Hv

3.3.6 TTT and CCT Calculation Using JMatPro

- Input composition, select advanced CCT or TTT and predict the austenitic grain size using:

$$D^a = Ct \exp\left(\frac{-Q}{RT}\right) \quad \text{Eq. 10}$$

Where:

D = Grain Size in mm, Q = Activation Energy

R = Gas Constant, T = Temperature in Kelvin

T = Time in seconds

a and C are material constants

- CCT or TTT generated using soak temperature and time as the variables in the formula above.

Element combinations were set as C-Mn-Si, C-Mn-Si-Cr and C-Mn-Si-Mo. And using a design of experiments in excel and setting levels for each element, with each different composition analysed. First, the simulated compositions were analysed against factors 1 and 2 and all the compositions that met these factors were then further analysed against factor 3. After all simulations, two C-Mn-Si, one C-Mn-Si-Cr, and one C-Mn-Si-Mo composition met all three factors.

3.3.7 ThermoCalc

The four compositions were studied in ThermoCalc. As for the mechanism of partitioning to be successful, there needs to be enough free carbon in the system for the austenite phase to be stabilised. So, it is vital that the competing reactions, such as the formation of cementite and other precipitates, are suppressed as these take up carbon in the system. Thermodynamic studies using TCFE7 and MOBFE2 databases were completed on each of the four alloys to see if the formation of cementite and precipitates was sufficiently suppressed.

i. Property Diagrams

A) Phase Formation

A temperature step calculation to compute the mass fraction of all phases. First, the composition in weight per cent is inputted along with the steel database. Then, the temperature steps from 1600°C down to 0°C in 100°C steps. At each temperature step, the mass fraction of phases is calculated. To view the results, the X-axis is the temperature, and the Y-axis is the mass fraction of all phases. Each corresponding phase will have a different coloured line plot, which allows relative ease in identifying the proportion of phases at different temperatures.

B) Gibbs Energy of Formation

To compute the most favourable phases to form, a temperature step calculation is completed. First, the composition in weight per cent is inserted along with the steel database. Then, the temperature steps from 1600°C down to 0°C in 10°C steps. At each temperature step, the Gibbs energy of all phases is calculated, which shows which phases are most likely to form, depending on which shows the lowest energy. Similarly, to the phase formation calculation, the Y and X-axis need to be set, X-axis is again set to a temperature, but the Y-axis is set to Gibbs energy of all phases. Again, each corresponding phase will have a different coloured line plot, making it simple to identify which phases show the lowest Gibbs energy.

C) Mass Fraction of Carbon in all Phases

A step-in temperature simulation was performed to calculate the mass fraction of carbon in all phases. First, the relevant databases were selected to start the simulation, and the composition was inputted in weight per cent, with iron set to balance. The condition was set to decrease the temperature from 1600°C to 0°C in 1°C steps. At each 1°C interval, the mass fraction of carbon in all phases is calculated. To view the result, the X-axis is set to temperature and the Y-axis variable was set to, Amount of Component in Phase – Per Mass in Gram – Carbon – All Phases – Grams. The Y-axis set to these conditions will show the result in weight per cent. Each corresponding phase will have a different coloured line plot, identifying the carbon mass fraction in all phases at different temperatures.

ii. TC-Prisma

A) Bulk Precipitate Volume Fraction

Before the precipitation simulation can be performed, a simple one-axis simulation must be completed. The formation of phases was calculated using the TCFE7 and MOBFE2 databases and stepping the temperature from 3000°C to 100°C in 50°C steps. A plot renderer was used with the X-axis set to Temperature – Celsius and axis type to linear, with the Y-axis set to Amount of phase – No normalization – All phases – Mole and again axis type linear. From this calculation, take note of the precipitates for the subsequent precipitation calculation. Next, right-click on the system definer and create a new successor called precipitation calculator 1. In the precipitation calculator, set the composition unit to mass per cent, matrix phase to BCC_A2 and add the precipitate phases present from the previous calculation. For each precipitate, set the nucleation sites to bulk and interfacial energy to be calculated. For these simulations, a non-isothermal calculation was selected, which allows you to create a thermal profile. An accurate representation could be simulated by using the designed heat treatments for the four alloys, namely, the cycles that aim to achieve a 40% primary martensite formation. To reduce simulation time, the heating ramps were removed, with the simulation starting from the soak hold down to final cooling, whilst still following the same times the cold rolled steel would travel through these sections on CAPL. Figure 24 shows the thermal profile used for the 0.15C-2.6Mn-1.4Si alloy. With all the settings now set, a plot renderer is created off the precipitation calculator, with the Y-axis axis variable set to Volume fraction – precipitate (cementite, M23C6, M5C2, M7C3 or M6C), with axis type set to logarithmic. Multiple Y-axis will be needed, depending on the number of precipitates formed in the previous calculation. The X-axis will be set to time, with the unit in seconds and axis type logarithmic. With the simulation set up and the axis variables set, the simulation was then performed, with the resulting graph showing the volume fraction of precipitates with time. This calculation was completed for all four alloys.

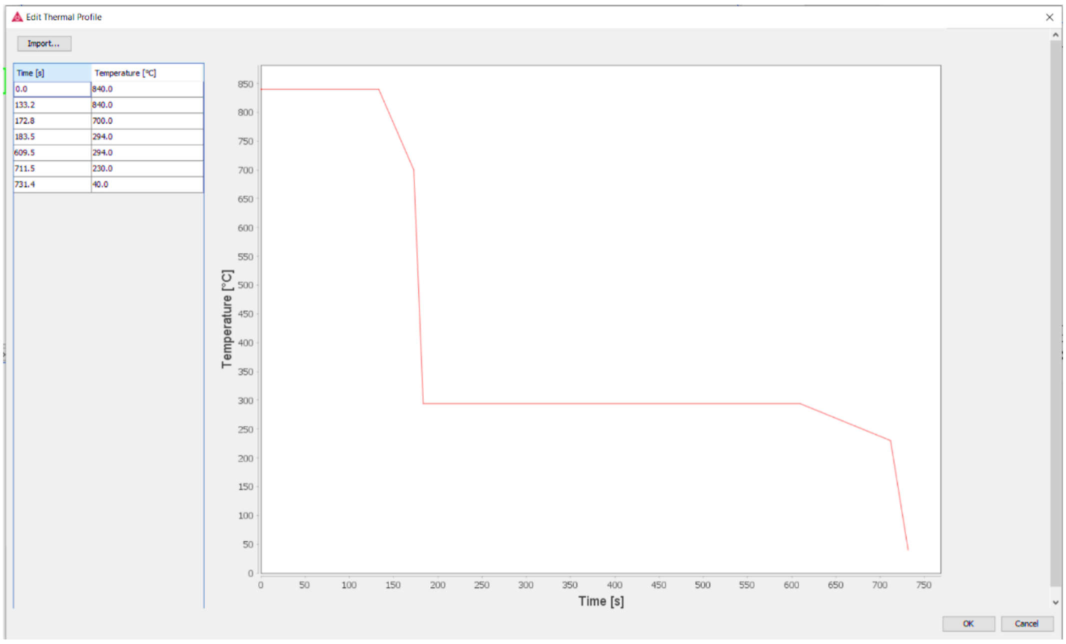

Time [s]	Temperature [°C]
0.0	840.0
133.2	840.0
172.8	700.0
183.5	294.0
609.5	294.0
711.5	230.0
731.4	40.0

Figure 24: Thermal profile used for the bulk precipitate volume fraction calculation for MnSiC$_{(0.15\%)}$.

.iii Scheil-Gulliver Calculator

Multiple forms of Scheil solidification were run for all four alloys to see how the phase proportions and freezing range would change. Types of Scheil solidification simulations include classic Scheil, classic Scheil with fast diffusion, back diffusion, and back diffusion with fast diffusion. First, define the system and select Scheil calculator to set up the calculation. For Scheil simulations, set the temperature to start from the liquidus and the temperature to step in 1°C intervals. The equilibrium amount and composition of the solid-liquid phase are then calculated at every temperature step. As the simulation steps to the next, any solid phase will be removed from the system with the remaining liquid used for the following calculation. These calculations will continue until all the liquid is removed. To run fast diffusion with classic Scheil, select carbon as a fast-diffusing element, or to run back diffusion, select back diffusion instead of classic Scheil. Similarly, select carbon as a fast-diffusing element to run fast diffusion with back diffusion. To view the results, either a plot renderer or table renderer can be used. The plot renderer will show the freezing curve and show how the phases change in relation to temperature. For analysis and ability to retrieve additional information a table renderer is more useful, as it gives the ability to see the phase proportions, freezing range and thermo-physical properties.

3.4 Heat Treatment Design

Using the Koistinen-Marburger relationship in conjunction with the simulated martensite start temperatures from JMatPro, the optimum quenching temperatures were calculated for a primary martensite fraction of 40%, 50% and 60%. See equation 12.

3.4.1 Koistinen-Marburger Relationship

Calculates the primary Martensite fraction.

$$f_M^{T_q} = 1 - e^{-1.1\times10^{-2}(M_s - T_q)} \qquad \text{Eq. 11}$$

Where:

$f_M^{T_q}$ = Primary Martensite Formation.

M_s = Martensite Start Temperature.

T_q = Quenching Temperature.

Now with the calculated quenching temperatures the heat treatment schedules can be created using Tata's in house mimic. CAPL mimic replicates the temperatures and times for each section of the CAPL line, controlled by the line speed.

3.4.2 1-Step Quenching and Partitioning Annealing Cycles

This section will show the designed heat treatment cycles for the MnSiC$_{(0.2\%)}$ Q&P alloy (Figure 25), with the cycles for MnSiC$_{(0.15\%)}$, CMnSiCr and CMnSiMo included in the appendix. The novel alloys must be heat-treated to achieve the desired microstructure and resulting properties. As mentioned previously, one-step quenching and partitioning heat treatments will be used. Two different one-step quenching and partitioning schedules were created (HT1 and HT2), each comprising three different cycles. For all cycles, the soak was fixed at 840°C, CGJC at 700°C, 2nd cooling at 230°C, and final cooling at 40°C. Times for each section of the annealing cycle were set depending on the line speed. As the line speed was fixed at 100mpm, the time for each section was also fixed. To ensure the times for each section relate to CAPL, TATAs in-house mimic is used to compute the cycles accurately. The only variables being the combined HGJC, and OA section denoted the partitioning stage, which was calculated using the Koistinen-Marburger relationship. Using the K&M relationship, the quenching temperature for a 40%, 50%, and 60% primary martensite formation was calculated. The main difference between HT1 to HT2 is heat treatment schedule two incorporates all the same sections and temperatures as the first heat treatment schedule but includes a 10°C drop in temperature during the partitioning step. This 10°C drop will determine if it affects the resulting properties and how sensitive the alloys are to any temperature fluctuation (Figure 26).

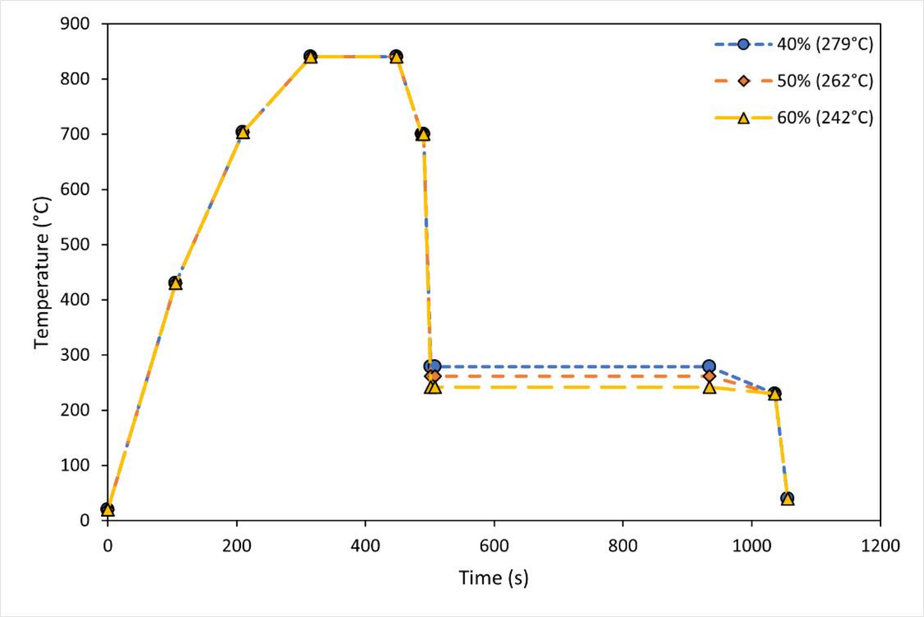

Figure 25: MnSiC$_{(0.2\%)}$ annealing cycles.

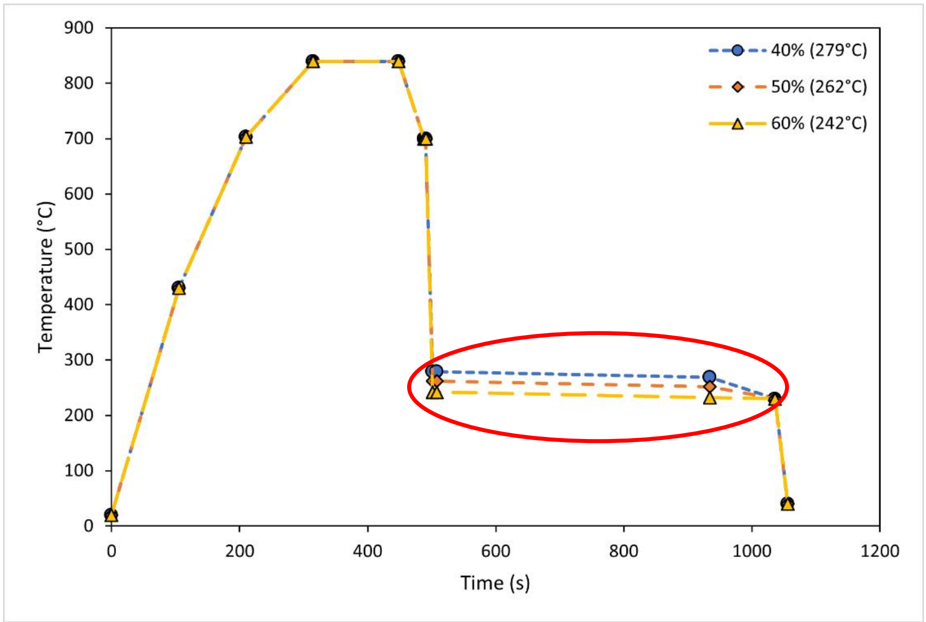

Figure 26: MnSiC$_{(0.2\%)}$ annealing cycles with 10°C drop.

3.4.3 Martensite Tempering Simulation (JMatPro)

A tempering simulation was run using the partitioning temperatures to assess if the designed HT1 heat treatments would get tensile stresses > 1300MPa. HT1 heat treatment comprises twelve different heat treatments, three for each composition. The quenching/partitioning temperatures were designed using the Koistinen-Marburger relationship, described in further detail in section 3.4.1. The heat treatments were designated as HT1: A-L, and the input temperatures were 279°C, 262°C, 242°C, 294°C, 276°C, 257°C, 280°C, 263°C, 243°C, 299°C, 283°C and 262°C. As mentioned, three temperatures for each composition were deduced to increase the level of martensite as the temperature lowered. The heat treatments were designed to be industrially viable, with each section relating to Tata's CAPL line and following the exact time at each section dependent on the line speed. The selected hold time was 4.2 minutes which is how long each of these steels is held at the partitioning temperature during the overage section. Martensite tempering was run for each alloy with these settings, providing results for hardness (Hv) and tensile stress (MPa). These results will be compared against the tensile and hardness results for HT-1.

3.4.4 Jominy Hardenability Simulation (JMatPro)

One way to measure the hardenability of steels is through the Jominy hardenability end quench test. This test will measure the capacity of the steel to harden in depth under a set of conditions. The chemical composition of the steel will drive its underlying hardenability. JMatPro provides a Jominy hardenability simulation, and the simulation setup will be described in this section. First, the four selected Q&P compositions from the transformation temperature analysis are inputted into JMatPro using the general steels module. The initial microstructure was selected to be normalised, and the austenisation temperatures were set to 60°C above the A_r^3. For the designated alloys, $MnSiC_{(0.2\%)}$, $MnSiC_{(0.15\%)}$, CMnSiCr and CMnSiMo, the inputted temperatures were 871°C, 885°C, 871.5°C and 888°C. A 30-minute hold time at this temperature was used with the length of the bar set to 10cm with 1cm steps. The cooling rate will vary along the length of the bar and will indicate the hardenability of the alloy, where initial cooling is very rapid, and at the other end of the bar, it would be equivalent to air cooling. Rapid cooling will promote martensitic structures and air cooling ferritic-pearlitic structures.

3.5 JMatPro Property Simulation using Measured Tensile Stress

Due to delays in getting material processed because of Covid-19, the full bank of properties have not been completed for the chosen alloys. After tensile testing, the four cycles with the best combinations in properties have been simulated in JMatPro to get fatigue. The following section will describe the simulation setup for fatigue.

3.5.1 Fatigue (JMatPro)

The optimised cycles from the tensile testing analysis were HT1-H&I for the CMnSiCr alloy, HT2-C for the $MnSiC_{(0.2\%)}$ alloy, and HT2-E for the $MnSiC_{(0.15\%)}$ alloy. No cycles were put forward for the CMnSiMo alloy as this alloy exceeded the hot rolling load limit during the hot rolled tensile testing, and its properties were inferior to the other cycles. Fatigue within JMatPro uses a low cycle fatigue mode controlled by strain amplitude and frequency. For all simulations, the strain amplitude was set to 1%, frequency 1 Hz, temperature 25°C, b = -0.1, which is the fatigue strength exponent and c = -0.9, which is the fatigue ductility exponent. These simulations estimate the fracture strain, fracture stress and young's modulus.

3.6 Alloy Processing

Before any heat treatments and experiments can be run on the designed alloys, they first need to be processed down to a cold-rolled strip steel.

3.6.1 VIM Casting

The ingots were cast using a 50 kg vacuum induction furnace under an inert atmosphere. Pure electrolytic iron and subsequent additions of elements were applied after each other. After carbon deoxidation was performed, analysis of C, S, P, N and O was made during the final composition adjustments.

3.6.2 Cogging

To reduce the gauge down to 36mm transfer bar, the ingot was heated to 1230°C and held for 1 hour before being placed between shaping dies, which encourages the final shape of the ingot. This works by rotating the hot ingot between the two dies causing the ingot to be repeatedly struck. Where, each subsequent blow causes the ingot to become longer, which lengthens and homogenises the grains of the metal.

3.6.3 Transfer Bar sectioning

Each transfer bar was cut into 7 sections for each of the 4 alloys with a specified section length of 75mm. This was completed using a horizontal band saw.

3.6.4 Hot Rolling

Sectioned transfer bars were pre-heated to 1250°C for 120 minutes and rolled in 7 passes from 36mm down to 3mm, with a finishing temperature between 600°C – 610°C when exiting the run-out table.

3.6.5 Cold Rolling

Hot-rolled plates went through a 65% cold reduction, reducing the gauge from 3mm to between 1.1mm – 1.2mm.

3.6.6 Gleeble Sectioning

For the cold rolled plates to be heat treated on a Gleeble 3500 they need to be sectioned. They were sectioned using a guillotine with a length of 180mm and width 17mm, (Figure 27).

Figure 27: Gleeble strip.

3.7 Gleeble 3500

3.7.1 Gleeble Sample Preparation

Before the strip can be heat treated using the Gleeble 3500, it must undergo several preparation steps.

- Gleeble-sized specimens, length 180mm and width 17mm, were sectioned from both 3827 and 3832 plates using a guillotine.
- A 3-stage grinding procedure to remove any oxides, oil, and debris off the strip: 120 grit, 600 grit and 1200 grit SiC paper with ethanol in successive stages.
- For the placement of thermocouple wires, a scribe mark was used to show the placement of the thermocouple in the centre of the specimen.

- A 30cm length of yellow and red K-type thermocouple wire is used and welded onto the Gleeble strip using a resistance spot welder. Figure 28 illustrates the guide marks and the location of the resistance welds.

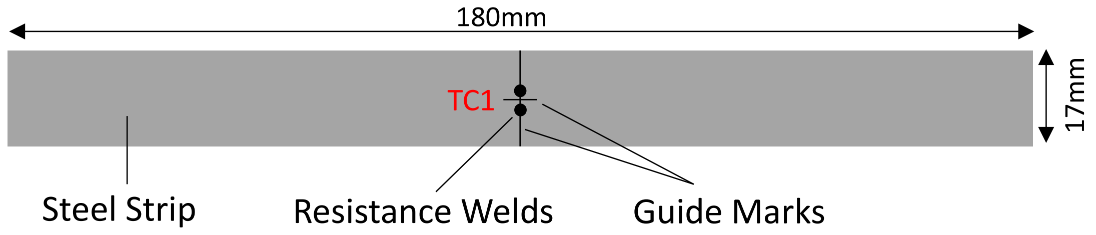

Figure 28: Gleeble specimen schematic.

3.7.2 Programming the Gleeble (Quiksim)

Before running the annealing simulations, they first need to be programmed. Simulations for the Gleeble are programmed using Quiksim. Quiksim is the software package provided by Dynamic Systems Inc, which allows the programming of heat treatment cycles using a table format (Figure 29). The heat treatment cycles are first composed using Tata's in-house Mimic to ensure accuracy. Mimic breaks the CAPL line into sections, where some will incorporate heating, holding, and cooling. The time spent at each section will directly relate to the time the strip travels through each section of the line. After creating the heat treatment cycle in Mimic, it can be inputted directly into Quiksim.

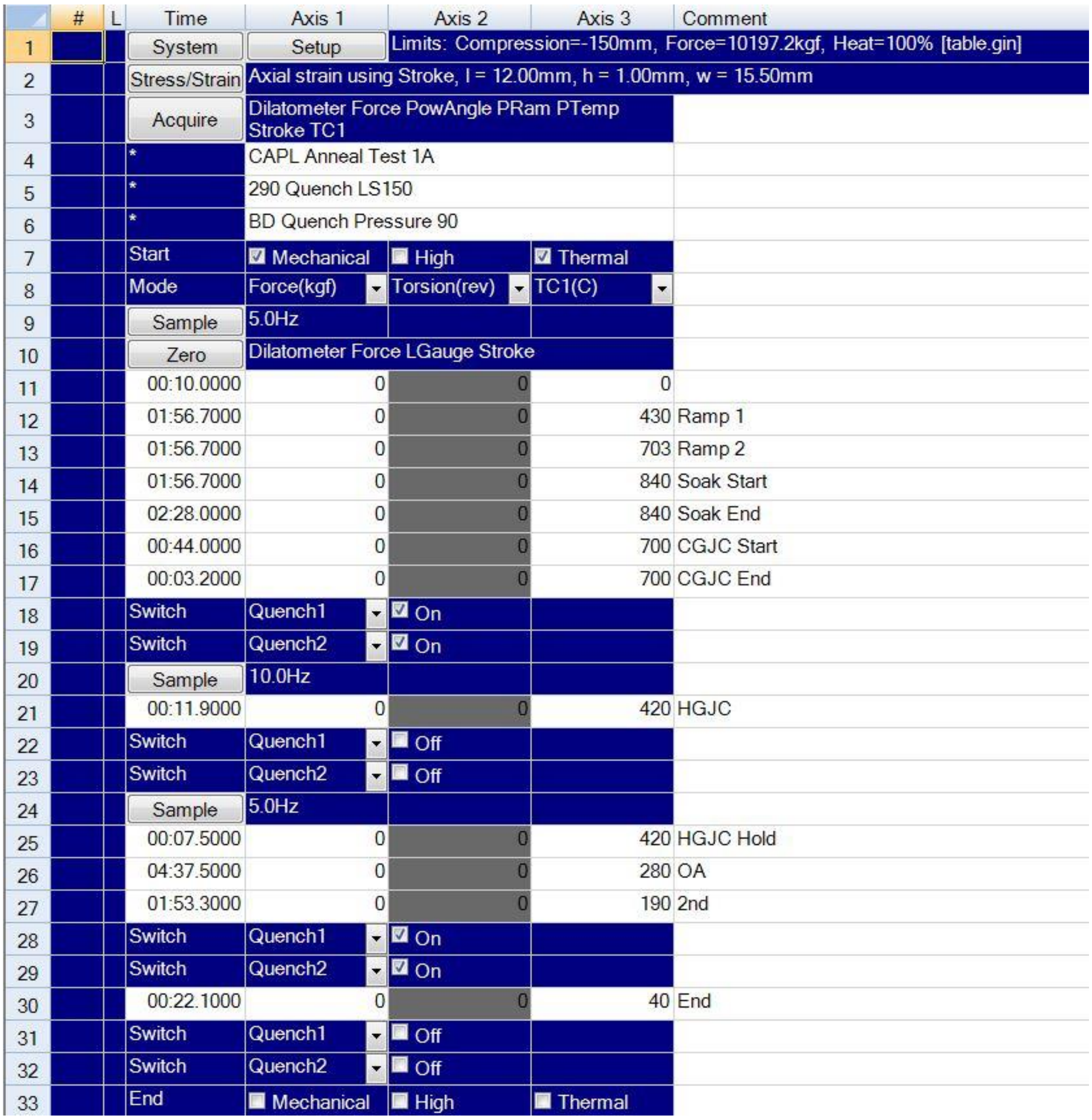

	#	L	Time	Axis 1	Axis 2	Axis 3	Comment
1			System	Setup	Limits: Compression=-150mm, Force=10197.2kgf, Heat=100% [table.gin]		
2			Stress/Strain	Axial strain using Stroke, l = 12.00mm, h = 1.00mm, w = 15.50mm			
3			Acquire	Dilatometer Force PowAngle PRam PTemp Stroke TC1			
4			*	CAPL Anneal Test 1A			
5			*	290 Quench LS150			
6			*	BD Quench Pressure 90			
7			Start	☑ Mechanical	☐ High	☑ Thermal	
8			Mode	Force(kgf)	Torsion(rev)	TC1(C)	
9			Sample	5.0Hz			
10			Zero	Dilatometer Force LGauge Stroke			
11			00:10.0000	0	0	0	
12			01:56.7000	0	0	430	Ramp 1
13			01:56.7000	0	0	703	Ramp 2
14			01:56.7000	0	0	840	Soak Start
15			02:28.0000	0	0	840	Soak End
16			00:44.0000	0	0	700	CGJC Start
17			00:03.2000	0	0	700	CGJC End
18			Switch	Quench1	☑ On		
19			Switch	Quench2	☑ On		
20			Sample	10.0Hz			
21			00:11.9000	0	0	420	HGJC
22			Switch	Quench1	☐ Off		
23			Switch	Quench2	☐ Off		
24			Sample	5.0Hz			
25			00:07.5000	0	0	420	HGJC Hold
26			04:37.5000	0	0	280	OA
27			01:53.3000	0	0	190	2nd
28			Switch	Quench1	☑ On		
29			Switch	Quench2	☑ On		
30			00:22.1000	0	0	40	End
31			Switch	Quench1	☐ Off		
32			Switch	Quench2	☐ Off		
33			End	☐ Mechanical	☐ High	☐ Thermal	

Figure 29: Quiksim cycle.

3.7.3 Gleeble setup

The steel strip was placed between the tension jaws and held with the stainless-steel wedge grips. Next, the sample is held in place and the bolts tightened until a compressive force of 50KgF shows on the computing unit. The compressive force is removed by pressing 'run mechanical' and gently rotating the stroke until there is a positive 80KgF. Next, the thermocouples are inserted into the readers and checked on the computing unit, ensuring a stable temperature reading. Finally, the door is closed, and the cycle is started by pressing run mechanical, turning the chiller on, and pressing the start button on the Quiksim program. Figure 30 shows the Gleeble 3500 used for these experiments.

Figure 30: Gleeble 3500.

3.8 Mechanical Testing and Characterisation 3827 & 3832

The proceeding section will cover the mechanical testing and characterisation techniques employed on the Tata tubes 3827 and 3832.

3.9 Tensile Testing (3827 & 3832)

3.9.1 Sample preparation

Small tensile specimens were milled from the centre of the heat-treated strips, Figure 31 displays a schematic for the tensile coupons used. After milling, the surface of the tensile coupons was cleaned using shot blasting.

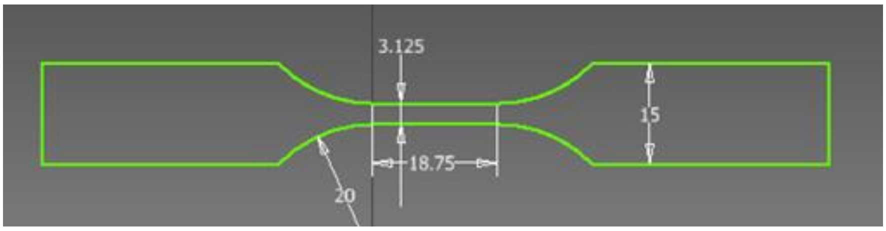

Figure 31: Tensile engineering drawing.

3.9.2 Tensile Testing

Testing was completed on a Tinius Olson tensile tester (25KN loadcell) with the extension recorded using a 16mm gauge length extensometer. The testing procedure followed BS EN ISO 6892-1_2016, using method A2. A2 is an open loop and involves the control of the estimated strain rate over the parallel length. This is done by calculating the crosshead separation rate, determined by multiplying the required strain rate by the parallel length [122]. See formula.

$$V_c = L_c \dot{e}_{L_c} \qquad \text{Eq. 12}$$

Where:

$\dot{e}_{L_c}$ is the estimated strain rate over the parallel length

L_c is the parallel length

Range 2 and range 4 were used to calculate the strain rates. Calculated strain rate for range 2 = 0.28125 mm/min, which was used up until the yield point. After yielding, the strain rate was accelerated to 7.5375 mm/min. These strain rates were calculated using the formula above with $\dot{e}_{L_c}$ = 0.00025 s^{-1} for range 2 and 0.0067 s^{-1} for range 4.

3.10 Metallography (3827 &3832)

3.10.1 Sample Preparation (3827 & 3832)

They must first undergo several sample preparations stages to inspect the microstructure of the heat-treated strips under a light optical microscope. A Precision saw was used to cut both sides from the centre of the strip, approximately 3mm on each side. After removing any burrs and rough edges, the sample was turned on its side and held with a mounting clip. It was turned on its side as this corresponds to the rolling direction of the strip. Next, the samples were mounted using a hot mount press with conductive Bakelite. The heat-treated samples were progressively ground in stages; 120 followed by 600 then 1200 grit size SiC grinding pads. Followed by polishing stages of a; 6µm, 3µm and 1µm finish for optical. Finally, etching was completed using 5% Nital. Nital was chosen as it exposes the grain boundaries.

3.10.2 Light Optical Microscope

The microstructures of the heat-treated 3827 and 3832 specimens were captured using a Zeiss optical microscope. In total 4 different heat treatment routes were captured under the microscope for comparison between steel grades and heat treatment route.

3.11 Mechanical Testing and Characterisation Q&P Steels

The proceeding section will cover the mechanical testing and characterisation techniques employed on the novel Q&P steels developed.

3.12 Hot Rolled Tensile Testing

A hot rolled plate was machined in to four tensile samples for each of the four compositions. Samples were machined according to ISO:6892 [122], following the A50 specification. The gauge length was 50mm, width 12.5mm±1, total length 200mm and thickness of the hot rolled plates at 3mm. The testing was completed on a Dartec servo-hydraulic tensile testing machine with a 250 KN load cell. During testing, the elongation direction was aligned with the rolling direction. Using a non-standard testing rate, a constant crosshead separation speed of 1mm/min was used. Tensile samples were gripped using flat plate wedge grips and aligned axially with all tests run at room temperature. Until the yield point, the gauge length was recorded by a mechanical clip-on extensometer (25mm gauge length); at this point, the extensometer was removed, and the test continued until fracture. From the tensile tests, load/elongation and stress/strain curves were constructed. For each different composition, four tests followed the same conditions, so properties could be compared to see if the results were repeatable.

3.13 Gleeble 3500

Both heat treatment schedules were run using a Gleeble 3500 thermomechanical simulator. Each of the four alloys had six different annealing cycles, three for each schedule. Each cycle was run three times, twice for tensile testing and once for metallography. Standard Gleeble operating procedure was followed to run the experiments. It was used in its tension configuration for all annealing simulations.

3.14 Tensile Testing after Cold Rolling and Annealing

For both heat treatments 1 & 2 there were 12 different schedules, totalling 24 unique heat treatment cycles. Each cycle was repeated twice for means of tensile testing. The heat-treated Gleeble strips were machined into subsize tensile samples following the ASTM E8 / E8M-21 standard [123]. The gauge length was 25mm ± 0.1, width 6mm ± 0.1, total length 76mm, a radius of fillet 6mm and thickness between 1.1-1.2mm. The testing was completed on a Tinius Olsen H25KS tensile tester with a 25 KN load cell. During testing, the elongation direction was aligned with the rolling direction. Using a non-standard testing rate, a constant crosshead separation speed of 1mm/min was used. Tensile samples were gripped using flat plate wedge grips and aligned axially with all tests run at room temperature. The width and thickness were recorded at three points for each sample to calculate the average. These dimensions were then set into Horizon software, including the gauge length and testing rate. Change in gauge length and resulting strain during testing was computed using an X-sight one video extensometer, which uses digital image correlation to track points on the specimen during testing. It can track the strain longitudinally and transversely.

3.15 Vickers Hardness Testing

Vickers hardness testing was completed on a Wilson VH3300. Testing was completed using ISO 6507-1:2018 [124]. Settings used were Hv 1, single line with 10 indents for a 15s dwell time completed on all the samples. All samples from HT1, HT2 and HDAS were indented and will be compared against each other in the following results chapters.

3.16 Nano-Indentation

The four cycles which showed the best overall combination in properties after testing and a DP800 sample were put forward for nanoindentation experiments. Nanoindentation experiments were run using a Hysitron Ti 980 Tribolndenter following ISO 14577-1-2015 [125]. The purpose of these experiments is to see if the Q&P heat treatments have led to a reduction in hardness mismatch between the phases. The samples need to be perfectly flat before you can run the experiments. The indenter load and spacing were optimised for each sample using an incremental loading array. Using in situ Scanning Probe Microscopy (SPM), the indents could be characterised for size and depth, so a suitable load and spacing could be calculated. Accelerated property mapping (XPM) was used to perform 400 indents over each sample. This was achieved by performing a 2*2 chain of a 10*10 array. The indenter load was set to 400µN with a 1µm spacing for the Q&P samples, and for the DP800 sample, the indenter load was 1000µN with a 3 µm spacing.

3.17 Hot Dip Annealing Simulator (HDAS)

The four cycles that showed the best property combination after annealing and tensile testing were put forward for HDAS simulations using HDPS EU A5 ICS. The sample size for HDAS simulations was the total width of the cold rolled plates (106mm - 113mm) and a length of 200mm. This sample size provides a large enough area for subsequent hole expansion testing.

3.17.1 Sample Preparation

Using a guillotine, the cold rolled plates were cut at 200mm sections along their length. Before annealing, each sample must be cleaned of oils, oxides, or debris. Sample preparation was completed using a 3-stage grinding procedure, 120 followed by 600 then 1200 grit size SiC grinding pads, with the sample cleaned at each interval stage with ethanol. The areas were marked off using a guide for thermocouple wires to be welded onto the sample. Also, the dimensions are noted for each sample, as the length width and gauge need to be inputted in to HDAS user interface.

3.17.2 Homogenisation

The HDAS has three separate heating zones, and the amount of power to each zone is controlled by the operator. Three separate thermocouples record the temperature at each of the zones. Homogenisation experiments were run to ensure a large enough isothermal region, with all three zones reading similar temperatures during the annealing cycle. The overall annealing cycle was reduced to minimise the amount of time needed for homogenisation experiments.

3.17.3 Procedure

First access the simulator's control interface (produced by Falk engineering) to initiate an annealing cycle using the Hot Dip Annealing Simulator (HDPS EU A5 ICS). Next, select the annealing parameters within the interface, such as temperature, time, atmosphere, and cooling rate. It is vital to ensure that the annealing temperature falls within the operating range of the simulator. The annealing time should be determined based on the material type and desired transformation kinetics. To establish the desired atmosphere within the annealing chamber the gas composition and flow rates can be set. Lastly, the cooling rate should be defined based on the desired microstructure and material properties. After programming these settings, it is possible to create complete annealing cycles that follow the exact temperature and times representative of CAPL or other industrial-based annealing lines.

The sample is loaded into the loading chamber, as illustrated in Figure 32, by attaching the sample with a pin to the transfer rod and the thermocouple inserted into the thermocouple connector. Next the loading door is closed with all four locking arms to maintain a controlled environment, tight seal and selected as closed on the user interface.

Before starting the annealing cycle, it is crucial to ensure that all parameters are correctly set and confirmed through the control interface. Once this is done, the annealing cycle can commence. Initially, the transfer rod will move the sample to the furnace, where IR heating elements will gradually heat up, raising the temperature to the specified annealing temperature, followed by a specified soak to homogenise the microstructure. After soaking, the transfer rod will move the sample back up to the cooling chamber and cool it to the specified quenching temperature. The cooling chamber has two plates with evenly distributed small holes, which helps to cool the whole area of the sample at the same rate. Following cooling, the transfer rod will move the sample back to the furnace to overage the material before again moving to the cooling chamber for the final quench. It is crucial to closely monitor the temperature throughout the annealing process using the temperature sensors integrated into the simulator. By doing so, any potential deviations or fluctuations can be detected and corrected.

Moreover, the HDAS can apply a coating to the material via the zinc bath, enabling the possibility of conducting annealing simulations based on industrial galvanizing lines. This allows for a thorough investigation of the material's potential to receive a metallic coating whilst maintaining the desired microstructural evolution and underlying properties. Notably, annealing cycles were all run without the Zinc bath.

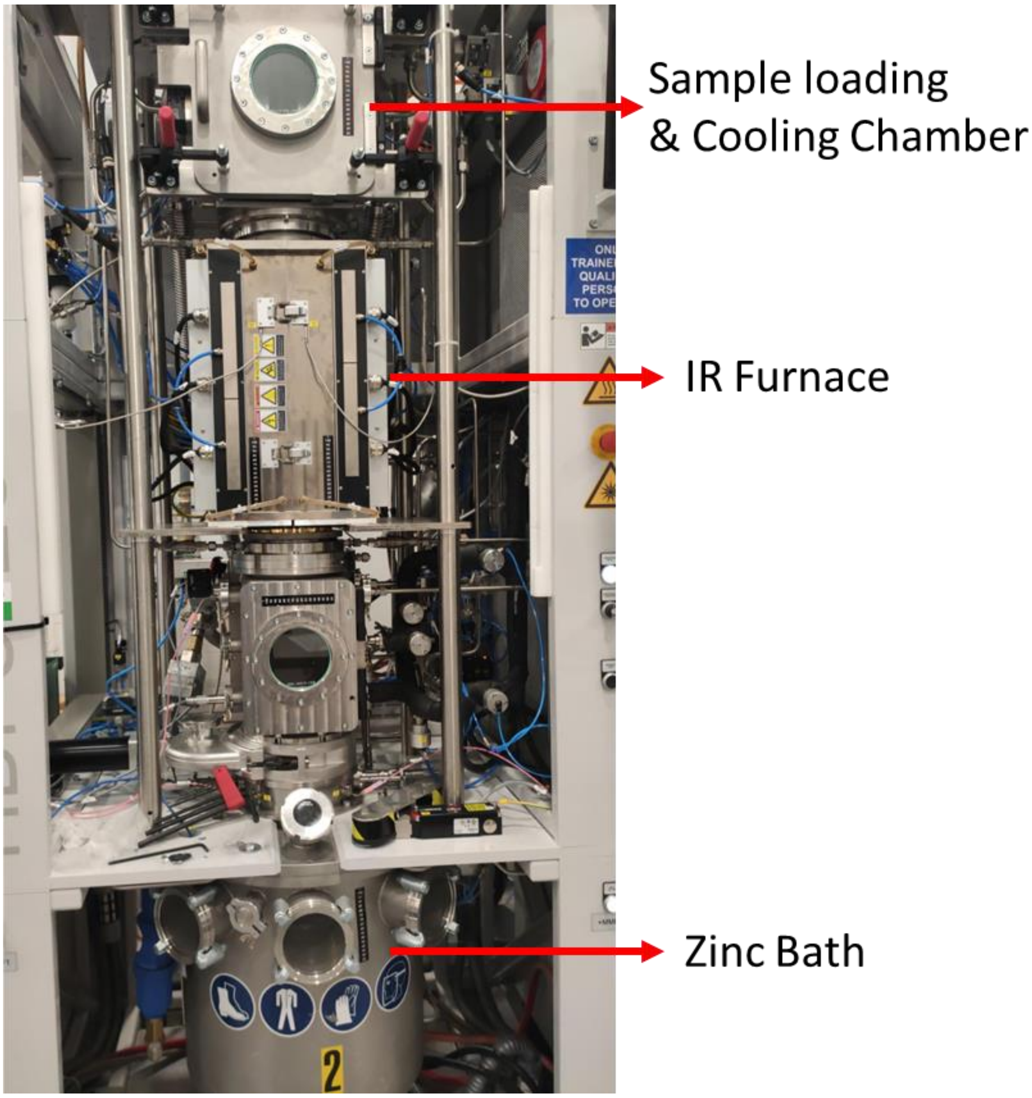

Figure 32: Hot dip annealing simulator (HDPS EU A5 ICS).

3.19 Hole Expansion Testing

The hole expansion ratio (HER) was determined using an Erichsen sheet metal testing machine. The testing procedure followed ISO 16630-2017, sheet and strip, hole expanding test [126]. During the test, the materials edge stretching capability is determined, depending on the edge conditions. Materials with a high HER are more likely to have superior local formability. The sample size for an HER test is 100mm * 100mm plate with a 10mm diameter hole at the centre. The edges were cut out using water cutting, and the centre diameter was removed using EDM (electrical discharge machining). EDM was chosen to remove the central diameter as it has been shown in the literature to be the best method for hole preparation. Paul et al. found that the maximum damage in hole preparation happens by punching processes and can be substantially improved when using EDM [127]. Once the sample is clamped, a conical punch with a 60° apex angle expands the initial hole. The test ends when a through-thickness crack is visible with a critical load drop. The HER is simply the per cent expansion of the initial diameter.

3.20 Microscopy

The microstructures of the experimental steels have been captured using both optical microscopy and scanning electron microscopy (SEM). Before the microstructures can be captured the material needs to go through several preparation steps.

3.20.1 Sample Preparation

A Precision saw was used to cut the centre of the strip out (3-5mm length and total width of strip). Samples were turned on their side to reveal the rolling direction, held with a mounting clip and mounted using a hot mount press with conductive Bakelite. Standard metallographic preparation techniques were used, and the samples were progressively ground in stages; 120 followed by 600 then 1200 grit size SiC grinding pads. Followed by polishing stages of a; 6µm, 3µm and 1µm finish for optical and 0.05 µm for analysis using SEM and nanoindentation. Etching was completed using 5% Nital or sodium metabisulfite. Nital was used to expose the grain boundaries for general metallography imaging, whereas sodium metabisulfite adds colour to the phases within the microstructure, which helps to differentiate between the different phases.

3.20.2 Optical Microscopy

The microstructures of the heat-treated Q&P steel specimens were captured using a Zeiss optical microscope. Each heat treatment schedule had nine different routes totalling eighteen different cycles. Images were captured at 20x, 50x and 100x for each cycle.

3.20.3 Scanning Electron Microscope

Heat-treated samples from cycles A-L for Heat-Treatment 1 (HT1) and Heat-Treatment 2 (HT2) were analysed using Zeiss Evo LS25 SEM. Images were captured in scanning electron mode with an accelerating voltage of 20Kv, a working distance between 6-10mm and a probe current of 50pA. A higher probe current of 75pA was also used for several image captures.

3.21 Gleeble Optimisation

A) Cooling Rate Improvement

The cooling in the Gleeble is achieved by forced air under pressure provided by the quenching tanks. For 1mm gauge strip steel, the maximum cooling rate was approximately 35°C/s, but to achieve the desired level of primary martensite formation for the designed Q&P alloys, the cooling rate needed to be 50°C/s. From inspection of the quench tanks, it was clear it only used one of the tanks to provide the forced air. Setting up the second quench tank improved the cooling rate to 50°C/s and now provides the desired level of cooling to achieve the designed fraction of primary martensite formation. Notably, on CAPL, the maximum cooling rate (CR) during the HGJC section is 90°C/s, and this was not achievable when heat treating in the lab on the Gleeble 3500. As CAPL can achieve these higher cooling rates, it highlighted the need to improve the attainable CR on the Gleeble 3500. For instance, if DP1000 and CP1000 were run at 150mpm during their processing on CAPL, their CR during the HGJC would be 39.4°C/s and 46.5°C/s, respectively, which underscores the importance of using 100mpm as the chosen line speed, as the Q&P steels are cooled to lower temperatures. This increases the CR to approximately 50°C/s, comparable to the DP/CP1000 AHSS cooling rates. See Figure 33, which shows the 90° elbow male-to-female pipe and the hose installed to take advantage of the second quench tank.

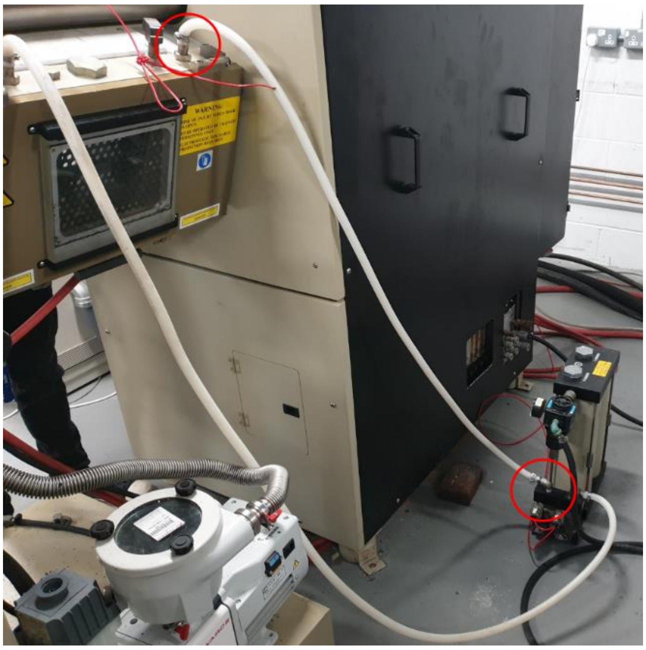

Figure 33: Gleeble quench tank, showing where the second hose was installed.

B) Isothermal Analysis

In the Gleeble 3500, the sample fixes between the stainless-steel wedge grips and the heating is via direct resistance heating. The stainless-steel grips provide a flat thermal profile. The heating will start at the centre of the strip and spread out. Due to this, it is vital to find an effective isothermal region. As the heated treated strips will be used for both microstructural analysis and tensile testing, it is crucial that the heating zone over this region is flat, ensuring the same microstructural evolution over the strip's length and width. Two experiments for length and width were carried out to find the isothermal region effectively. After completing the sample preparation of the steel strip, instead of just welding one thermocouple to the strip, three were used over a length profile of 32mm and a width profile of 16mm. For the length and width experiments, the control thermocouple TC2 is welded in the centre with both TC1, and TC3 welded 16mm on either side of it for the length and 8mm above and below the centre for the width. Figure 34 shows the placement of the thermocouples along the length and width. A standard CAPL cycle was used for the heat treatment with a soak temperature of 840°C and an overage temperature of 400°C. The CAPL cycle breaks down into nine sections, Ramp 1, Ramp 2, Soak Start, Soak Hold, CGJC, HGJC, Overage, 2nd Cooling and final cooling. Using the absolute average temperature difference over each of these nine sections, the temperature difference ± from the control thermal couple TC2 was calculated for both TC1 and TC3 for the length and width experiments. Results for the Gleeble isothermal analysis are included in Appendix 6.

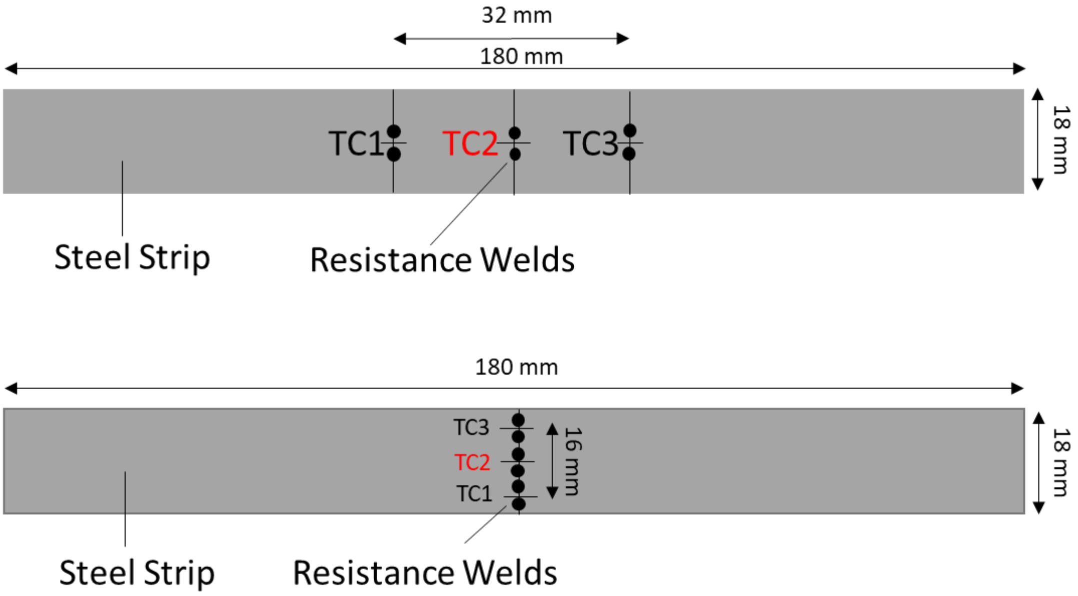

Figure 34: Length and width thermocouple placement.

Chapter 4

3827 and 3832 Results Chapter

4. Results Chapter 3827 and 3832

This section covers the transformation temperature calculations in ThermoCalc and JMatPro, including elemental effects. In addition, their subsequent heat-treated microstructures followed by the mechanical response of 3827 and 3832 during tensile testing.

4.1 ThermoCalc and JMatPro Transformation Temperature Comparison

From Table 3, it is clear both JMatPro and ThermoCalc provide remarkably similar values for A_r^1 and A_r^3. With 3827, the A_r^1 temperature was 698.2°C when using JMatPro and 698°C when using ThermoCalc, showing a minimal difference < 0.5%. For the A_r^3, it was 821.0°C when using JMatPro and 819.4°C when using ThermoCalc, similarly a minimal difference of just 1.6°C, again < 0.5%. ThermoCalc bases its calculations on experimental databases, and JMatPro uses property models to calculate, adding confidence when using these transformation temperatures to design heat treatments. Figures 35 and 36 are the simulated TTT and CCT diagrams for 3827. The transformation temperatures from JMatPro were from simulated TTT and CCT diagrams. For 3832, the A_r^1 temperature calculation was 698.0°C when using JMatPro and 697.6°C when using ThermoCalc, again only a slight temperature difference. When using JMatPro, the A_r^3 temperature was 824.9°C and 823.2°C when using ThermoCalc, showing only a temperature difference of 1.7°C. With JMatPro, it is also possible to calculate different transformation temperatures, such as M_s, $M_{50\%}$, $M_{90\%}$ and B_s, which are helpful when designing a heat treatment route. With knowledge of all these transformation temperatures, it is possible to create a heat treatment which achieves the desired microstructural evolution and resulting properties. Figures 37 and 38 are the TTT and CCT diagrams for 3832.

Table 3: ThermoCalc & JMatPro transformation temperature comparison.

	JMatPro Transformation Temperatures (°C)					**ThermoCalc Transformation Temperatures (°C)**	
Grade	**A_r^1**	**A_r^3**	**M_s**	**$M_{50\%}$**	**$M_{90\%}$**	**A_r^1**	**A_r^3**
3827	698.2	821.0	410.2	377.0	300.1	698.0	819.4
3832	698.0	824.9	415.8	382.8	306.1	697.6	823.2

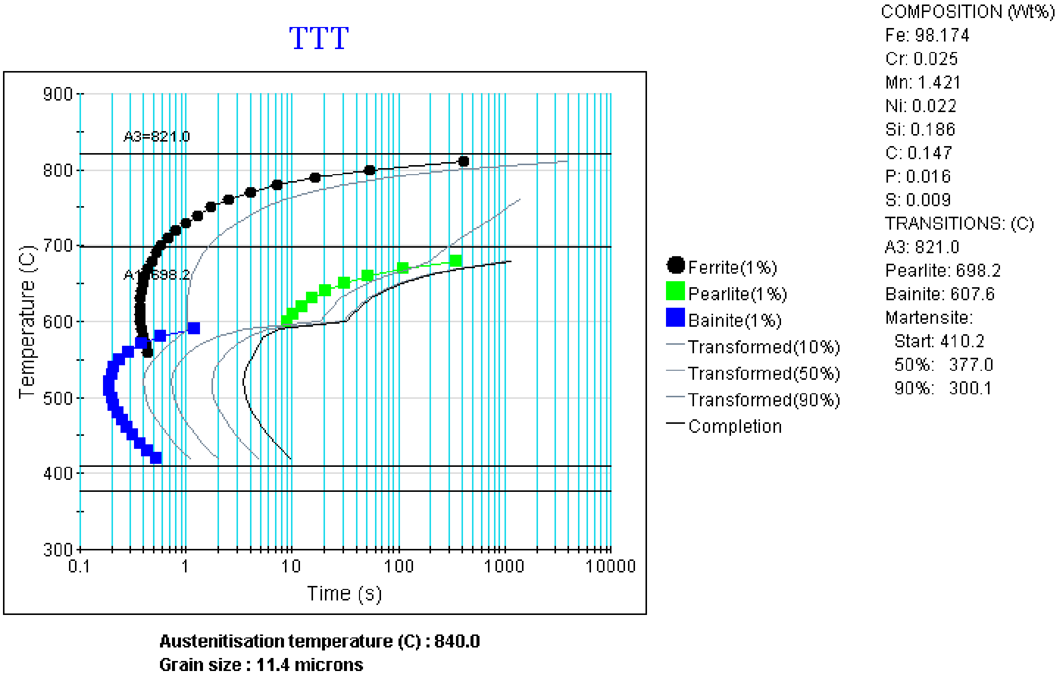

Figure 35: TTT diagram for 3827 showing the transformation temperatures.

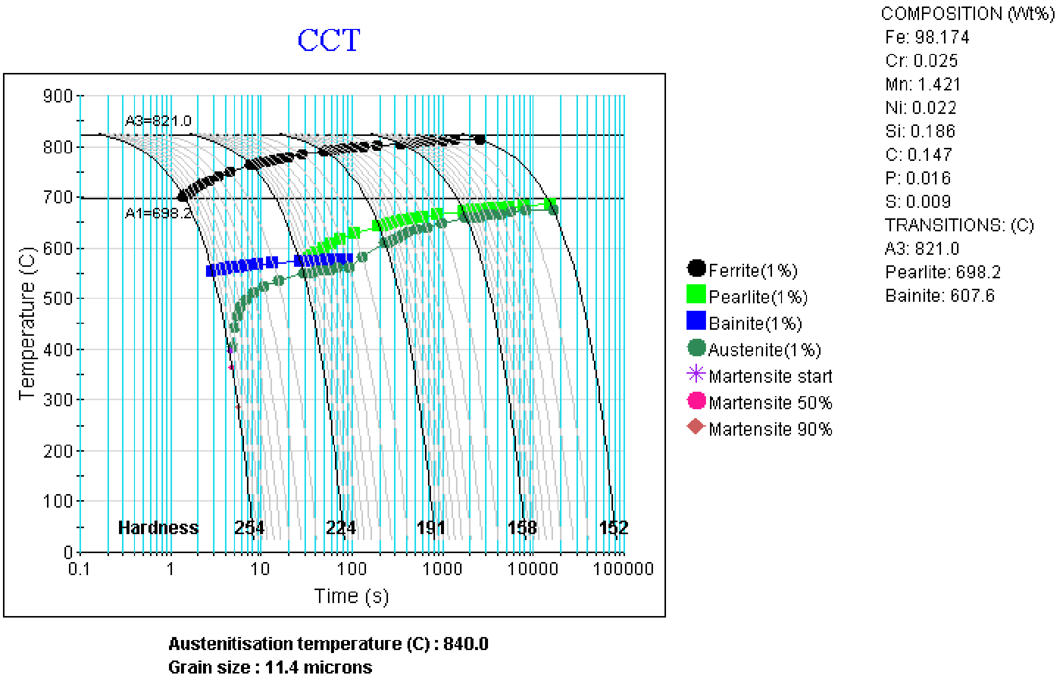

Figure 36: CCT diagram for 3827.

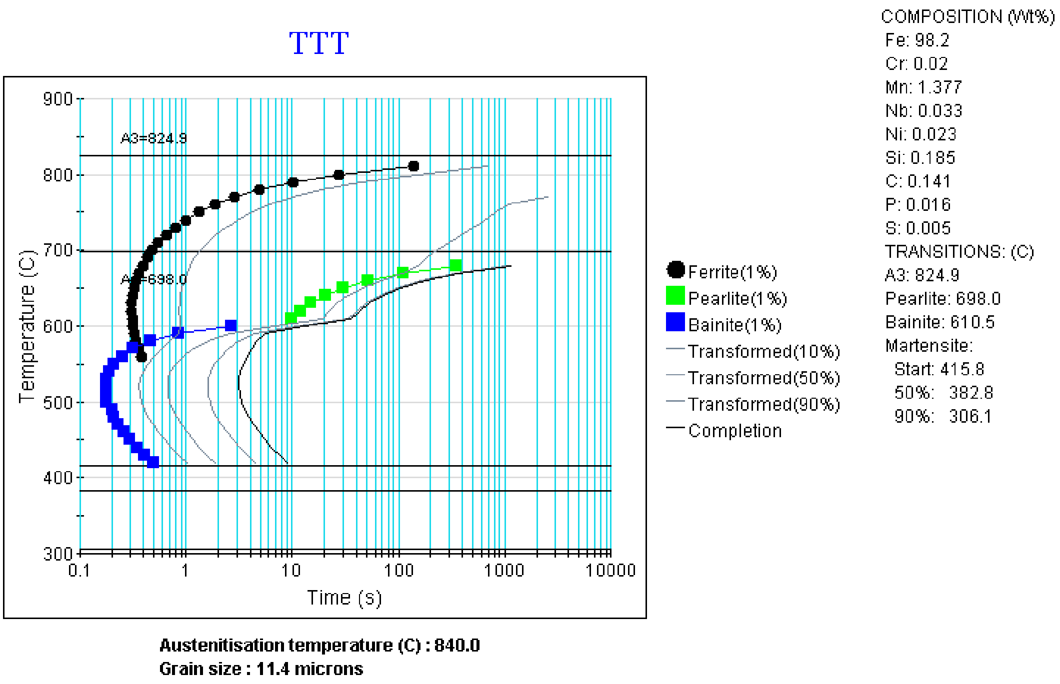

Figure 37: TTT diagram for 3832 showing the transformation temperatures.

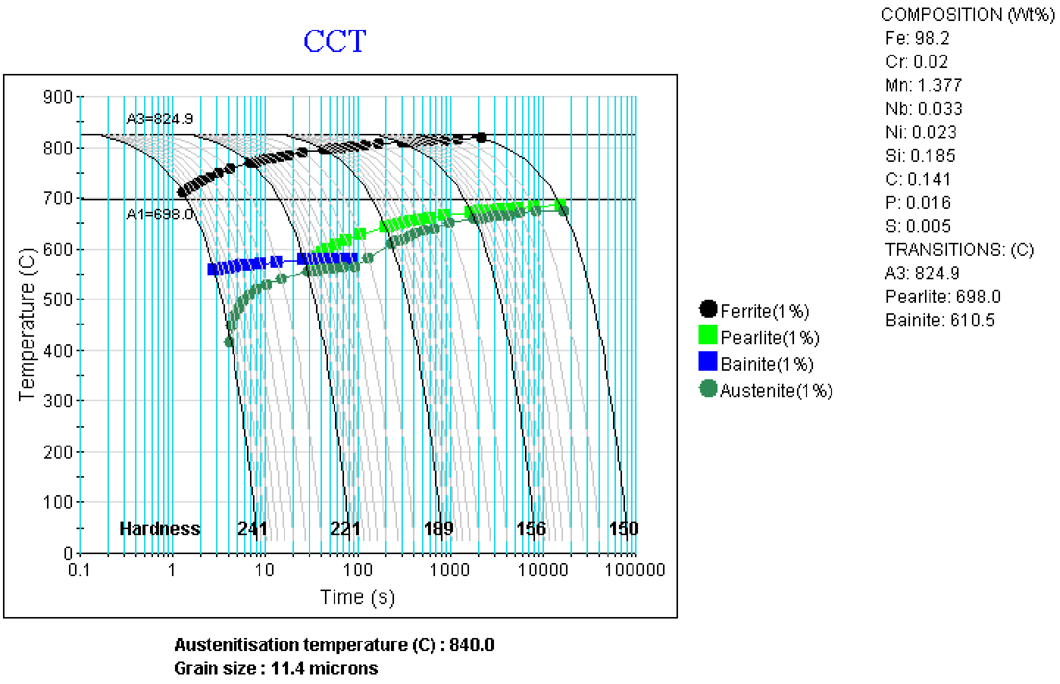

Figure 38: CCT diagram for 3832.

4.2 ThermoCalc Element Effects on the Ar^3 Temperatures for 3827 & 3832

See section 3.2.2 B, which describes the calculation setup in ThermoCalc. For both 3827 and 3832, when the carbon addition level varies from 0.1-0.5 Wt.%, the A_r^3 reduces by approximately 80°C for both grades. Carbon is a strong austenising element, which has the most significant effect on the Ms temperature. It also broadens the austenite phase field by raising the A_r^4 temperature, where δ-ferrite changes to austenite and lowering the A_r^3, where austenite reverts to α-ferrite. Carbon is insoluble in ferrite but soluble with γ-iron, so the formation of ferrite and cementite is delayed with increasing carbon content [128].

Similarly, increasing manganese content from 1.4-2.4 Wt.%, the A_r^3 temperature reduces by approximately 30°C. Manganese is classed as an austenite stabilising element and has similar effects on steel to carbon. Manganese additions will influence the hardness and strength of the steel and lower the temperature where austenite starts to decompose. The literature also shows Mn to reduce the critical cooling rate during hardening, increasing hardenability [129], [130]. When silicon additions increase for 3827 and 3832 from 0.1-0.5 Wt.%, the A_r^3 temperature increases by approximately 15°C. Silicon is a ferrite-stabilising element that increases the temperature, whereas austenite will start to decompose as silicon content increases. Silicon also shifts pearlitic transformations to longer times and higher temperatures on a TTT diagram [131]. Figures 39 and 40 illustrates the ThermoCalc step in concentration calculation results for 3827 and 3832.

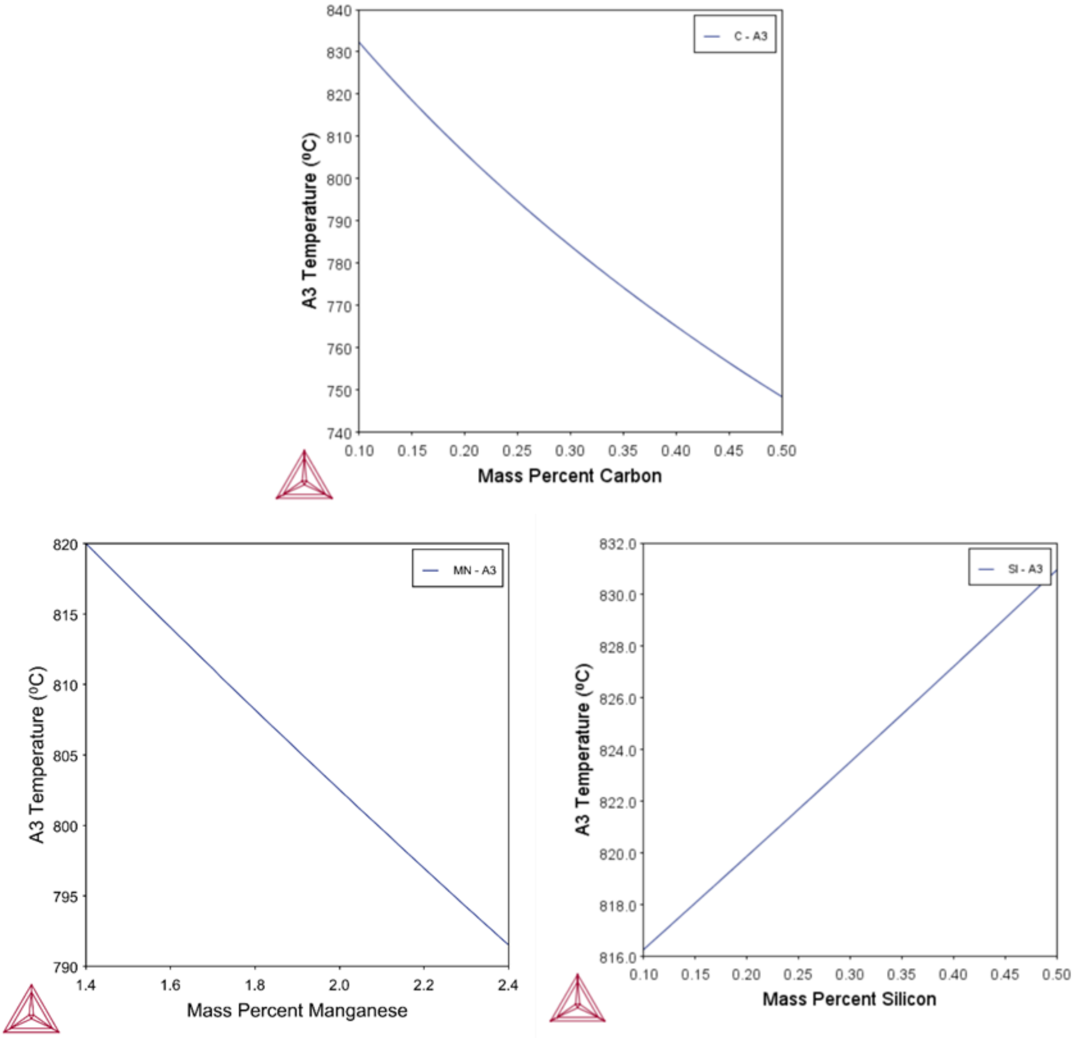

Figure 39: Shows how the A_r^3 temperature changes with increasing amounts of C, Mn, and Si for 3827.

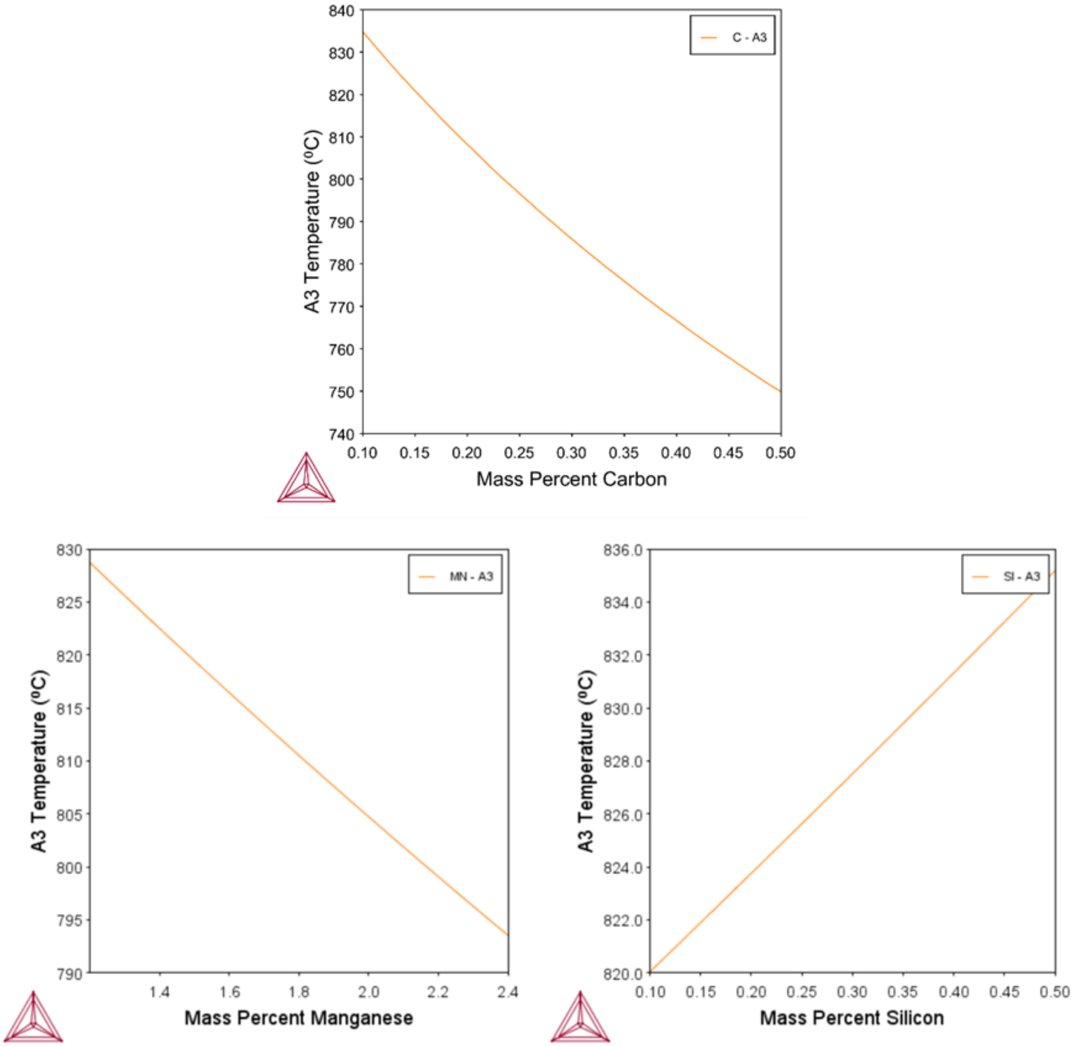

Figure 40: Shows how the A_r^3 temperature changes with increasing amounts of C, Mn, and Si for 3832.

4.3 Gleeble Thermomechanical Simulator

Figure 41 illustrates the recorded heat treatment profile for cycle A1-3827 and emphasizes the accuracy achieved using the Gleeble. PTemp is the programmed cycle, and TC1 is the temperature recorded by the thermocouple during heating and cooling. On inspection of the graph, it is clear the Gleeble could accurately follow the programmed heat treatment with the temperature only varying by ± 0.2°C. This illustrates that it was possible to achieve very accurate heat treatment cycles when using the Gleeble 3500. Designed heat treatment cycles are illustrated in section 3.2.1.

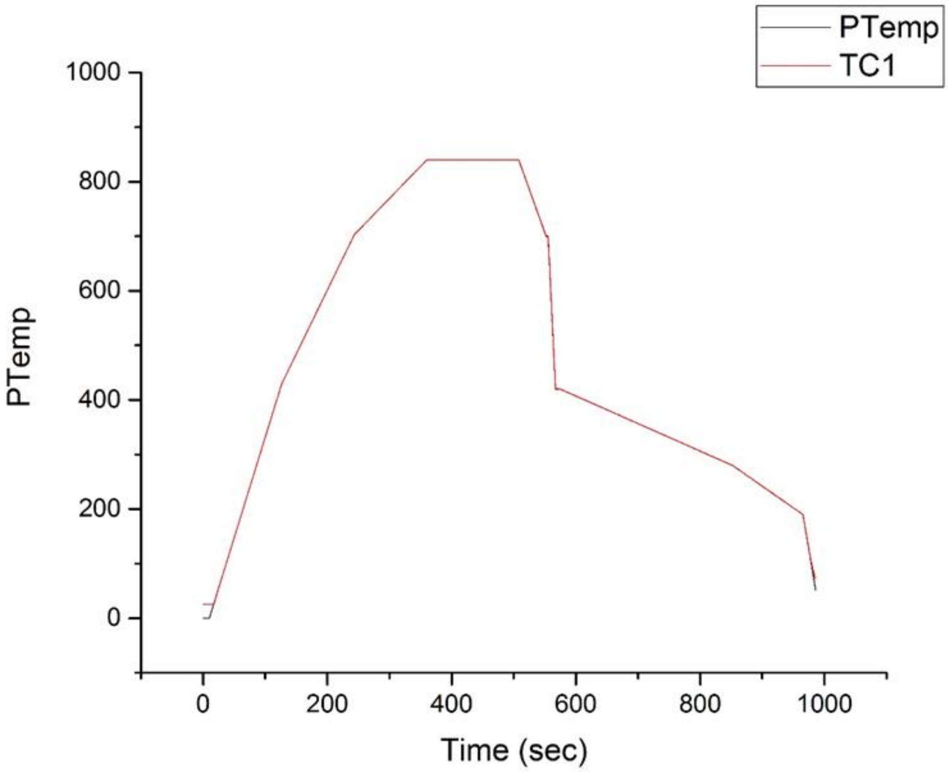

Figure 41: Level of accuracy achieved during Gleeble thermomechanical heat treatments.

4.4 Tensile Testing Results (3827 & 3832)

During tensile testing, displacement, and force data records until fracture. After the sample fractures, using the raw data, stress and strain curves are constructed. For all A and B samples, a stress-strain curve was plotted. Mechanical properties such as 0.2% Yield stress, ultimate tensile strength, total elongation, and uniform elongation were calculated from the stress-strain curves. It is also clear that the stress-strain curves follow a similar pattern with the elastic region followed by discontinuous yielding, an increase in stress up to the UTS followed by necking with a reduction in stress until the final fracture. For comparison of the steel grades, graphs show the effects of different CGJC and HGJC temperatures on each grade's mechanical response. Looking at Figures 42 and 43, which show the average UTS and Yield stress for the steel grades, 3832 has a higher tensile property overall, with almost all combinations of CGJC and HGJC temperatures achieving over 600MPa, except for cycle 1A, which achieved 596MPa and cycle 7B 588MPa. The tensile range is between 588-643MPa for 3832 and between 524-644MPa for 3827, showing a difference of 120MPa for 3827 and 55MPa for 3832. 3832 is less sensitive to the variation in CGJC and HGJC temperatures. Also, by looking at the average UTS result for both compositions, 3832 was 617MPa, and 3827 603MPa. In comparing the Yield stress for the compositions, 3832 achieves higher Yield stress for all heat treatment routes, shown by taking the average of all Yield stresses for both, where 3832 average response was 436MPa compared to 383MPa for 3827. The Yield stress for 3832 ranges between 358-478MPa and 3827 between 316-484MPa. The Yield stress results for both grades are sensitive to the different HGJC and CGJC temperatures, where for 3827, the total range is 168MPa, and for 3832, 120MPa. Figures 44 and 45 show both steel grades' average total/uniform elongation. Firstly, both grades have achieved very high levels of uniform elongation. 3832 scatters between 14.3%-18.6%, whereas 3827 scatters between 13.9%-18.3%, showing a total scatter of 4.3% and 4.4%, respectively. Both compositions achieved excellent levels of total elongation, showing they responded well to the designed heat treatment routes. 3832 had a range between 20.6%-28.6% and 3827 between 20.6%-28.0%. Cycle 9B is an outlier for both compositions and prematurely failed during tensile testing, where the total elongation should have been between 26%-28%. The range was 8% for 3832 and 7.4% for 3827. Indicating these compositions are sensitive to different HGJC and CGJC temperatures.

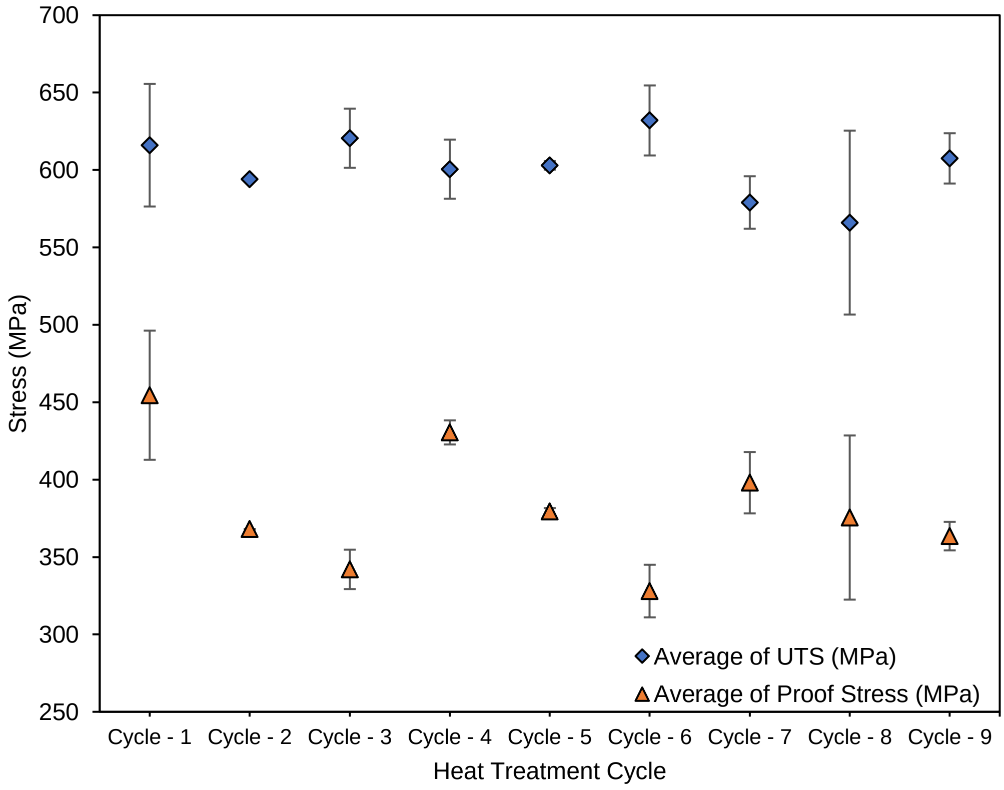

Figure 42: Average UTS and yield stress result for 3827.

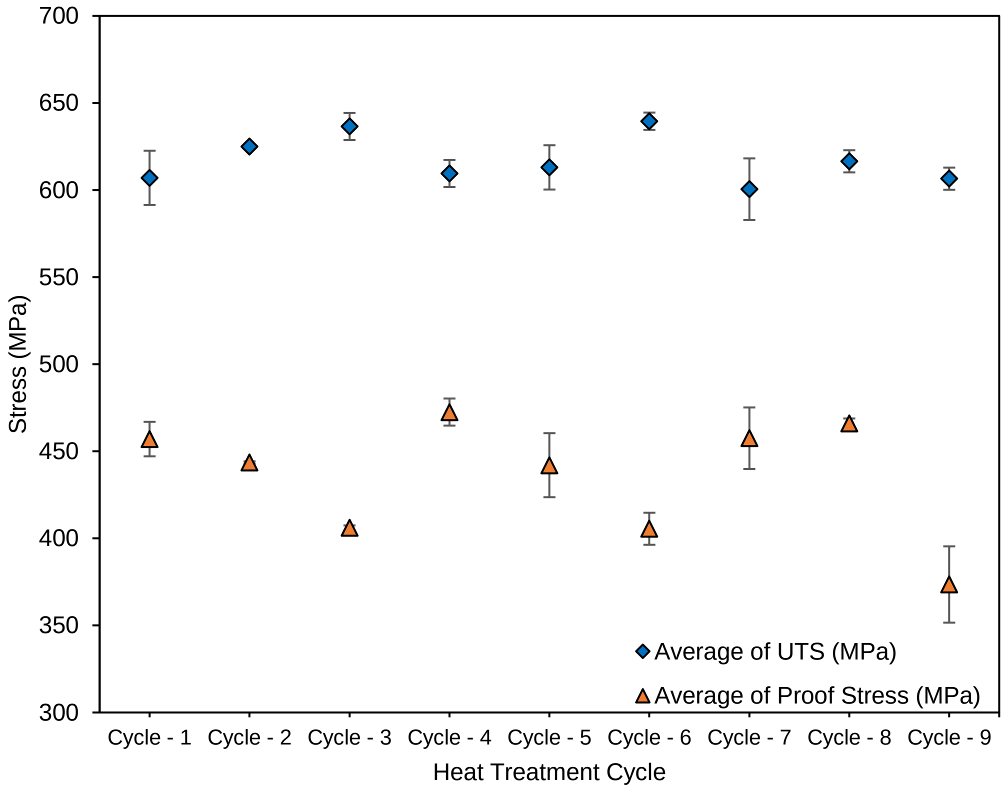

Figure 43: Average UTS and yield stress results for 3832.

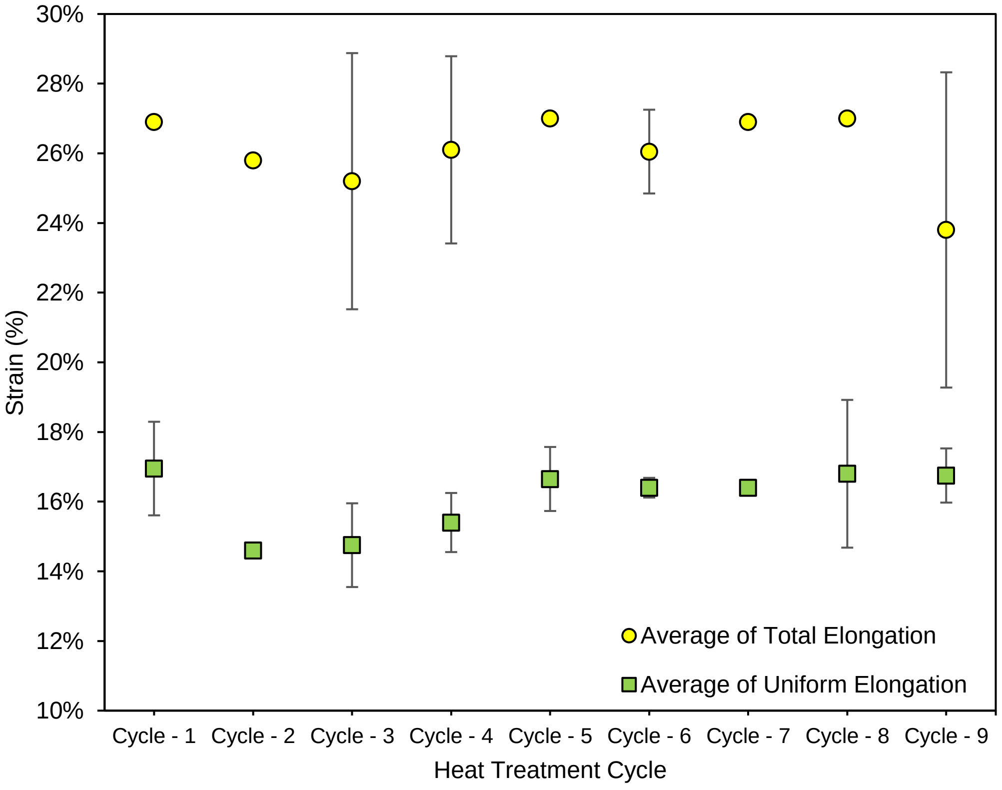

Figure 44: Average uniform and total elongation result for 3827.

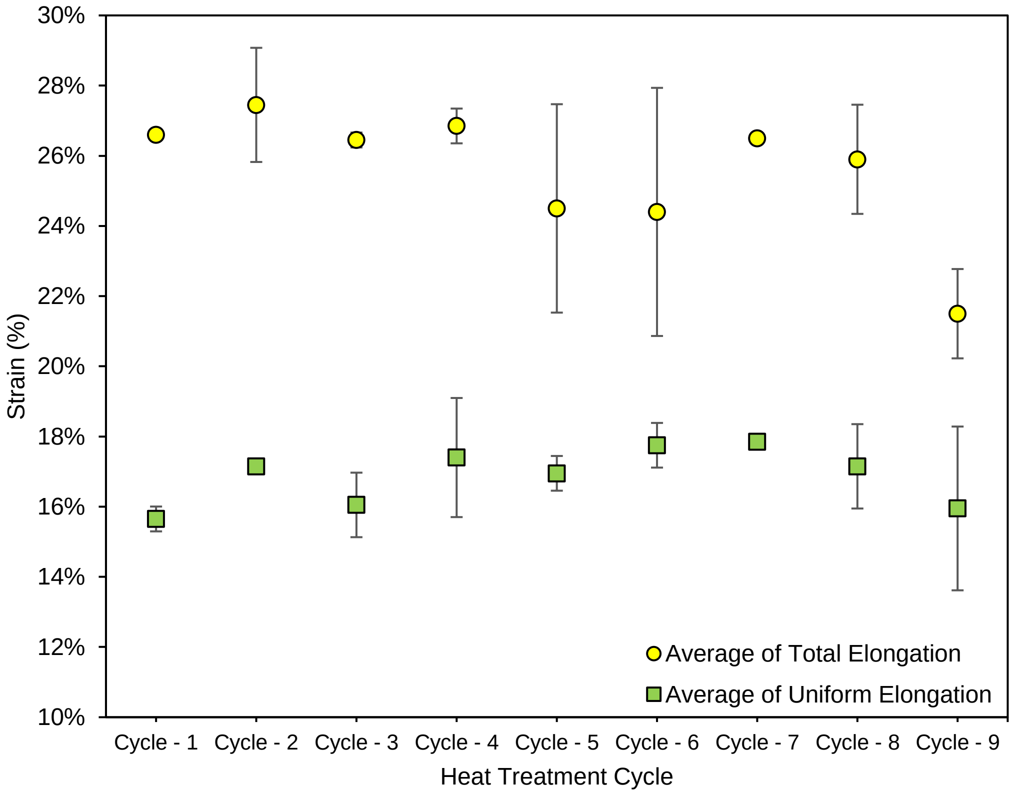

Figure 45: Average uniform and total elongation result for 3832.

Table 4: Average results for 3827.

Cycle	Yield Stress (MPa)	UTS (MPa)	Uniform Elongation	Total Elongation
Cycle - 1	454.5	616	16.95%	26.90%
Cycle - 2	368	594	14.60%	25.80%
Cycle - 3	342	620.5	14.75%	25.20%
Cycle - 4	430.5	600.5	15.40%	26.10%
Cycle - 5	379.5	603	16.65%	27.00%
Cycle - 6	328	632	16.40%	26.05%
Cycle - 7	398	579	16.40%	26.90%
Cycle - 8	375.5	566	16.80%	27.00%
Cycle - 9	363.5	607.5	16.75%	23.80%

Table 5: Average results for 3832.

Cycle	Yield Stress (MPa)	UTS (MPa)	Uniform Elongation	Total Elongation
Cycle - 1	457	607	15.65%	26.60%
Cycle - 2	443.5	625	17.15%	27.45%
Cycle - 3	406	636.5	16.05%	26.45%
Cycle - 4	472.5	609.5	17.40%	26.85%
Cycle - 5	442	613	16.95%	24.50%
Cycle - 6	405.5	639.5	17.75%	24.40%
Cycle - 7	457.5	600.5	17.85%	26.50%
Cycle - 8	466	616.5	17.15%	25.90%
Cycle - 9	373.5	606.5	15.95%	21.50%

4.5 3827 & 3832 Heat Treated Microstructures

Microstructures for heat treatment cycles 1, 3, 4 and 6 were captured using a Zeiss optical microscope for 3827 and 3832 Tata tube steel grades.

4.5.1 3827 Micrographs

Figure 46 shows that all the microstructures for 3827 are composed of a mixture of ferrite, bainite and pearlite, which agrees with the phase formation simulation in JMatPro. A and B have higher cementite proportions than C and D. This would be due to different CGJC temperatures, where A and B cool to 700°C and C and D cool to 660°C. Cooling to 700°C would have a smaller proportion of ferrite forming. Because of this, during the subsequent cool to the HGJC temperature, more austenite would be available to go through a transformation as it cools past the eutectoid temperature into the ferrite + pearlite phase field. These observations agree with the tensile data in section 4.4, as both A and B have higher tensile strength than C and D.

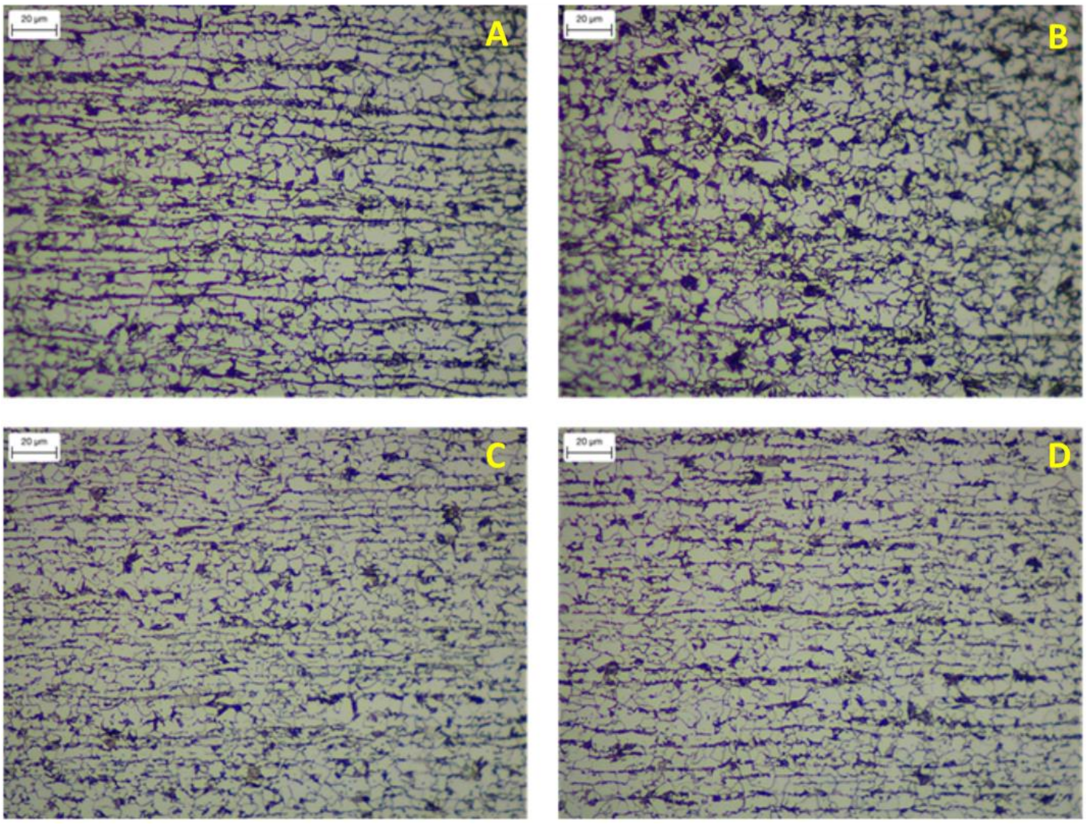

Figure 46: 3827 microstructures - A. Cycle 1 700/420, B. Cycle 2 700/360, C. Cycle 4 660/420, D. Cycle 6 660/360.

4.5.2 3832 Micrographs

Figure 47 shows that all the microstructures for 3832 are composed of a mixture of ferrite, bainite and pearlite, which agrees with the phase formation simulation in JMatPro. E and F have higher proportions of cementite than G and H due to the different CGJC temperatures, where E and F cool to 700°C and G and H cool to 660°C. Cooling to 700°C could have a smaller proportion of ferrite forming, so during the subsequent cool to the HGJC temperature, more austenite would be available to go through a transformation as it cools past the eutectoid temperature into the ferrite + pearlite phase field. These observations show that E and F both have higher tensile strength than G and H. Comparing the 3827 microstructures against 3832, the niobium in the 3832 chemistry has led to grain refinement and is also why it has achieved better properties overall. The niobium provides strengthening through grain refinement and precipitation strengthening. 3832 also had higher formability due to less of a hardness mismatch between phases, as niobium precipitates could help increase the hardness in the ferrite phase [132].

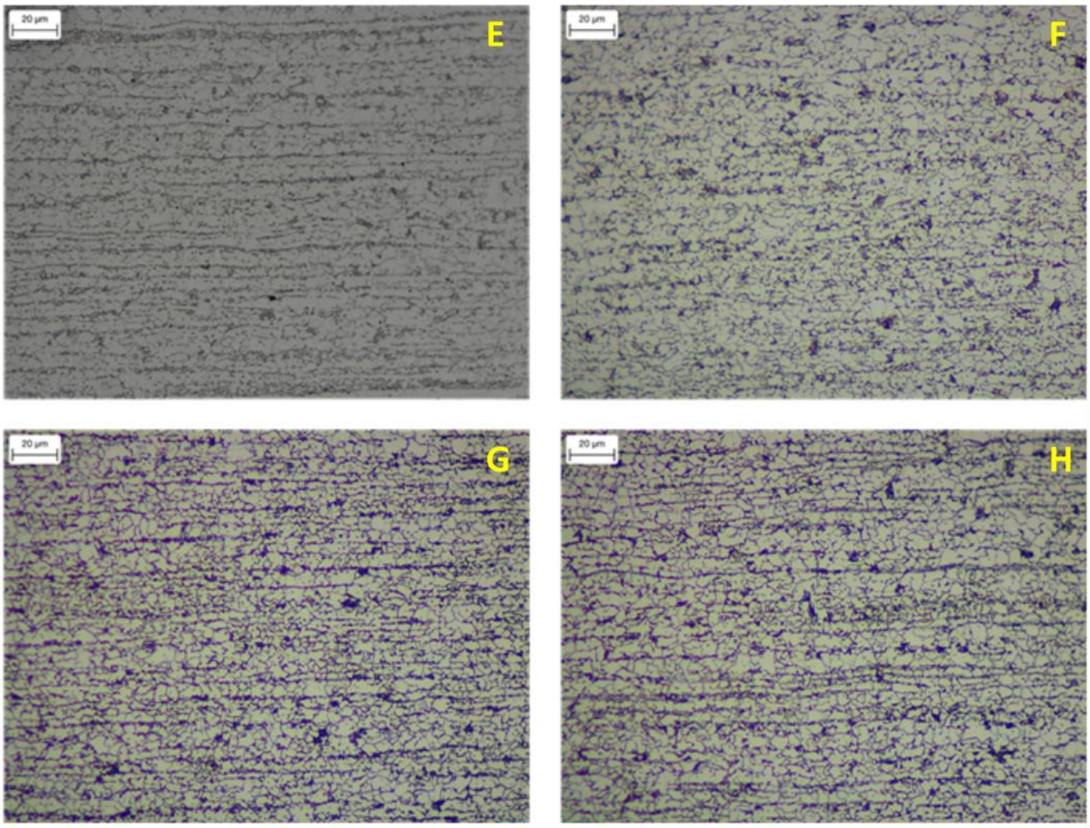

Figure 47: 3832 microstructures - E. Cycle 1 700/420, F. Cycle 2 700/360, G. Cycle 4 660/420, H. Cycle 6 660/360.

4.6 Discussion of Results

Overall, 3832 shows higher strength levels in comparison to 3827, which is because 3832 has an addition of Niobium to its chemistry, which provides a strength increase through grain refinement and precipitation strengthening [35]. Not surprisingly, the heat-treated 3827 and 3832 samples achieved good combinations in properties. Firstly, looking at cycles 1, 4 and 7, all quenched down to the low-temperature bainite region with a slow cooling temperature of 700°C, 660°C and 620°C. Whereas this temperature lowers, there is an increase in pro-eutectoid ferrite formation. Confirmed in the average results, where for cycles 1, 4 and 7, the 3827 UTS lowers from 616MPa to 579MPa, and for 3832, 607MPa to 600.5MPa. For 3832, there is less difference in UTS for these cycles due to the Niobium addition. For these cycles, the aim was to achieve ferritic bainitic steel, where the strength levels increase as the proportion of bainite increases. The strength increases through grain refinement, the inherent high dislocation density of bainitic phases and precipitation strengthening due to Nb additions for the 3832 alloy, which is why there was less difference in UTS amounts. Compared to HSLA and DP steels, Ferritic-bainitic steels have advantages such as improved stretchability, higher strain hardening and total elongation. This improvement results from a reduction in hardness mismatch between the phases as the difference in hardness between ferrite and bainite to ferrite and martensite is reduced. Causing the microstructure to be more homogeneous, reducing the incidence of micro-cracks forming at the interface of the softer matrix to harder microstructure constituents [4], [133].

For cycles 2, 3, 5, 6, 8 and 9, the aim was to achieve a complex phase microstructure composed of a mixture of ferrite, bainite, pearlite and martensite, see section 3.2.1, Figure 20, which shows how the different CGJC and HGJC temperatures promote different phases:

- On inspection of cycles 2 and 3 for 3827 and 3832, which achieved the lowest ferrite levels with an increasing proportion of martensite as the HGJC temperature lowered. The results for cycles 2 and 3 show the UTS increases as the HGJC temperature (quenching temperature) lowers because the proportion of martensite to bainite increased for cycle 3 for both compositions.
- Looking at cycles 5 and 6, where the amount of ferrite increased by lowering the CGJC temperature with different proportions of martensite and bainite as the HGJC lowered. For both compositions, the UTS increased as the HGJC reduced.
- Cycles 8 and 9, where the proportion of ferrite further increased, have led to the lowest UTS values overall for both compositions.

As mentioned, the aim was to achieve a CP microstructure, as CP steels have been shown in the literature to achieve substantial grain refinement through microalloying with Nb [35]. Compared to other AHSS, such as DP steels, CP achieves a higher tensile and yield ratio. Other benefits of CP steels, compared to DP steels, are higher energy absorption levels, good hole expansion due to less hardness mismatch between the phases and superior stretch flangeability [48], [134], [135]. Also, on inspection of the micrographs, it is clear the grains are smaller for 3832, compared to 3827.

4.7 Conclusion of Results

This study investigated the properties of low-alloyed tube steels, specifically Tata tube materials 3827 and 3832, by applying various heat treatments. The primary objective was to establish the groundwork for developing novel Q&P steels with improved mechanical properties. The chemical composition of both steel grades was relatively lean, with C, Mn, and Si as the primary elemental additions. To determine the optimal heat treatment regimens for inducing desired microstructural changes, TTT and CCT diagrams were simulated using JMatPro software. The resulting heat treatments were applied to samples 3827 and 3832, and the microstructures were characterised using optical microscopy. The results of the heat treatment experiments demonstrated that carefully controlling the heating and cooling rates induced the desired microstructural changes, resulting in significant improvements in mechanical properties. ThermoCalc software was used to evaluate the impact of elemental variations on transformation temperatures and provided insights into the starting point for developing novel Q&P steels. Overall conclusions below:

- 3832 outperformed 3827 during tensile testing and achieved a UTS > 600MPa and total elongation > 21.5% for all heat-treatment routes.
- Increased mechanical properties was due to the small Nb addition, which helps to refine the grains of the steel. In addition, the micrographs show clear evidence of grain refinement for 3832.
- Overall, 3832 has achieved comparable properties to DP600 but with less alloying additions.
- Property enhancement was achieved through cleverly designed heat-treatments to induce the desired microstructural evolution.
- Skills developed through modelling and heat treatment design will be utilised to design novel alloys in the next chapter.
- C-Mn-Si will be the start point for designing novel Q&P alloys.

In summary, the experimental findings of this study have laid the groundwork for developing novel Q&P steels with enhanced mechanical properties. Additionally, using simulation software to design heat treatments and evaluate the impact of elemental variations has provided valuable insights into the microstructural evolution of low-alloyed tube steels.

Chapter 5

Q&P Alloy Design Results Chapter

5. Quenching and Partitioning Steels - Alloy Design Results

This section will review the CCT and TTT results for the four chosen alloys, alloy validation using ThermoCalc, martensite tempering and Jominy hardenability using JMatPro. In addition, the design of heat-treatments using the Koistinen-Marburger relationship will be covered.

5.1 TTT and CCT Results

TTT and CCT results for the four alloys will be described throughout this section.

5.1.1 TTT

The quantities such as A_r^1, A_r^3, B_s, M_s, $M_{50\%}$ and $M_{90\%}$ from TTT diagrams were tabulated. Referring to the design factors in section 3.3.5, all four alloys have an A_r^3 temperature below 840°C. For the A_r^1 temperature, all but one of the alloys are below 700°C. The alloy above 700°C is $MnSiC_{(0.2\%)}$ at 701.5°C. It is over the design factor, but by looking at the transformation time at 700°C for $MnSiC_{(0.2\%)}$, it will take approximately 30s to transform 1% ferrite. As the slow cool section takes 42.5s to cool to 700°C, there will be very little time for ferrite formation. Figures 48-51 show the TTT diagrams for the four alloys, followed by Table 6 summarising the transformation temperatures.

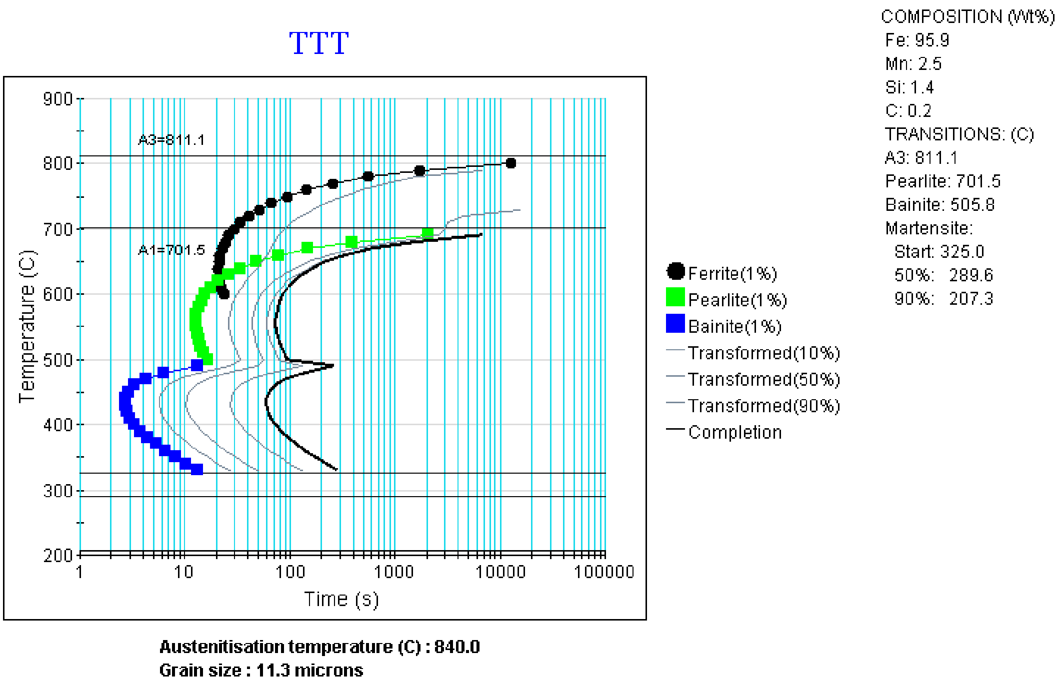

COMPOSITION (Wt%)
Fe: 95.9
Mn: 2.5
Si: 1.4
C: 0.2
TRANSITIONS: (C)
A3: 811.1
Pearlite: 701.5
Bainite: 505.8
Martensite:
Start: 325.0
50%: 289.6
90%: 207.3

Austenitisation temperature (C) : 840.0
Grain size : 11.3 microns

Figure 48: JMatPro TTT diagram for MnSiC$_{(0.2\%)}$.

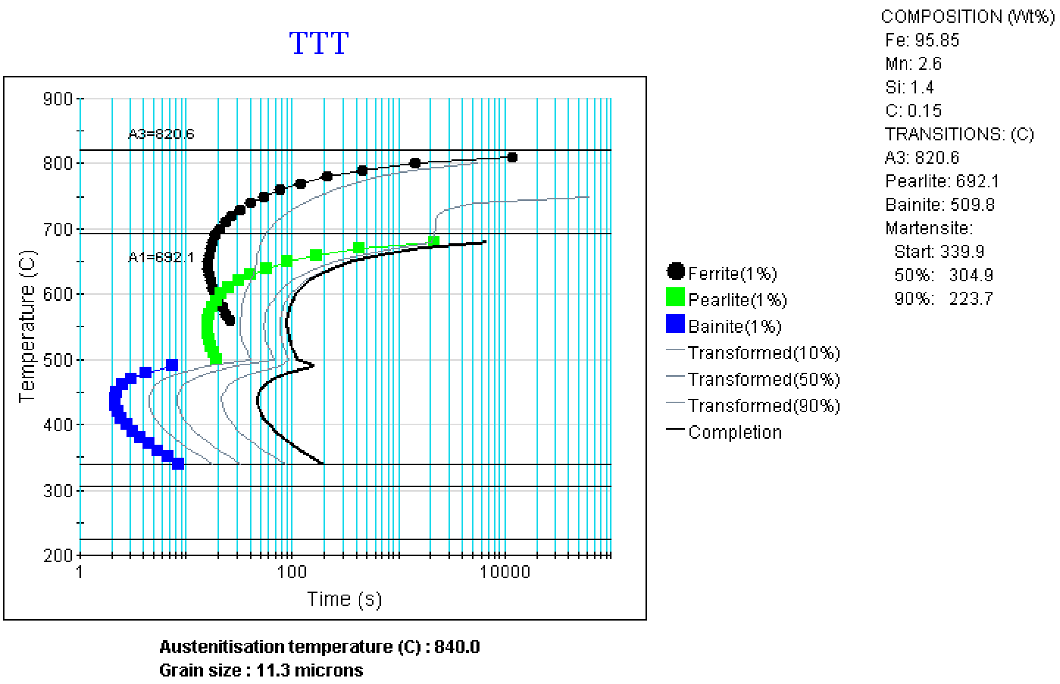

COMPOSITION (Wt%)
Fe: 95.85
Mn: 2.6
Si: 1.4
C: 0.15
TRANSITIONS: (C)
A3: 820.6
Pearlite: 692.1
Bainite: 509.8
Martensite:
Start: 339.9
50%: 304.9
90%: 223.7

Austenitisation temperature (C) : 840.0
Grain size : 11.3 microns

Figure 49: JMatPro TTT diagram for MnSiC$_{(0.15\%)}$.

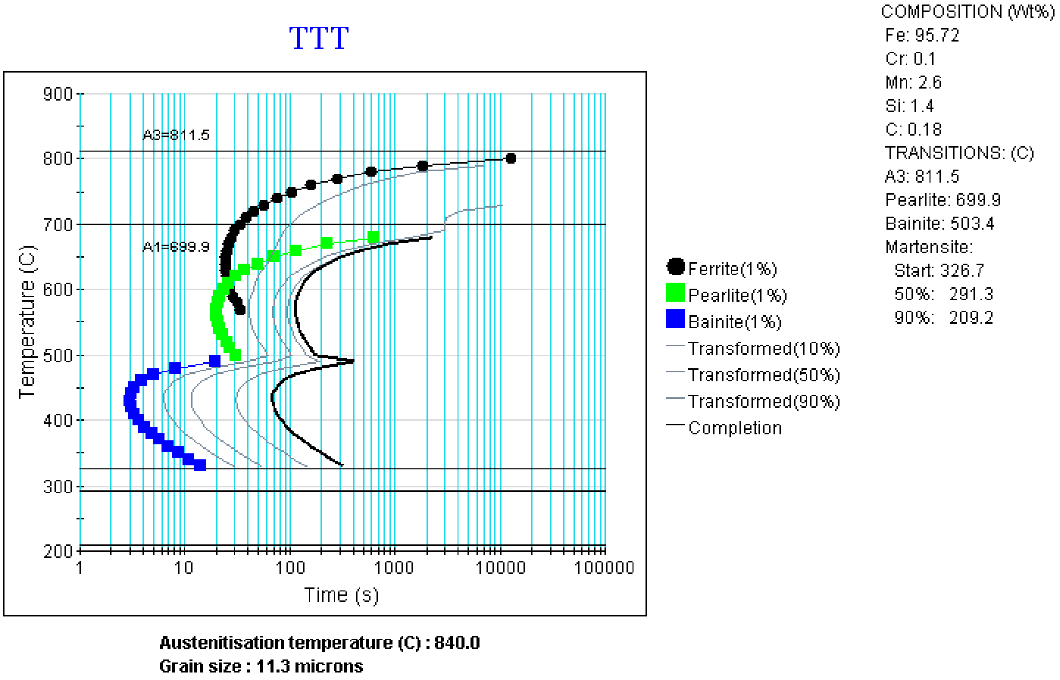

COMPOSITION (Wt%)
Fe: 95.72
Cr: 0.1
Mn: 2.6
Si: 1.4
C: 0.18
TRANSITIONS: (C)
A3: 811.5
Pearlite: 699.9
Bainite: 503.4
Martensite:
Start: 326.7
50%: 291.3
90%: 209.2

Austenitisation temperature (C) : 840.0
Grain size : 11.3 microns

Figure 50: JMatPro TTT diagram for CMnSiCr.

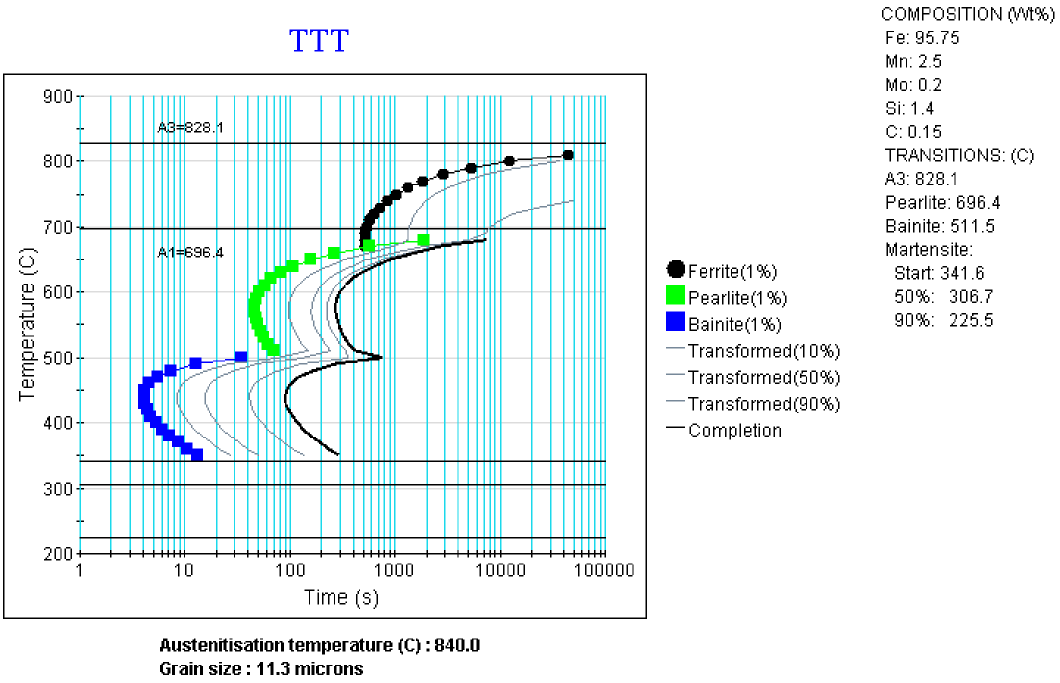

COMPOSITION (Wt%)
Fe: 95.75
Mn: 2.5
Mo: 0.2
Si: 1.4
C: 0.15
TRANSITIONS: (C)
A3: 828.1
Pearlite: 696.4
Bainite: 511.5
Martensite:
Start: 341.6
50%: 306.7
90%: 225.5

Austenitisation temperature (C) : 840.0
Grain size : 11.3 microns

Figure 51: JMatPro TTT diagram for CMnSiMo.

Table 6: Transformation temperatures summarised for the four alloys.

	Transformation Temperatures (°C)					
Alloy	A_r^1	A_r^3	B_s	M_s	$M_{50\%}$	$M_{90\%}$
MnSiC$_{(0.2\%)}$	702	811	506	325	290	207
MnSiC$_{(0.15\%)}$	692	821	510	340	305	224
CMnSiCr	700	812	503	327	291	209
CMnSiMo	697	829	511	341	225	226

5.1.2 CCT

The CCT simulation will also provide the transformation temperatures, but in addition, it will also show what cooling rates will form martensite, indicating the hardenability of the material. Another feature within JMatPro is the ability to retrieve point information by selecting the different cooling curves. Each cooling curve will have a predicted formation of phases, tensile/yield stress, and hardness. Also, the hardness values at room temperature are across the bottom of the cooling curves. One significant difference between TTT and CCT is that the C-curves shift to the right. The CCT diagram shows that the time and temperature for ferrite and pearlite formation increased. Figures 52-55 show the CCT diagrams for the four alloys.

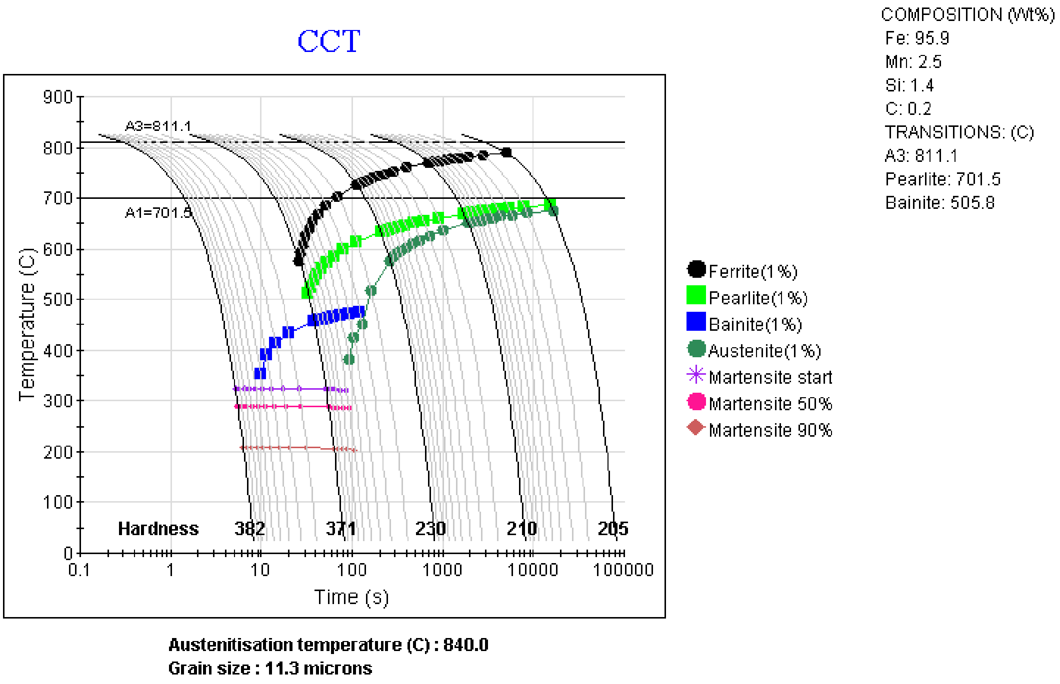

Figure 52: JMatPro CCT diagram for MnSiC$_{(0.2\%)}$.

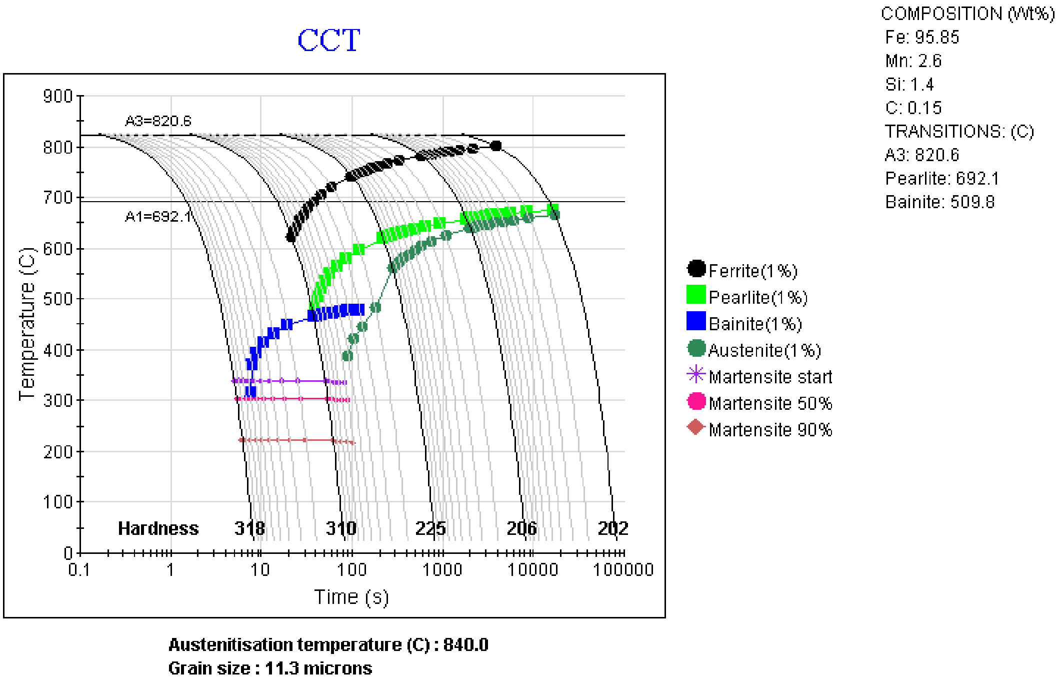

Figure 53: JMatPro CCT for MnSiC$_{(0.15\%)}$.

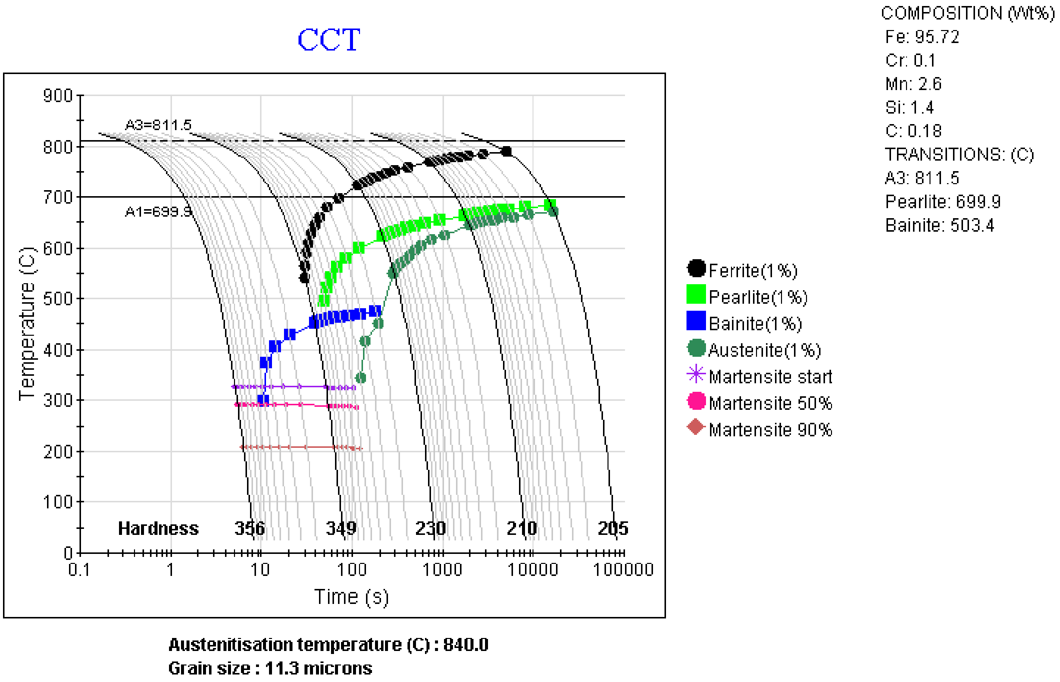

Figure 54: JMatPro CCT diagram for CMnSiCr.

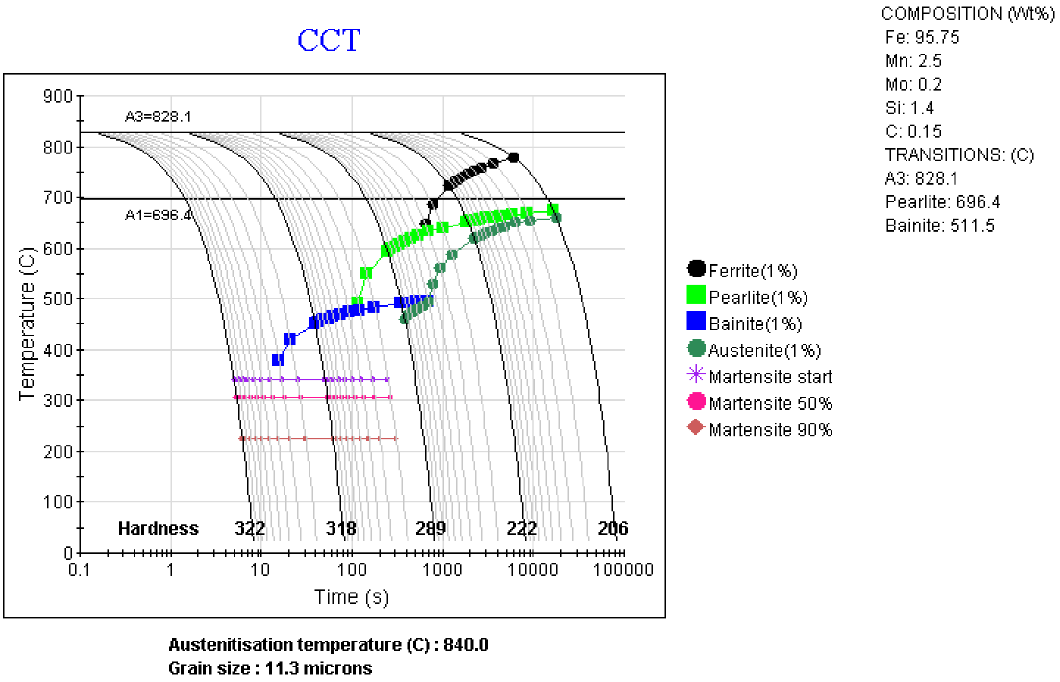

Figure 55: JMatPro CCT diagram for CMnSiMo.

5.2 ThermoCalc Validation of Alloys

Before the alloys went forward for lab casting and processing, they were validated in ThermoCalc to ensure the formation of ferrite and precipitates was sufficiently suppressed. The suppression of precipitates will provide enough free carbon in the system to saturate the austenite phase during the partitioning step.

5.2.1 Property Diagrams

This section will review the property diagram results using the TCFE7 database in ThermoCalc. For each alloy, simulation of phase formation, Gibbs energy of formation and carbon mass fraction in all phases. On these property diagrams, it is possible to observe how the phases will form with the temperature lowering from 1600°C - 0°C. An essential aspect of these simulations is that they run under equilibrium conditions, so there is a finite time for the transformations to complete. Only a minimal amount of cementite and other precipitates will form for all four alloys, even under these equilibrium settings. See Figure 56, showing phase formation for each of the four alloys.

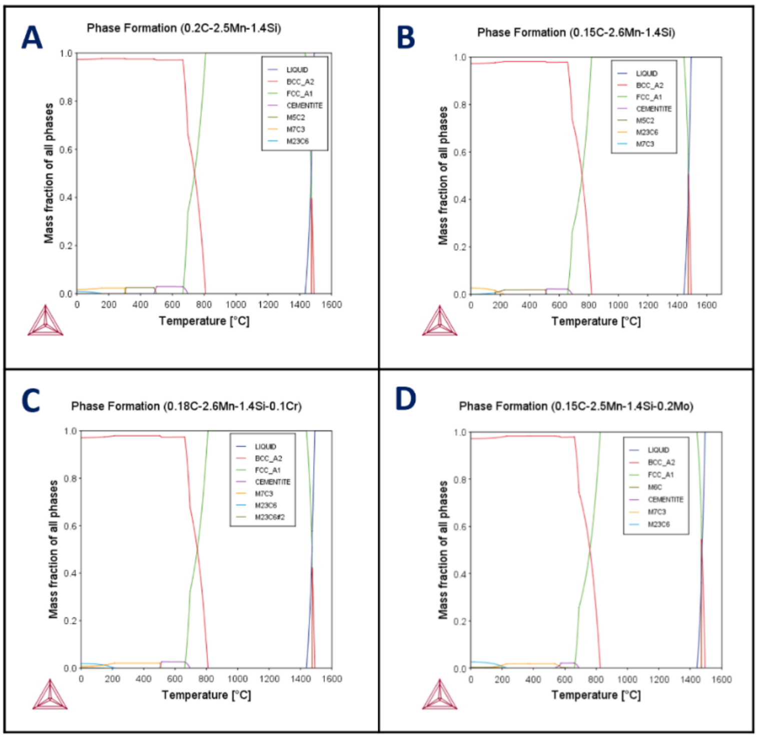

Figure 56: Phase formation diagrams - A. MnSiC$_{(0.2\%)}$, B. MnSiC$_{(0.15\%)}$, C. CMnSiCr, D. CMnSiMo.

i. Gibbs Energy of Formation

For a phase transformation to complete, it needs to lower the system's free energy, meaning it is a favourable reaction. Gibbs energy of formation looks at what phases will form, depending on which has the lowest Gibbs energy as the temperature stepped from 1600°C - 0°C. The purpose of these simulations is to see if the formation of cementite and precipitates is an unfavourable reaction based on its Gibbs energy contribution. The TCFE7 steel and iron database in ThermoCalc was used for these simulations. Similarly, this simulation runs under equilibrium conditions. At higher temperatures above approximately 1450° for all four alloys, the liquid phase is the most favourable as it lowers the overall free energy of the system. During cooling below the liquidus, the liquid phase will be consumed by the formation of FCC (austenite), as this phase now lowers the free energy and is the most favourable reaction. Once the temperature drops below the A_r^1 temperature, FCC will transform to BCC (ferrite), as this BCC phase now has the lowest free energy. At this point, cementite and precipitates' formation is unfavourable for all four alloys as there is a minimal contribution to lowering the system's free energy. Figure 57 shows the Gibbs energy of formation for the four alloys.

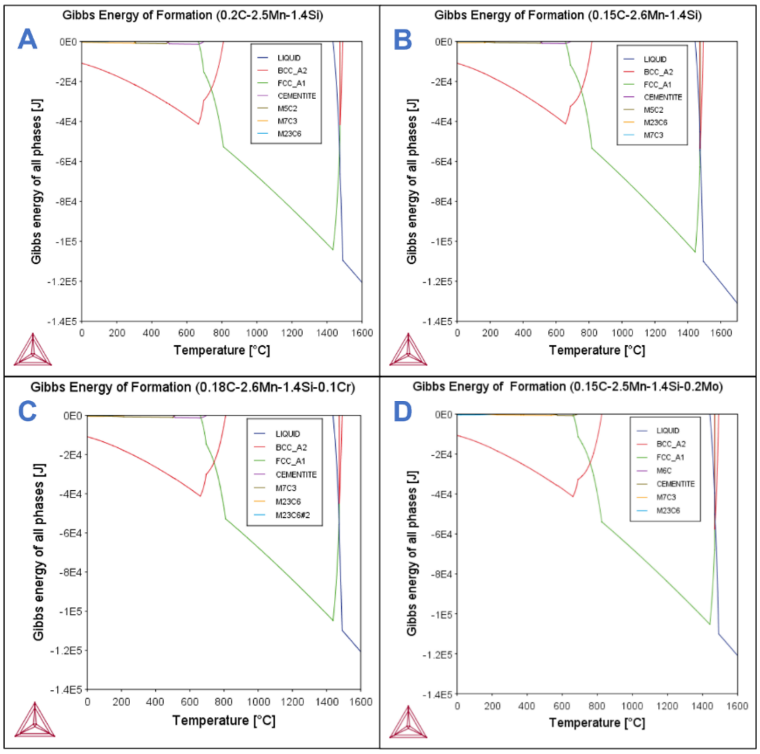

Figure 57: Gibbs energy of formation - A. MnSiC$_{(0.2\%)}$, B. MnSiC$_{(0.15\%)}$, C. CMnSiCr, D. CMnSiMo.

ii. Mass Fraction of Carbon in all Phases

Figure 58 illustrates the mass fraction of carbon in all phases. These four property diagrams show the four alloys' carbon mass fraction in all phases. For all four alloys, it is the M7C3 precipitate that takes up the most significant amount of carbon, but it is at deficient levels, < 0.09 Wt.%. Like previous simulations, the temperature steps from 1600°C - 0°C and calculates the amount of carbon in all phases at each interval. With these four alloys, minimal carbon is taken up by these competing reactions, showing their suitability for the partitioning mechanism.

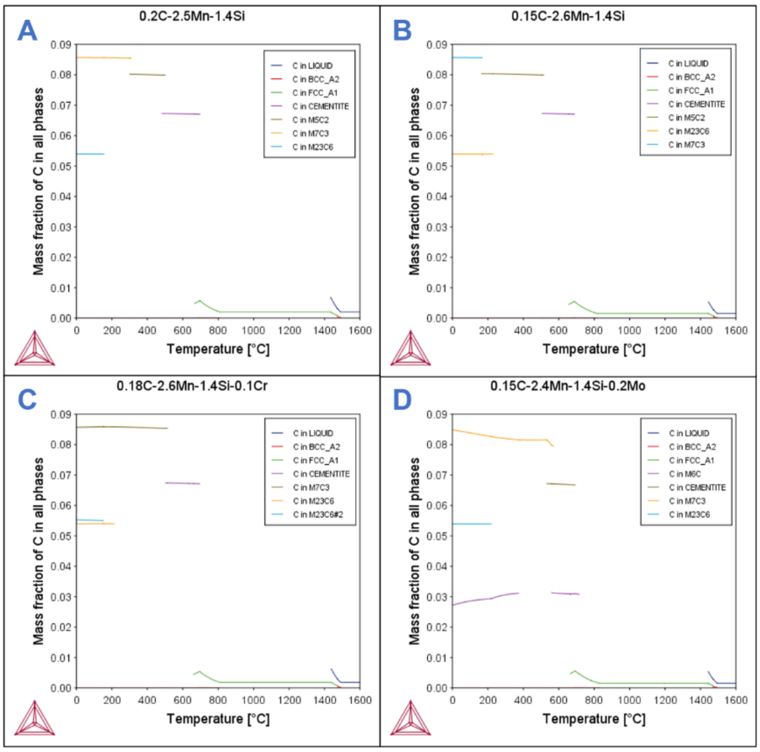

Figure 58: Mass fraction of carbon in all phases - A. MnSiC$_{(0.2\%)}$, B. MnSiC$_{(0.15\%)}$, C. CMnSiCr, D. CMnSiMo.

iii. TC-PRISMA Bulk Precipitate Volume Fraction

Unlike the previous ThermoCalc simulations, TC-PRISMA uses non-equilibrium conditions using the Langer-Schwartz theory and Kampmann-Wagner numerical approach. There are multiple articles which have used this approach to model the precipitation during the complete evolution [90], [92], [93], [136]. A system will seldom approach equilibrium; it will be metastable by nature, and because of this, non-equilibrium simulations help to get a better understanding of the material. The set-up for these calculations is described extensively in the experimental chapter, 3.3.7 ii. A), including Figure 24 which shows the non-isothermal heat treatment profile used for the calculations. As a result, by taking non-equilibrium conditions, the amount of precipitates is reduced compared to the last simulation, which had very few precipitates forming. Figure 59 shows the bulk precipitate volume fraction for the four alloys.

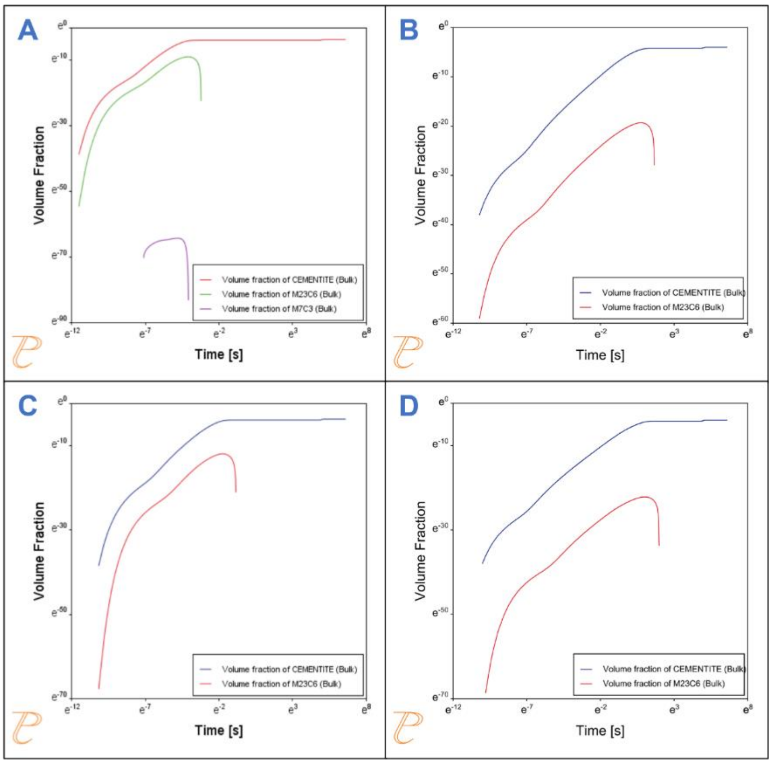

Figure 59: A. MnSiC$_{(0.2\%)}$, B. MnSiC$_{(0.15\%)}$, C. CMnSiCr, D. CMnSiMo.

.iv Scheil-Gulliver Calculator

Each mode of Scheil uses different assumptions, and therefore, the proportions of phases and freezing range change, depending on the type of calculation. Table 7 illustrates the calculated liquidus, solidus, resulting freezing range and proportion of phases at the solidus. Classic Scheil and Scheil with back diffusion provide very similar results. Classic Scheil has a slightly longer freezing range, and the cementite proportion increases. When carbon is set as a fast-diffusing element, it significantly influences the freezing range and reduces by >250°C. Additionally, with fast diffusion, there is a substantial impact on the proportion of precipitate phases, whereas, for all alloys, the proportion of precipitates reduces to zero. Figures 60 and 61 demonstrate the amount of phases and varying freezing ranges.

Table 7: Calculated phases and freezing range using Scheil.

Sample	Type Of Scheil	Liquidus	Solidus	Freezing Range (°C)	Phases @ Solidus (Mass %)			
					FCC	BCC	Cementite	M6C
MnSiC$_{(0.15\%)}$	Classic Scheil	1494.2	1078.0	416	53%	46%	0.029%	
	C Fast Diffuser	1494.1	1346.1	148	53%	46%		
	Back Diffusion	1494.1	1085.4	409	49%	50%		
	C Fast Diffuser & BD	1494.1	1349.3	145	51%	48%		
MnSiC$_{(0.2\%)}$	Classic Scheil	1490.5	1078.3	412	62%	37%	0.205%	
	C Fast Diffuser	1490.5	1343.3	147	61%	38%		
	Back Diffusion	1490.5	1080.9	410	60%	39%	0.149%	
	C Fast Diffuser & BD	1490.5	1345.4	145	60%	39%		
CMnSiCr	Classic Scheil	1491.4	1080.0	411	60%	39%	0.120%	
	C Fast Diffuser	1491.5	1345.6	146	59%	40%		
	Back Diffusion	1491.5	1081.8	410	57%	42%	0.094%	
	C Fast Diffuser & BD	1491.5	1347.6	144	58%	41%		
CMnSiMo	Classic Scheil	1494.0	1077.9	416	50%	49%	0.101%	0.039%
	C Fast Diffuser	1494.1	1330.3	164	48%	51%		
	Back Diffusion	1494.1	1085.2	409	45%	54%		0.026%
	C Fast Diffuser & BD	1494.1	1334.5	160	47%	52%		

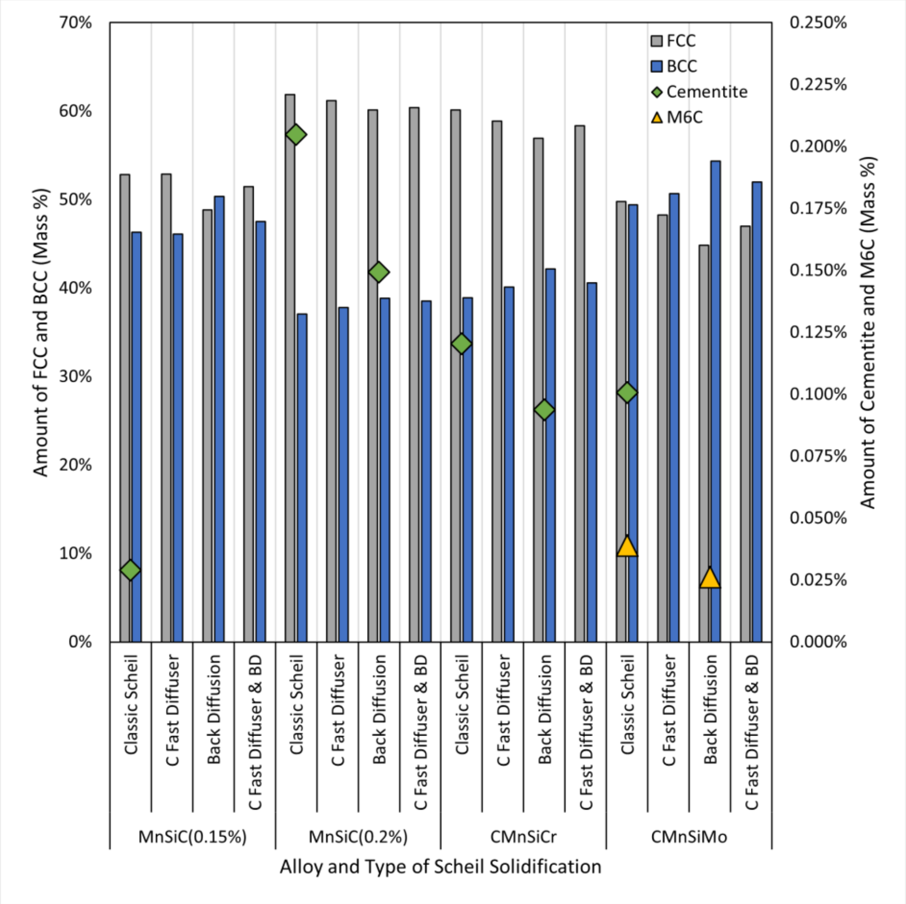

Figure 60: Amount of phases at the solidus.

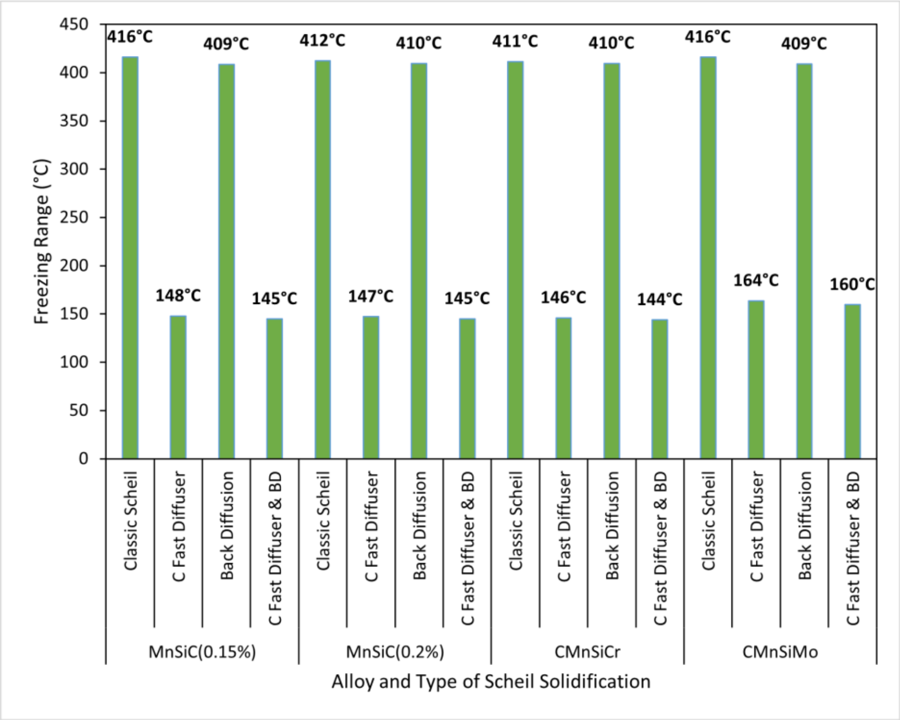

Figure 61: Varying freezing range with different modes of Scheil.

5.3 VIM Casting Results

After final compositional adjustments, a sample of the melt was taken for analysis using OES (optical emissions spectroscopy). OES is a rapid method that determines the elemental composition of metals. Table 8 illustrates the target vs actual composition achieved.

Table 8: VIM casts - target vs actual composition.

Comparing Target Composition to Result

Alloy		C	Mn	Al	Si	P	Ti	Cr	Mo	V	B	N
Target	1	0.200	2.500		1.400							
Actual	MnSiC$_{(0.2\%)}$	0.197	2.458	0.032	1.360	0.001	0.001		0.001	0.002	0.0001	0.0004
Target	2	0.150	2.600		1.400							
Actual	MnSiC$_{(0.15\%)}$	0.147	2.630	0.035	1.420		0.001		0.002	0.002	0.0001	0.0012
Target	3	0.180	2.600		1.400			0.100				
Actual	CMnSiCr	0.179	2.638	0.036	1.425		0.001	0.101	0.002	0.002	0.0001	0.0008
Target	4	0.150	2.500		1.400				0.200			
Actual	CMnSiMo	0.149	2.515	0.036	1.403	0.001	0.001		0.192	0.002	0.0002	0.0005

5.4 Heat Treatment Design

For the heat treatments, transformation temperatures from JMatPro TTT simulations were used within the Koistinen-Marburger relationship to calculate quenching/partitioning temperatures. For a complete description of the Koistinen-Marburger relationship, see section 3.4.1. Ensuring the heat treatments are industrially viable is essential. The heat treatment profiles were inputted in Tata's in-house mimic, using these calculated quenching temperatures. Mimic provides the exact times for each of Tata's CAPL line sections in Port Talbot. Using the Koistinen-Marburger relationship, calculations were completed for quenching temperatures for a primary martensite fraction of 40%, 50%, 60%, 70% and 80%. The quenching temperatures for a 70% and 80% primary martensite fraction would not be viable as they were both past the lowest possible quenching temperature for the CAPL. Due to this, selected quenching temperatures are 40%, 50% and 60% primary martensite formation. Figure 62 shows the calculated quenching temperatures for the four alloys.

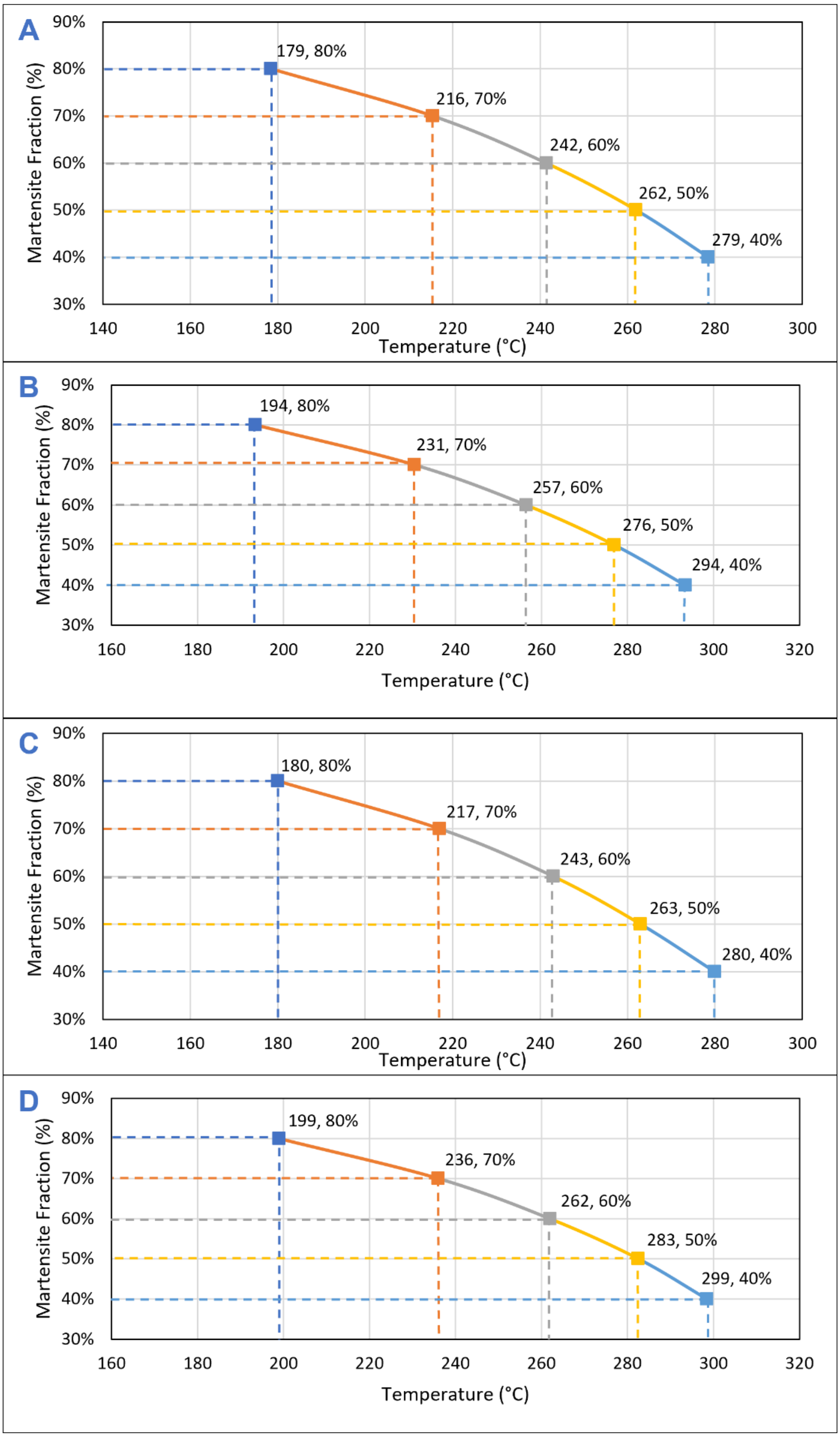

Figure 62: Calculated quenching temperatures using the Koistinen-Marburger relationship. A. MnSiC$_{(0.2\%)}$, B. MnSiC$_{(0.15\%)}$, C. CMnSiCr, D. CMnSiMo.

5.4.1 Martensite Tempering (JMatPro)

To predict if the tensile stress will be > 1300MPa for the designed heat treatments, the martensite tempering simulation in JMatPro was employed. Full details of this calculation setup are in section 3.4.3. These simulations will calculate the tensile stress for an isothermal hold over the quenching temperature; previous heating and cooling sections are not in this simulation. Even without these sections, it will be a reasonable indication of the tensile stress and if the heat treatments are suitable. Results for martensite tempering will be compared against measured tensile stress values in chapter 6. A simulation was run on the three quenching temperatures for the four alloys, incorporating all the quenching temperatures from the HT1 heat treatments. Figure 63 shows the predicted tensile stress for each alloy. $MnSiC_{(0.2\%)}$ predicts its tensile stress >1500MPa for each quenching temperature, with a range of 7.7MPa and a mean of 1513MPa. The $MnSiC_{(0.15\%)}$ alloy showed simulated tensile stresses between 1422-1433MPa, with a range of 10.2MPa and a mean value of 1428MPa. For CMnSiCr, the simulated tensile stress was between 1477-1485MPa, showing a range of 8MPa and a mean of 1481MPa. For CMnSiMo, the simulated tensile stress was between 1421-1432MPa, with its range being 11.1MPa and mean 1426MPa.

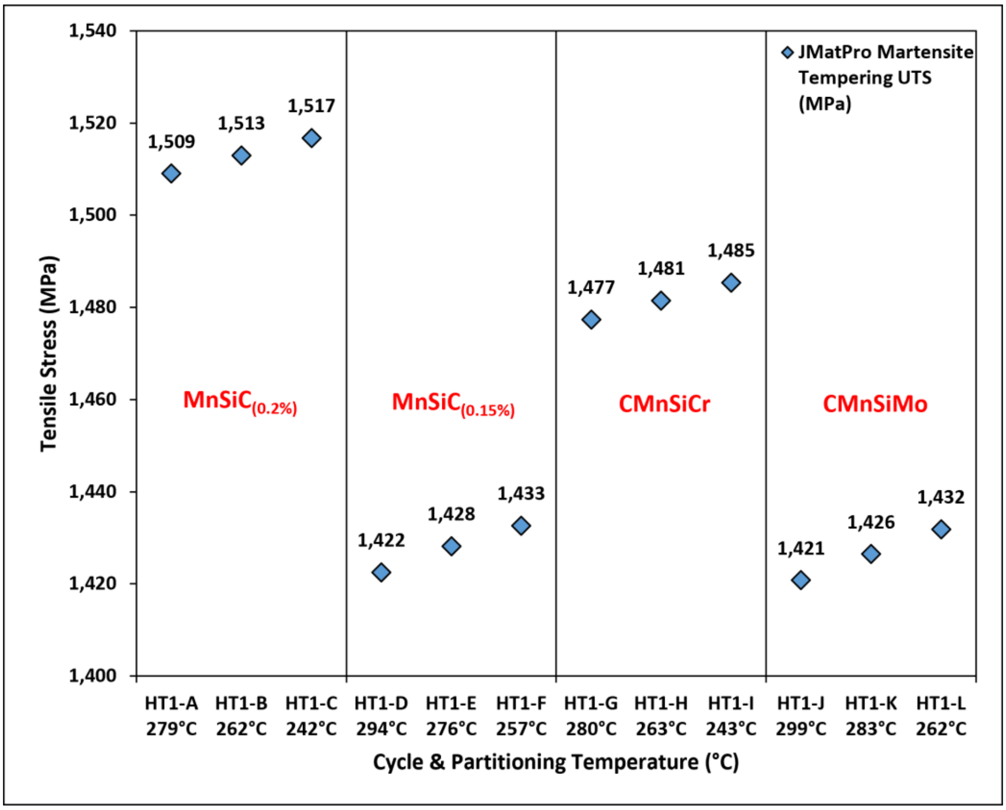

Figure 63: Predicted tensile stress from martensite tempering (JMatPro).

In addition to the tensile stress, the Vickers hardness was simulated. Like the tensile stress simulation, martensite tempering in JMatPro was utilised to see if all heat treatment routes would lead to a Vickers hardness value >400Hv. Figure 64 shows the predicted Vickers hardness for all HT1 heat treatments. Simulated heat treatments for the $MnSiC_{(0.2\%)}$ alloy resulted in a mean Vickers hardness value of 482Hv, with a small range of 2.5Hv. For $MnSiC_{(0.15\%)}$, the mean value was 454Hv, and a range of 3.3Hv. For CMnSiCr, the mean was 471Hv and a range of 2.6Hv; for CMnSiMo, the mean was 453Hv and a range of 3.6Hv.

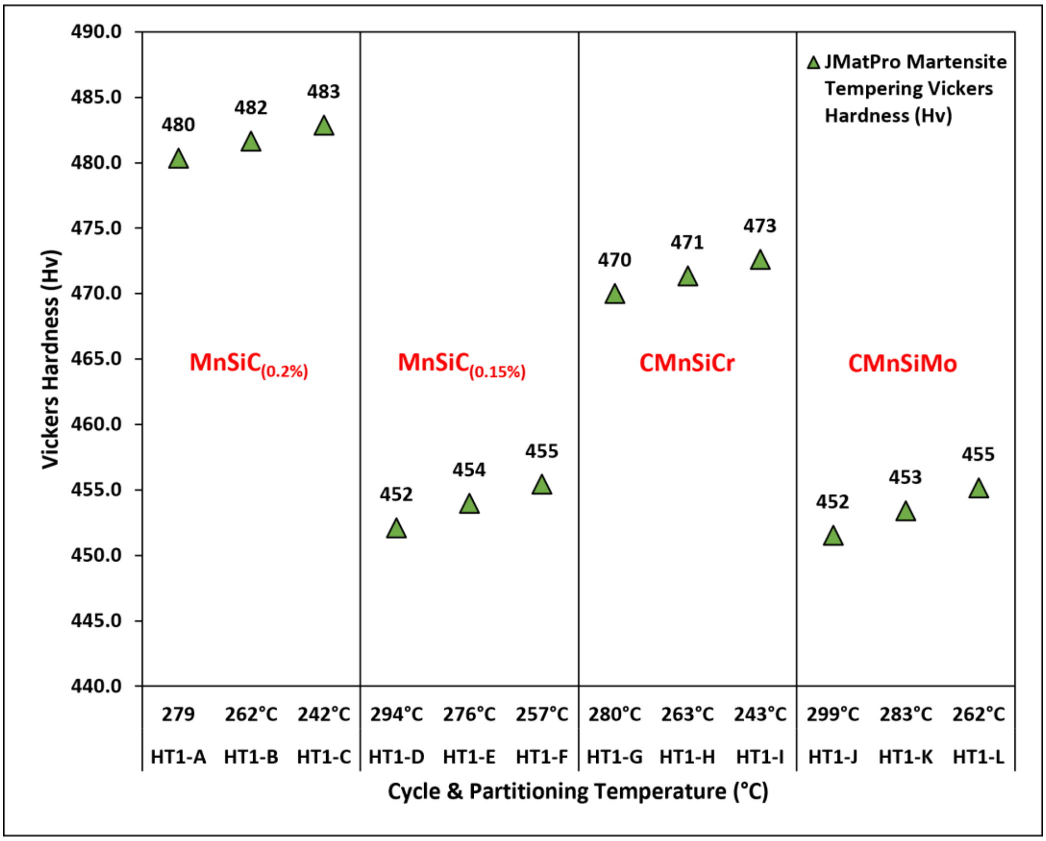

Figure 64: JMatPro martensite tempering, predicted Vickers hardness.

5.4.2 Jominy Hardenability (JMatPro)

The desired end state for these alloys is a cold rolled strip. Due to this, the alloys need to be hot, and cold rolled. For hot rolling, there is an upper limit in tensile strength where they would exceed the rolling load limit. Jominy hardenability simulations using JMatPro will give an idea about the hardenability of the alloys. Full details on the calculation setup are in section 3.4.4. These results show how the tensile, yield and hardness vary along the length of a bar, going from rapid cooling to air cooling at the other end of the bar. They also cover how the microstructure varies across the length of the bar. The following section will cover the property and phase variation for each of the four alloys.

5.4.2.1 MnSiC$_{(0.2\%)}$ Jominy Hardenability

At the start point, the microstructure is fully martensitic and at its maximum level for tensile, yield and hardness. As the distance increases, the tensile stress drops by 8.3%, yield stress by 10.5% and hardness by 9.2% at 3cm along the bar. Beyond 3cm, the drop is more significant. At 4cm, the tensile stress has dropped by 20.8%, yield stress by 26.3% and hardness by 21.1%, followed by a further drop at 5cm with properties starting to plateau at 6cm through to 10cm. In terms of microstructure, at 1cm, it is composed of a mixture of martensite and bainite. At 2cm, it is almost entirely bainitic, and at 3cm, a small amount of pearlite forms. At 4cm, the microstructure is now composed of bainite, pearlite and ferrite. At 5cm, there is almost complete consumption of the bainitic phase, and at 6cm, the alloy is now ferritic-pearlitic. Once it is ferritic-pearlitic, there is very little change in properties up to 10cm. These results indicate that MnSiC$_{(0.2\%)}$ alloy will be suitable for hot rolling without hitting the rolling load limit. Figure 65 shows the Jominy hardenability for MnSiC$_{(0.2\%)}$ alloy.

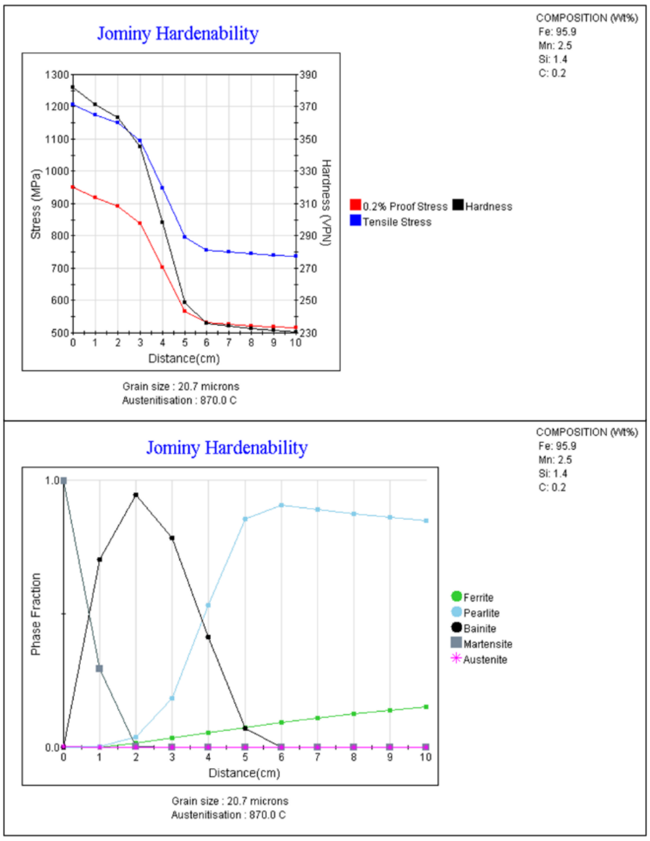

Figure 65: Jominy hardenability MnSiC$_{(0.2\%)}$.

5.4.2.2 $MnSiC_{(0.15\%)}$ Jominy Hardenability

This alloy shows a similar response to the $MnSiC_{(0.2\%)}$ alloy with small differences. The large drop in strength and hardness comes in at 5cm compared to 4cm for the $MnSiC_{(0.2\%)}$ alloy, with the tensile stress dropping by 13%, yield stress by 15.8% and hardness by 13.3%. Followed by another large drop at 6cm, where the tensile stress decreased by 21.3%, yield stress by 25.6% and hardness by 21.8%. At 7cm, very minimal bainite remains, with the structure almost fully ferritic-pearlitic. At this point, there is very little difference in properties up until 10cm. In terms of microstructural evolution, the microstructure of the quenched end is composed of 99.8% martensite with 0.2% austenite. At 1cm the microstructure is 75% bainite / 25% martensite. At 2cm, the microstructure is almost fully bainitic with small amounts of martensite, ferrite and pearlite. From 3-7cm, the amount of bainite reduces with ferrite and pearlite increasing. The structure is fully ferritic-pearlitic through 8-10cm. Again, these results show that this alloy would be suitable for hot rolling. See Figure 66, showing Jominy hardenability results for $MnSiC_{(0.15\%)}$ alloy.

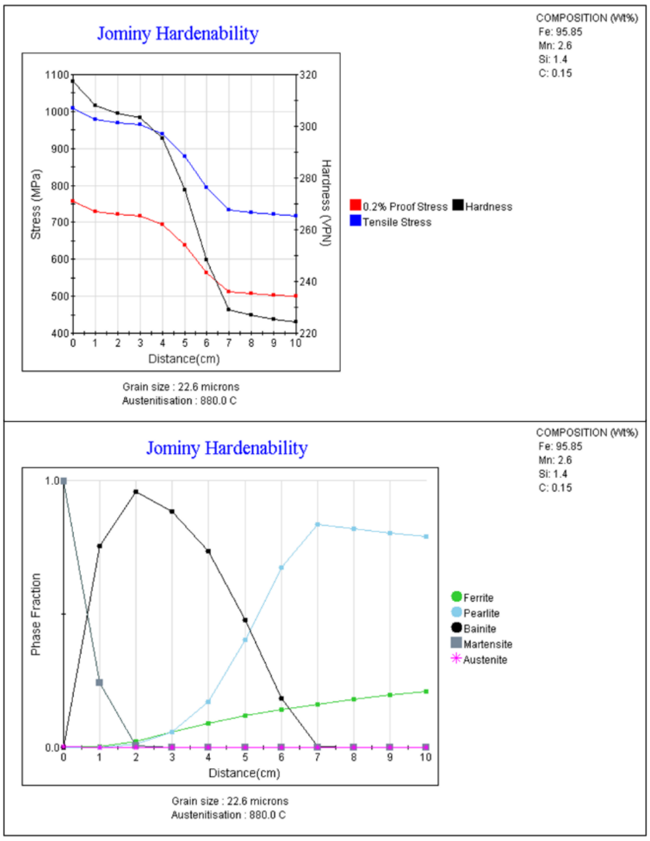

Figure 66: Jominy hardenability $MnSiC_{(0.15\%)}$.

5.4.2.3 CMnSiCr Jominy Hardenability

Figure 67 illustrates Jominy hardenability for CMnSiCr alloy. This alloy has very little change in properties from 0-4cm. At 4cm, the tensile stress reduces by 6.5%, yield stress by 8.1% and hardness by 6.7%. A substantial reduction in properties is seen at 5cm, where the tensile stress reduces by 11.2%, yield stress by 13.8% and hardness by 11.5%. At 6cm and 7cm, the reduction is even more apparent. Tensile stress reduces by 19.2% and 28.3%, yield stress by 23.5% and 33.8% and hardness by 19.7% and 28.9%. The properties plateau between 8-10cm and go through minimal reductions. In terms of microstructural evolution, the microstructure of the quenched end is composed of 99.7% martensite with 0.3% austenite. At 1cm the microstructure is 65% bainite / 35% martensite. At 2cm, the microstructure is almost fully bainitic with small amounts of martensite, ferrite, and pearlite. From 3-8cm, martensite and bainite reduce, with ferrite and pearlite phases increasing. The structure is fully ferritic-pearlitic through at 9 and 10cm. CMnSiCr is a more hardenable alloy than the previous two, but these results indicate it would be suitable for hot rolling without exceeding the rolling load limit.

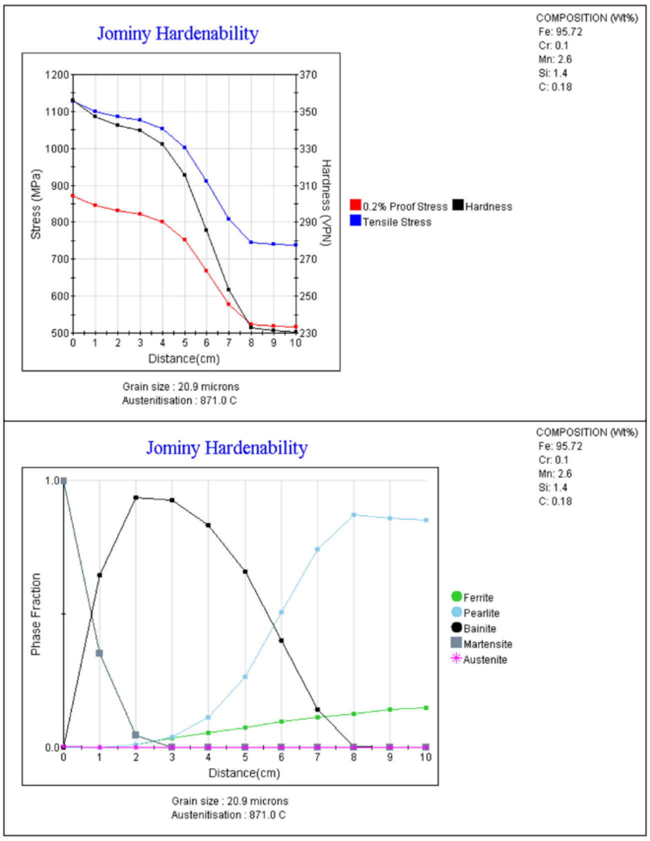

Figure 67: Jominy hardenability CMnSiCr.

5.4.2.4 CMnSiMo Jominy Hardenability

The Jominy results show that this alloy has a high hardenability level, with minimal drop in properties over the whole length of bar. Over the entire length of the bar, the tensile stress only drops by 6.1%, yield stress by 7.5% and hardness by 6.2%. On inspection of the phase formation results, this alloy is almost entirely bainitic for the total length, except when it is initially 99.8% martensite with 0.2% austenite. At 1cm, it is 69% martensite, and 31% bainite with the martensite then reduced to 15% and bainite increased to 85% at 2cm. From 3-10cm, the proportion of bainite is between 89%-99% with small amounts of ferrite and pearlite. Consequently, there is a chance this alloy will be over the rolling load limit during hot rolling due to the minimal drop in properties. Figure 68 illustrates that the tensile properties do not drop below 800MPa, with the minimum tensile stress for CMnSiMo alloy being 958.7Mpa.

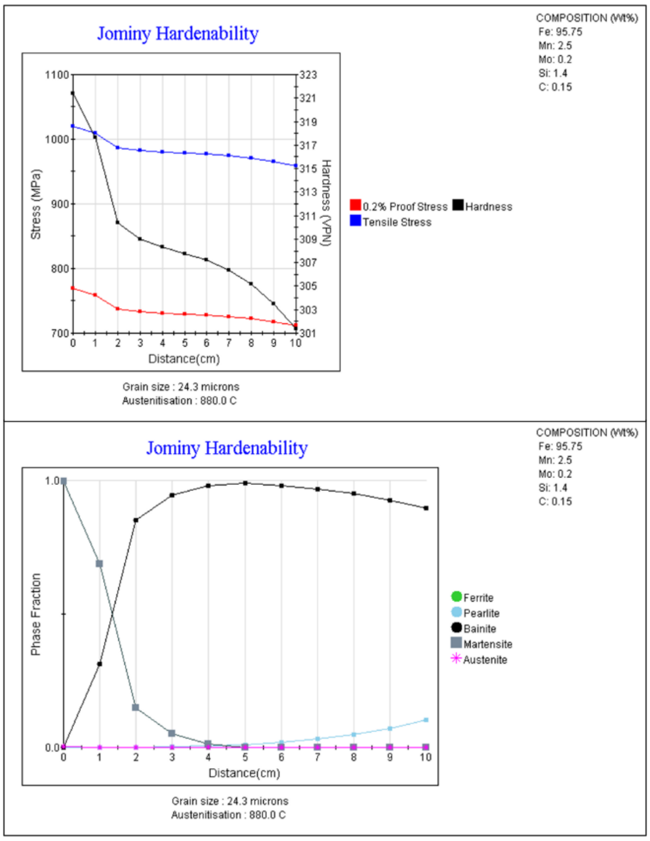

Figure 68: Jominy hardenability CMnSiMo.

5.5 Discussion of Results

The four alloys have been designed with industry settings in mind, as these alloys will need to be processed at TATA steel UK Port Talbot. The most important part of the processing is the continuous annealing which imparts the microstructural evolution. 1-Step quenching and partitioning steels require the microstructure to be austenitic before subsequent quenching to the partitioning temperature. Understanding the limits of CAPL was vital in designing these alloys. CAPL has a maximum soak temperature of 880°C and a maximum CGJC (slow cool) of 700°C and can realistically quench down to 240°C and hold this temperature throughout the overage section. With these limits, the soak was fixed at 840°C, CGJC 700°C and quenching temperature down to a minimum of 240°C.

5.5.1 TTT and CCT Simulations

Simulation of CCT and TTT diagrams in JMatPro was utilised to find compositions that fit in with these limits. TTT diagram, which stands for time-temperature-transformation diagram, is a temperature plot versus the logarithm of time. A TTT diagram determines when a transformation begins and ends at a constant temperature. This information gives the kinetics of isothermal transformations. During the heat treatment of metals and alloys, the temperature changes and continuously cools to room temperature. Due to this, TTT diagrams on their own are not practical as the designed alloys are cooled at different rates and are only isothermally held during the partitioning stage. To cater for this, CCT diagrams were simulated in JMatPro. CCTs are termed continuously-cooled-transformation diagrams, and to account for the temperature constantly changing; the isothermal curves are shifted to longer times and lower temperatures for the reactions to start and end [24]. Using both in combination has proven critical in designing the novel Q&P alloys developed in this thesis. One of the design factors was to have the soak temperature < 840°C, and this has been achieved by simulating TTT and CCT diagrams and finding compositions with an A_r^3 below 840°C. Another design factor was to suppress all ferrite formation during the slow cool to 700°C, and this was achieved by either lowering the A_r^1 below 700°C or ensuring the kinetics for ferrite formation was longer than the slow cool section. Three of the designed alloys were below 700°C, and the $MnSiC_{(0.2\%)}$ alloy was just above, but its kinetics for ferrite formation was at longer times than the slow cool section.

Achieving these factors means the alloys in question can be fully austenitic during the soak and completely suppress ferrite formation during the slow cool section.

TTT and CCT diagrams calculate the most critical transformation temperatures, such as A_r^1, A_r^3, B_S, M_S, $M_{50\%}$ and $M_{90\%}$. Simulation of these temperatures was validated by Saunders et al [137]. For the validation, Saunders et al. compared the simulated TTT and CCT diagrams against experimentally determined diagrams from ‘The Atlas of Isothermal Transformation Diagrams of BS En Steels’ [138] and ‘ASM Atlas of Isothermal Transformation and Cooling Transformation Diagrams’ [139]. One hundred calculated TTT diagrams were compared, covering low alloy to highly alloyed steels. There was a good agreement between the experimental to the simulated, and 80% of the results were within a factor of three and 90% in a factor of four [137]. In addition, the simulated M_S temperature was compared against experimental values from ‘BSC Atlas of Continuous Cooling Diagrams’ [140]. Illustrated in Figure 69 it is clear a high level of accuracy was achieved.

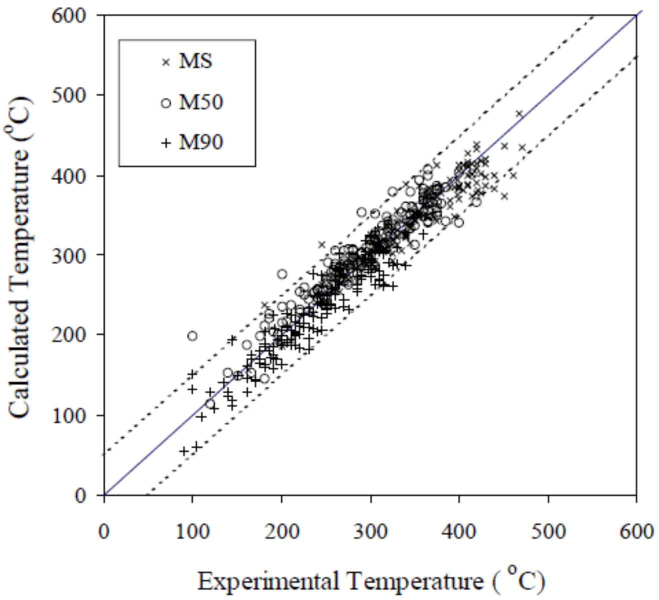

Figure 69: Comparing experimental to calculated martensite temperatures for various steels [109].

5.5.2 ThermoCalc Validation of Alloys

After designing the compositions through repeated simulations of CCT and TTT diagrams in JMatPro, the chosen alloys have been simulated in ThermoCalc to determine if the formation of ferrite, cementite and precipitates are sufficiently suppressed. The first ThermoCalc simulation looked at the mass fraction of all phases between 1600°C and 0°C, and it is clear that the formation of undesirable phases is sufficiently suppressed. The silicon addition is the key to suppressing cementite formation and leaving free carbon in the system, assisting in retaining the austenite phase. Silicon is known to suppress the formation of cementite when >= 1.4 Wt.% and is vital for high-strength steels, particularly when the tempering of martensite is needed. [141]. When in the temperature region for tempering of martensite, the mobility of substitutional atoms is restricted, and the silicon becomes trapped in cementite during para-equilibrium growth. These mechanisms reduce the free energy change related to cementite precipitation and reduce the precipitation kinetics. Essentially the driving force for cementite precipitation is hindered as the cementite phase is forced to inherit silicon [142]. Cementite needs to be suppressed because it is known to act as a damage initiation site in high-strength steels. Silicon has very low solubility in cementite and assists in retarding the precipitation of cementite particles from the parent austenite phase. During partitioning, the rejected carbon atoms from the martensitic laths have no place to go other than to saturate the austenite phase. As the austenite phase is saturated in carbon, it becomes thermodynamically stable at room temperature [143]. An additional simulation looked at the Gibbs energy of formation and showed which phases are most favourable to form based on lowering the system's free energy. The formation of cementite has minimal impact on lowering the system's free energy, meaning its formation would be unfavourable. The final ThermoCalc simulation using the TCFE7 database looked at the mass fraction of carbon in all phases, and it was found that the precipitate phases take up very little carbon. Due to the reasons stated above, the available carbon is saturated into the austenite phase as the kinetics for cementite precipitation is hindered by the silicon additions. These three simulations are based on equilibrium settings, and only transformation thermodynamics are considered. Equilibrium will not be reached; the phases that form will be metastable by nature. ThermoCalc has an additional program called TC-PRISMA which calculates the kinetics of phase transformations. TC-PRISMA has been used to determine the precipitate volume fraction under non-equilibrium conditions. These simulations showed less precipitate formation compared to the thermodynamic-based simulations.

5.5.3 JMatPro Property Simulation

To assess if the designed alloys would meet factors 4, 5 and 8 (section 3.3.5), which are hot rolled tensile stress < 700MPa, UTS > 1300MPa and Vickers hardness > 400Hv, martensite tempering and Jominy hardenability simulations in JMatPro were completed. The martensite tempering results show that all HT1 cycles will lead to a UTS > 1400MPa and hardness > 400Hv, satisfying both factors 5 and 8. As the partitioning stage is essentially tempering at different martensitic temperatures, it is reasonable to expect the tensile stress and hardness to be close to the predicted. Two in-house reports by Sente software (JMatPro) on the 'tempering of steels' and 'tempered hardness of martensitic steels' showed a good agreement between calculated and experimental hardness values for a range of steels at varying tempering temperatures [144], [145]. Also, there was less agreement between the calculated and experimental at higher carbon levels. On the 'tempering of steels,' various steels varying between low to high carbon were compared against experimental results. It was found there was a good agreement until the carbon levels reached 0.82 Wt.%, where at this point, the measured values were significantly lower [145]. As the novel alloys studied throughout this thesis have carbon levels below 0.2 Wt.%, there should be a reasonable agreement between the calculated to the experimental results. In chapter 6 the predicted tensile stress and hardness from martensite tempering will be directly compared against the measured results.

Hot rolling is one of the processing steps the alloys will undergo, and the rolling mill at Tata Port Talbot has a rolling load limit of 700MPa. It is crucial that the hot rolled tensile stress is less than 700MPa, to ensure the rolling load limit is not exceeded. The Jominy hardenability results indicate that alloys $MnSiC_{(0.15\%)}$, $MnSiC_{(0.2\%)}$ and CMnSiCr show a substantial drop in properties across the length of the bar. As the distance across the bar increases, the tensile stress drops below 800MPa and approaches 700MPa. These results indicate that the tensile stress after hot rolling will be very close to 700MPa, either just above or below the limit. In an article by Guo et al., the simulated Jominy hardenability of 4140 and 20MnCr5 steels were compared against experimental results. There was a good agreement between the predicted hardness across the length and the calculated hardness. There was also a good agreement between the predicted phase proportions to the calculated for a 20MnCr5 steel.

Alloy CMnSiMo Jominy hardenability results differed from the other novel alloys, showing a minimal drop in properties over the whole bar length. The Jominy results indicate that the tensile stress does not drop below 950MPa over the whole length. It is reasonable to expect the tensile stress after hot rolling to exceed the rolling load limit. The molybdenum addition in this alloy provides superior hardenability compared to the other alloys. Molybdenum is a carbide-forming element that refines the microstructure and increases the amount of martensite in the structure. Tartaglia et al. [146] studied 'the effects of martensite contents on the mechanical properties of quenched and tempered 0.2%C-Ni-Cr-Mo steels' and found that when increasing Mo additions, the content of martensite increased, increasing the tensile, toughness and fatigue life properties.

5.5.4 VIM Casting – Compositional Accuracy

The results (Table 8) show that achieving the target composition with VIM casting can be challenging but possible with careful control and monitoring. The actual composition of the alloys produced is very close to the target composition in terms of the major elements, such as carbon, manganese, and silicon. However, there is a pickup of non-intentional elements, such as aluminium, titanium, and boron. To ensure the composition is hit, the raw materials are carefully selected and weighed to ensure the correct proportions are used. The vacuum condition in the furnace helps to remove any gas or other impurities that may affect the composition. During the casting process, the temperature and cooling rate are carefully controlled to prevent the formation of defects, such as porosity or cracks, which can affect the composition. Overall, the results demonstrate that achieving the target composition with VIM casting is possible with careful control and monitoring of the melting, casting, and cooling processes. Accurate compositions were achieved for the novel Q&P steels, which further demonstrates the effectiveness of VIM casting in producing high-quality alloys with precise compositions [147].

5.6 Conclusion of Results

- JMatPro has proven invaluable in designing novel Q&P steels which fit in with the capabilities of TATA UK Port Talbot CAPL.
- Alloying additions have been kept below 4.5 Wt.%, achieving factor 7 in section 3.3.5.
- $MnSiC_{(0.15\%)}$, $MnSiC_{(0.2\%)}$, CMnSiCr and CMnSiMo Q&P steels were designed and demonstrate the potential to achieve the desired microstructural evolution.
- The calculated A_r^3 is below 840°C for the four alloys.
- The calculated A_r^1 is below 700°C for three of the alloys, with the A_r^1 just above 700°C for the $MnSiC_{(0.2\%)}$ alloy. Even though the A_r^1 is just above design factor 2, the kinetics for ferrite formation is at longer times than the CGJC section on CAPL. $MnSiC_{(0.2\%)}$ alloy will still be suitable as it has achieved factor 3 from section 3.3.5, and ferrite formation will be sufficiently suppressed.
- The four alloys have been validated in ThermoCalc, showing minimal cementite precipitation due to the Si additions. Si is known to suppress cementite formation when >= 1.4 Wt.%.
- The mass fraction of all phases in ThermoCalc indicates minimal formation of cementite and other precipitate phases, even though the calculations involve equilibrium conditions.
- In terms of free energy, ThermoCalc illustrates that the formation of cementite and precipitates is an unfavourable reaction for the designed Q&P steels.
- Free carbon in the system is needed to stabilise the austenite phase. The mass fraction of carbon in all phases helps validate the designed alloys and shows that the formation of cementite and precipitates takes up very minimal carbon.
- TC-Prisma simulation adds further confidence to the designed alloys, as it involves non-equilibrium using the Langer-Schwartz theory and Kampmann-Wagner numerical approach. The bulk precipitate volume fraction simulation in ThermoCalc again highlights an in-significant volume fraction of cementite and other precipitates. The four alloys showed a maximum volume fraction of cementite <= e^{-4}.

- Martensite tempering simulation in JMatPro has shown that the four alloys will achieve tensile stress of > 1300MPa, achieving design factor 5 in section 3.3.5.
- Jominy hardenability simulation in JMatPro has proven beneficial to get an idea about through thickness hardenability. Alloys $\mathrm{MnSiC}_{(0.2\%)}$, $\mathrm{MnSiC}_{(0.15\%)}$ and CMnSiCr all showed a significant drop in tensile stress as the distance increased, indicating these alloys will be suitable for hot rolling. Alloy CMnSiMo showed a minimal drop in tensile stress over the total length. This alloy may exceed the rolling load limit due to having more significant hardenability.
- Compositional accuracy was achieved for all novel Q&P ingots.

Chapter 6

Q&P Mechanical Properties

6. Quenching and Partitioning Steels - Mechanical Property Results

This chapter will cover the mechanical response of the alloys in their hot rolled state and after cold rolling and annealing. Tensile testing was completed after hot rolling and will be directly compared to the cold rolled and annealed tensile results. In addition, hardness testing of HT1 heat-treated alloys, with all results from hardness and tensile compared against JMatPro property simulations. Also, further JMatPro simulations for fatigue using the tensile stress from the cold rolled and annealed samples will be discussed.

6.1 Hot Rolled Tensile Testing

After hot rolling (section 3.6.4), one plate for each alloy was removed and processed into tensile coupons. (See section 3.12 for a complete description describing the sample preparation and tensile testing procedure). The aim of this investigation is to ensure that the UTS is below the rolling load limit of 700MPa, which would allow ease of production at Tata Steel UK - Port Talbot. During testing, the extension was recorded using a 25mm extensometer to yield and crosshead separation rate of 1mm/min until the final fracture. On completion of testing, the raw displacement and force data were converted into stress-strain curves to calculate the mechanical response of the alloys. The stress-strain curves show yield stress, ultimate tensile stress, uniform elongation, and total elongation. A total of four tensile tests was completed for each alloy; the average results will be in the following sections. See Table 9 shows the average results and standard deviation. Figures 70-73 illustrate the results graphically, including error bars to show repeatability.

Table 9: Average hot rand tensile testing results.

Average Result including Standard Deviation - Hot Rolled Tensile Testing					
Notation	UTS (MPa)	Yield Stress (MPa)	Strain to Failure	Uniform Elongation	Product of Stress Elongation (GPa. %)
$MnSiC_{(0.2\%)}$	693±17	491±30	26%±0.4%	19%±0.5%	18%±0.4%
$MnSiC_{(0.15\%)}$	675±10	531±13	24%±0.7%	18%±1.2%	16%±1.2%
CMnSiCr	676±3	509±9	26%±0.8%	19%±0.4%	18%±1.4%
CMnSiMo	1136±6	1079±21	15%±1.5%	10%±0.7%	17%±1.2%

A) $MnSiC_{(0.2\%)}$

For UTS, this alloy had a mean of 693MPa, a range of 38.1MPa and a standard deviation of 16.5MPa. All four tests are within bounds using a 95% confidence level against the UTS response. For Yield stress, the mean was 491MPa, range 70.9MPa and standard deviation of 30MPa. 95% confidence level showed all repeats were within the bounds, but one of the tests was close to the upper limit. For uniform and total elongation, the mean was 19% and 26%, the range was 1.1% and 1%, and the standard deviation was 0.5% and 0.4%. Similarly, to the Yield and UTS, all four tests are within the confidence bounds, which infers, this alloy will not exceed the rolling load limit of 700MPa.

B) $MnSiC_{(0.15\%)}$

The ultimate tensile stress for $MnSiC_{(0.15\%)}$ has a mean value of 675MPa, a range of 20.8MPa and a standard deviation of 9.5MPa. The tests were repeated, emphasising a minimal range between the minimum and maximum values. Also, all four repeats were within the 95% confidence level. The Yield stress response has a mean of 531MPa, a range of 27.5MPa and a standard deviation of 13MPa. For uniform and total elongation, the mean was 18% and 24%, the range was 2.7% and 1.7%, and the standard deviation was 1.2% and 0.7%. Like the UTS and Yield stress, all four repeats fell within the 95% confidence level, showing the tests were repeatable and, most importantly, the UTS is below 700MPa, indicating it will not exceed the rolling load limit.

C) CMnSiCr

Like the previous two alloys, the average UTS response was below the rolling limit of 700MPa, with its mean being 676MPa. Of all the alloys, this alloy showed the smallest range in UTS of just 6.7MPa and a standard deviation of 3MPa. Not surprisingly, all four tests for this alloy are within the 95% confidence level bounds. This alloy also shows the smallest range for Yield stress, at just 18.5MPa with a standard deviation of 9MPa and its mean Yield stress of 509MPa. For uniform and total elongation, the mean was 19% and 26%, the range was 1% and 1.8%, and the standard deviation was 0.4% and 0.8%. These results indicate there would be no issues hot rolling this alloy at Tata Port Talbot.

D) CMnSiMo

The average ultimate tensile stress for this alloy was 1136MPa, indicating that this alloy would not be able to be hot rolled in an industrial setting at Tata Port Talbot. The range was 13.4MPa and a standard deviation of 6MPa, with this alloy shown to exceed the rolling load limit by > 428MPa, over the four repeats. For Yield stress, the mean was 1079MPa, showing there was not much of an increase in strength after yielding. The Yield stress ranged between a minimum of 1050MPa and a maximum of 1098MPa with a standard deviation of 21MPa. For uniform and total elongation, the mean was 10% and 15%, the range was 1.5% and 2.8%, and the standard deviation was 0.7% and 1.5%. These results indicate this alloy would not be able to be hot rolled at Tata Port Talbot, but it will still be experimented on for comparison.

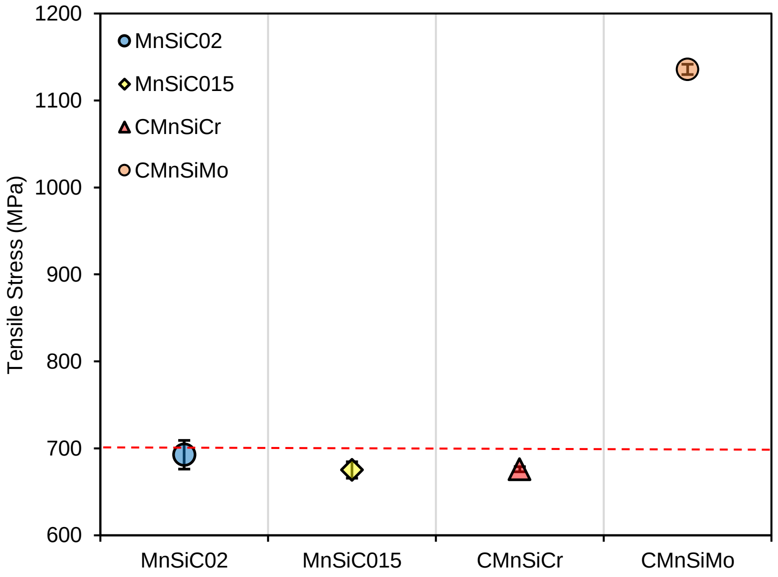

Figure 70: Average hot rolled tensile stress.

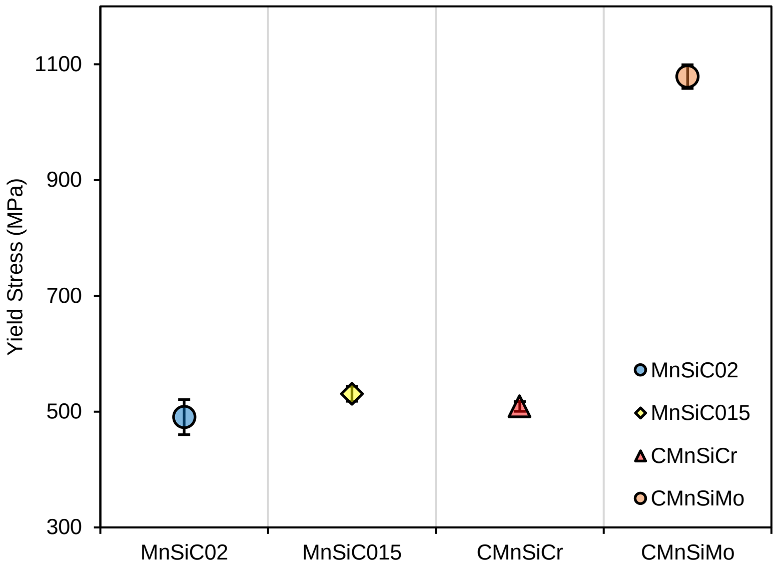

Figure 71: Average hot rolled yield stress.

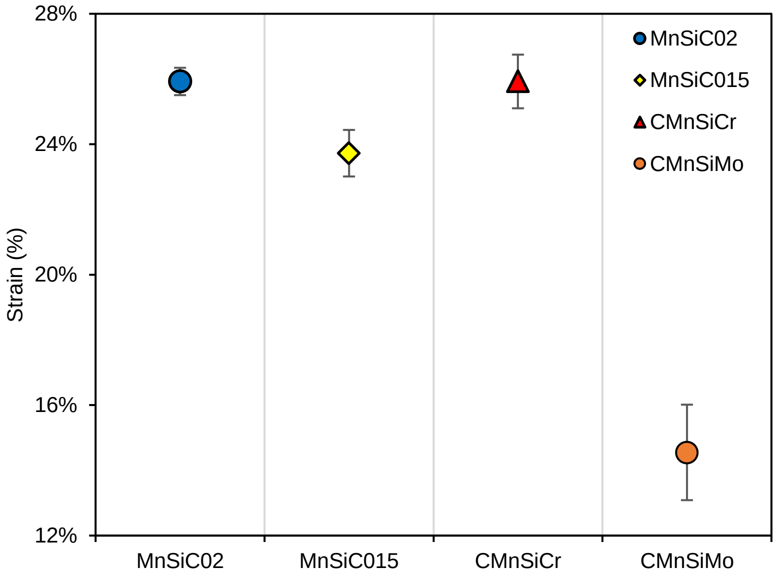

Figure 72: Average hot rolled total elongation.

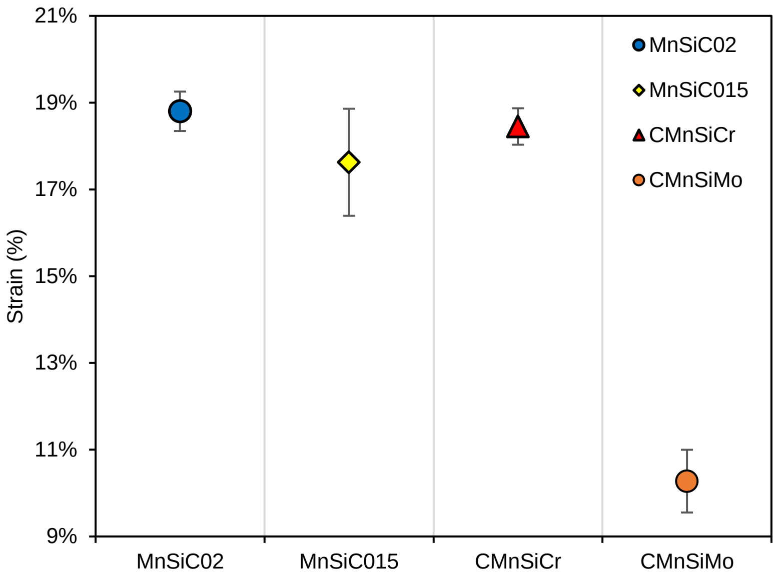

Figure 73: Average hot rolled uniform elongation.

6.2 Tensile Testing After Cold Rolling and Annealing

After hot rolling, the alloys underwent a 65% cold reduction to reduce the gauge from 3.2mm-1.1mm; see section 3.6.5 for a complete cold rolling description. After cold rolling, the plates were cut using a guillotine into Gleeble-sized specimens; see section 3.6.6 for full description. The heat treatments were run using a Gleeble 3500 thermomechanical simulator using the designed HT1 and HT2 heat treatments, see section 3.4.2. The Gleeble can do heat treatments very accurately, with the temperature only varying by ± 0.2°C and following the exact times the strip would travel through each section of the line at Tata Port Talbot CAPL. See Appendix 5 for stress-strain curves for HT1 and HT2.

6.2.1 Heat Treatment 1 (HT1)

There were three individual heat treatment routes for each of the alloys, with HT1 including twelve different heat treatments in total. Table 10 shows the average results for each of the four alloys. Figure 74 shows average yield stress and UTS for each of the four alloys, including custom error bars using the standard deviation between repeats. Figure 75 shows the average uniform and total elongation, including custom error bars using the standard deviation between repeats. The following section will describe the individual results for each of the alloys.

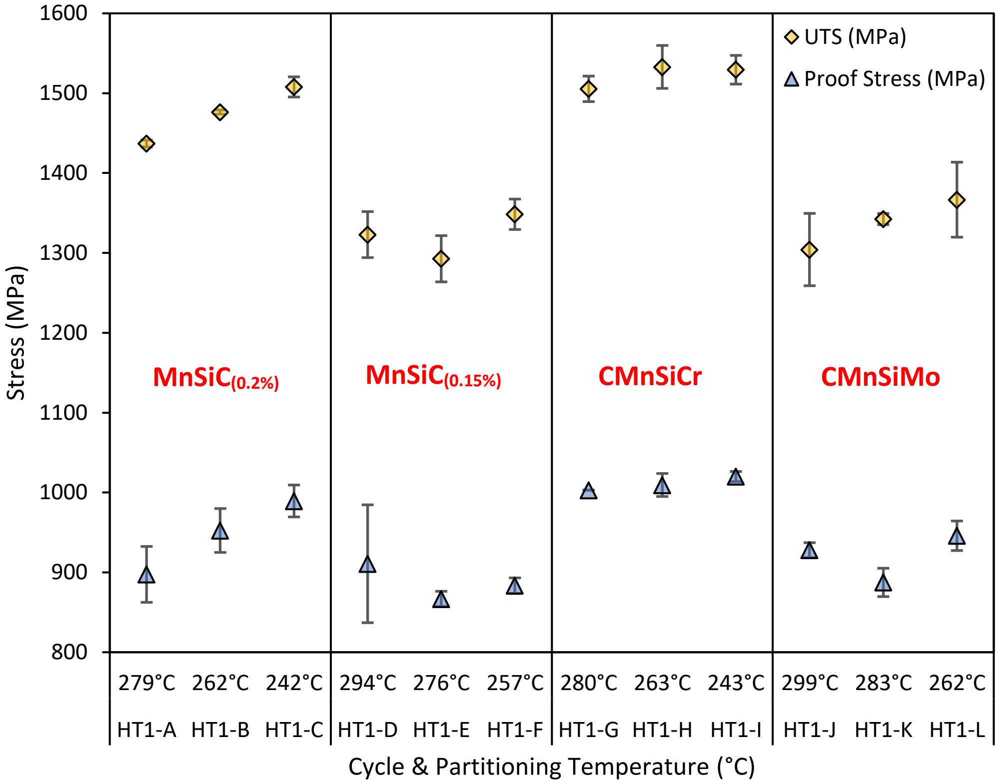

Figure 74: HT1 average UTS and yield stress.

Table 10: HT1 average tensile testing results.

			HT1 - Average Results				
Steel	Code	Partitioning Temperature	Yield Stress (MPa)	UTS (MPa)	Uniform Elongation (%)	Total Elongation (%)	Product of Stress Elongation (GPa.%)
MnSiC$_{(0.2\%)}$	HT1-A	279°C	897	1437	7.0	12.9	18.5
	HT1-B	262°C	952	1476	6.8	12.1	17.9
	HT1-C	242°C	989	1508	6.8	12.6	19.0
MnSiC$_{(0.15\%)}$	HT1-D	294°C	911	1323	7.2	13.6	18.0
	HT1-E	276°C	867	1293	7.4	13.7	17.7
	HT1-F	257°C	883	1348	6.7	12.0	16.2
CMnSiCr	HT1-G	280°C	1003	1505	7.0	12.8	19.3
	HT1-H	263°C	1009	1533	6.8	12.7	19.5
	HT1-I	243°C	1020	1529	7.3	13.6	20.9
CMnSiMo	HT1-J	299°C	928	1304	7.5	14.4	18.7
	HT1-K	283°C	887	1342	7.2	13.7	18.4
	HT1-L	262°C	946	1367	7.2	13.7	18.7

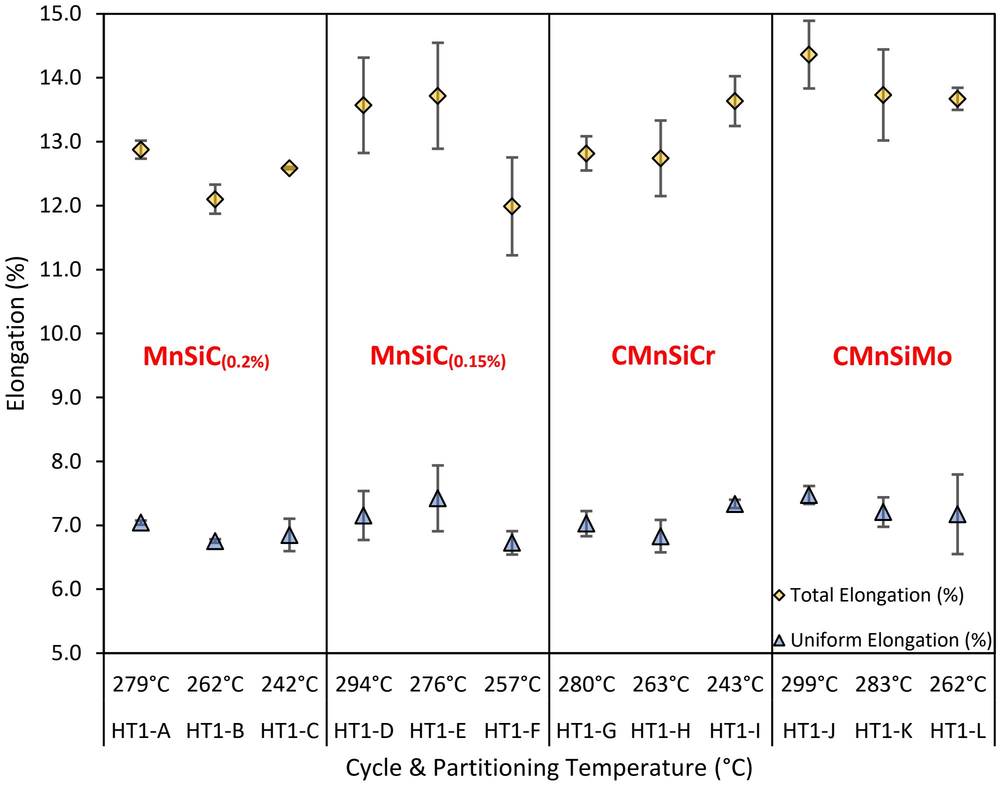

Figure 75: HT1 average uniform and total elongation.

A) MnSiC$_{(0.2\%)}$

After converting the raw tensile data to stress-strain curves, properties such as yield stress, ultimate tensile stress, and uniform and total elongation can be calculated. Using descriptive statistics in the data analysis add-in in excel, the mean response for yield and UTS for cycles A, B, and C are 897Mpa and 1437MPa, 952MPa and 1476MPa, 989MPa and 1508MPa. There was a higher range between repeats for the yield stress compared to the UTS for cycles A, B and C. The Yield stress range for cycles A, B and C were 49MPa, 39MPa and 28MPa, whereas, for UTS, the range was only 6MPa, 4MPa and 18MPa. Additionally, the MnSiC$_{(0.2\%)}$ alloy shows high strain hardening ability as there is a substantial increase in strength after the yielding. Cycles A, B and C showed an increase of 540MPa, 524MPa and 518MPa, respectively, with a yield ratio of 0.62, 0.65 and 0.66. For uniform and total elongation, the mean response was 7% and 12.9%, 6.8% and 12.1%, and for cycle C, 6.8% and 12.6%. It is important to note that the alloy's sensitivity to varying quenching temperatures does not significantly impact its ultimate tensile strength (UTS), yield stress, and total elongation. Only 71MPa, 92MPa, and 0.8% differences are exhibited, respectively. Therefore, changes in quenching temperature do not significantly affect the alloy.

B) MnSiC$_{(0.15\%)}$

For yield stress and ultimate tensile stress, the mean response for cycles D, E, and F were 911MPa and 1323MPa, 867MPa and 1293MPa, and for F, 883MPa and 1348MPa. The range between the minimum and maximum for cycles D, E and F for yield stress was 104MPa, 13MPa and 14MPa, and for the UTS was 41MPa, 41MPa and 27MPa. There was a much more extensive range for cycle D compared to the other cycles. This alloy shows a reasonable level of strain hardenability, but to a lesser degree than the MnSiC$_{(0.2\%)}$ and CMnSiCr alloys. After yielding, the strength increased by 412MPa, 426MPa and 465MPa for cycles D, E and F, with a yield ratio of 0.69, 0.67 and 0.66. The mean result for uniform and total elongation for each cycle was 7.2% and 13.6%, 7.4% and 13.7%, and for F, 6.7% and 12%. Also, the results for uniform elongation showed a narrow range of just 0.5%, 0.7% and 0.3% showing the minimal spread between the repeats for uniform elongation. A more extensive spread for the total elongation was seen for cycles D, E and F at 1.1%, 1.2% and 1.1%. When analysing the sensitivity between the various quenching temperatures, it is important to note that the ultimate tensile strength, yield stress, and total elongation only slightly differ by 55MPa, 44MPa, and 1.6%, respectively. These results suggest that the various quenching temperatures do not affect MnSiC$_{(0.15\%)}$.

C) CMnSiCr

This alloy shows a mean response of 1003MPa and 1505MPa, 1009MPa and 1533MPa, and 1020MPa and 1529MPa for yield stress and UTS for cycles G, H, and I. The CMnSiCr alloy shows repeatability between the tests, as it has a narrow range between the minimum and maximum for all yield stress and UTS results. The range for cycles G, H and I was 0.3MPa, 20MPa and 9MPa for yield stress and UTS, 23MPa, 38MPa and 25MPa. Also, these results show this alloy has high strain hardening ability as the average increase in strength from yield to UTS was 502MPa, 524MPa and 509MPa for cycles G, H and I. Additionally, this alloy shows a low yield ratio for G, H and I of 0.67, 0.66 and 0.65, indicating good ductility. For uniform and total elongation, the mean response was 7% and 12.8%, 6.8% and 12.7%, 7.3% and 13.6% for cycles G, H, and I. There was a small range between the minimum and maximum for uniform elongation of just 0.28%, 0.36% and 0.09%, and total elongation was

0.38%, 0.84% and 0.55%. Upon careful analysis of the HT1 results for the CMnSiCr alloy, it is evident that this alloy exhibits minimal sensitivity when subjected to varying quenching temperatures. The ultimate tensile stress, yield stress, and total elongation display minor variations of 28MPa, 17MPa, and 0.9%, respectively. This outcome is remarkable as the quenching temperature fluctuates by as much as 37°C between the minimum and maximum temperatures, yet the resulting properties remain almost unaffected. Overall, the CMnSiCr alloy has shown the best combinations in properties compared to the other tested alloys.

D) CMnSiMo

The mean result for yield stress and UTS for this alloy was 928MPa and 1304MPa, 887MPa and 1342MPa, 946MPa and 1367MPa for cycles J, K and L. The range in yield stress for the CMnSiMo alloy is low, indicating repeatability between the tests. It was 13MPa, 25MPa and 26MPa for cycles J, K and L. The UTS result shows a vast range, particularly for cycles J and L. The range for all cycles was 64MPa, 10MPa and 66MPa for J, K and L. After yielding, this alloy shows less of an increase in strength compared to the CMnSiCr and $MnSiC_{(0.2\%)}$ alloys, with the strength increase after yielding 376MPa, 454MPa and 421MPa for cycles J, K and L. The resulting yield ratio for cycles J, K and L is 0.71, 0.66 and 0.69, indicating the alloy will be ductile. For uniform and total elongation, the mean result was 7.5% and 14.4%, 7.2% and 13.7%, 7.2% and 13.7% for cycles J, K and L. Overall, the uniform elongation range for each of the cycles was 0.20%, 0.33% and 0.88% respectively. For total elongation, the range was 0.75%, 1.01% and 0.25%, showing a more significant range than uniform elongation. It is important to note that altering the quenching temperature shows minor sensitivity to the CMnSiMo alloy's ultimate tensile strength, yield stress, and total elongation. The differences in these properties are minimal - only 63MPa, 59MPa, and 0.7%, respectively. Therefore, adjusting the quenching temperature is not expected to substantially alter the alloy's properties. Overall, the CMnSiMo alloy has shown a great combination in properties, comparable to the combination realised with the $MnSiC_{(0.2\%)}$ alloy but inferior to the CMnSiCr alloy.

6.2.2 Heat Treatment 2 (HT2)

Heat treatment 2 follows the same heating and cooling sections as HT1, with the only difference being a 10°C drop in temperature during the partitioning section. The 10°C drop in temperature will infer the alloys sensitivity. Table 11 shows the average results for the HT2 heat-treated alloys. The average yield stress and ultimate tensile stress are shown in Figure 76, and the average uniform and total elongation are shown in Figure 77. Both graphs include custom error bars using the standard deviation between repeats.

Table 11: HT2 average tensile testing results.

			HT2 - Average Results				
Steel	**Code**	**Partitioning Temperature**	**Yield Stress (MPa)**	**UTS (MPa)**	**Uniform Elongation (%)**	**Total Elongation (%)**	**Product of Stress Elongation (GPa.%)**
MnSiC$_{(0.2\%)}$	HT2-A	279°C	895	1447	6.9	12.4	17.9
	HT2-B	262°C	885	1471	6.6	12.7	18.6
	HT2-C	242°C	942	1505	7.2	12.7	19.2
MnSiC$_{(0.15\%)}$	HT2-D	294°C	862	1266	7.7	13.9	17.6
	HT2-E	276°C	890	1301	8.0	15.3	20.0
	HT2-F	257°C	841	1326	7.2	12.9	17.1
CMnSiCr	HT2-G	280°C	916	1427	7.1	13.2	18.8
	HT2-H	263°C	925	1476	6.6	12.3	18.2
	HT2-I	243°C	953	1464	6.7	12.1	17.8
CMnSiMo	HT2-J	299°C	888	1282	6.9	12.4	15.9
	HT2-K	283°C	864	1336	7.2	13.4	17.9
	HT2-L	262°C	872	1349	7.5	14.6	19.8

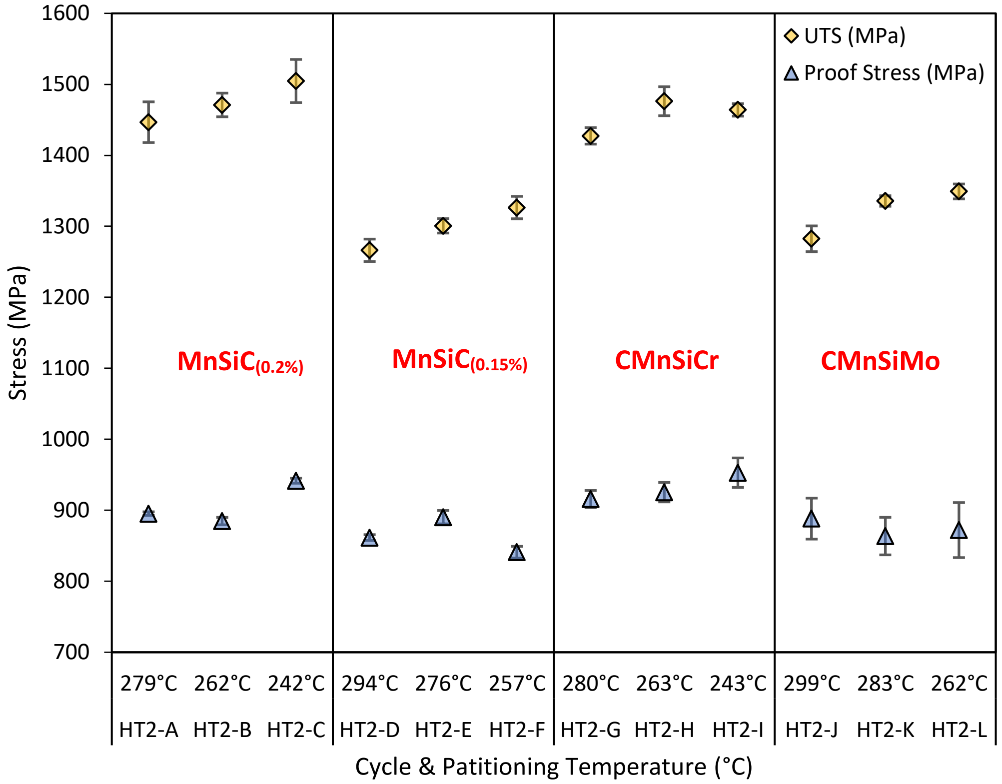

Figure 76: HT2 average UTS and yield stress.

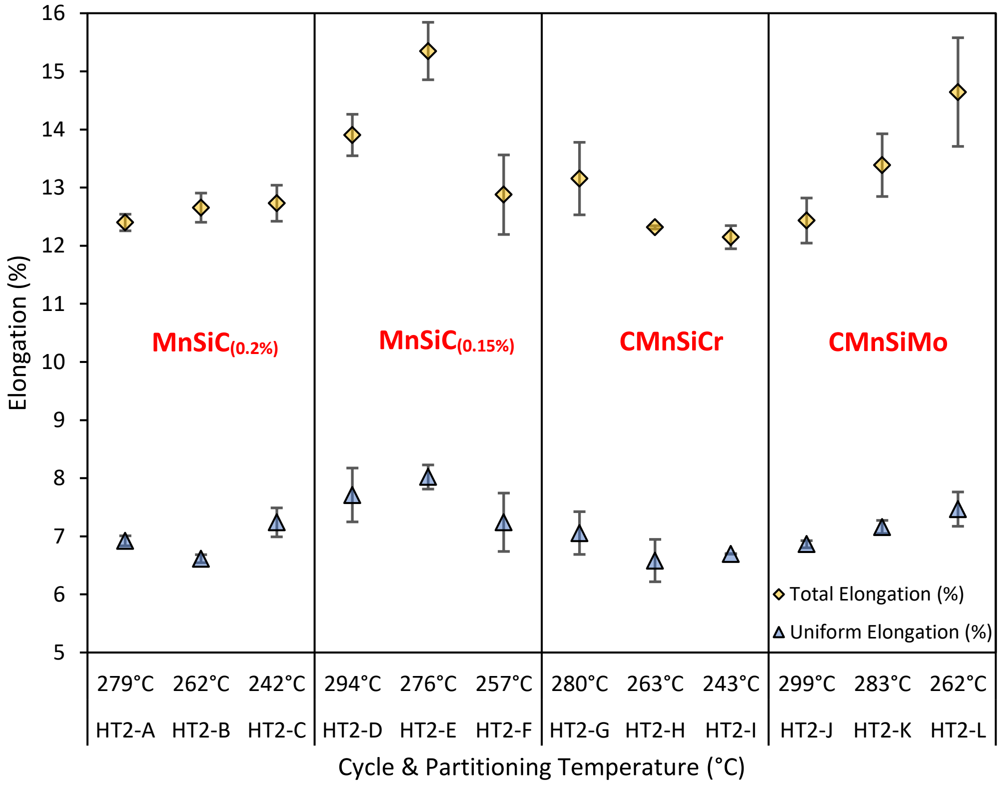

Figure 77: HT2 average uniform and total elongation.

A) MnSiC(0.2%)

For this second heat treatment schedule, MnSiC(0.2%) showed a mean response of 895MPa and 1447MPa, 885MPa and 1471MPa, and 942MPa and 1505MPa for yield stress and UTS for cycles A, B and C. The MnSiC(0.2%) alloy shows repeatability between the tests, as it has a narrow range between the minimum and maximum for yield stress and a moderate range for the UTS. The range for cycles A, B and C was 4MPa, 7MPa and 5MPa for yield stress; for UTS, it was 41MPa, 24MPa and 43MPa. Also, these results show this alloy has high strain hardening ability as the average increase in strength from yield to UTS was 551MPa, 586MPa and 563MPa for cycles, which is notably a more considerable increase compared to the HT1 result for this alloy. Additionally, this alloy shows a low yield ratio for A, B and C of 0.62, 0.6 and 0.63, respectively, indicating good ductility. For uniform and total elongation, the mean response was 6.9% and 12.4%, 6.6% and 12.6%, 7.2% and 12.7% for cycles A, B and C. These results show a slight decrease in both uniform and total elongation compared to the HT1 schedule. There was a small range between the minimum and maximum for uniform elongation of just 0.12%, 0.10% and 0.35%, and total elongation was 0.20%, 0.36% and 0.44%. Similarly, post-HT2, the alloy continues to demonstrate slight sensitivity towards different quenching temperatures with minimal impact on ultimate tensile strength (UTS), yield stress, and total elongation. There are only subtle differences of 58MPa, 44MPa, and 1.6%, respectively. Hence, it can be concluded that the alloy is not significantly affected by variations in quenching temperature and the 10°C drop in temperature during partitioning.

B) MnSiC(0.15%)

For yield stress and ultimate tensile stress, the mean response for cycles D, E, and F were 862MPa and 1266MPa, 890MPa and 1301MPa, and for F, 841MPa and 1326MPa. The range between the minimum and maximum for cycles D, E and F for yield stress was 6MPa, 13MPa and 12MPa, and for the UTS was 22MPa, 14MPa and 22MPa. This alloy shows a reasonable level of strain hardenability, like the CMnSiMo alloy, but to a lesser degree than the MnSiC(0.2%) and CMnSiCr alloys. After yielding, the strength increased by 405MPa, 410MPa and 485MPa for cycles D, E and F, with a yield ratio of 0.68, 0.68 and 0.63. The mean result for uniform and total elongation for each cycle was 7.7% and 13.9%, 8.0% and 15.3%, and for F, 7.2% and 12.9%. Additionally, the results for uniform elongation showed a narrow range of just 0.7%, 0.3% and 0.7% showing the minimal spread between the repeats for uniform elongation. The range for total elongation is 0.5%, 0.7% and 1.0%. Upon analysing the sensitivity between different quenching temperatures for HT2, it is observed that the ultimate tensile strength and yield stress differ only slightly by 60MPa and 49MPa, respectively. The total elongation is more sensitive, with a total variation of 2.6%. These findings suggest that the various quenching temperatures for HT2 have little to no effect on $MnSiC_{(0.15\%)}$ for UTS and yield stress. However, it should be noted that the outlier cycle HT2-E showed a significant increase in total elongation, which is the reason for the more considerable variation in elongation. Comparing HT1 to HT2 for this alloy, there is a small reduction in strength, but there was a moderate increase in uniform and total elongation. Looking at the combination in properties, HT2 has improved this alloy's overall properties.

C) CMnSiCr

This alloy shows a mean response of 916MPa and 1427MPa, 925MPa and 1476MPa, and 953MPa and 1464MPa for yield stress and UTS for cycles G, H, and I. The CMnSiCr alloy shows repeatability between the tests, as it has a narrow range between the minimum and maximum for all yield stress and UTS results. The range for cycles G, H and I was 17MPa, 19MPa and 29MPa for yield stress and UTS, 17MPa, 29MPa and 12MPa. Similarly, to HT1, these results show a high strain hardening ability as the average strength increase from yield stress to UTS was 512MPa, 551MPa and 511MPa for cycles G, H and I. Additionally, this alloy shows a low yield ratio for G, H and I of 0.64, 0.63 and 0.65. For uniform and total elongation, the mean response was 7.1% and 13.2%, 6.6% and 12.3%, 6.7% and 12.1% for cycles G, H, and I. There was a small range between the minimum and maximum for uniform elongation of just 0.52%, 0.51% and 0.008%, and total elongation was 0.88%, 0.04% and 0.28%. It is intriguing to observe that the behaviour of HT2 resembles that of HT1 for the CMnSiCr alloy. Even with the quenching temperature fluctuating by up to 37°C between the minimum and maximum temperatures, the ultimate tensile stress, yield stress, and total elongation display only slight variations of 49MPa, 37MPa, and 1.1%, respectively. This result underscores the uniformity and reliability of the resulting properties, which is truly impressive. When comparing the results obtained from HT1 to HT2, it is vital to note that the temperature decrease has led to a reduction in both the strength and formability properties. This suggests that the CMnSiCr alloy is susceptible to changes in temperature during partitioning and therefore requires an isothermal hold to achieve the optimal combination of properties.

D) CMnSiMo

The mean result for yield stress and UTS for this alloy was 888MPa and 1284MPa, 864MPa and 1336MPa, 872MPa and 1349MPa for cycles J, K and L. The range in yield stress for the CMnSiMo alloy is 41MPa, 37MPa and 55MPa for cycles J, K and L. The range for UTS was 26MPa, 11MPa and 15MPa for J, K and L. After yielding, this alloy shows less of an increase in strength compared to the CMnSiCr and $MnSiC_{(0.2\%)}$ alloys, with a strength increase of 394MPa, 472MPa and 477MPa for cycles J, K and L. The resulting yield ratio for cycles J, K and L is 0.69, 0.65 and 0.65. For uniform and total elongation, the mean result was 6.9% and 12.4%, 7.2% and 13.4%, 7.5% and 14.6% for cycles J, K and L. Overall, the uniform elongation range for each of the cycles was 0.09%, 0.16% and 0.88% respectively. The range of total elongation was 0.55%, 0.76% and 1.32%, showing a more significant range than the uniform elongation. It is worth noting that adjusting the quenching temperature has a small impact on the ultimate tensile strength and yield stress of the CMnSiMo alloy, but it is more sensitive to total elongation. The differences in these properties are minimal, with only 67MPa and 24MPa, respectively. However, there is a more significant difference in total elongation, with a difference of 2.2%. Therefore, while modifying the quenching temperature may not have a substantial effect on the alloy's strength properties, it will undoubtedly affect its elongation. Comparing HT1 and HT2 for this alloy shows a reduction in strength and elongation properties, indicating this alloy is sensitive to the 10°C drop in temperature.

6.3 HT1 Vickers Hardness Results

Vickers hardness testing was completed on a Wilson VH3300. HT1 comprises twelve different heat treatments, broken down into three cycles for each of the four alloys. For each heat-treated sample, ten indents were performed across a straight line, spaced 0.5mm apart, with a dwell time of 15s. Testing followed ISO 6507-1:2018 standard [124]. Figure 78 shows the average Vickers hardness results, including custom error bars using the standard deviation. The average hardness increases as the quenching/partitioning temperature lowered for each of the four alloys. Three of the alloys show a gradual increase as the temperature is lowered, except for the

$MnSiC_{(0.2\%)}$ alloy, which has a sharp increase in hardness at its lowest quenching/partitioning temperature. The following section will describe the individual hardness results for each of the alloys. A confidence level of 99% was utilised to set the confidence intervals above and below the sample mean.

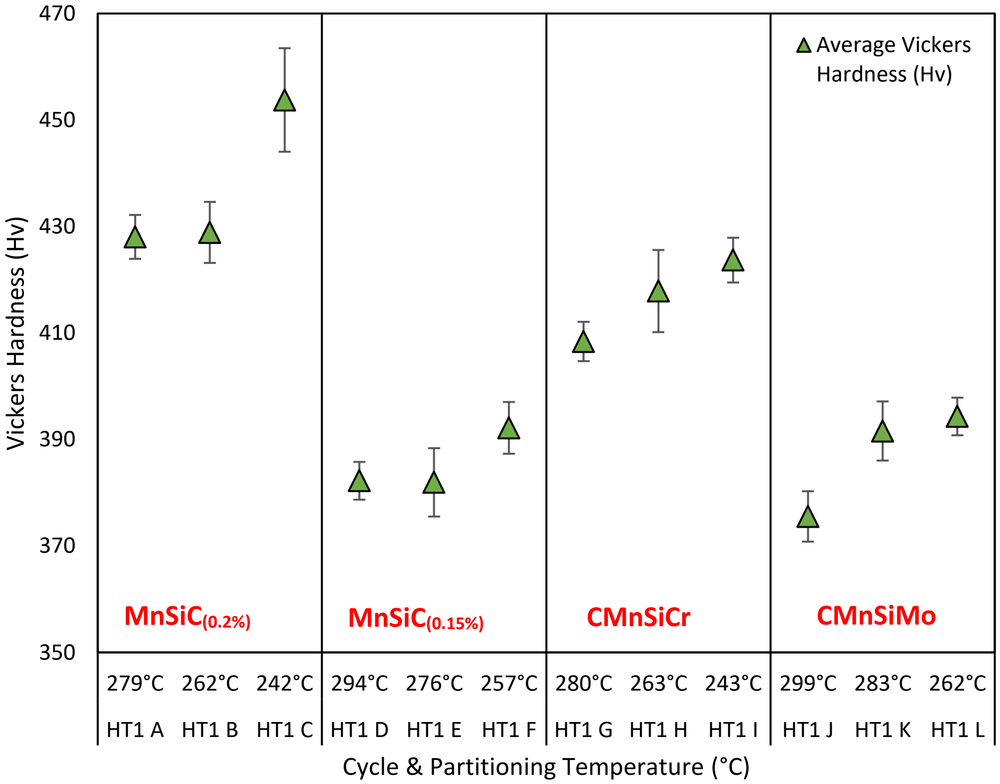

Figure 78: Average Vickers hardness (Hv).

A) $MnSiC_{(0.2\%)}$

For this alloy, three different heat-treated samples have been tested. The mean and range for HT1-A, B, and C were 428Hv and 12.8Hv, 429Hv and 16Hv, 453Hv and 27.7Hv, respectively. Figure 79 clearly shows HT1-A has the tightest spread in data, with only two data points out of ten sitting outside the confidence intervals. For HT1-B&C, four data points are outside the confidence intervals. Also confirmed by the calculated confidence levels of 3.6, 6.6 and 5.0 for cycles HT1-D, E and F.

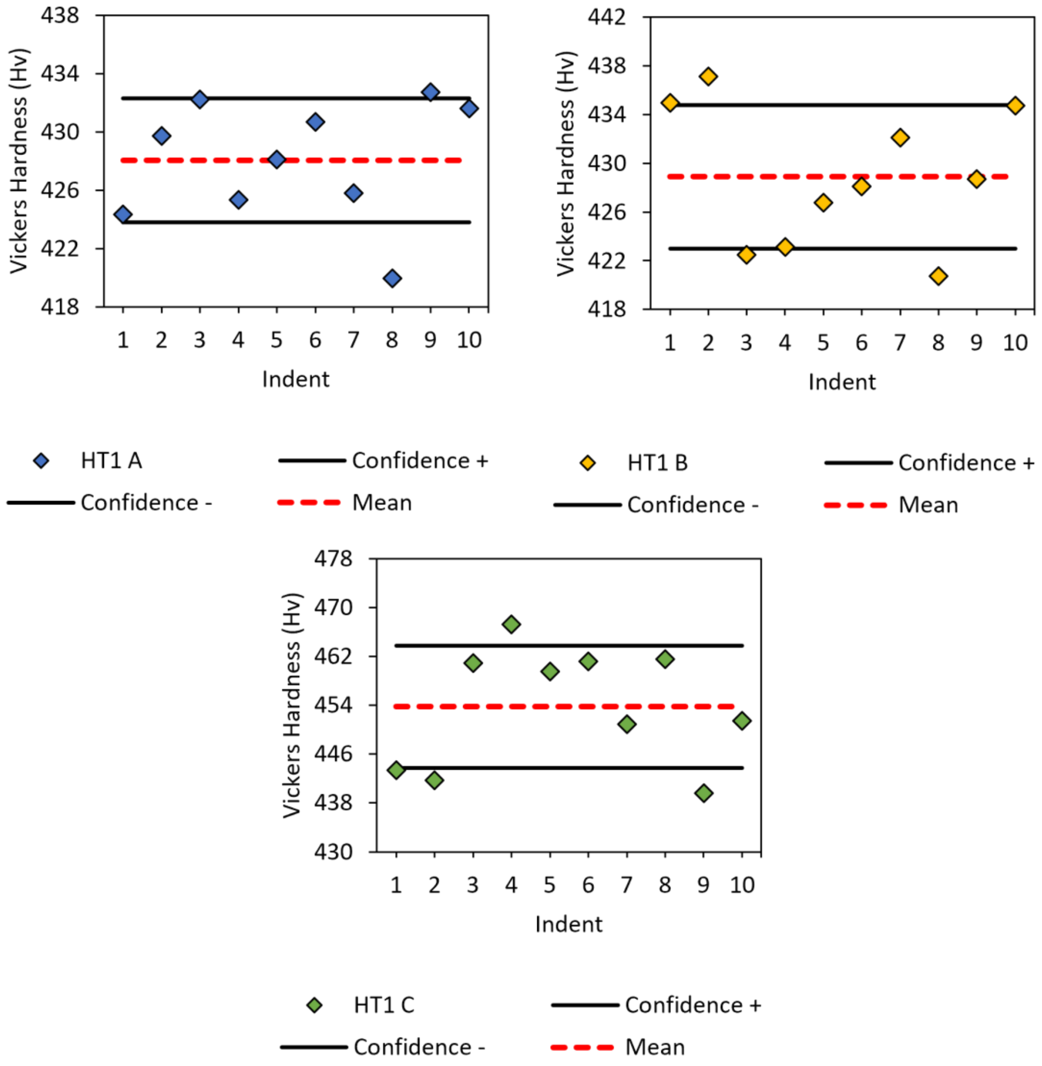

Figure 79: MnSiC$_{(0.2\%)}$ hardness results.

B) MnSiC$_{(0.15\%)}$

Three different heat-treated samples have been hardness tested for MnSiC$_{(0.15\%)}$. Figure 80 shows how the data points vary around the mean and if they are within the confidence intervals. For HT1-D, E and F, the mean and range were 382Hv and 10.3Hv, 382Hv and 17.4Hv, 392Hv and 14Hv, respectively. HT1-D illustrates the tightest spread in data, with only one data point outside the confidence intervals. This can also be shown numerically, as the 99% confidence level for HT1-D is 3.6, and for HT1-E&F, it is 6.6 and 5, respectively. For both HT1-E&F, there are three data points outside the confidence intervals.

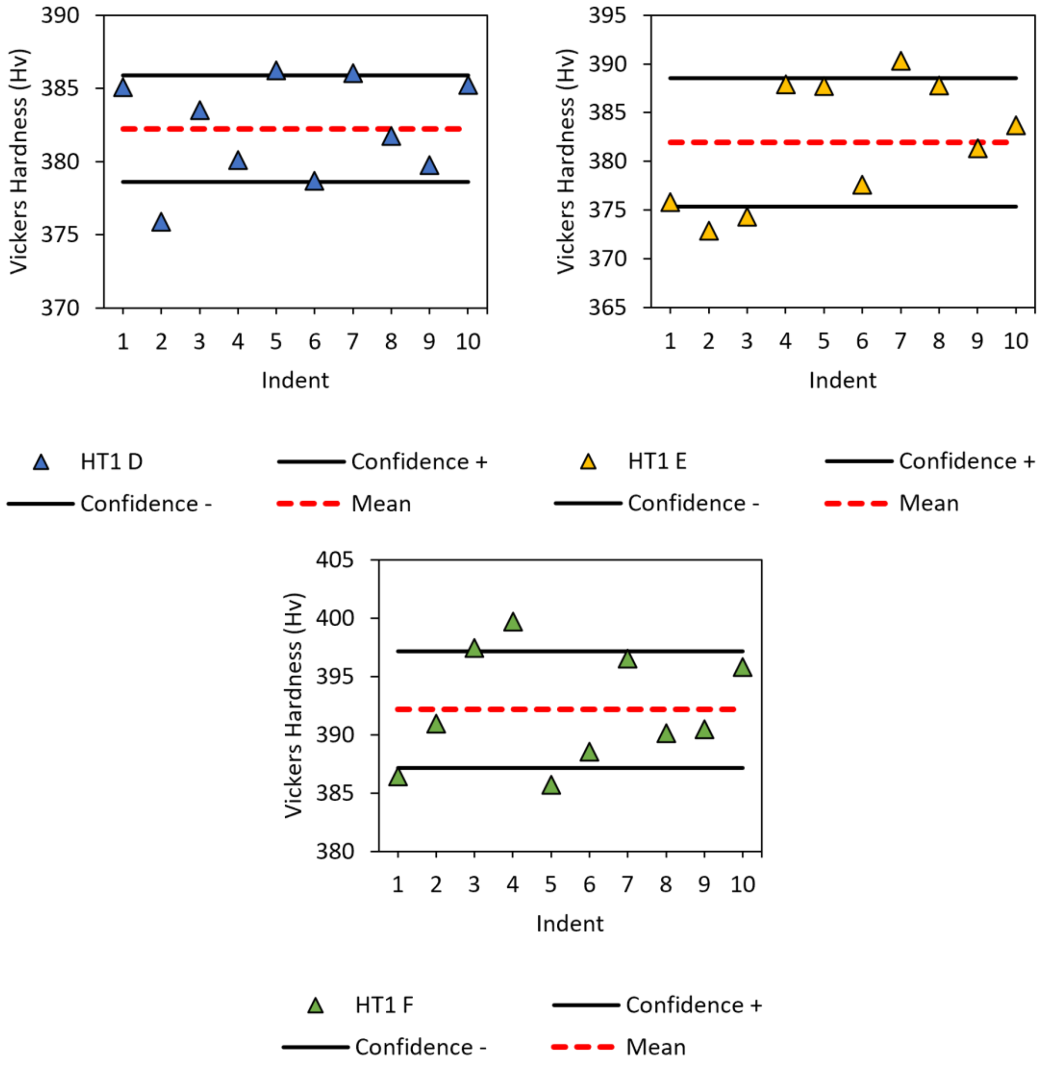

Figure 80: MnSiC$_{(0.15\%)}$ hardness results.

C) CMnSiCr

Hardness testing on three samples with varying heat treatment routes on CMnSiCr alloy was completed, termed HT1-G, H, and I. To validate the hardness testing, a confidence level of 99% has been used to set the confidence intervals. The mean and range in hardness were 408Hv and 11.4Hv, 418Hv and 26Hv, 424Hv and 11.8Hv, for HT1-G, H, and I, respectively. As can be seen in Figure 81, HT1-G had the tightest range in hardness variation, confirmed numerically with a calculated confidence level of just 3.8, whereas for H and I, it was 7.9 and 4.3. Additionally, with G, only one indent fell outside the confidence intervals; for H and I, it was 2 and 3 indents.

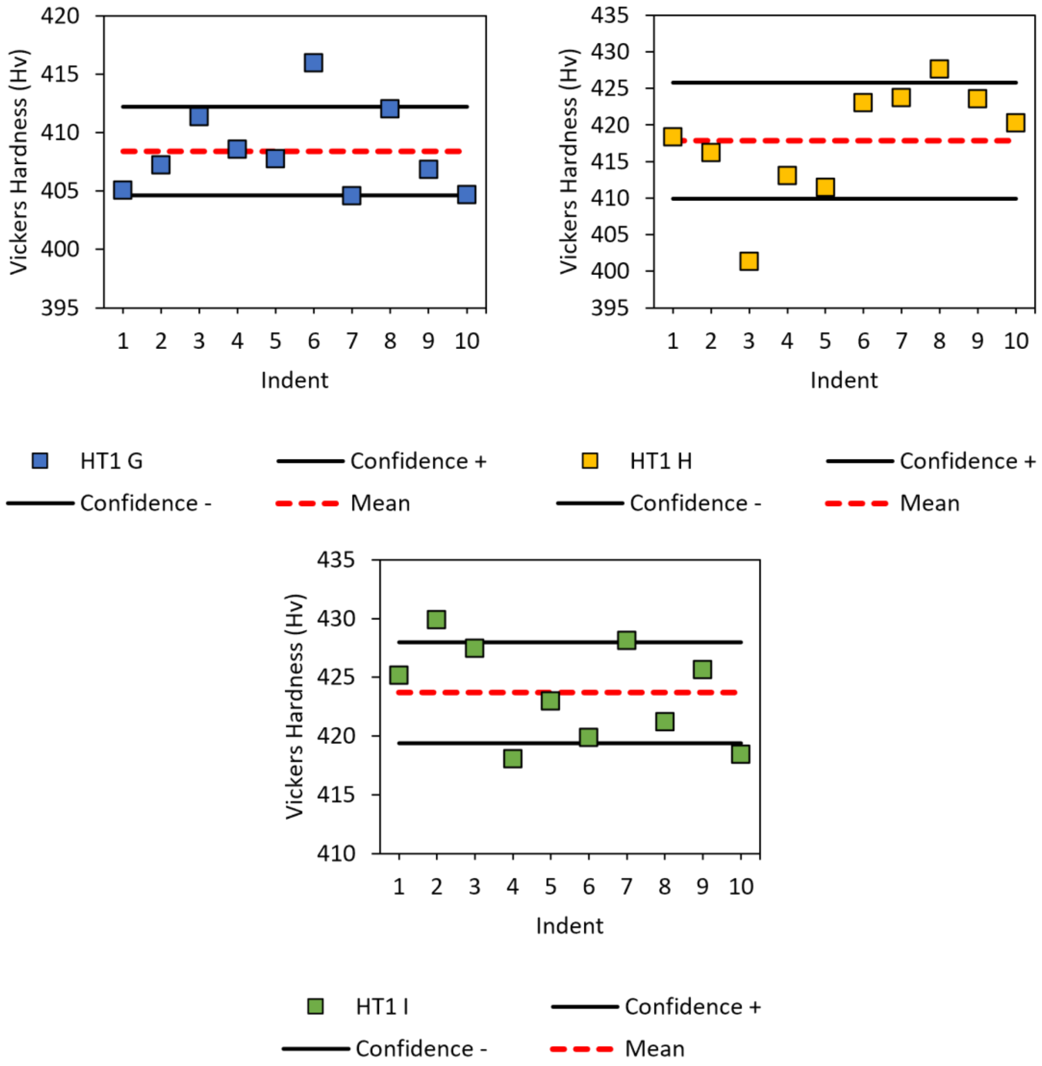

Figure 81: CMnSiCr hardness results.

D) CMnSiMo

Similarly, to the other alloys, three samples were tested under different heat treatment conditions. The three samples had a mean hardness and range of 376Hv and 13.6Hv, 392Hv and 14.8Hv, 394Hv and 11.3Hv, for alloys HT1-J, K and L, respectively. Figure 82 illustrates that L has the tightest range, and only three indents were outside the confidence intervals, whereas J and K had four indents outside the limits.

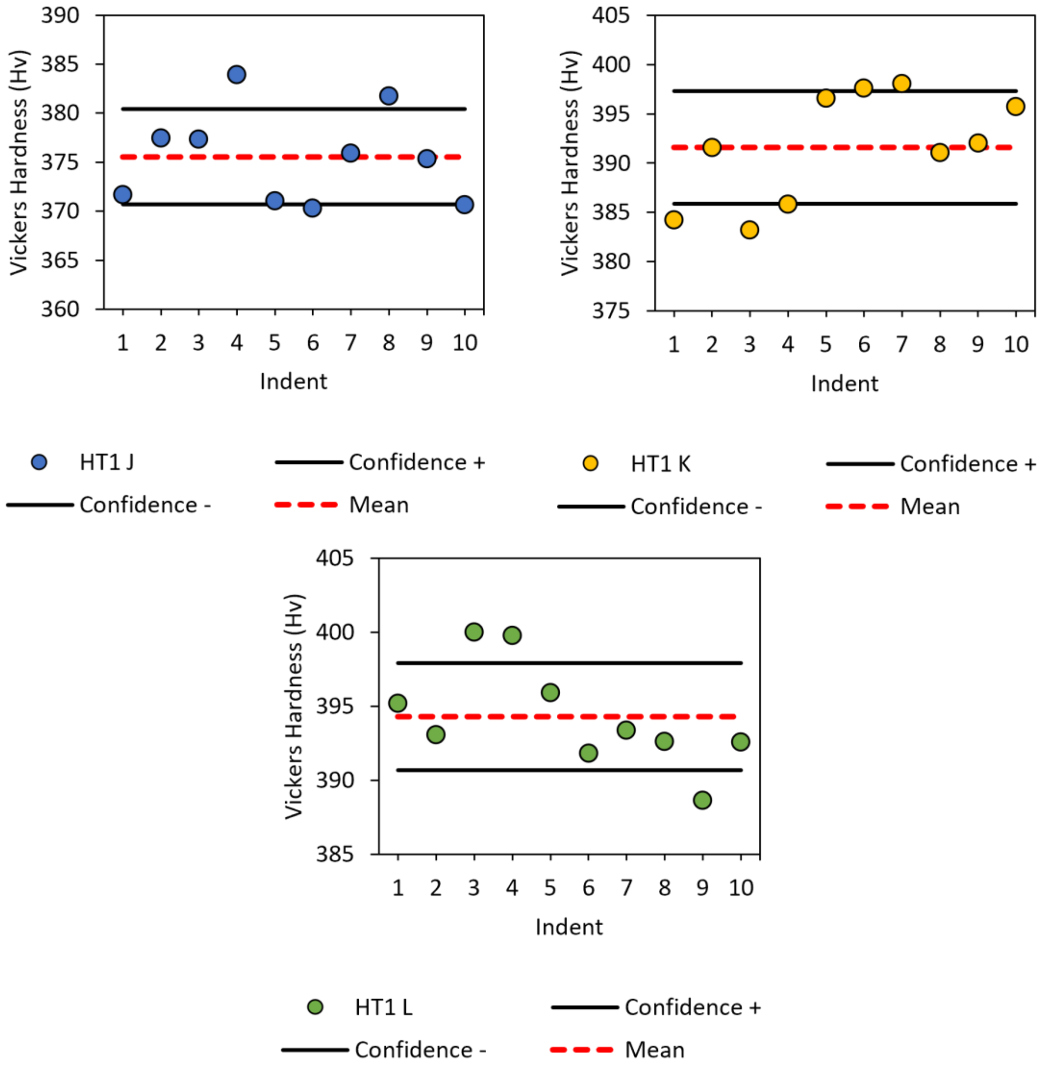

Figure 82: CMnSiMo hardness results.

6.4 HT2 Vickers Hardness Results

Too see if the designed alloys are sensitive to the 10°C drop in temperature during partitioning, Vickers hardness experiments have been run on all the HT2 samples. These results will be directly compared against the HT1 results. Figure 83 illustrates the average Vickers hardness comparison between HT1 and HT2 heat treated samples. The results show comparable levels of hardness independent of the type of heat treatment schedule employed. There was one outlier, HT2-E which showed a substantial increase in hardness, but notably, this was also reciprocated in tensile results for MnSiC$_{(0.15\%)}$.

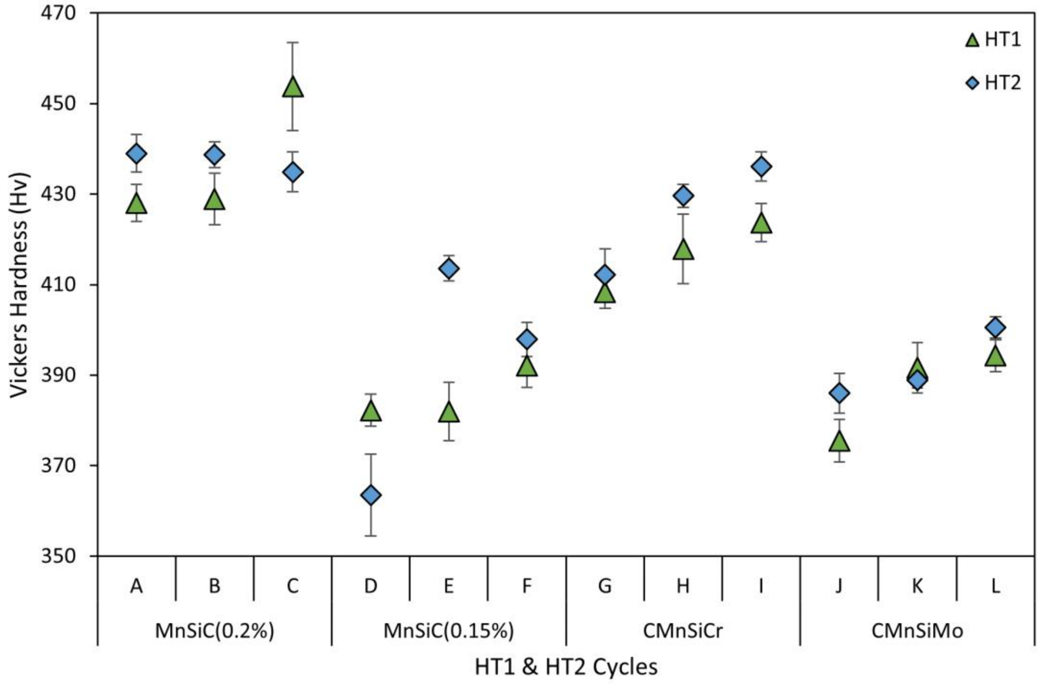

Figure 83: Vickers hardness comparison, HT1 to HT2.

6.5 JMatPro Martensite Tempering Validation

This section will compare the simulated ultimate tensile stress and Vickers hardness from JMatPro to the properties realised through experimentation. The properties from HT1 heat treatments will be compared, see Figure 84. Table 12 illustrates the measured properties against the simulated, including the difference. First, looking at the UTS for MnSiC$_{(0.2\%)}$, as the quenching temperature was lowered, the simulated stress compared to the measured is in closer agreement. Initially, the simulated tensile stress was 72MPa higher than the measured tensile, which lowered to 37MPa and 9MPa for HT1-B and C. The MnSiC$_{(0.15\%)}$ alloy is seen to have the most significant difference from the simulated to the measured properties of the four alloys. Like the MnSiC$_{(0.2\%)}$ alloy, the difference in properties was at its least at the lowest quenching temperature. The CMnSiCr alloy was the only one whose measured tensile stress exceeded the simulated property and was in the closest agreement. The simulated values were underestimated by 28MPa, 51MPa and 44MPa for HT1-G, H, and I. The CMnSiMo alloy had the most significant difference in stress at its highest quench temperature, like the MnSiC$_{(0.2\%)}$ alloy. It also behaves similarly, reducing this difference as the quench temperature is lowered. The difference was 117MPa, 84MPa and 64MPa for

HT1-J, K and L. As mentioned in section 3.4.3, the martensite tempering simulation ignores any heating and cooling sections and focuses purely on tempering within the martensitic region. It is reasonable to expect a difference in properties, but ultimately, this simulation aimed to see if these compositions and heat treatments will lead to tensile stress > 1300MPa. This goal has been achieved for tensile stress. Additionally, martensite tempering provides simulated Vickers hardness values, and Figure 85 illustrates the measured hardness against the simulated hardness values. As seen with the tensile simulation, as the quenching temperature is lowered, there is a closer agreement between the simulated and measured values. Martensite tempering has proven to be a valuable tool to quickly assess if a composition and heat treatment will lead to properties comparable to a UHSS.

Table 12: Simulated vs measured tensile and hardness.

		JMatPro		Experimental		Difference	
Alloy	**Heat Treatment**	**UTS (MPa)**	**Hardness (Hv)**	**UTS (MPa)**	**Hardness (Hv)**	**UTS (MPa)**	**Hardness (Hv)**
MnSiC$_{(0.2\%)}$	HT1-A	1509	480	1437	428	72	52
	HT1-B	1513	482	1476	429	37	53
	HT1-C	1517	483	1508	454	9	29
MnSiC$_{(0.15\%)}$	HT1-D	1422	452	1323	382	100	70
	HT1-E	1428	454	1293	382	135	72
	HT1-F	1433	455	1348	392	84	63
CMnSiCr	HT1-G	1477	470	1505	408	-28	62
	HT1-H	1481	471	1533	418	-51	53
	HT1-I	1485	473	1529	424	-44	49
CMnSiMo	HT1-J	1421	452	1304	376	117	76
	HT1-K	1426	453	1342	392	84	62
	HT1-L	1432	455	1367	394	65	61

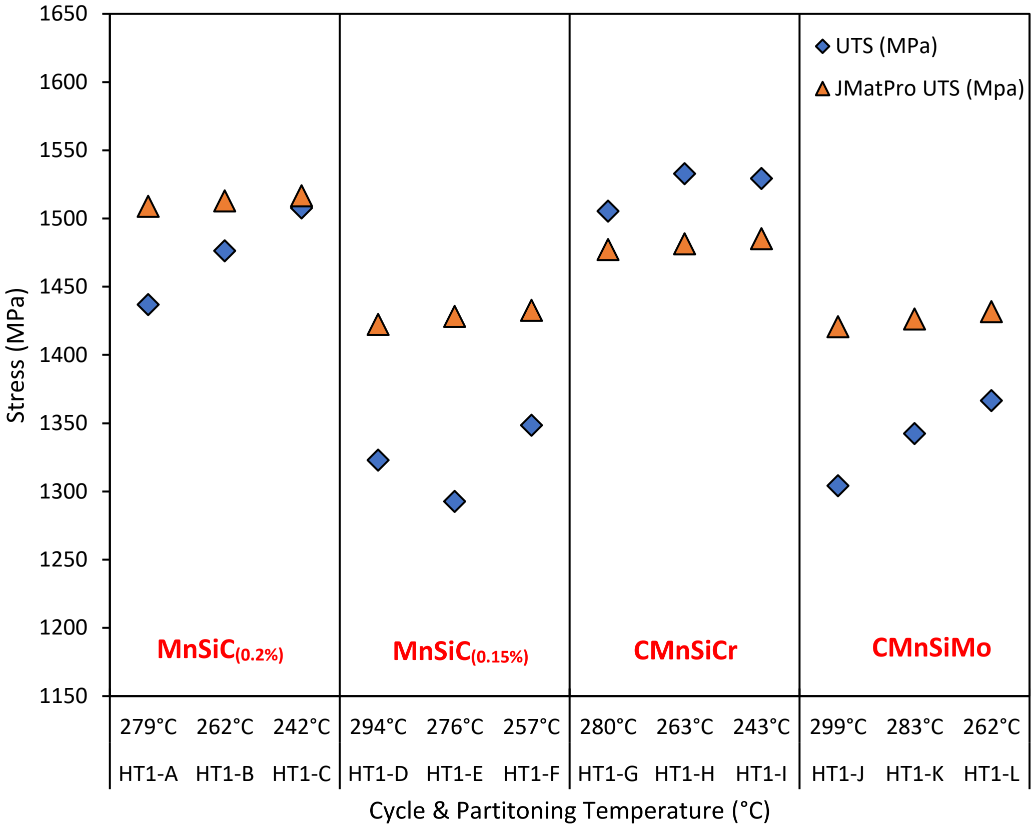

Figure 84: Simulated vs measured UTS.

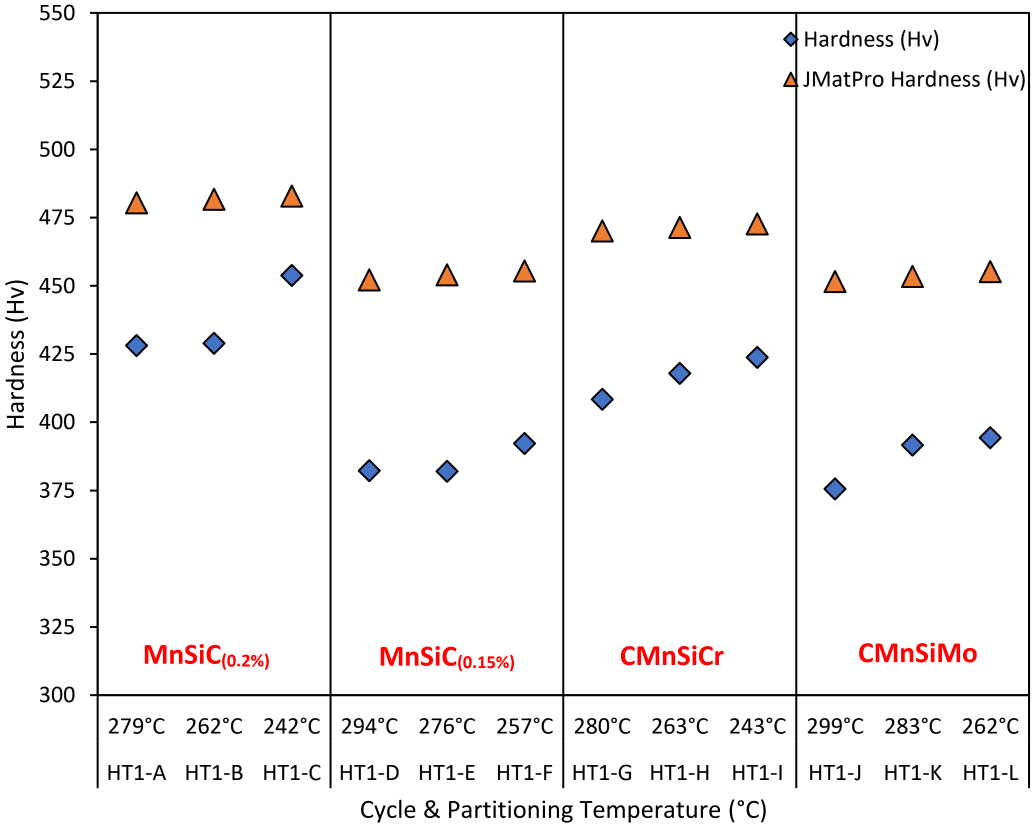

Figure 85: Simulated vs Measured Vickers hardness.

6.6 Mechanical Property Comparison - Hot rolled/Cold Rolled and Annealed

Designing these alloys to be industrially viable has been key to this project, and one essential requirement is for the tensile stress to be <700MPa in its hot rolled state. The project dictates that these alloys need to be of ultra-high strength in combination with high formability, and because of both factors, the alloys will need to have a high level of strain hardenability with a low yield ratio. The following sections will describe the evolution in properties from the hot rolled to cold rolled and annealed samples.

6.6.1 Ultimate Tensile Stress

Table 13 comprises the average hot rolled UTS for all alloys and their resulting tensile stress after cold-rolling and heat treatment following HT1 and HT2 schedules. It shows the percentage increase in tensile stress. The $MnSiC_{(0.2\%)}$ alloy shows a substantial increase in tensile stress for HT1 and HT2 compared to the hot rolled tensile stress. For HT1 and HT2 cycles, A increased by 106% and 108%, B by 112% and 111%, and C by 116% and 116%. These results indicate that the $MnSiC_{(0.2\%)}$ alloy shows no sensitivity to the drop in temperature for tensile stress. The $MnSiC_{(0.15\%)}$ alloy also showed a substantial increase, for D, it was 96% and 88%, for E, 92% and 93%, and F, 100% and 96%. This result for the $MnSiC_{(0.15\%)}$ alloy also shows minor sensitivity to the drop in temperature incorporated into the partitioning stage for HT2. The CMnSiCr has shown a remarkable increase in tensile stress after cold rolling and annealing, particularly for the HT1 heat-treated samples. HT1 and HT2 samples G, H and I, the tensile stress increased by 123% and 111%, 127% and 118%, 126% and 117%. These results indicate that the CMnSiCr alloy shows some sensitivity to the temperature drop during partitioning for tensile stress, but notably there is large increases in UTS for both schedules. Finally, the CMnSiMo alloy showed the most negligible improvement in tensile stress after cold rolling and annealing. It only increased by 15% and 13%, 18% and 18%, 20% and 19% for HT1 and HT2 samples.

Table 13: UTS increase after heat-treatment.

Composition	Average Hot rolled UTS (MPa)	Heat Treatment	UTS After Heat Treatment 1 (MPa)	Percentage Increase	Heat Treatment	UTS After Heat Treatment 2 (MPa)	Percentage Increase
MnSiC$_{(0.2\%)}$	697	HT1-A	1437	**106%**	HT2-A	1447	**108%**
		HT1-B	1476	**112%**	HT2-B	1471	**111%**
		HT1-C	1508	**116%**	HT2-C	1505	**116%**
MnSiC$_{(0.15\%)}$	675	HT1-D	1323	**96%**	HT2-D	1266	**88%**
		HT1-E	1293	**92%**	HT2-E	1301	**93%**
		HT1-F	1348	**100%**	HT2-F	1326	**96%**
CMnSiCr	676	HT1-G	1505	**123%**	HT2-G	1427	**111%**
		HT1-H	1533	**127%**	HT2-H	1476	**118%**
		HT1-I	1529	**126%**	HT2-I	1464	**117%**
CMnSiMo	1136	HT1-J	1304	**15%**	HT2-J	1282	**13%**
		HT1-K	1342	**18%**	HT2-K	1336	**18%**
		HT1-L	1367	**20%**	HT2-L	1349	**19%**

6.6.2 Yield Stress

Table 14 illustrates how the yield stress evolves from its hot rolled state to cold rolled and annealed. Like the tensile stress comparison, alloys MnSiC$_{(0.2\%)}$, MnSiC$_{(0.15\%)}$ and CMnSiCr all show significant property increases in overall partitioning temperatures for HT1 and HT2. The percentage increase for these mentioned alloys is similar for HT1 and HT2, indicating the yield stress is not sensitive to the drop in temperature during partitioning. The yield stress for the CMnSiMo alloy reduces after cold rolling and annealing for all partitioning temperatures over HT1 and HT2.

Table 14: Yield stress increase after heat-treatment.

Composition	Average Hot Band Yield Stress (MPa)	Heat Treatment	Yield Stress After Heat Treatment 1 (MPa)	Percentage Increase	Heat Treatment	Yield Stress After Heat Treatment 2 (MPa)	Percentage Increase
MnSiC$_{(0.2\%)}$	491	HT1-A	897	**83%**	HT2-A	895	**82%**
		HT1-B	952	**94%**	HT2-B	885	**80%**
		HT1-C	989	**101%**	HT2-C	942	**92%**
MnSiC$_{(0.15\%)}$	531	HT1-D	911	**72%**	HT2-D	862	**62%**
		HT1-E	867	**63%**	HT2-E	890	**68%**
		HT1-F	883	**66%**	HT2-F	841	**58%**
CMnSiCr	509	HT1-G	1003	**97%**	HT2-G	916	**80%**
		HT1-H	1009	**98%**	HT2-H	926	**82%**
		HT1-I	1020	**100%**	HT2-I	953	**87%**
CMnSiMo	1079	HT1-J	928	**-14%**	HT2-J	888	**-18%**
		HT1-K	887	**-18%**	HT2-K	864	**-20%**
		HT1-L	946	**-12%**	HT2-L	872	**-19%**

6.6.3 Total Elongation

Table 15 shows the percentage decrease in total elongation from the hot rolled to the cold rolled and annealed samples. First, looking at CMnSiMo, there is a minimal drop in total elongation for all partitioning temperatures for HT1 and HT2. MnSiC$_{(0.2\%)}$ and CMnSiCr alloy's total elongation was reduced by approximately 50% for all partitioning temperatures over both HT1 and HT2 schedules. This is an impressive result as both alloys produced the most significant increase in strength properties with this moderate reduction in elongation, leading to a superior combination in properties. The total elongation for MnSiC$_{(0.15\%)}$ alloy was reduced by only 43%, 42% and 49% as the partitioning temperature was reduced, and with the tensile stress increase, it also shows a good combination of properties.

Table 15: Total elongation decrease after heat-treatment.

Composition	Average Hot Band Total Elongation	Heat Treatment	Total Elongation After Heat Treatment 1	Percentage Decrease	Heat Treatment	Total Elongation After Heat Treatment 2	Percentage Decrease
MnSiC$_{(0.2\%)}$	25.9%	HT1-A	12.9%	**50%**	HT2-A	12.4%	**53%**
		HT1-B	12.1%	**53%**	HT2-B	12.7%	**51%**
		HT1-C	12.6%	**51%**	HT2-C	12.7%	**51%**
MnSiC$_{(0.15\%)}$	23.7%	HT1-D	13.6%	**43%**	HT2-D	13.9%	**41%**
		HT1-E	13.7%	**42%**	HT2-E	15.4%	**35%**
		HT1-F	12.0%	**49%**	HT2-F	12.9%	**46%**
CMnSiCr	25.9%	HT1-G	12.8%	**51%**	HT2-G	13.2%	**49%**
		HT1-H	12.7%	**51%**	HT2-H	12.3%	**52%**
		HT1-I	13.6%	**47%**	HT2-I	12.2%	**53%**
CMnSiMo	14.6%	HT1-J	14.4%	**1%**	HT2-J	12.4%	**15%**
		HT1-K	13.7%	**6%**	HT2-K	13.4%	**8%**
		HT1-L	13.7%	**6%**	HT2-L	14.6%	**0%**

6.7 JMatPro Property Simulation

Due to delays in getting the alloys cast and processed because of Covid-19 restrictions, not all material properties have been analysed. Using the measured tensile stress and yield stress, fatigue has been simulated in JMatPro. Ideally, these simulated properties need to be validated against the measured properties, but this has not been possible due to limited time. The four cycles that showed the best property combination after cold rolling and annealing have been put forward for these simulations. The four cycles are HT1-H, HT1-I, HT2-C and HT2-E.

6.7.1 Fatigue

Table 16 shows the calculated properties from simulated S-N curves in Figure 86. All fatigue simulations were run with the same settings described in section 3.5.1. Cycles H, I and C all achieved a fracture strain of 0.15, whereas E achieved a fracture strain of 0.16. The fracture stress was 1918MPa, 1913MPa, 1882MPa and 1642MPa for H, I, C and E, respectively. They also all had a very similar young's modulus of 204.6GPa for H, I and C and 204.5GPa for E.

Table 16: Simulated fatigue results.

Sample	Strain amplitude (%)	Loading frequency (Hz)	b value	c value	Fracture Strain	Fracture Stress (MPa)	Young's Modulus (GPa)
HT1-H	1	1	-0.1	-0.9	0.15	1917.6	204.6
HT1-I	1	1	-0.1	-0.9	0.15	1913.3	204.6
HT2-C	1	1	-0.1	-0.9	0.15	1882.8	204.6
HT2-E	1	1	-0.1	-0.9	0.16	1642.5	204.5

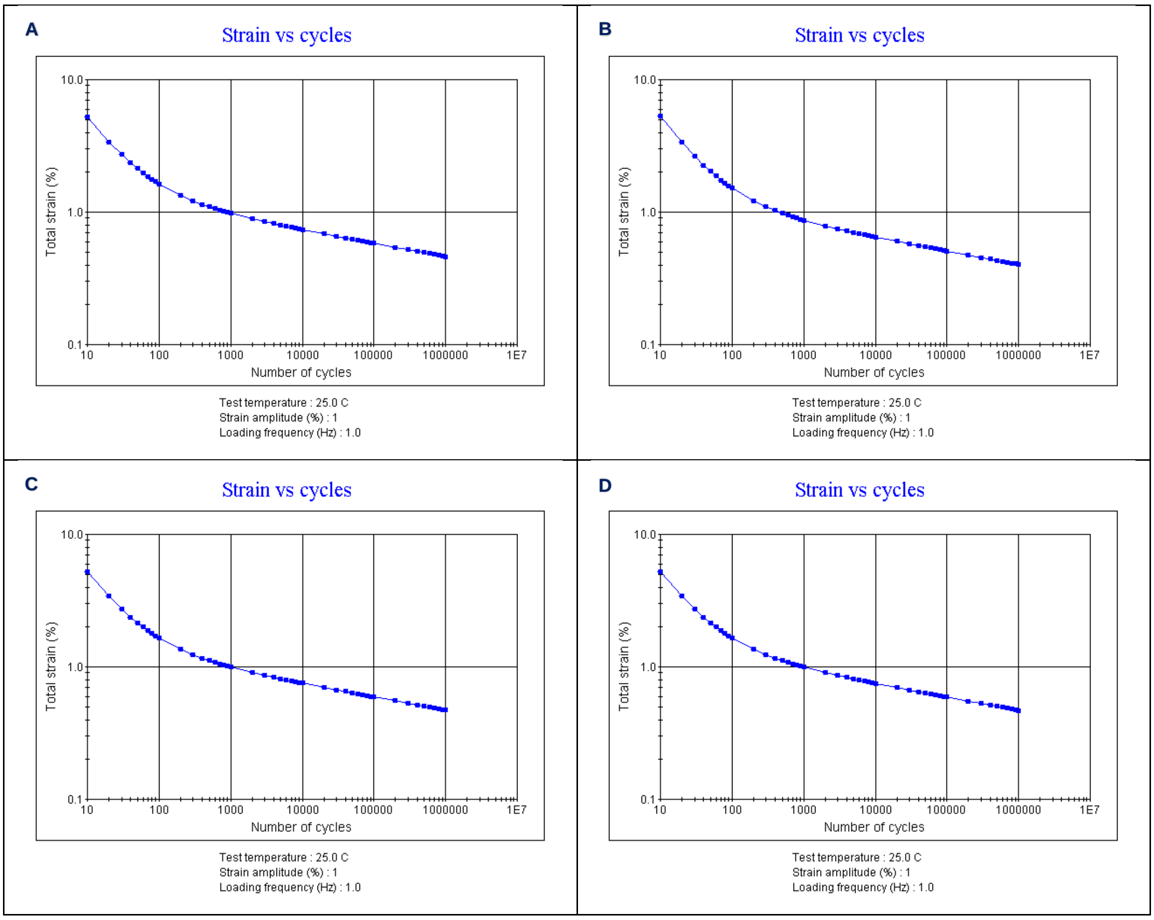

Figure 86: Simulated S-N Curves. A. HT1-H, B. HT1-I, C. HT2-C, D. HT2-E

6.8 Scanning Electron Microscope

All images were captured using a Zeiss Evo LS25 SEM, with an accelerating voltage of 20Kv, a working distance between 6-10mm and a probe current between 50pA-75pA.

A) $MnSiC_{(0.2\%)}$

Figure 87 illustrates the different microstructures achieved dependent on the quenching/partitioning temperature. It is clear as the temperature is lowered, there is a higher proportion of martensite. In total these micrographs are composed of proportions of partitioned martensite, MA (martensite/austenite) islands, fresh martensite, bainite and small amounts of retained austenite. Comparing the microstructures between HT1 and HT2 it is clear there is very little difference. This indicates the microstructure evolution is not sensitive to the small drop in temperature during partitioning. This is also backed up by the tensile results for $MnSiC_{(0.2\%)}$, which showed little difference in properties between HT1 to HT2. The prior austenite grain boundaries can be seen, and the size is approximately 5µm-10µm.

B) $MnSiC_{(0.15\%)}$

Figure 88 illustrates how the microstructure evolution changed dependent on the quenching/partitioning temperature. The microstructures are composed of a mixture of partitioned martensite, M-A islands, fresh martensite, bainite, small amounts of retained austenite and because of the lower carbon content, very small amounts of ferrite. There is a noticeable difference in the appearance of the microstructures between HT1 to HT2 but strangely this did not lead to a large reduction in properties during tensile testing. For tensile, yield and total elongation there was only a moderate reduction in properties and for HT2-E there was a large increase in total elongation.

C) CMnSiCr

The micrographs in relation to different quenching/partitioning temperatures are illustrated in Figure 89. The microstructures for the CMnSiCr alloy are composed of a mixture of partitioned martensite, M-A islands, fresh martensite, bainite and small amounts of retained austenite. For this alloy, the distance between martensitic laths is smaller in comparison to the other alloys and the prior austenite grain boundaries appear to be smaller as the quenching/partitioning temperature is reduced, particularly for the HT1 schedule. Retained austenite forms between the martensitic laths and as a more globular blocky form within the prior austenite grain boundaries. HT2-I shows evidence of the formation of globular blocky retained austenite. Also, to note there is not any discernible difference between the microstructures for the two heat treatment schedules, indicating this alloy microstructural evolution is not sensitive to the drop in temperature during partitioning.

D) CMnSiMo

The different microstructures for CMnSiMo alloy are illustrated in Figure 90. The microstructures for the CMnSiMo alloy are composed of a mixture of partitioned martensite, M-A islands, fresh martensite, bainite and small amounts of retained austenite. This alloy shows the largest proportion of partitioned martensite, which is carbon depleted and tempered. Due to the large proportion of partitioned martensite, it will improve the elongation, and this is confirmed by the CMnSiMo alloy on average having the highest total elongation between the alloys. There is not a large difference between microstructures for HT1 and HT2 except for HT2-L which appears to have a larger proportion of lath martensite.

HT1-A: 279°C

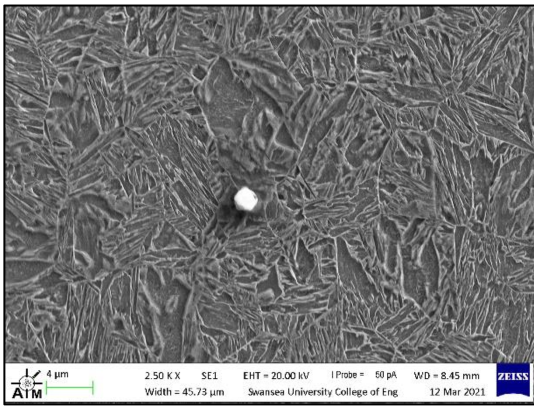

HT1-B: 262°C

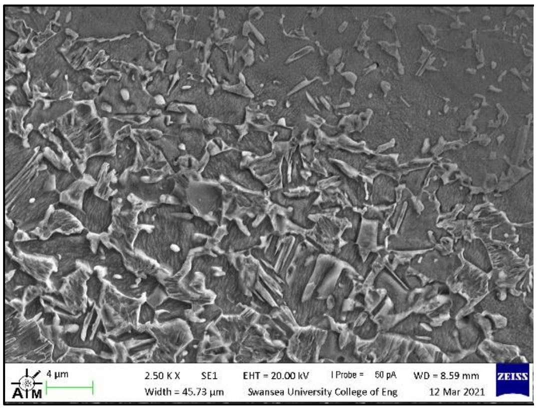

HT1-C: 242°C

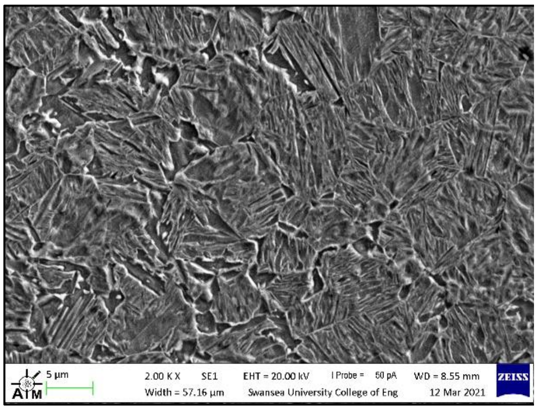

HT2-A: 279-269°C

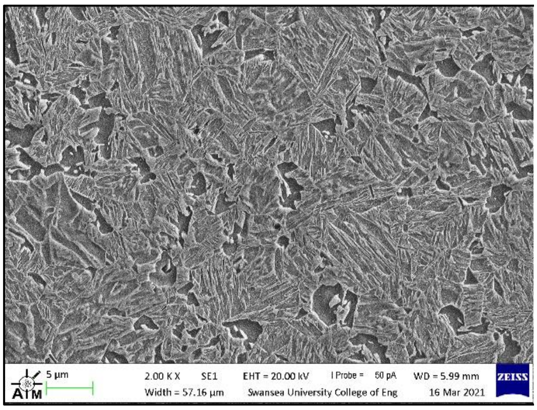

HT2-B: 262-252°C

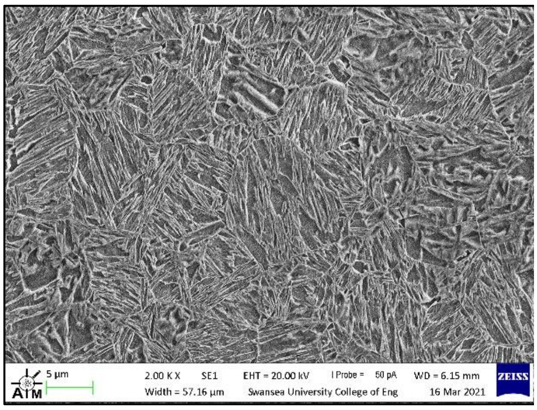

HT2-C: 242-232°C

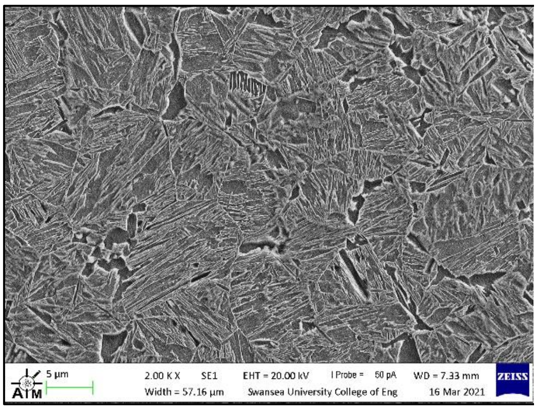

Figure 87: MnSiC$_{(0.2\%)}$ Micrographs.

HT1-D: 294°C **HT1-E: 276°C**

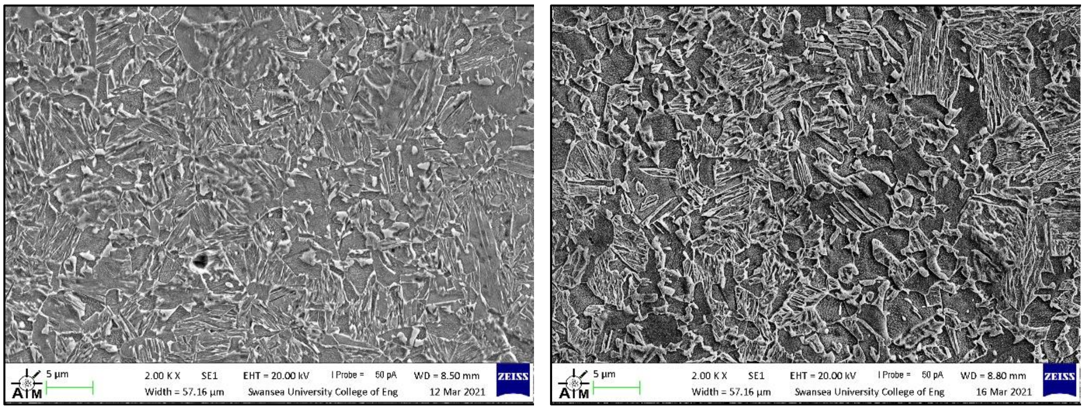

HT1-F: 257°C **HT2-D: 294-284°C**

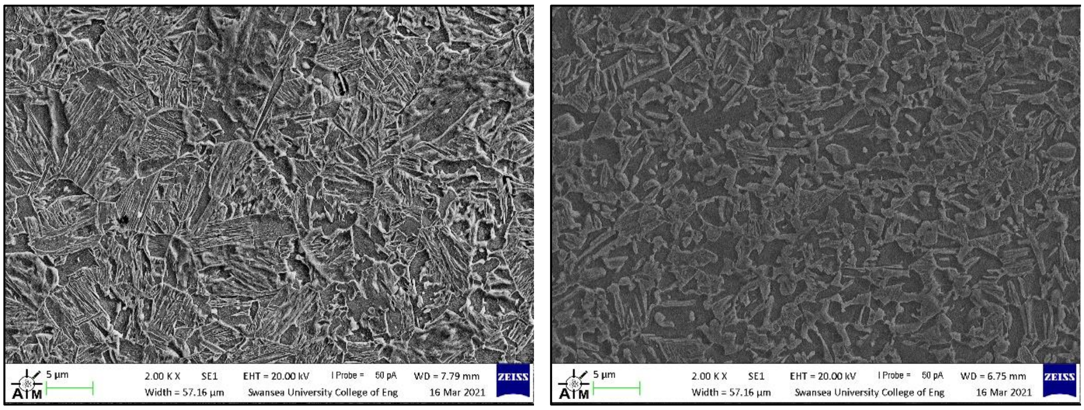

HT2-E: 276-266°C **HT2-F: 257-247°C**

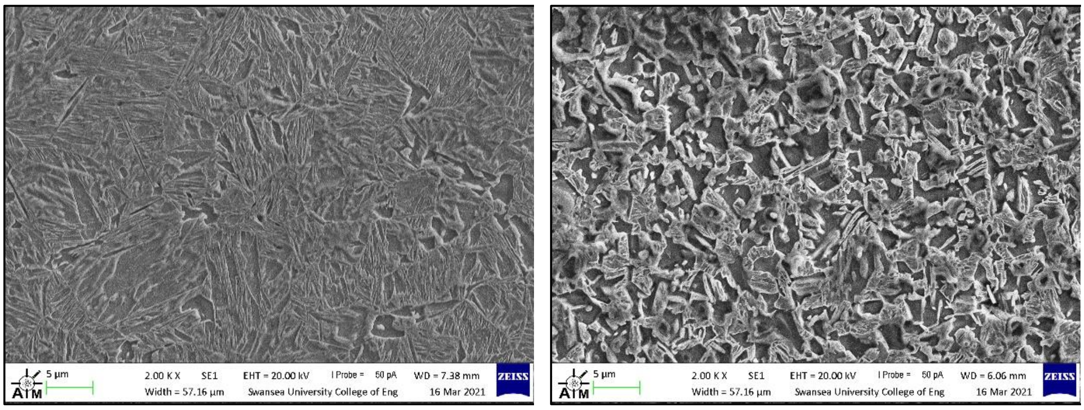

Figure 88: MnSiC$_{(0.15\%)}$ Micrographs.

HT1-G: 280°C

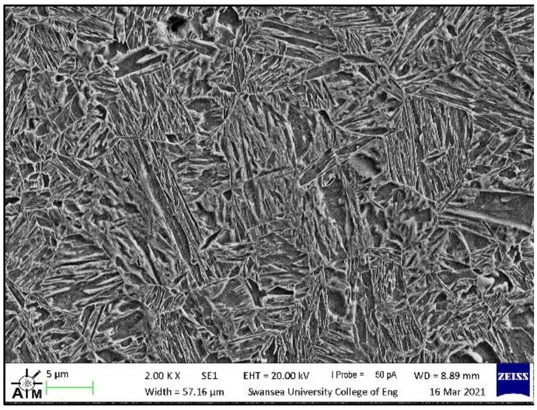

HT1-H: 263°C

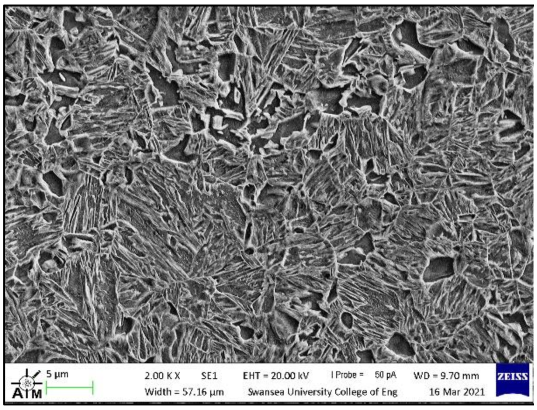

HT1-I: 243°C

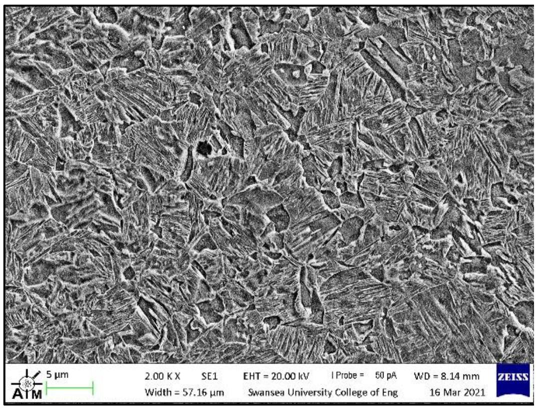

HT2-G: 280-270°C

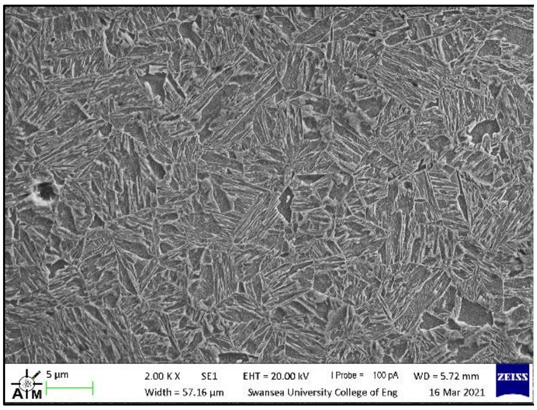

HT2-H: 263-253°C

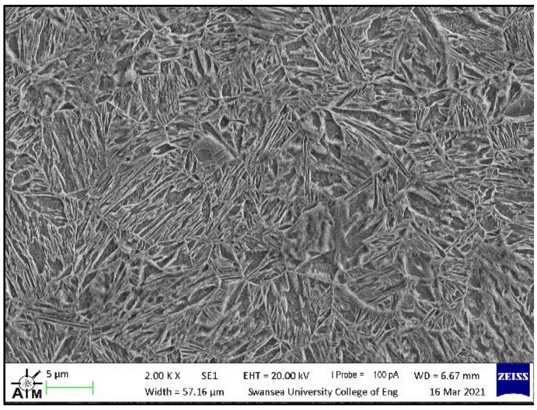

HT2-I: 243-233°C

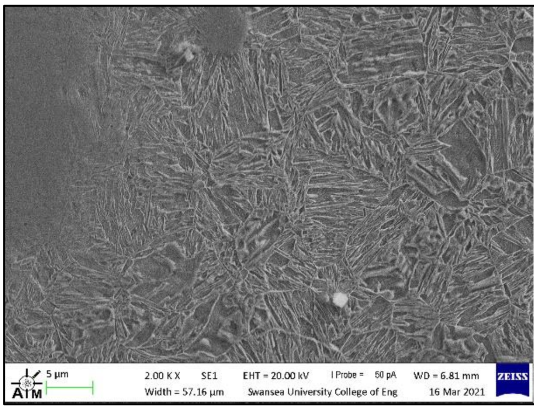

Figure 89: CMnSiCr Micrographs.

HT1-J: 299°C **HT1-K: 283°C**

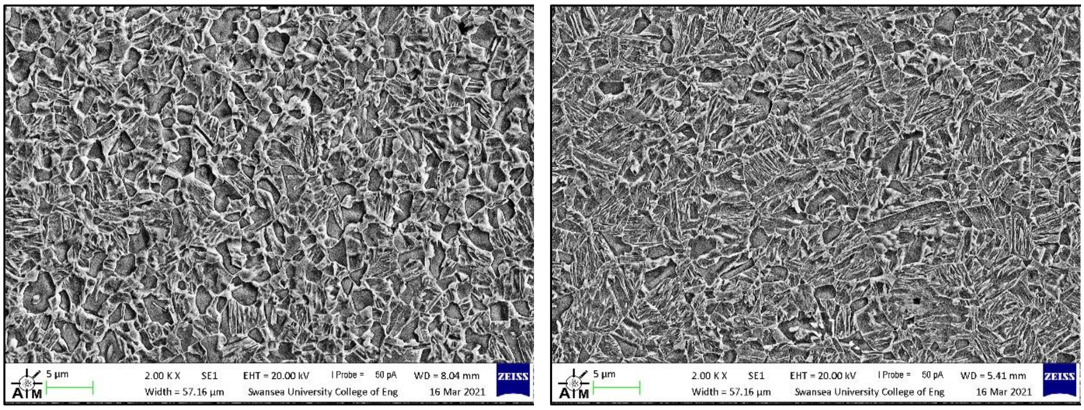

HT1-L: 262°C **HT2-J: 299-289°C**

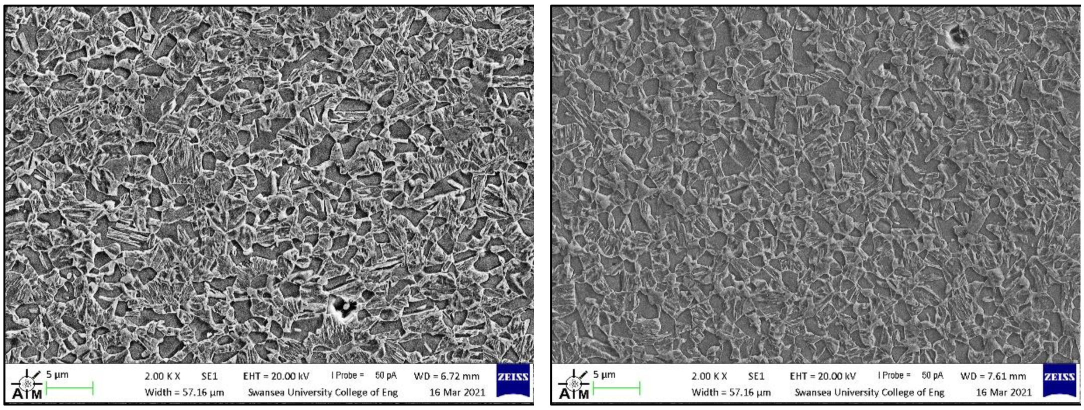

HT2-K: 283-273°C **HT2-L: 262-252°C**

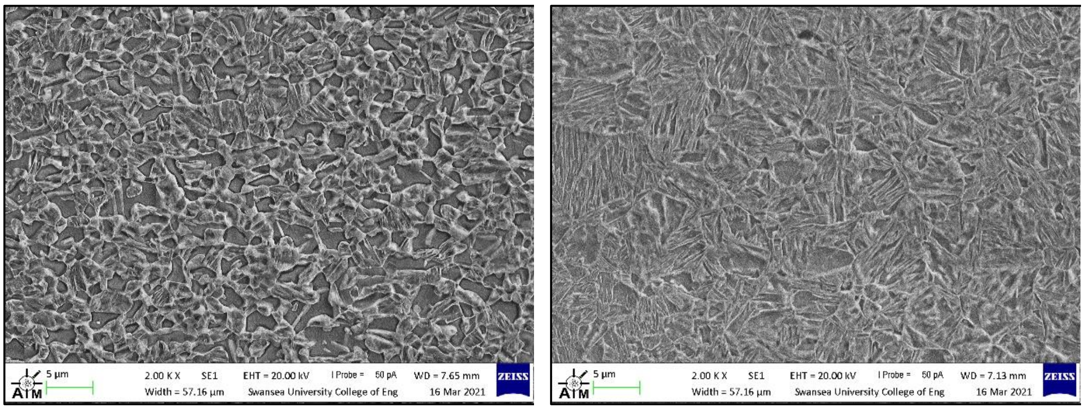

Figure 90: CMnSiMo Micrographs.

6.9 Optimised Cycles

The cycles which have achieved the best combination in properties will go forward for further testing in chapter 7. It was decided, only the cycles which showed a product of stress elongation (PSE) of >= 19.5GPa.% in conjunction with Vickers hardness > 410Hv will be selected for further testing.

6.9.1 PSE and Vickers Hardness Limits

The product of stress elongation (PSE) measures a material's ability to undergo plastic deformation without fracturing. It is defined as the product of the maximum engineering stress and the total elongation at maximum stress. PSE is a critical parameter for understanding the mechanical behaviour of steels, particularly in applications where formability and strength are both critical. Generally, a high PSE for steels indicates good formability/ductility while maintaining high strength. The relationship between PSE, formability, and strength is complex, and the exact values of these parameters depend on the steel's microstructure, composition, and processing conditions. High PSE values are generally desirable for steels used in applications where both formability and strength are essential, such as automotive or aerospace applications. In an article by Huang et al, a PSE of 18-20GPa.% was classed as a high PSE and is why 19.5GPa.% was chosen as the minimum level needed for further testing [148]. High Vickers hardness > 410Hv level was set, as a combination of high PSE and Vickers hardness means the material is both formable and ductile, as well as resistant to wear and abrasion. This can lead to increased efficiency, reduced costs, and improved performance in a variety of applications. As illustrated in Figure 91, two cycles for CMnSiCr alloy, HT1-H, and I and one cycle for alloy $MnSiC_{(0.15\%)}$, HT2-E, satisfied these requirements. Notably, cycle HT2-C for alloy $MnSiC_{(0.2\%)}$ was just under this requirement, with its hardness at 435Hv but its PSE just below 19.5GPa.% at 19.2GPa.%. A modified version of HT2-C, incorporating a longer partitioning time will be put forward for further testing, and will be termed HT3-C.

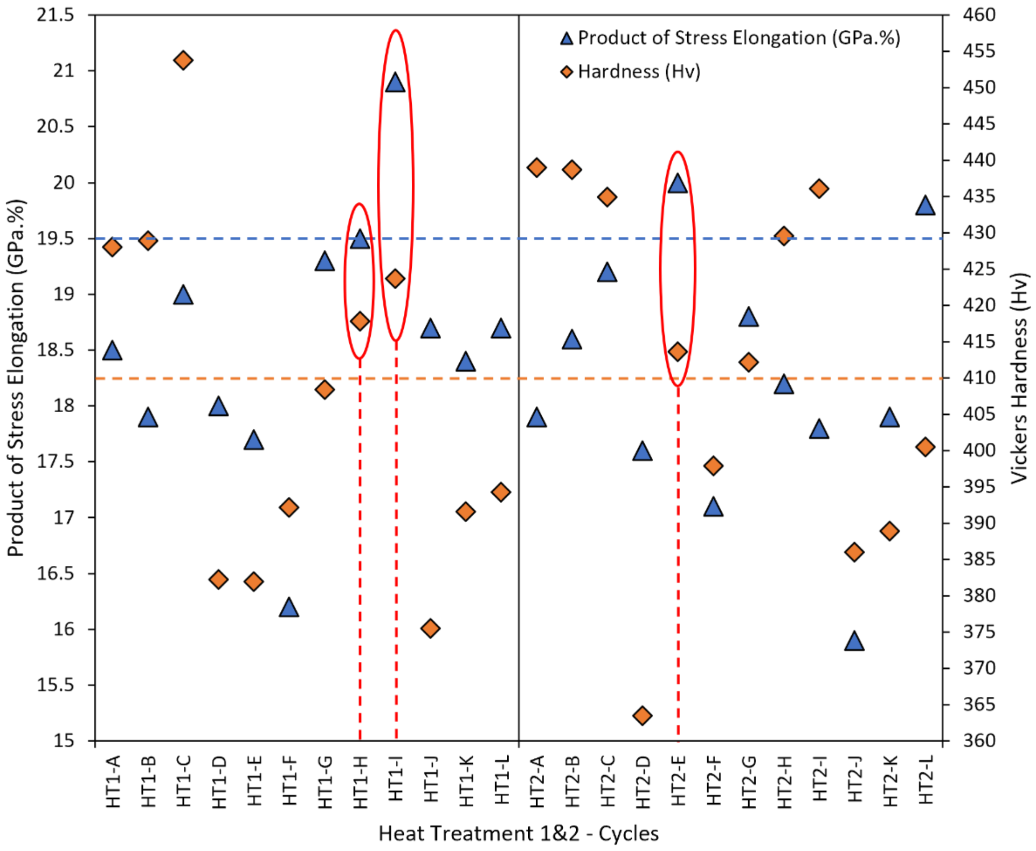

Figure 91: Optimised cycles.

6.10 Discussion of Results

Hot rolled tensile results have shown that three of the alloys are below the rolling load limit, with only the CMnSiMo alloy exceeding this limit. In section 5.4.2 on Jominy hardenability simulation. Jominy hardenability simulations indicated the CMnSiMo alloy would likely exceed the rolling load limit as it showed a minimal drop in tensile properties over the whole length of the bar. It was also fully bainitic over the total length, and the molybdenum in this alloy has increased its hardenability. Molybdenum suppresses the formation of ferrite and pearlite to longer times and higher temperatures on CCT and TTT diagrams and raises the temperature where martensite will start to form. Mohrbacher et al. [121] studied the effects of critical alloying elements on the resulting properties of martensitic steels for automotive applications. It was found that increasing Mo in the combination of B reduced to critical cooling rate to form 90% martensite. Jominy hardenability simulation has proven to be a valuable tool in the design of these Q&P alloys. Landgraf et al. [149] looked at the influence of thermal treatments on the properties of martensitic steel X30Cr13 using JMatPro simulations to model the phase formation at different temperatures and Jominy hardenability simulations against experimental data. Landgraf et al. found the use of JMatPro key in reducing the number of experiments and suitable to find optimum processing windows.

Analysis of the tensile results after cold rolling and annealing, three of the alloys showed substantial improvements in tensile stress with only a moderate reduction in total elongation. These alloys showed a vast improvement in tensile stress due in combination of hot/cold rolling and the partitioning treatment. During hot/cold-rolling, energy stores in the material, which increases the driving force for nucleation of new grains during the heat treatment and ultimately leads to grain refinement [150]. The Hall-Petch relationship shows as the grain size reduces the yield stress increases, which is shown in the tensile results for the alloys [151]. The large window from yielding to ultimate tensile stress experienced by the novel Q&P alloys is influenced by the retained austenite content. This is because of the (transformation-induced plasticity) TRIP effect, where the austenite phase has a high density of dislocations associated with the martensitic transformation. This provides the alloys with enhanced strain hardening ability, whereas the alloy starts to yield austenite will transform to martensite and ultimately increase the tensile stress, but whilst keeping reasonable levels for elongation. Additionally, the large window between yield to UTS, infers the designed alloys show a high level of formability. To show the low level of sensitivity exhibited by these alloys, it is worth comparing the yield and UTS variation to AHSS datasheets by Tata for DP800/DP1000 and CP800. For the UTS DP800/1000 and CP1000 varies by 120MPa, 150MPa and 140MPa, respectively. Similarly, for yield stress the variation is 110MPa, 150MPa and 140MPa, respectively [152]–[154]. When comparing to the novel Q&P steels, the degree of variability in properties is substantially lower.

On analysis of the hardness results for the HT1 heat treated alloys, they all increase in hardness as the quenching/partitioning temperature was lowered. This is expected because as the temperature is lowered there is a larger proportion of primary martensite formation. Martensite is known to be the hardest phase in steels and as the proportion of this phase is increased, it will increase the overall hardness of the steel [146], [155]. JMatPro martensite tempering simulations were employed to find if the tensile stress would be >1300MPa, and in all cases this was achieved. Comparing the simulated to the measured, they were in good agreement, especially for the heat treatments which aimed to achieve a 60% primary martensite formation. For the four alloys the difference between the simulated to measured for the 60% cycles was, 0.6%, 5.9%, 2.9% and 4.5%, for $MnSiC_{(0.2\%)}$, $MnSiC_{(0.15\%)}$, CMnSiCr and CMnSiMo, respectively. Similarly, the simulated Vickers hardness was in reasonable agreement with the measured values, validating the martensite tempering simulations. Notably there was less of an agreement compared to the tensile, for the 60% cycle the difference between the simulated to the measured hardness was, 6%, 13.8%, 10.4% and 13.4%, for $MnSiC_{(0.2\%)}$, $MnSiC_{(0.15\%)}$, CMnSiCr and CMnSiMo, respectively. In two reports by JMatPro on the tempering of steels and the tempered hardness of martensitic steels, the results indicate a very good agreement between the simulated hardness to the measured hardness, further validating the use of martensite tempering simulations to aid in the design of new martensitic alloys [144], [145].

The mechanisms at play during a quenching and partitioning cycle lead to superior combinations in properties compared to conventional heat treatments. Initially, the steel is heated above the A_r^3 and soaked at this temperature to form homogenous austenite; next, it is quenched down to the designed heat treatment temperatures to form either 40%, 50% or 60% primary martensite formation. It is then held at this temperature isothermally, where the excess carbon in the martensitic phase will diffuse into the austenite phase, stabilising it. As the carbon in the martensite phase reduces, this naturally lowers the hardness whilst simultaneously increasing the hardness of the austenite phase as it becomes saturated with carbon. Additionally, the martensite is tempered during the isothermal hold, decreasing its hardness further. All these mechanisms at play lead to a reduction in hardness mismatch between the phases [62], [111], [156]–[159]. It is believed that as the hardness mismatch between phases reduces, the complex multiphase steel will behave similarly to a homogenous single-phase alloy [116]. During deformation events, there is a preference for the softer phase to preferentially deform over the harder phase, leading to failures at lower stress levels than expected. As the hardness between the different phases is much closer, significant increases in tensile stress combined with moderate elongation reductions can be realised. In previous work, Pathak et al. [160] investigated the damage evolution in CP and DP steels during edge stretching and found that CP steels outperformed DP steels for stretch flangability. Pathak et al. determined the DP showed a worse performance due to the more significant strength differential between the martensite and ferrite phases. In another article, Pathak et al. demonstrated that CP steel has an improvement in hole expansion, even though the DP steel had higher ductility [161].

The purpose of the tensile tests after cold rolling and annealing was to find the optimised cycles that showed the best property combination. From the analysis of the results, HT1-H, and I, and HT2- E, showed the best combination in properties. To quickly assess the optimised cycles, the product of stress elongation was employed, and these cycles all had a PSE > 19.5GPa.%. In addition, a modified HT2-C cycle termed HT3-C will be examined, as the PSE for HT2-C was just below 19.5GPa.%. A longer partitioning time will be incorporated to the HT2-C cycle. Additionally, the properties realised for the optimal cycles on the novel alloys went through a further simulation in JMatPro to calculate the fatigue lifetimes. Based on the research conducted by Guo and colleagues using JMatPro fatigue simulations, it was found that there is a high degree of agreement between the experimental S-N curves and those generated through the simulation. This suggests confidence of the simulated findings presented for the novel Q&P alloys [162]. These four heat-treatments will be examined in the following chapter, with an emphasis on proving a reduction in hardness mismatch.

6.11 Conclusion of Results

- Alloys $MnSiC_{(0.2\%)}$, $MnSiC_{(0.15\%)}$ and CMnSiCr achieved a hot rolled tensile stress below the rolling load limit of 700MPa.
- CMnSiMo exceeded the rolling limit during hot rolled tensile testing. This result was expected as this composition showed high hardenability in the Jominy hardenability simulations and did not drop below 960MPa over the whole length of the bar.
- Alloys $MnSiC_{(0.2\%)}$, $MnSiC_{(0.15\%)}$ and CMnSiCr all had substantial increases in tensile stress, particularly $MnSiC_{(0.2\%)}$ and CMnSiCr, which both increased by over 100% for all heat treatment routes. This substantial increase in strength only led to a 50% reduction in total elongation.
- $MnSiC_{(0.2\%)}$ and CMnSiCr alloys' tensile stress was >1400MPa with the total elongation between 12.1-13.6%. With this combination of properties, the BiW components could be downgauged whilst providing the stringent safety

requirements. Benefits include less material usage and a reduction in emissions.

- It has been observed that the Q&P alloys developed have demonstrated an impressively low sensitivity towards various partitioning temperatures, especially when compared to the data sheets of the AHSS DP and CP grades offered by Tata. HT1 and HT2 heat treatments examined how sensitive the alloys resulting properties would be to the drop in temperature during partitioning. These results indicate that these alloys were not sensitive to this temperature drop.
- Martensite tempering simulation was employed to determine if the alloys would result in a tensile stress >1300MPa. The simulation for each alloy achieved a tensile stress >1300MPa, which was also the case for the measured tensile stress after tensile testing.
- The simulated tensile stress at the lowest quenching temperature was in the closest agreement between the simulated and measured results. Again, JMatPro has been invaluable in the design of these alloys.
- For a material to be suitable for roll forming, it needs to have a large window between its yield and tensile stress. MnSiC$_{(0.2\%)}$ and CMnSiCr have a large window between yield and tensile stress over all heat-treatment routes. Cycles A, B and C for MnSiC$_{(0.2\%)}$ had a window of 540MPa, 524MPa and 518MPa. Cycles G, H, and I for CMnSiCr had a window of 503MPa, 523MPa and 509MPa.
- Referring to the design factors in section 3.3.5, alloys MnSiC$_{(0.2\%)}$, MnSiC$_{(0.15\%)}$ and CMnSiCr achieved all seven factors. Only the CMnSiMo alloy failed to achieve all factors due to its hot rolled strength exceeding the rolling load limit.

Chapter 7

Hardness Mismatch Reduction

7. Hardness Mismatch Reduction

This chapter will summarise and discuss the nano-indentation results for the optimised cycles and will be compared against nano results for DP800. To show scalability the optimised heat treatments have been run on a hot dip annealing simulator. In addition, hole expansion testing using the HDAS annealed samples and XRD analysis to show the austenite and martensite contents.

7.1 Nano-Indentation

Three nanoindentation experiments using accelerated property mapping (XPM) for each optimised heat treatment cycle (see section 6.9, optimised cycles) and a conventional DP800 steel as a comparison. Section 3.16 describes the experimental setup for nanoindentation. The CMnSiCr alloy had both HT-H & I cycles put forward for nanoindentation, and for MnSiC$_{(0.15\%)}$ cycle HT2-E. For the MnSiC$_{(0.2\%)}$ alloy, none of the cycles had a PSE over 19.5GPa.%, the best combination in properties was HT2-C which had 19.2GPa.% with a Vickers hardness of 435Hv. Due to this, it was decided to change the HT2-C cycle, by extending the partitioning step. This cycle for MnSiC$_{(0.2\%)}$ will be termed HT3-C. No cycles were put forward for the CMnSiMo alloy, as this alloy exceeded the rolling load limit and saw only a slight improvement in properties after heat treatment. Figure 92 illustrates the results for DP800. The micrograph is captured with in-situ scanning probe microscopy (SPM) and shows the placement of the indents across the 2*2 chained 10*10 array, totalling 400 indents. The hardness and reduced modulus maps are generated from the load-displacement curves, and there are significant hardness variations over the DP800 microstructure. This is seen visually on the hardness map, with large blue shaded areas and confirmed by having a significant standard deviation of 1.65. Comparing the results for the CMnSiCr (Figures 93 and 94) and MnSiC$_{(0.2\%)}$ (Figure 95) alloys to the DP800 results, it is clear that both have reduced hardness mismatch over all three positions. This is seen visually with all the hardness maps for these alloys, primarily green and yellow points with a small amount of blue and red points. The scale between the minimum and maximum is most prominent for the DP800 sample. The maximum standard deviation for HT1-H and I was 1 and 1.07, and for HT3-C, 1.08. For cycle HT2-E (Figure 96), there was notably less of a reduction in hardness mismatch, particularly for position three, which had a standard deviation of 1.4. Also, a more significant proportion of blue points, which are on the softer end of the hardness scale.

DP800

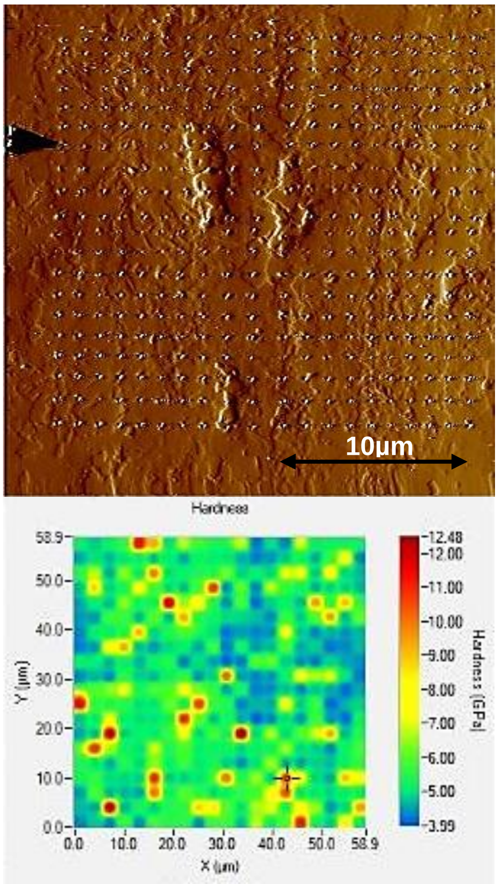

Figure 92: DP800 XPM results.

Table 17: DP800 XPM results.

Average Hardness & Standard Deviation	
5.60GPa	1.65

Table 18: Novel Q&P alloys XPM results.

	Average Hardness (GPa) & Standard Deviation		
Alloy	**Position 1**	**Position 2**	**Position 3**
CMnSiCr - HT1-H	7.9 ± 1.0	8.1 ± 1.0	8.2 ± 0.9
CMnSiCr - HT1-I	8.1 ± 1.1	8.2 ± 0.9	8.6 ± 0.9
$MnSiC_{(0.2\%)}$ - HT3-C	7.9 ± 1.1	8.0 ± 0.9	8.9 ± 0.8
$MnSiC_{(0.15\%)}$ - HT2-E	7.4 ± 0.9	7.2 ± 1.2	7.1 ± 1.4

HT1-H (CMnSiCr Alloy)

Position 1

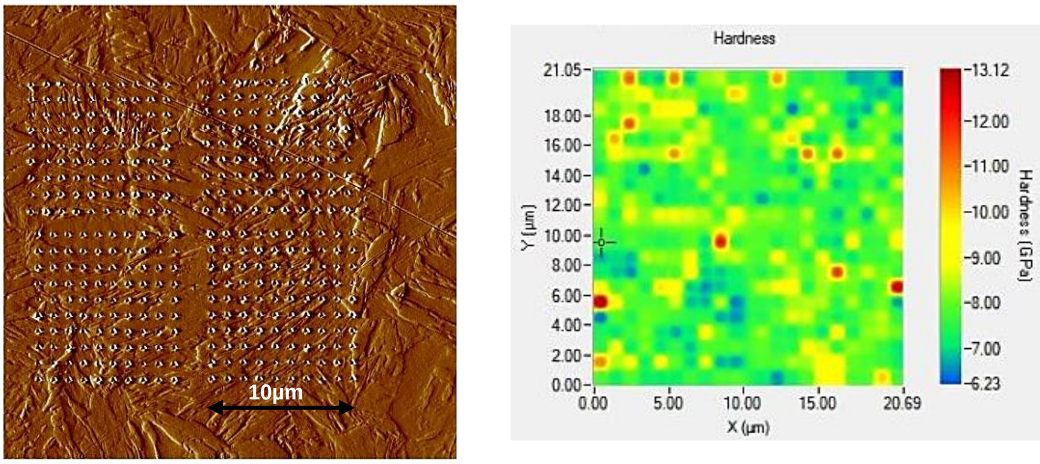

Position 2

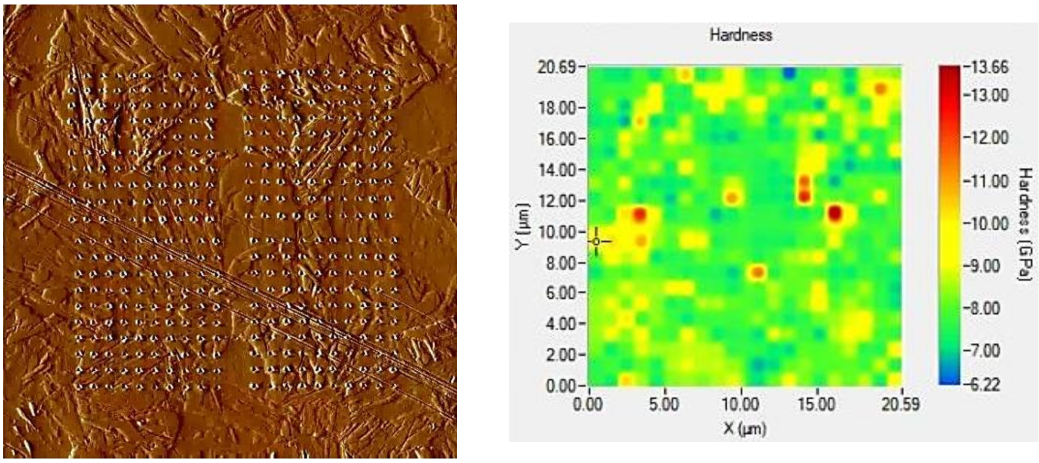

Position 3

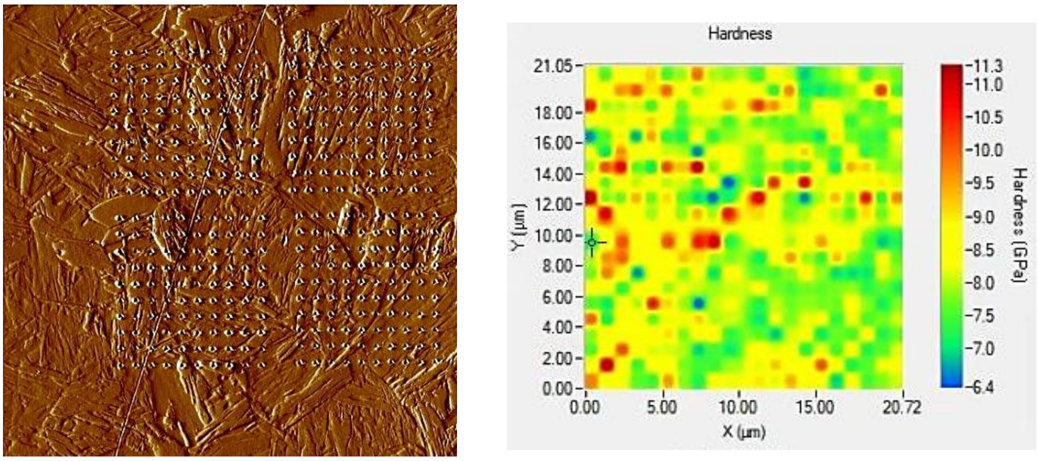

Figure 93: CMnSiCr, HT1-H XPM Results.

HT1-I (CMnSiCr Alloy)

Position 1

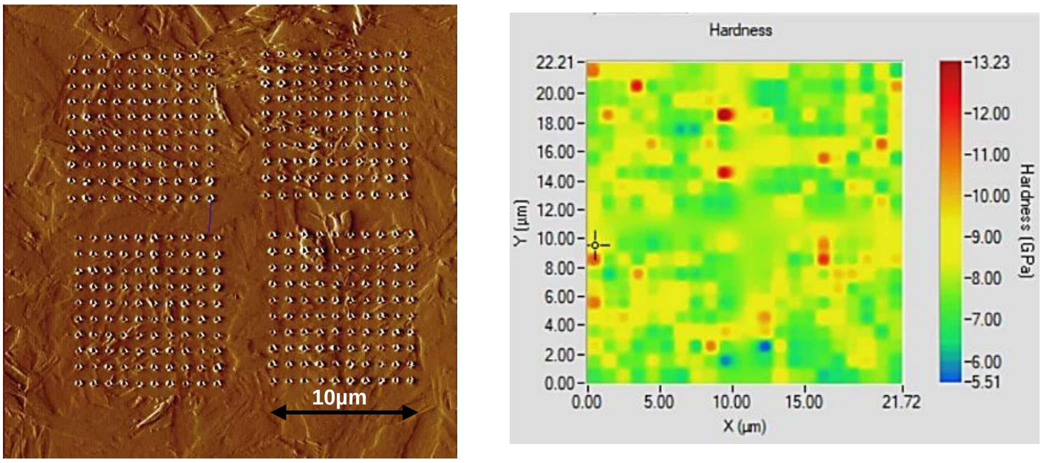

Position 2

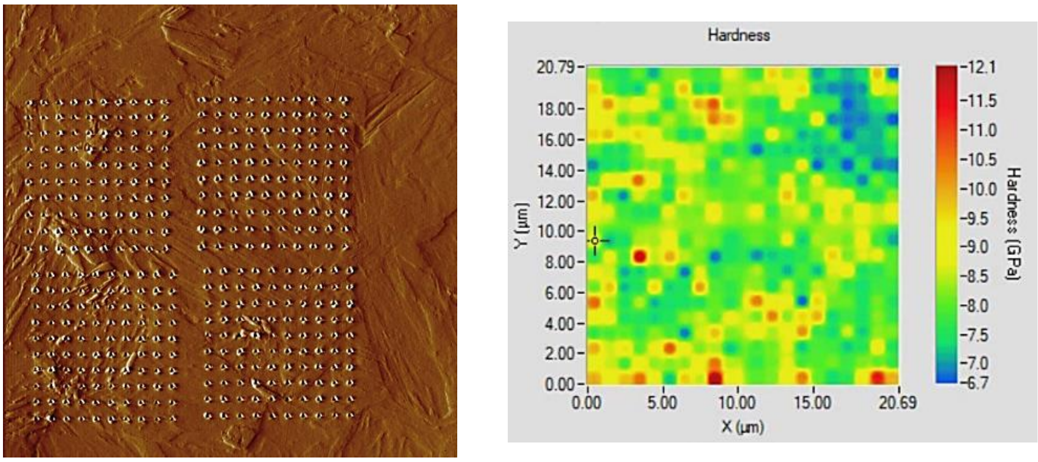

Position 3

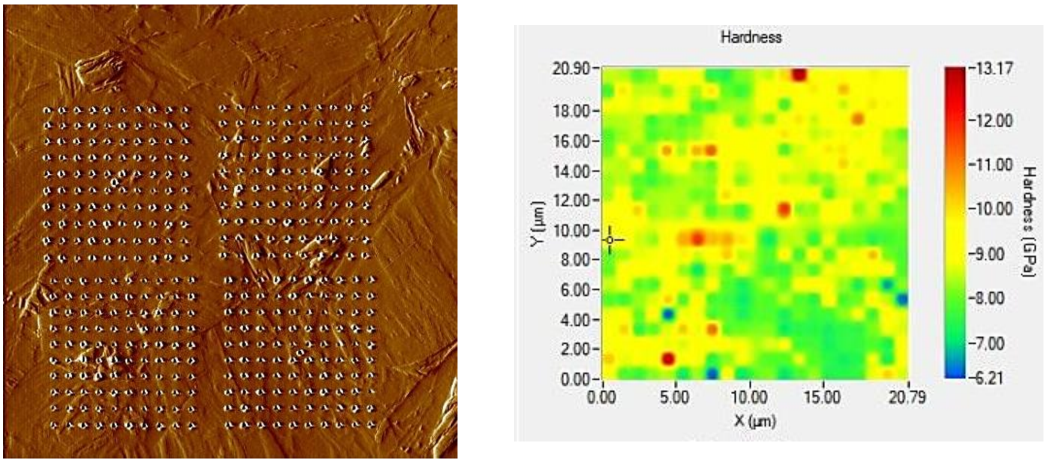

Figure 94: CMnSiCr, HT1-I XPM Results.

HT3-C (MnSiC$_{(0.2\%)}$ Alloy)

Position 1

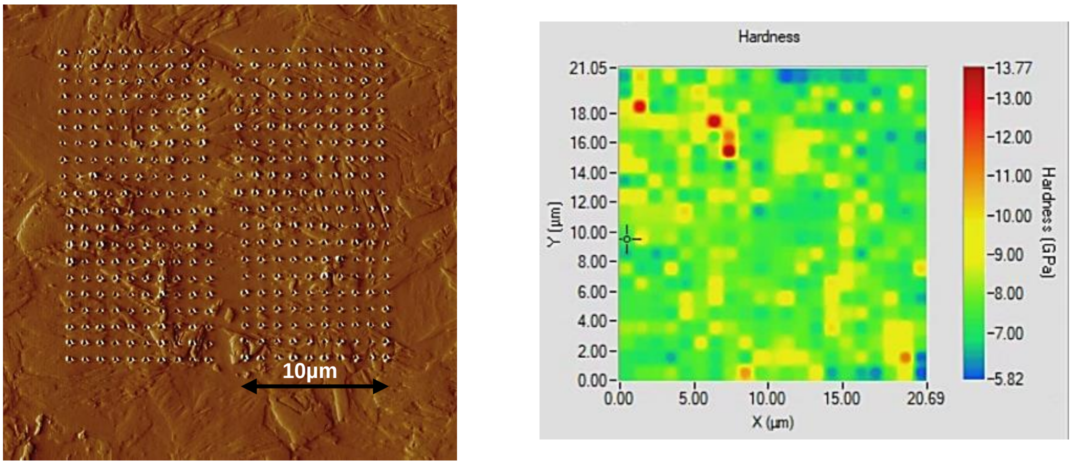

Position 2

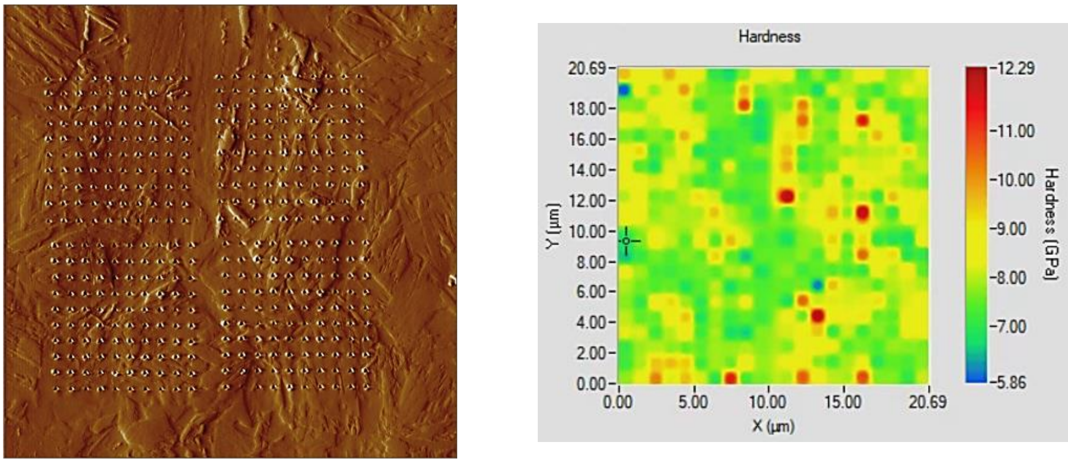

Position 3

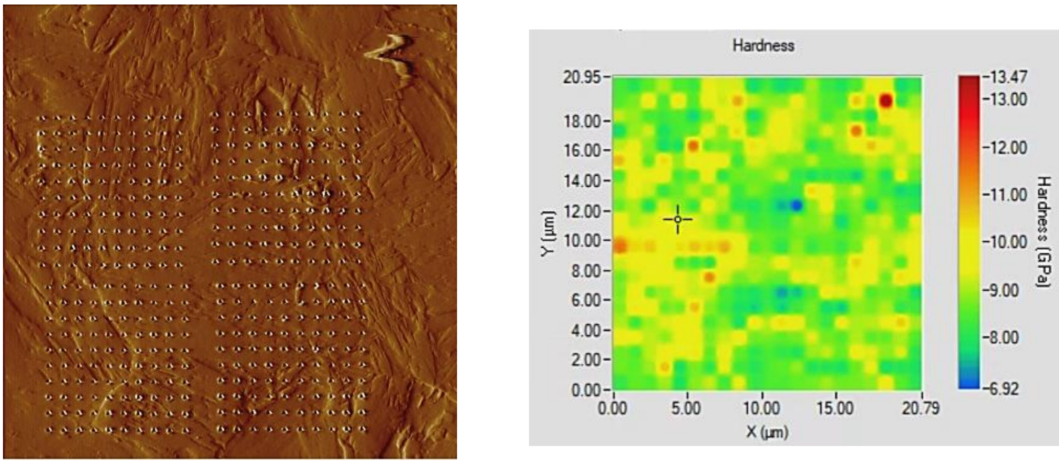

Figure 95: MnSiC$_{(0.2\%)}$, HT3-C XPM results.

HT2-E (MnSiC$_{(0.15\%)}$ Alloy)

Position 1

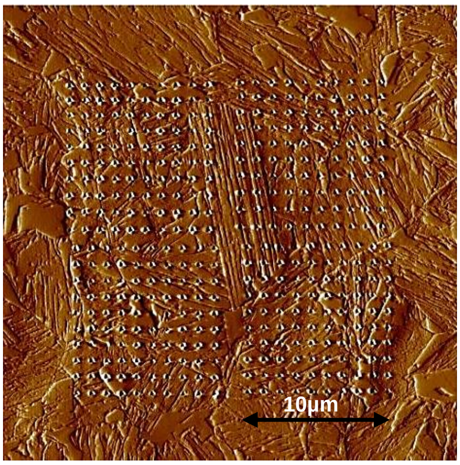

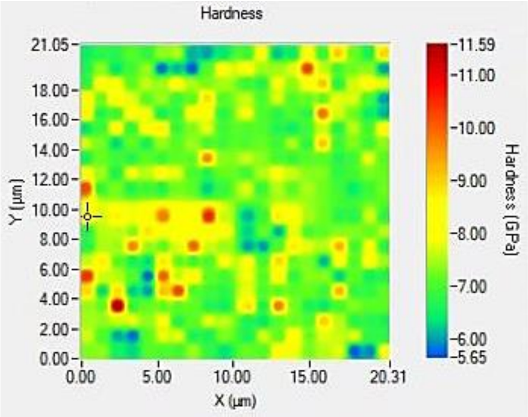

Position 2

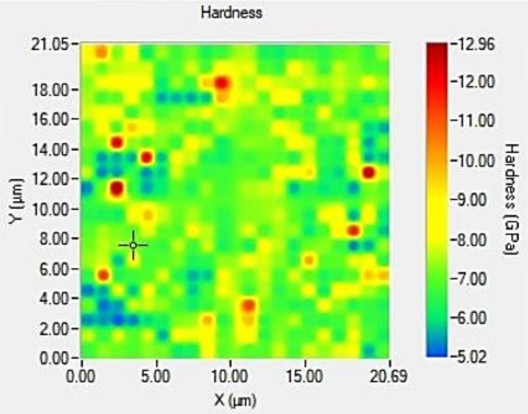

Position 3

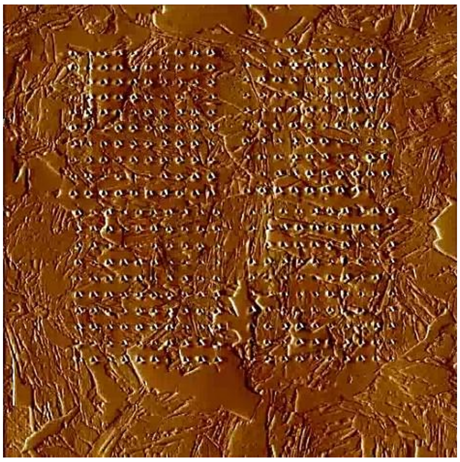

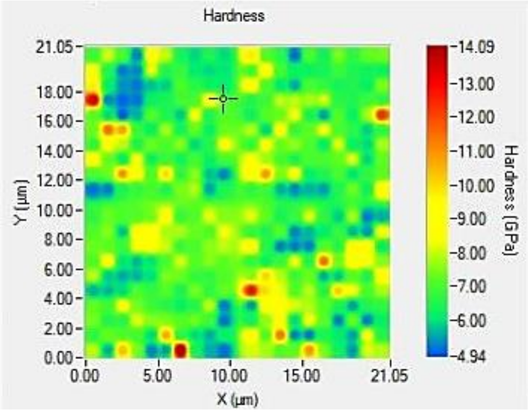

Figure 96: MnSiC$_{(0.15\%)}$, HT2-E XPM Results.

7.2 Hot Dip Annealing Simulator (HDAS)

These experiments show the feasibility of scaling up the sample size for heat treatments. Heat treatments involving the Gleeble only use a small amount of material (17mm width and 180mm length), while heat treatments on the HDAS use (120mm width and 200mm length). One HDAS heat treatment uses the same amount of material as seven Gleeble-sized samples. To note, due to the size of the cold rolled plates having a width between 112-113mm, the whole plate had to be used, whereas a proportion of the cold rolled plate is usually removed. A proportion is removed as the centre is more homogenous than the outer edges.

See section 3.17 for the HDAS experimental procedure. Figure 97 highlights the level of control achieved during the heat-treatment cycles. TC1 is the recorded temperature, PTemp is the programmed temperature, and the blue line shows the amount of oxygen in ppm. HDAS heat treatment is more comparable to CAPL, with the oxygen content controlled and cooling achieved using nitrogen and hydrogen or a mixture of both. It was decided on the previous experiment (section 7.1) to examine a modified HT2-C cycle termed HT3-C, in hindsight it would have made more sense examining HT2-C. The PSE for HT2-C was very close to the target, and it would not be possible to run the modified cycle on CAPL. Due to these reasons HT2-C will examined for the feasibility of scaling up and HER.

Cycles HT1-H & I and HT2-C follow the programmed cycle very closely, with only the final cooling section taking longer than the programme. For HT2-E, there is a delay before the secondary cooling section kicks in. HT2-E cycle took approximately an extra 200s to complete. In total, each heat treatment was repeated five times. In addition, hardness testing was completed on the HDAS samples, which will be directly compared against the Gleeble heat treated samples. Figure 98 illustrates comparable levels of hardness between the HDAS and Gleeble heat treated samples. To note the exact same heat treatment cycle has been run on both the Gleeble and HDAS samples. See Table 19 which illustrates the absolute difference in hardness between the Gleeble and HDAS heat treated samples.

This result indicates that alloys CMnSiCr and MnSiC$_{(0.2\%)}$ can be scaled up whilst still achieving a high level of temperature control. All heat-treated samples will go forward for hole expansion testing.

HT1-H (CMnSiCr) **HT1-I (CMnSiCr)**

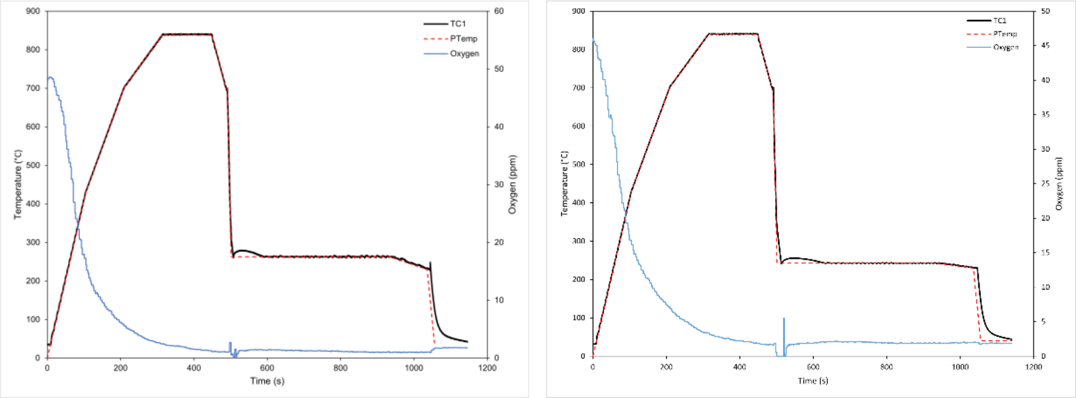

HT2-C ($MnSiC_{(0.2\%)}$) **HT2-E ($MnSiC_{(0.15\%)}$)**

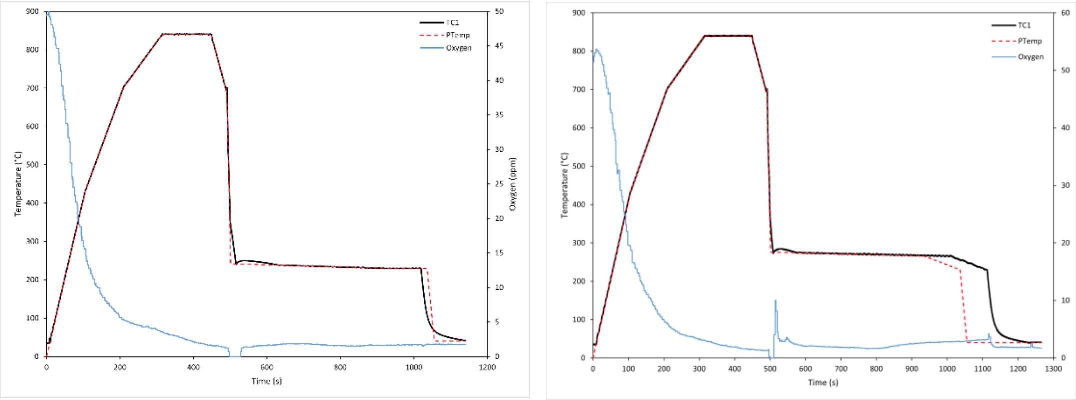

Figure 97: HDAS heat-treatments.

Table 19: Gleeble vs HDAS Vickers hardness.

	Average Hardness (Hv)		
Cycle	Gleeble	HDAS	ABS Difference (±)
HT1-H	418	424	6.3
HT1-I	424	426	2.3
HT2-C	435	437	2.3
HT2-E	414	401	12.7

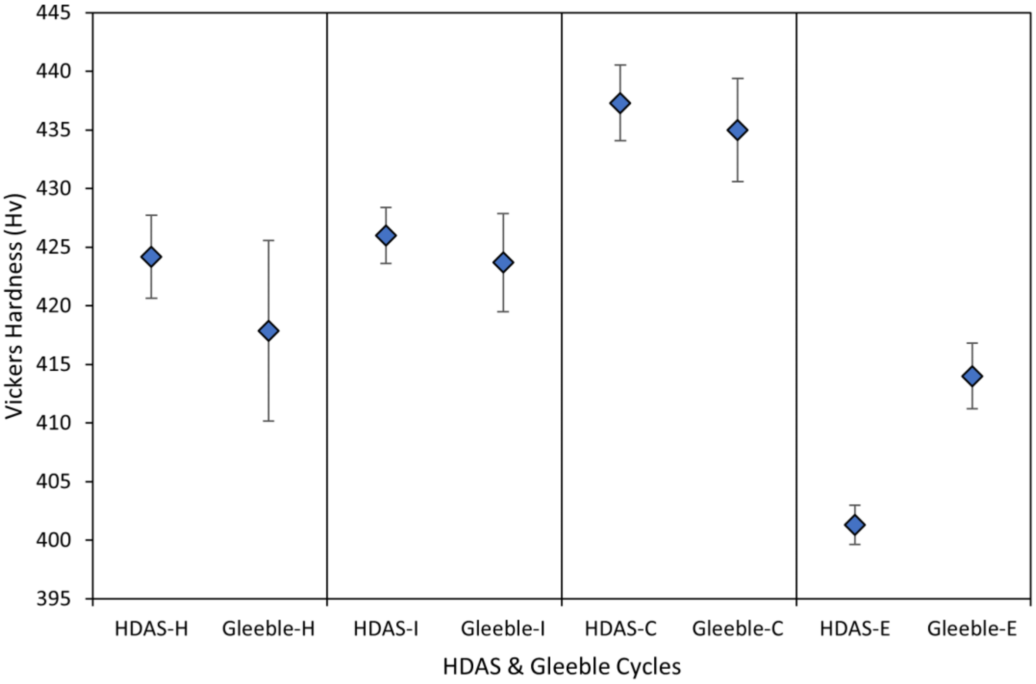

Figure 98: Gleeble vs HDAS Vickers hardness.

7.3 Hole Expansion Testing

Figure 99 shows the reported HER for QP980/QP1180 and DP980 by Wang et al [8]. Table 20 and Figure 100 show the average hole expansion for the different heat treatment schedules. Figure 101 illustrates the repeatability between tests, using a 95% confidence level. Two heat treatment schedules for the CMnSiCr alloy have been tested to find their hole expansion ratio. HT1-H&I showed a mean hole expansion ratio of 64.7% and 60.5%, respectively, with a total range of 11.3% and 8.5%. Only four repeats were completed for H as one of the specimens failed during testing. Both schedules for the CMnSiCr alloy, showed a minimal standard error, at just 2.6% and 1.5%, with the 95% confidence level calculated to 8.2% and 4.2% for H and I. For H, all results are within the confidence bounds, and for I, one result was just outside the bounds. These results indicate that the hole expansion tests were repeatable for this alloy. Cycle HT2-C had a mean hole expansion of 58.6%, range of 11.9%, minimal standard error of just 1.9% and standard deviation of 4.3%. The calculated 95% confidence level was 5.4%, three results are within the bounds, with one at the limit and one outside the bounds. For cycle HT2-E the mean result for hole expansion was 57.2%, range 28%, standard error 5.6% and standard deviation 12.5%. There was more variability in the hole expansion results for this heat treatment schedule compared the other schedules, with its calculated 95% confidence level at 15.5%. Four out of five of the hole expansion results are within bounds, with just one of the results on the limit. Overall, it is clear these Q&P alloys have achieved a substantial increase in hole expansion ratio in comparison to the reported figures from the DP1000 data sheet. Comparing to the DP1000 with 20% HER, in all cases the HER has almost had a three-fold increase. In addition, the HER of the novel Q&P alloys are very similar to the commercially available QP1180, which had a HER between 60-75%, dependent on a punched or machined hole geometry. Notably, the composition for QP1180 has a similar level of alloying additions to the novel Q&P steels designed in this thesis. The compositions for QP980/1180 are shown in section 2.2.10 in Table 1. Also, it is worth noting alloys CMnSiCr and MnSiC$_{(0.2\%)}$ had higher tensile stress but still achieved comparable HER for all heat treatment cycles. The tensile stress was > 1500MPa with a total elongation between 12.1-13.6%. It is clear the novel Q&P alloys designed throughout this thesis have a superior combination of properties to the commercially available QP1180.

Table 20: Average hole expansion (%).

Alloy	Heat Treatment	Average Hole Expansion (%)	Standard Deviation
CMnSiCr	**HT1-H**	65%	5.1%
CMnSiCr	**HT1-I**	61%	3.4%
MnSiC$_{(0.2\%)}$	**HT2-C**	59%	4.3%
MnSiC$_{(0.15\%)}$	**HT2-E**	57%	12.5%
*DP1000 LY-GI	**Standard DP1000 Tata CAPL Cycle**	15%	-
*DP1000 HY-GI	**Standard DP1000 Tata CAPL Cycle**	20%	-
*QP980	**Two-Step QP Cycle**	30-50%	-
*QP1180	**Two-Step QP Cycle**	60-75%	-

*Hole expansion ratio is taken from Tata data sheet for Cold-rolled DP1000-GI [163].

*Hole expansion ratio reported by Wang et al. for QP980 and QP1180 [8].

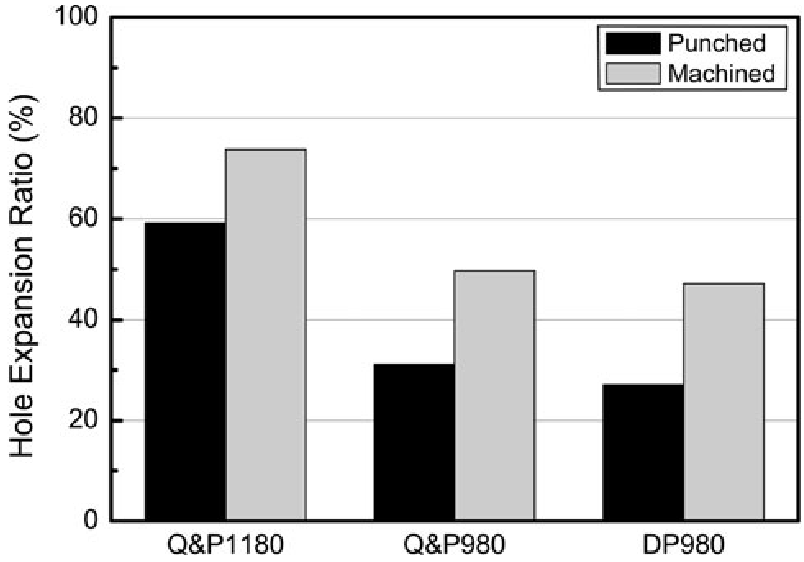

Figure 99: QP980/1180 HER [145].

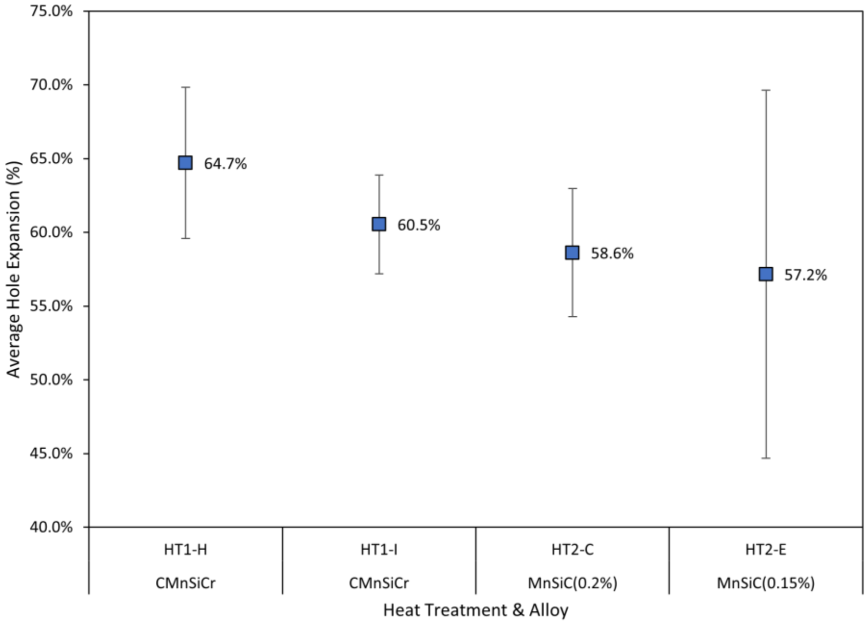

Figure 100: Average hole expansion (%).

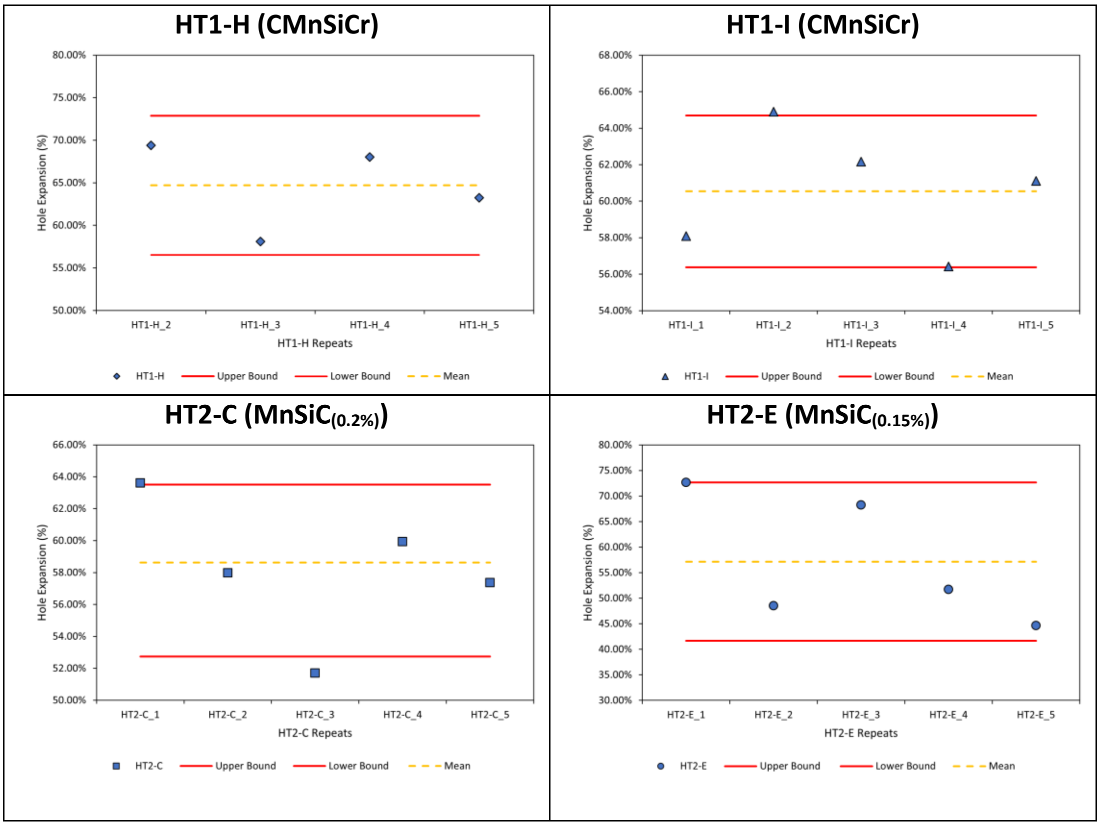

Figure 101: HER testing confidence bounds.

7.4 X-Ray Diffraction

Figure 102 illustrates the diffraction patterns for the four optimised heat-treatment cycles. The X-axis shows the 2theata angle in degrees, and the Y-axis shows the intensity in arbitrary units. Patterns have been offset to view all results on one graph. Table 21 shows the calculated phase proportions. Phase proportions were calculated using Rietveld refinement in MAUD software with iron-α and iron-γ cif files. Sigma values for iron-α were all zero. Additionally, minimal sigma values for iron-γ of 0.8, 0.58, 0.86 and 0.51 for HT1-H, HT1-I, HT2-C and HT2-E were seen. Notably, all diffraction patterns were similar, with all of them showing peaks in the same locations.

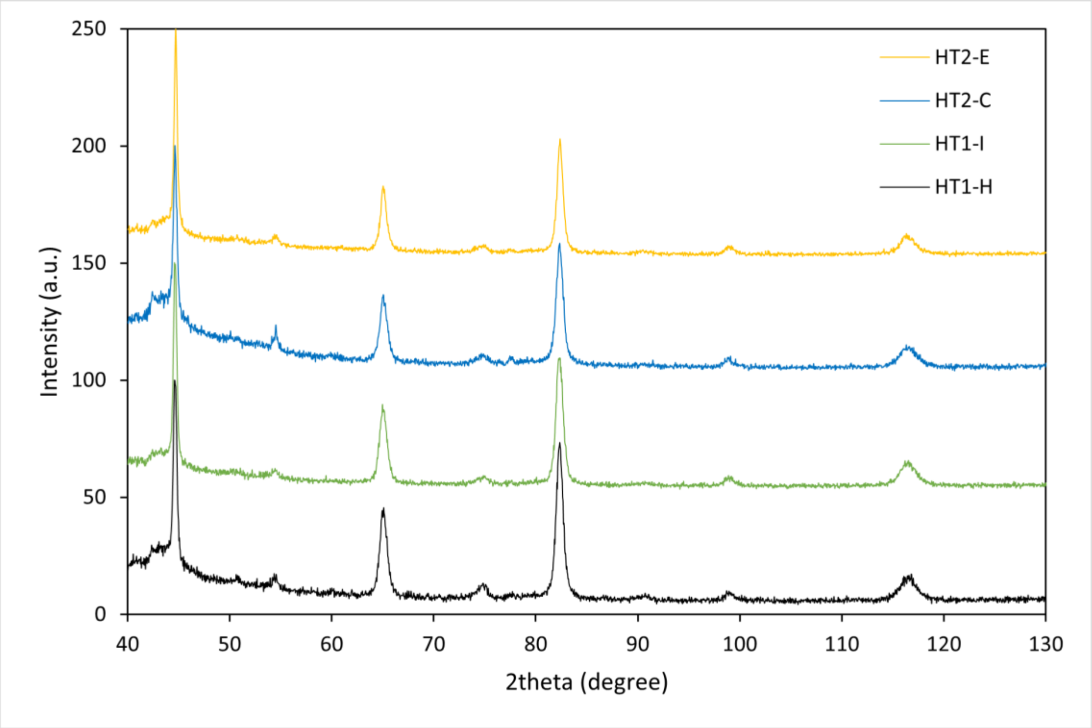

Figure 102: XRD Patterns.

Table 21: Phase proportions.

Alloy	Heat-Treatment	Martensite	Sigma (±)	Austenite	Sigma (±)
CMnSiCr	HT1-H	88.76	0	11.24	0.8
CMnSiCr	HT1-I	93.73	0	6.27	0.58
MnSiC$_{(0.2\%)}$	HT2-C	86.92	0	13.08	0.86
MnSiC$_{(0.15\%)}$	HT2-E	92.37	0	7.63	0.51

7.5 Property Comparison to Commercially Available Q&P Steels

The mechanical properties of alloys CMnSiCr and MnSiC$_{(0.2\%)}$ have been directly compared against commercially available 3rd generation Q&P/DP steels. Properties for QP980/1180 are taken from the BaoSteel catalogue on automotive high-strength steel and properties for DOCOL-DH grades are taken from SSAB data sheets [64]–[66], [164]. Notably, DOCOL-DH are 3rd generation dual-phase steels, but they undergo a quenching and partitioning heat treatment, with the only difference being intercritical annealing. Intercritical annealing is utilised to form a proportion of pro-eutectoid ferrite before cooling to the quenching temperature. Table 22 illustrates the measured properties of the designed Q&P steels and the commercially available 3rd generation Q&P/DP steels. First, comparing the measured results of the novel Q&P

alloys to the commercially available Q&P alloys, both have a similar hole expansion ratio, but notably, the new alloys have far superior tensile stress. Compared to QP980, the tensile stress increases by > 500MPa, and QP1180 increases by > 320MPa. This substantial increase in tensile stress only led to a moderate reduction in total elongation compared to QP980/1180. The PSE looks at the combination of tensile stress with total elongation, and it can be noted that the PSE is superior for the novel alloys. There was no hole expansion data for the DOCOL-DH steel grades, so only the tensile properties could be compared. Again, the novel alloys are shown to have a superior combination of properties, confirmed by the enhanced PSE.

Table 22: Novel Q&P steels compared against commercially available 3rd generation AHSS.

Alloy	Yield Stress (MPa)	Tensile Stress (MPa)	Total Elongation (%)	Hole Expansion Ratio (%)	Yield Ratio	Product of Stress Elongation (GPa.%)
CMnSiCr-HT1-H	1009	1533	12.7	65%	0.66	19.5
CMnSiCr-HT1-I	1020	1529	13.6	61%	0.67	20.8
MnSiC$_{(0.2\%)}$-HT2-C	942	1505	12.7	59%	0.63	19.2
HC600/980QP	600-850	980	15	30-50%	0.61-0.87	14.7
HC600/980QP-EL	600-850	980	20.0	30-50%	0.61-0.88	19.6
HC820/1180QP	820-1100	1180	8	60-75%	0.69-0.93	9.4
HC820/1180QP-EL	820-1100	1180	14.0	60-75%	0.69-0.94	16.5
DOCOL 600DH	330-430	590-700	26	-	0.47-0.73	15.3-18.2
DOCOL 800DH	440-550	780-900	18	-	0.49-0.71	14.0-16.2
DOCOL CR590Y980T-DH	590-740	980-1180	14	-	0.5-0.71	13.7-16.5
DOCOL CR700Y980T-DH	700-850	980-1180	13	-	0.59-0.87	12.7-15.3

7.6 Discussion of Results

The microstructural heterogeneity influences the mechanical response of alloys, and the mechanical behaviour of a heterogeneous material is dependent on the constitutive behaviour of existing constituents [165]–[167]. This chapter explores how differences in local formability impact the hole expansion ratio (HER) of three Q&P alloys and will discuss how they compare to the reported HER for TATA's DP1000 and the commercially available QP980 and QP1180 steels. Additionally, the nanoindentation results will be compared and discussed against DP800.

Interestingly, even though dual-phase steels are shown to have superior global formability, their HER will be much lower than Q&P steels. This is down to the inferior local formability seen in DP steels. This local formability is dictated by the hardness difference between microstructural constituents (phases) and correlates to the HER. All the steels studied have quantities of manganese in their compositional makeup. Mn is known to segregate into Mn-enriched and Mn-depleted bands, and it is known that the hardness of Mn-enriched bands is more significant than that of the Mn-depleted bands [168]. In a study by Chang et al. [169] it was shown that the hardness in Mn-enriched bands was higher for a DP800 material compared to a CP800 material. Chang et al. determined that the increase in hardness on a local scale was increased in DP800 as a higher fraction of martensite formed within the Mn-enriched zones. Martensite formed in an Mn-enriched zone has a substantial increase in hardness compared to the Mn-depleted zones.

The Q&P alloys studied in this chapter go through an isothermal hold after quenching, and it is this partitioning mechanism that helps to reduce hardness mismatch between constituent phases. During partitioning, the excess carbon in the martensitic phase diffuses into the austenite phase, enriching it with carbon. During this process, multiple mechanisms reduce the hardness mismatch between phases. As carbon is reduced in the martensite phase, it causes its local hardness to reduce. It is also tempering within this region, causing a further decrease in hardness and a reduction in stored energy. As the austenite is enriched in carbon, its local hardness increases and as these mechanisms progress, the balance in hardness between the phases becomes more homogenous. It is believed that as the local hardness becomes homogenous, the alloy will then behave the same way as a single-phase alloy during deformation events [170]. Alloys with a significant difference in local hardness between phases will preferentially deform at the boundary between the hard and soft phases. For DP steel, this is more pronounced as its microstructure is composed of a soft ferrite matrix with hard martensitic islands, whereas Q&P steel is composed of carbon-depleted tempered martensite with carbon-enriched retained austenite. The results shown in this chapter help confirm these theories. First, on inspection of the nano results, the load-displacement curve is much broader for DP800. This means there are more significant proportions of soft and hard phases, as the penetration depth for ferrite is much more prominent than that of martensite. It can also be noted that the CMnSiCr and $\mathrm{MnSiC}_{(0.2\%)}$ alloys showed the narrowest spread on the load-displacement curves, indicating these alloys show a minor variation in hardness on a local scale. The reduction in hardness mismatch on a local scale is also confirmed by the standard deviation being much lower than DP800. On a local scale, this reduction in hardness mismatch has led to drastic improvements in HER compared to DP1000 and a comparable HER to QP1180 produced by BaoSteel. Also, it is worth noting both QP980/1180 can be purchased galvanised, and as the novel Q&P alloys designed in this thesis are quite similar to that of QP1180, there is confidence these new alloys could also be galvanised. Notably, the complexity of the heat treatment is reduced for the novel Q&P alloys designed in this thesis. QP1180 is heat treated via a two-step quenching and partitioning cycle, whereas the novel Q&P alloys were heat treated via the one-step quenching and partitioning cycle. The one-step cycle was chosen because there is no mechanism to heat the steels after quenching on Tata's CAPL line. There was an emphasis on designing and making Q&P steels which could be heat treated without making any infrastructure changes to Tata's CAPL line.

7.6.1 Nano-Indentation

The XPM results showed two of the novel alloys achieved a reduction in hardness mismatch, confirmed visually from the hardness maps and numerically by the DP800 sample having a substantially larger standard deviation. The two alloys were CMnSiCr and $\mathrm{MnSiC}_{(0.2\%)}$. Plastic deformation begins with the localisation of plastic flow in softer phases such as retained austenite or ferrite. With both CMnSiCr and $\mathrm{MnSiC}_{(0.2\%)}$ alloys, the Q&P processing has led to a balanced structure in terms of hardness. Even though the structures are very complicated and composed of many different micro-constituents, such as carbon-depleted tempered martensite, fresh martensite, bainite and retained austenite, there are very few points on the incredibly soft and hard ends of the hardness maps. The diffusion of carbon from martensite to austenite leads to an inhomogeneous distribution of carbon atoms across the constituent phases, but this leads to a more homogenous hardness distribution. Seo et al. [81] studied the constituent properties in Q&P processed steels and found that the hardness of the carbon-enriched austenite was comparable to the hardness of the low-carbon primary martensite. Seo et al. determined that the comparable hardness was because the carbon content in the solid solution in the austenite was much higher than the primary martensite. Not surprisingly, with a higher proportion of carbon in solid solution in the austenite phase, the hardness of this constituent increases and the hardness of the primary martensite reduced as its carbon reduced. Additionally, the primary martensite will be tempered, in turn lowering its hardness further. XPM is a very fast an effective method to map the hardness distribution of complicated multiphases steels. Traditional nano-indentation measurement takes 90s per indent, whereas with XPM 6 indents can be performed per second. For example, the tests run on these alloys would have taken 10 hours to complete using standard methods and just over 1 minute with XPM. It is worth noting these nano-indentation experiments will need to be repeated with improved compliance, but these initial results are showing promising trends. It is likely repeated tests would still show a reduction in hardness mismatch.

7.6.2 Scale Up

Heat treatments run on the hot dip annealing simulator (HDAS) have confirmed the feasibility of scaling up. Three out of four of the alloys followed the programmed cycle very closely. Only the HT2-E cycle (MnSiC$_{(0.15\%)}$-alloy) deterred from the programme and took an extra 200s to complete. Unsurprisingly, the three cycles that followed the programmed cycle very closely achieved comparable Vickers hardness to that of the Gleeble heat-treated samples. The Vickers hardness for the HDAS heat-treated HT2-E was softer than the Gleeble heat-treated sample. This hardness reduction is due to the HDAS sample taking an extra 200s for the cycle to complete, which extended the partitioning stage, causing further tempering of the martensitic structures and lowering the hardness. Heat treating on the HDAS is more representative of TATA’s CAPL line, as oxygen content is controlled, and cooling is achieved by nitrogen, hydrogen, or a mixture of both.

7.6.3 Hole Expansion Testing

The hole expansion results show that alloys CMnSiCr and MnSiC(0.2%) have achieved comparable hole expansion ratio (HER) levels to the commercially available QP1180. Notably, these novel Q&P alloys are far more robust than QP1180, with tensile stress > 320MPa higher. Karelova et al. [48] studied the hole expansion of DP and CP steels and found that the HER was directly related to the microstructural heterogeneity and properties between the constituent phases. Karalova found it depended on the hardness differential between the matrix phase and other constituents. It was also found that the hole preparation procedure had a strong influence on the HER, where hole punching and drilling can negatively impact this property. Q&P alloys are different to CP steels, but there are similarities; they are both complex by nature, having three or more phases and have a smaller hardness differential between their phases compared to DP steels. CP steels are composed of large amounts of martensitic and bainitic phases, both hard. The QP alloys are composed of a variety of martensitic phases and carbon-induced retained austenite. The lowering of carbon from the martensitic phase and the increase of carbon in the austenite phase brings the hardness of these constituents closer. Because there is less of a hardness differential between the phases, the preference for deformation to start at the interphase between phases is massively reduced. It is believed the alloy will now behave similarly to a single-phase alloy.

7.7 Conclusions

- Nano-indentation has proved a fast and effective method to show a reduction in hardness mismatch.
- Alloys CMnSiCr and $MnSiC_{(0.2\%)}$ have realised a reduction in hardness mismatch for their optimised heat treatment schedules. This is shown visually by the hardness maps and confirmed by the standard deviation being much more significant for the DP800 sample.
- Heat treating using the HDAS has proven the feasibility of scaling up for alloys CMnSiCr and $MnSiC_{(0.2\%)}$.
- The CMnSiCr alloy achieved the highest hole expansion ratio compared to the other alloys and was in closest agreement to the reported HER for QP1180.
- All alloys achieved a substantial improvement in hole expansion, compared to the reported values for DP1000.
- These results combined with the results from the previous chapters show both CMnSiCr and $MnSiC_{(0.2\%)}$ alloys have achieved all design factors (section 3.3.5) and would be suitable candidates for an industrially viable quenching and partitioning steels.
- $MnSiC_{(0.15\%)}$ would not be a suitable candidate, as its combination in properties is lesser than the other two alloys and it is clear a sufficient reduction in hardness mismatch was not achieved.
- XRD results show all the alloys have proportions of retained austenite, indicating the partitioning has helped to stabilise the austenite phase.
- By comparing the novel Q&P alloys to the commercially available 3rd generation QP/DP alloys, it is clear the novel alloys designed have superior properties.

- Referring to Table 1 in section 2.2.10, it can be noted the novel alloys have a comparable amount of alloying additions to the QP1180 alloy, but are leaner, compared to the DOCOL-DH grades. DOCOL-DH grades had between 6.21-7.69 Wt.%, whereas the novel alloys were between 4.1-4.28 Wt.%.

Chapter 8

Conclusion

8. Conclusions

8.1 Tata Tubes - 3827 and 3832

The study delved into the properties of low-alloyed tube steels, specifically Tata tube materials 3827 and 3832. The primary objective was establishing a foundation for developing new Q&P steels and to substantially improve the properties of 3827 and 3832. Both steel grades had a lean chemical composition, adding C, Mn, and Si as the primary elements.

TTT and CCT diagrams were simulated using JMatPro software to determine the optimal heat treatment regimens. The resulting heat treatments were applied to samples 3827 and 3832, and the microstructures were analysed using optical microscopy. The heat treatment experiments showed that carefully controlling the heating and cooling rates induced the desired microstructural changes, significantly improving mechanical properties. ThermoCalc software was used to evaluate the impact of elemental variations on transformation temperatures, providing insights into the starting points for developing novel Q&P steels.

The results showed that 3832 outperformed 3827 during tensile testing, achieving a UTS > 600MPa and total elongation > 21.5% for all heat-treatment routes. This increased mechanical performance was due to the small Nb addition, which helped refine the steel grains. The micrographs also showed clear evidence of grain refinement for 3832. Overall, 3832 achieved comparable properties to DP600 with fewer alloying additions. The study demonstrated that property enhancement was achieved through cleverly designed heat treatments to induce the desired microstructural evolution.

In summary, using simulation software to design heat treatments and evaluate the impact of elemental variations has provided insights in developing the novel Q&P steels.

8.2 Q&P Steels

The design of novel quenching and partitioning steels using a combination of JMatPro and ThermoCalc has proven to be highly valuable tools for achieving the desired microstructural evolution and resulting properties. Through careful alloying and by keeping the additions below 4.5 Wt.%, design factor 7 was achieved. The designed $\mathrm{MnSiC_{(0.15\%)}}$, $\mathrm{MnSiC_{(0.2\%)}}$, CMnSiCr, and CMnSiMo Q&P steels have shown great potential in achieving the desired microstructural evolution. All the simulated A_r^3 temperatures were below 840°C, and simulated A_r^1 temperatures were below 700°C for three of the four alloys. Only the $\mathrm{MnSiC_{(0.2\%)}}$ alloy showed a slightly higher temperature at 701°C, but the time for ferrite transformation at 700°C was sufficiently suppressed, which infers no ferrite formation during the slow cooling to 700°C.

The ThermoCalc and TC-Prisma simulations provided additional confidence in the designed alloys, with minimal cementite precipitation and an insignificant volume fraction of other precipitates observed. The martensite tempering simulation demonstrated that the four alloys would achieve tensile stress of over 1300MPa, achieving design factor 5.

Furthermore, the mechanical properties of the designed alloys showed that alloys $\mathrm{MnSiC_{(0.2\%)}}$, $\mathrm{MnSiC_{(0.15\%)}}$, and CMnSiCr achieved a hot rolled tensile stress below the rolling load limit of 700MPa, which agrees with the conclusions drawn from the Jominy hardenability simulations. It can be inferred from the data that the novel alloys, including $\mathrm{MnSiC_{(0.2\%)}}$, $\mathrm{MnSiC_{(0.15\%)}}$, and CMnSiCr, have been engineered to not only optimise their properties after cold rolling and annealing but also to attain the desired properties after hot rolling. Using JMatPro to model material properties has been validated and proven invaluable during the design stage for exploring novel compositions.

It should be noted that the alloys $\mathrm{MnSiC_{(0.2\%)}}$ and CMnSiCr exhibited a significant increase in tensile stress after annealing, with the value increasing by more than 100% for all heat treatment routes. The alloys' tensile stress exceeded 1400MPa, while the total elongation ranged between 12.1-13.6%. These experimental outcomes validate using martensite tempering simulations during the design phase to screen the alloys. A conclusion can be drawn from the minimal sensitivity displayed by the novel Q&P alloys for the different partitioning temperatures employed. Each alloy showed a smaller property window than three of Tata's AHSS, namely DP800/1000 and CP800. For instance, the UTS property window for Tata's AHSS was 120MPa, 150MPa, and 140MPa, respectively, whereas for alloys $MnSiC_{(0.15\%)}$, $MnSiC_{(0.2\%)}$, CMnSiCr, and CMnSiMo, the values were 49MPa, 71MPa, 28MPa, and 63MPa, respectively. Moreover, a further heat-treatment study dubbed HT2 examined the impact of reducing the temperature by 10°C for the partitioning temperature hold. The results of this study imply that the designed Q&P steels are also not sensitive to this temperature drop.

Supplementary to the minimised property window, the Q&P steels that have been designed have realised a substantial processing window, which results in improved ductility. The extensive processing window is demonstrated by the low yield ratios of the novel Q&P steels. For the CMnSiCr alloy, the two optimised cycles (HT1-H and I) yielded a ratio between 0.66-0.67, while for $MnSiC_{(0.2\%)}$, the optimised cycle was 0.63. A low yield ratio indicates that the steel has the potential to undergo significant strain hardening during forming processes, whereby the material becomes stronger as it is deformed. Increased levels of strain hardening can, in turn, lead to improved formability, increased resistance to localised deformation (such as necking or tearing) and enable the material to be fashioned into complex shapes with greater ease. This combination of properties allows the BiW components to be downgauged while providing stringent safety requirements.

Nano-indentation has proven to be a fast and effective method for showing a reduction in hardness mismatch, with alloys CMnSiCr and $MnSiC_{(0.2\%)}$ realising a reduction in hardness mismatch for their optimised heat treatment schedules. The feasibility of scaling up heat treatment using the HDAS was also demonstrated for alloys CMnSiCr and $MnSiC_{(0.2\%)}$, supplemented by the positive HER results for these alloys in question. In addition, the Vickers hardness was comparable for Gleeble and HDAS heat treated material.

Moreover, it is noteworthy that all the Q&P alloys demonstrated a significant enhancement in hole expansion and tensile stress compared to the values reported for DP1000, exhibiting a remarkable 300%-400% increase in HER and a 33% increase in tensile stress whilst maintaining similar levels of elongation. In contrast to commercially accessible 3rd generation QP/DP alloys, the newly developed Q&P alloys exhibit exceptional properties. Regarding the hole expansion ratio, the new and commercially available Q&P alloys exhibit similar results, but the new alloys possess significantly superior tensile stress. Compared to QP980, the tensile stress increases by over 500MPa, and QP1180 increases by more than 320MPa. Even with this substantial increase in tensile stress, there is only a moderate reduction in total elongation compared to QP980 but comparable to QP1180. The PSE assesses the combination of tensile stress with total elongation, and it is noteworthy that the PSE is more significant for the newly developed Q&P alloys. Unfortunately, there was no hole expansion data for the DOCOL-DH steel grades, so only the tensile properties could be compared. Despite this, the newly developed Q&P alloys still exhibit superior properties, as confirmed by the enhanced PSE and the additional benefit of the compositions being far leaner.

The successful achievement of all design factors outlined in section 3.3.5 has resulted in developing two innovative alloys with immense potential for use as industrially viable quenching and partitioning steels. Among these alloys, $\mathrm{MnSiC}_{(0.2\%)}$ and CMnSiCr stand out as highly promising candidates. The implications of these findings for the advancement of materials science and engineering cannot be overstated. They have the potential to make a significant impact on the future development of high-strength and formable steel for automotive BiW.

Chapter 9

Future Work

9. Future Work

This section will cover the future experimentation needed for the novel Q&P steels to be taken to market. Followed by the marketability and operational costs versus other steel grades.

9.1 Future Experimentation

Further investigations and experiments are needed to expand the understanding and explore the potential of the novel Q&P steels $\mathrm{MnSiC}_{(0.2\%)}$ and CMnSiCr. These studies will involve conducting heat treatment cycles on the HDAS (hot dip annealing simulator), both with and without the Zinc pot attached, with specific objectives in mind. Additionally, welding-based experimentation, using the Gleeble 3500 to run HAZ (heat-affected zone) simulations, expansive mechanical testing, and, finally, rolling forming experiments to assess the material's ability to be incrementally shaped into defined geometries.

Firstly, including the Zinc pot during the heat treatment cycles would aim to assess the coatability of the novel Q&P steels. Coatability plays a crucial role in the practical applications of these steels, particularly in industries where zinc coating is required for corrosion resistance and other surface-related properties. By studying the behaviour of the Q&P steels in the presence of the Zinc pot, it will be possible to determine the feasibility and effectiveness of applying a zinc coating to these materials. The evaluation will analyse the adhesion, uniformity, and quality of the zinc coating on the Q&P steels, providing valuable insights into their potential use in automotive BiW applications. It is important to note that QP980 and QP1180 are commercially available as uncoated and galvanised. Their compositions are similar to the designed Q&P steels, which provides reassurance regarding the potential coatability.

In addition to the investigations involving the Zinc pot, future work would also focus on studying the full range of mechanical properties of the Q&P steels. A comprehensive assessment will be required to understand and characterise these steels' mechanical behaviour. The evaluation will include tensile testing with larger samples (A50 specification), fatigue testing, Charpy Impact testing, and three-point bend testing.

The tensile testing of A50 specimens would aim to examine if the same properties are achieved in comparison to the ASTM E8 sub-size tensile properties. Fatigue testing would assess the fatigue strength and durability of the steels, examining their ability to withstand cyclic loading and resist failure over extended periods. Charpy Impact testing will evaluate the steel's toughness and resistance to brittle fracture under impact loading. Three-point bend testing will provide insights into the steel's flexural properties, such as modulus of elasticity, yield strength, and fracture toughness. By studying this comprehensive bank of properties, a deeper understanding of the novel Q&P steels' mechanical behaviour will be achieved. These findings would contribute to the steels' fundamental knowledge and assist in selecting and optimising further the novel Q&P steels.

Further experiments will involve welding-based studies using the Gleeble 3500 to analyse the effects of welding on the Q&P steels $MnSiC_{(0.2\%)}$ and CMnSiCr, with a specific focus on the Heat-Affected Zone (HAZ). The Gleeble will enable precise control over welding parameters, allowing for a detailed examination of microstructural changes and potential property variations induced in the HAZ. The post-welding analysis will involve microstructural and mechanical property evaluations to assess HAZ's susceptibility to cracking, brittleness, or softening.

Finally, a roll-forming based experiment will need to be employed. Numerous factors can be considered and controlled during a roll-forming experiment, including roll geometry, roll speeds, strip thickness, and strip material properties. A V-section will be the chosen geometry for experimentation. The formed V-section samples can be collected at various stages of the roll-forming process for subsequent analysis and characterisation. Post-roll forming analysis will evaluate the formed V-sections' dimensional accuracy and surface quality. The aim is to ensure the desired dimensional precision and repeatability of the roll-formed V-sections. The mechanical properties of the roll-formed V-sections will also be evaluated through testing methods such as tensile testing, hardness testing, and microstructural analysis, providing insights into the material's behaviour and potential changes induced by the roll-forming process. Comparisons with the initial Q&P steel properties will help assess the impact of roll forming on the material's mechanical performance.

The future work outlined above further explores the potential and practicality of the novel Q&P steels $MnSiC_{(0.2\%)}$ and CMnSiCr. By assessing coatability with the Zinc pot, the comprehensive evaluation of mechanical properties, the material's weldability and roll-formability, a complete understanding of the steel's performance would be achieved, paving the way for its successful integration into automotive BiW.

9.2 Product Marketability

Quenching and partitioning (Q&P) steels have become increasingly popular due to their remarkable combination of high strength and good ductility. This innovative steel design concept involves a two-step or one-step heat treatment process that enhances their intrinsic properties. One of the key benefits of using quenching and partitioning steels is their superior strength-to-weight ratio. These steels can achieve high tensile strengths while maintaining excellent formability, making them highly sought-after for industries where weight reduction is critical, such as the automotive sector. By utilising Q&P steels, manufacturers can create lighter components without compromising structural integrity, resulting in improved fuel efficiency, overall performance, and less material usage to manufacture the part. Furthermore, the unique microstructure of these steels provides enhanced mechanical properties, including improved toughness and resistance to brittle fracture, leading to increased durability and reliability. Figure 103 illustrates the potential weight savings for a variety of AHSS's compared to using mild steel for a B-pillar component [171]. Both generation three and press hardened steels show the highest potential in reducing the weight of components, over 40%. Notably the novel Q&P steels designed had a tensile strength over 1500MPa taking the potential weight savings to 42%.

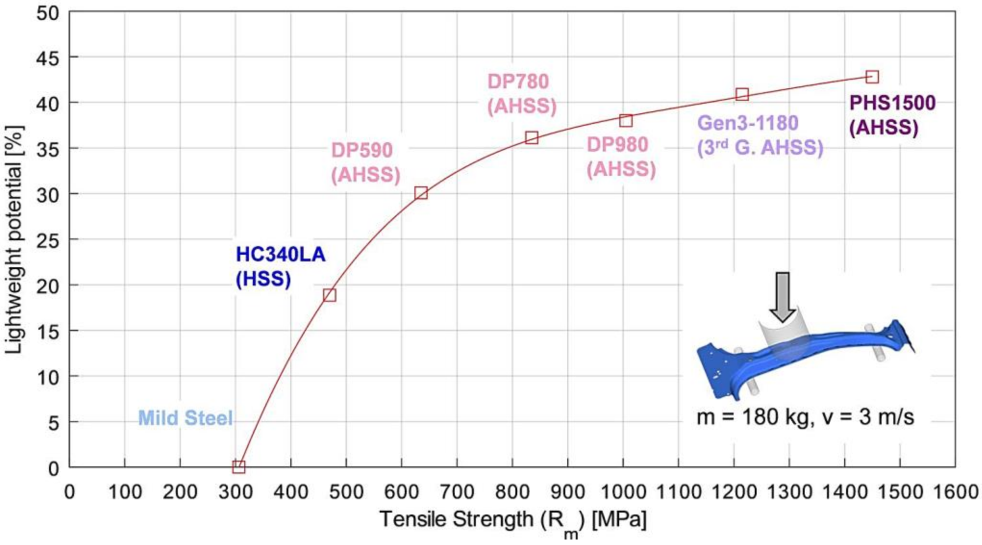

Figure 103: Lightweight potential of several steel grades, compared to mild steel [171].

Quenching and partitioning steels offer excellent opportunities for tailored material properties. The process parameters, such as the quenching temperature and partitioning time, can be adjusted to achieve specific mechanical characteristics based on the intended application. This flexibility enables the customisation of Q&P steels to meet the requirements of different industries.

To summarise, the marketability of quenching and partitioning steels is driven by their exceptional combination of high strength, good ductility, and customisable properties. These steels have the potential to revolutionise various sectors by providing lightweight yet strong materials that contribute to energy efficiency, improved product performance, and overall sustainability. As research and development in the field continue to advance, the market demand for Q&P steels is expected to grow, making them a promising choice for manufacturers.

9.3 Transferability

The heat treatment process is critical in improving various properties of steel, such as strength, hardness, toughness, and fatigue resistance. Traditional heat treatment design methods rely on empirical techniques and trial-and-error experimentation. Still, a more systematic and scientific approach can be achieved by employing thermodynamics and kinetics, improving efficiency and accuracy.

This thesis utilised a unique approach that combines thermodynamics and kinetics to guide the design and optimisation of heat treatment processes for very low alloyed steels (Tata tubes 3827 and 3832) and medium alloyed Q&P steels. Alloy composition, phase transformations, and diffusion kinetics can influence the resulting material properties. Critical factors can be identified by analysing these factors.

The approach has shown significant enhancements in strength and ductility for very low alloyed steels and medium alloyed Q&P steels by carefully adjusting the heating and cooling rates. By controlling the formation of desired phases, such as martensite, bainite, and retained austenite in optimised proportions, the resulting mechanical properties of the steel were improved.

This systematic understanding of phase transformations and diffusion kinetics provides a scientific basis for tailoring the properties of steel. The successful application of this approach in designing novel Q&P steels with optimised microstructures and properties, specifically focusing on the absence of undesired phases like ferrite and precipitates, demonstrates its potential for transferring to other steel grades. Integrating phase transformation theory, repeated TTT and CCT simulations using JMatPro, and validation in ThermoCalc provided a systematic and efficient framework for designing the novel Q&P steels. The transferability of this approach to other steel grades holds significant potential for advancing the field of steel design. By adapting phase transformation theory and utilising simulation tools such as JMatPro and ThermoCalc, material scientists can explore and optimise the heat treatment parameters and elemental variations to design new steels, quickly and effectively.

References

[1] UltraLight Steel Auto Body Consortium, “ULSAB-AVC - Advanced Vehicle Concepts Overview Report.,” 2001. [Online]. Available: https://www.worldautosteel.org/downloads/ulsab-avc-downloads/

[2] WorldAutoSteel, “FutureSteelVehicle Results and Reports & Cost Model.” https://www.worldautosteel.org/projects/future-steel-vehicle/phase-2-results/ (accessed Dec. 09, 2022).

[3] J. N. Hall, “Importance of Life Cycle Emissions Considerations in Vehicle Regulations,” 2016. [Online]. Available: www.smdisteel.org

[4] Department for Business Energy and Industrial Strategy, “Net Zero Strategy: Build Back Greener,” 2021. [Online]. Available: https://www.gov.uk/government/publications/net-zero-strategy

[5] S. Mridha, “Metallic Materials,” *Ref. Modul. Mater. Sci. Mater. Eng.*, pp. 1–7, 2016, doi: 10.1016/b978-0-12-803581-8.04097-2.

[6] H. Bhadeshia and R. Honeycombe, *Iron and Its Interstitial Solutions*, 4th ed. Elsevier Ltd, 2017. doi: 10.1016/B978-0-08-100270-4.00001-9.

[7] M. K. Banerjee, *Fundamentals of Heat Treating Metals and Alloys*, vol. 2–3. Elsevier Ltd., 2016. doi: 10.1016/B978-0-12-803581-8.09185-2.

[8] L. Wang and J. G. Speer, “Quenching and Partitioning Steel Heat Treatment,” *Metallogr. Microstruct. Anal.*, vol. 2, no. 4, pp. 268–281, 2013, doi: 10.1007/s13632-013-0082-8.

[9] H. Elsayed *et al.*, “Resistance of Quench and Partitioned Steels Against Hydrogen Embrittlement,” *J. Mater. Eng. Perform.*, 2022, doi: 10.1007/s11665-022-07438-4.

[10] H. Pan *et al.*, “The effects of Q&P on microstructures and mechanical properties of a 18CrNiMo7-6 steel,” *Mater. Sci. Eng. A*, vol. 861, no. September, p. 144374, 2022, doi: 10.1016/j.msea.2022.144374.

[11] T. Nyyssönen, O. Oja, P. Jussila, A. Saastamoinen, M. Somani, and P. Peura, “Quenching and Partitioning of Multiphase Aluminum-Added Steels,” *Metals (Basel).*, vol. 9, no. 3, p. 373, 2019, doi: 10.3390/met9030373.

[12] M. Madrid, C. J. Van Tyne, S. Sriram, E. J. Pavlina, J. Hu, and K. D. Clarke, “Hole expansion ratio in intercritically annealed QP 980/1180 steel grades as a function of testing condition,” *IOP Conf. Ser. Mater. Sci. Eng.*, vol. 418, no. 1, 2018, doi: 10.1088/1757-899X/418/1/012083.

[13] S. Louhenkilpi, *Continuous Casting of Steel*, vol. 3. Elsevier Ltd., 2014. doi: 10.1016/B978-0-08-096988-6.00007-9.

[14] B. G. Thomas, “Continuous Casting: Complex Models,” in *Encyclopedia of Materials: Science and Technology*, 2001. doi: 10.1016/b0-08-043152-6/00285-0.

[15] A. Nicholas Grundy, S. Münch, S. Feldhaus, and J. Bratberg, “Continuous Casting of High Carbon Steel: How Does Hard Cooling Influence Solidification, Micro - And Macro Segregation?,” *IOP Conf. Ser. Mater. Sci. Eng.*, vol. 529, no. 1, 2019, doi: 10.1088/1757-899X/529/1/012069.

[16] M. C. Theyssier, *Manufacturing of advanced high-strength steels (AHSS)*. Elsevier Ltd, 2015. doi: 10.1016/B978-0-85709-436-0.00003-5.

[17] C. Beckermann, “Macrosegregation,” in *Encyclopedia of Materials: Science and Technology*, 2001. doi: 10.1016/b0-08-043152-6/00824-x.

[18] K. H. J. Buschow *et al.*, “Encyclopedia of Materials: Science and Technology,” in *Encyclopedia of Materials*, 2001, pp. 4733–4739. doi: 10.1016/B0-08-043152-6/00824-X.

[19] I.V.Samarasekera, “HOT ROLLING.,” in *Encyclopedia of Materials: Science and Technology*, vol. 2nd, 2001, pp. 3836–3843. doi: 10.1016/b0-08-043152-6/00683-5.

[20] C. Zheng, N. Xiao, D. Li, and Y. Li, “Microstructure prediction of the austenite recrystallization during multi-pass steel strip hot rolling: A cellular automaton modeling,” *Comput. Mater. Sci.*, vol. 44, no. 2, pp. 507–514, 2008, doi: 10.1016/j.commatsci.2008.04.010.

[21] Z. Y. Jiang, H. T. Zhu, and A. K. Tieu, “Mechanics of roll edge contact in cold rolling of thin strip,” *Int. J. Mech. Sci.*, vol. 48, no. 7, pp. 697–706, 2006, doi: 10.1016/j.ijmecsci.2006.01.017.

[22] P. Kusakin, A. Belyakov, C. Haase, R. Kaibyshev, and D. A. Molodov, “Microstructure evolution and strengthening mechanisms of Fe-23Mn-0.3C-1.5Al TWIP steel during cold rolling,” *Mater. Sci. Eng. A*, vol. 617, pp. 52–60, 2014, doi: 10.1016/j.msea.2014.08.051.

[23] H. Abe and S. Satoh, “Progress of continuous annealing technology for cold rolled sheet steels and associated product development,” *Kawasaki steel Tech. Rep.*, vol. 22, no. May, pp. 48–56, 1990, [Online]. Available: file://ce/rd_organisation/PTA-MAD/Common/10 Literature/2010/Abe (1990) # Progress of continuous annealing technology for cold rolled sheet steels and associated product development.pdf

[24] W. Callister and D. Rethwisch, *Materials Science and Engineering*, 8th Edt. John Wiley & Sons, 2011.

[25] Ll. Kacar and F. Ozturk, “ROLL FORMING APPLICATIONS FOR AUTOMOTIVE INDUSTRY,” 2014, no. May, pp. 1–6. [Online]. Available: https://www.researchgate.net/publication/282567993_ROLL_FORMING_APPLICATIONS_FOR_AUTOMOTIVE_INDUSTRY

[26] G. T. Halmos, *Roll Forming Handbook*, 1st ed., vol. 1. CRC Press, 2005. doi: doi.org/10.1201/9781420030693.

[27] M. Weiss, B. Abeyrathna, B. Rolfe, A. Abee, and H. Wolfkamp, “Effect of coil set on shape defects in roll forming steel strip,” *J. Manuf. Process.*, vol. 25,

pp. 8–15, 2017, doi: 10.1016/j.jmapro.2016.10.005.

[28] B. Shirani Bidabadi, H. Moslemi Naeini, and R. Azizi Tafti, “Experimental and numerical study of required torque in the cold roll forming of symmetrical channel sections,” *J. Manuf. Process.*, vol. 27, pp. 63–75, 2017, doi: 10.1016/j.jmapro.2017.04.026.

[29] W. gi Cha and N. Kim, “Study on twisting and bowing of roll formed products made of high strength steel,” *Int. J. Precis. Eng. Manuf.*, vol. 14, no. 9, pp. 1527–1533, 2013, doi: 10.1007/s12541-013-0206-8.

[30] J. H. Wiebenga, M. Weiss, B. Rolfe, and A. H. Van Den Boogaard, “Product defect compensation by robust optimization of a cold roll forming process,” *J. Mater. Process. Technol.*, vol. 213, no. 6, pp. 978–986, 2013, doi: 10.1016/j.jmatprotec.2013.01.006.

[31] A. Abvabi, B. Rolfe, P. D. Hodgson, and M. Weiss, “The influence of residual stress on a roll forming process,” *Int. J. Mech. Sci.*, vol. 101–102, pp. 124–136, 2015, doi: 10.1016/j.ijmecsci.2015.08.004.

[32] X. Liu, J. Cao, X. Chai, J. Liu, R. Zhao, and N. Kong, “Investigation of forming parameters on springback for ultra high strength steel considering Young’s modulus variation in cold roll forming,” *J. Manuf. Process.*, vol. 29, pp. 289–297, 2017, doi: 10.1016/j.jmapro.2017.08.001.

[33] B. Abeyrathna, B. Rolfe, and M. Weiss, “The effect of process and geometric parameters on longitudinal edge strain and product defects in cold roll forming,” *Int. J. Adv. Manuf. Technol.*, vol. 92, no. 1–4, pp. 743–754, 2017, doi: 10.1007/s00170-017-0164-x.

[34] P. Efthymiadis *et al.*, “Revealing the mechanical and microstructural performance of multiphase steels during tensile, forming and flanging operations,” *Mater. Sci. Eng. A*, vol. 701, no. June, pp. 174–186, 2017, doi: 10.1016/j.msea.2017.06.056.

[35] “Advanced High-Strength Steels Application Guidelines Version 7.0,” *WorldAutoSteel*, 2021. www.ahssinsights.org (accessed Aug. 09, 2022).

[36] WorldAutoSteel, “ULSAB Overview Report,” 2015. Accessed: May 25, 2023. [Online]. Available: https://www.worldautosteel.org/downloads/ulsab-programme-report-downloads/

[37] R. KUZIAK, R. KAWALLA, and S. WAENGLER, “Advanced high strength steels for automotive industry,” *Arch. Civ. Mech. Eng.*, vol. 8, no. 2, pp. 103–117, 2008, doi: 10.1016/S1644-9665(12)60197-6.

[38] S. Keeler, M. Kimchi, and P. J. Mooney, “Advanced High-Strength Steels Apllication Guidelines Version 6.0,” no. September, p. 314, 2017, [Online]. Available: http://www.worldautosteel.org/download_files/AHSS Guidelines V6/00_AHSSGuidelines_V6_20170430.pdf

[39] A. P. Pierman, O. Bouaziz, T. Pardoen, P. J. Jacques, and L. Brassart, “The influence of microstructure and composition on the plastic behaviour of

dual-phase steels," *Acta Mater.*, vol. 73, pp. 298–311, 2014, doi: 10.1016/j.actamat.2014.04.015.

[40] Q. Lai *et al.*, "Influence of martensite volume fraction and hardness on the plastic behavior of dual-phase steels: Experiments and micromechanical modeling," *Int. J. Plast.*, vol. 80, pp. 187–203, 2016, doi: 10.1016/j.ijplas.2015.09.006.

[41] H. Mirzadeh, M. Alibeyki, and M. Najafi, "Unraveling the Initial Microstructure Effects on Mechanical Properties and Work-Hardening Capacity of Dual-Phase Steel," *Metall. Mater. Trans. A Phys. Metall. Mater. Sci.*, vol. 48, no. 10, pp. 4565–4573, 2017, doi: 10.1007/s11661-017-4246-z.

[42] M. Papa Rao, V. Subramanya Sarma, and S. Sankaran, "Microstructure and Mechanical Properties of V-Nb Microalloyed Ultrafine-Grained Dual-Phase Steels Processed Through Severe Cold Rolling and Intercritical Annealing," *Metall. Mater. Trans. A Phys. Metall. Mater. Sci.*, vol. 48, no. 3, pp. 1176–1188, 2017, doi: 10.1007/s11661-016-3889-5.

[43] J. Zhao and Z. Jiang, "Thermomechanical processing of advanced high strength steels," *Prog. Mater. Sci.*, vol. 94, pp. 174–242, 2018, doi: 10.1016/j.pmatsci.2018.01.006.

[44] H. Bhadeshia and R. Honeycombe, *Solutes that Substitute for Iron*, 4th ed. Elsevier Ltd, 2017. doi: 10.1016/B978-0-08-100270-4.00004-4.

[45] H. Bhadeshia and R. Honeycombe, *Strengthening of Iron and Its Alloys*, 4th ed. Elsevier Ltd, 2017. doi: 10.1016/B978-0-08-100270-4.00002-0.

[46] A. Knaislová, D. Rudomilova, P. Novák, T. Prošek, A. Michalcová, and P. Beran, "Critical assessment of techniques for the description of the phase composition of advancedv high-strength steels," *Materials (Basel).*, vol. 12, no. 24, pp. 1–14, 2019, doi: 10.3390/MA12244033.

[47] K. Sugimoto and M. Mukherjee, *TRIP aided and complex phase steels*. Elsevier Ltd, 2016. doi: 10.1016/B978-0-08-100638-2.00008-0.

[48] A. Karelova, C. Krempaszky, E. Werner, P. Tsipouridis, T. Hebesberger, and A. Pichler, "Hole Expansion of Dual-phase and Complex-phase AHS Steels - Effect of Edge Conditions," *Steel Res. Int.*, vol. 80, pp. 71–77, 2009, doi: 10.2374/SRI08SP110.

[49] Y. jun Zhao, X. ping Ren, Z. liu Hu, Z. ping Xiong, J. min Zeng, and B. yu Hou, "Effect of tempering on microstructure and mechanical properties of 3Mn-Si-Ni martensitic steel," *Mater. Sci. Eng. A*, vol. 711, no. November 2017, pp. 397–404, 2018, doi: 10.1016/j.msea.2017.11.037.

[50] L. Tosal-Martínez, L. Cretteur, O. Moriau, and A. I. Koruk, "Characterization of cold rolled TRIP steels for structural crash-relevant applications in the automotive industry," *SAE Tech. Pap.*, vol. 111, no. 2002, pp. 927–934, 2002, doi: 10.4271/2002-01-2068.

[51] S. Oliver, T. B. Jones, and G. Fourlaris, "Dual phase versus TRIP strip steels:

Comparison of dynamic properties for automotive crash performance," *Mater. Sci. Technol.*, vol. 23, no. 4, pp. 423–431, 2007, doi: 10.1179/174328407X168937.

[52] S. Oliver, T. B. Jones, and G. Fourlaris, "Dual phase versus TRIP strip steels: Microstructural changes as a consequence of quasi-static and dynamic tensile testing," *Mater. Charact.*, vol. 58, no. 4, pp. 390–400, 2007, doi: 10.1016/j.matchar.2006.07.004.

[53] P. J. Jacques, E. Girault, a. Mertens, B. Verlinden, J. Van Humbeeck, and F. Delannay, "The Developments of Cold-rolled TRIP-assisted Multiphase Steels. Al-alloyed TRIP-assisted Multiphase Steels.," *ISIJ Int.*, vol. 41, no. 9, pp. 1068–1074, 2001, doi: 10.2355/isijinternational.41.1068.

[54] K. G. Chin *et al.*, "Effects of Al addition on deformation and fracture mechanisms in two high manganese TWIP steels," *Mater. Sci. Eng. A*, vol. 528, no. 6, pp. 2922–2928, 2011, doi: 10.1016/j.msea.2010.12.085.

[55] S. Hong *et al.*, "Effects of inclusions on delayed fracture properties of three twinning induced plasticity (TWIP) steels," *Metall. Mater. Trans. A Phys. Metall. Mater. Sci.*, vol. 44, no. 2, pp. 776–786, 2013, doi: 10.1007/s11661-012-1472-2.

[56] M. Madivala, A. Schwedt, S. L. Wong, F. Roters, U. Prahl, and W. Bleck, "Temperature dependent strain hardening and fracture behavior of TWIP steel," *Int. J. Plast.*, vol. 104, no. February, pp. 80–103, 2018, doi: 10.1016/j.ijplas.2018.02.001.

[57] T. Dieudonné *et al.*, "Role of copper and aluminum additions on the hydrogen embrittlement susceptibility of austenitic Fe-Mn-C TWIP steels," *Corros. Sci.*, vol. 82, pp. 218–226, 2014, doi: 10.1016/j.corsci.2014.01.022.

[58] S. Hong *et al.*, "Serration phenomena occurring during tensile tests of three high-manganese twinning-induced plasticity (TWIP) steels," *Metall. Mater. Trans. A Phys. Metall. Mater. Sci.*, vol. 45, no. 2, pp. 633–646, 2014, doi: 10.1007/s11661-013-2007-1.

[59] Y. Bai, Y. Momotani, M. C. Chen, A. Shibata, and N. Tsuji, "Effect of grain refinement on hydrogen embrittlement behaviors of high-Mn TWIP steel," *Mater. Sci. Eng. A*, vol. 651, pp. 935–944, 2016, doi: 10.1016/j.msea.2015.11.017.

[60] I. J. Park, S. min Lee, H. hee Jeon, and Y. K. Lee, "The advantage of grain refinement in the hydrogen embrittlement of Fe-18Mn-0.6C twinning-induced plasticity steel," *Corros. Sci.*, vol. 93, pp. 63–69, 2015, doi: 10.1016/j.corsci.2015.01.012.

[61] D. K. Matlock, J. G. Speer, E. De Moor, and P. J. Gibbs, "Recent developments in advanced high strength sheet steels for automotive applications: an overview," *Jestech*, vol. 15, no. 1, pp. 1–12, 2012.

[62] N. Zhong, X. D. Wang, L. Wang, and Y. H. Rong, "Enhancement of the

mechanical properties of a Nb-microalloyed advanced high-strength steel treated by quenching-partitioning-tempering process," *Mater. Sci. Eng. A*, vol. 506, no. 1–2, pp. 111–116, 2009, doi: 10.1016/j.msea.2008.11.014.

[63] C. B. Finfrock, A. J. Clarke, G. A. Thomas, and K. D. Clarke, "Austenite Stability and Strain Hardening in C-Mn-Si Quenching and Partitioning Steels," *Metall. Mater. Trans. A Phys. Metall. Mater. Sci.*, vol. 51, no. 5, pp. 2025–2034, 2020, doi: 10.1007/s11661-020-05666-8.

[64] SSAB, "Docol 600DH," 2022. https://www.ssab.com/en/brands-and-products/docol/automotive-steel-grades/dual-phase-steel/high-formability/docol-600dh (accessed May 28, 2023).

[65] SSAB, "Docol 800DH," 2022. https://www.ssab.com/en/brands-and-products/docol/automotive-steel-grades/dual-phase-steel/high-formability/docol-800dh (accessed May 28, 2023).

[66] SSAB, "Preliminary Docol 1000DH," 2022. https://www.ssab.com/en/brands-and-products/docol/automotive-steel-grades/dual-phase-steel/high-formability (accessed May 28, 2023).

[67] M. J. Kähkönen, E. De Moor, J. Speer, and G. Thomas, "Carbon and Manganese Effects on Quenching and Partitioning Response of CMnSi-Steels," *SAE Int. J. Mater. Manuf.*, vol. 8, no. 2, pp. 419–424, 2015, doi: 10.4271/2015-01-0530.

[68] Y. Toji, G. Miyamoto, and D. Raabe, "Carbon partitioning during quenching and partitioning heat treatment accompanied by carbide precipitation," *Acta Mater.*, vol. 86, pp. 137–147, 2015, doi: 10.1016/j.actamat.2014.11.049.

[69] G. Thomas, E. De Moor, and J. G. Speer, "Tensile properties obtained by Q&P processing of Mn-Ni steels with room temperature quench temperatures," in *Proceedings of the international symposium on new developments in advanced high-strength sheet steels*, 2013, pp. 23–27.

[70] M. J. Santofimia, T. Nguyen-Minh, L. Zhao, R. Petrov, I. Sabirov, and J. Sietsma, "New low carbon Q&P steels containing film-like intercritical ferrite," *Mater. Sci. Eng. A*, vol. 527, no. 23, pp. 6429–6439, 2010, doi: 10.1016/j.msea.2010.06.083.

[71] Y. Toji, H. Matsuda, M. Herbig, P. P. Choi, and D. Raabe, "Atomic-scale analysis of carbon partitioning between martensite and austenite by atom probe tomography and correlative transmission electron microscopy," *Acta Mater.*, vol. 65, pp. 215–228, 2014, doi: 10.1016/j.actamat.2013.10.064.

[72] D. De Knijf, C. Föjer, L. A. I. Kestens, and R. Petrov, "Factors influencing the austenite stability during tensile testing of Quenching and Partitioning steel determined via in-situ Electron Backscatter Diffraction," *Mater. Sci. Eng. A*, vol. 638, pp. 219–227, 2015, doi: 10.1016/j.msea.2015.04.075.

[73] D. De Knijf, E. P. Da Silva, C. Föjer, and R. Petrov, "Study of heat treatment parameters and kinetics of quenching and partitioning cycles," *Mater. Sci.*

Technol. (United Kingdom), vol. 31, no. 7, pp. 817–828, 2015, doi: 10.1179/1743284714Y.0000000710.

[74] E. J. Seo, L. Cho, and B. C. De Cooman, “Application of Quenching and Partitioning Processing to Medium Mn Steel,” *Metall. Mater. Trans. A Phys. Metall. Mater. Sci.*, vol. 46, no. 1, pp. 27–31, 2015, doi: 10.1007/s11661-014-2657-7.

[75] V. L. Arlazarov, O. A. Slavin, V. V. Farsobina, and A. G. Khovanskii, “The search for the optimal position during the comparison of digitized images,” *Sci. Tech. Inf. Process.*, vol. 41, no. 5, pp. 293–301, 2014, doi: 10.3103/S0147688214050013.

[76] I. de Diego-Calderón *et al.*, “Global and local deformation behavior and mechanical properties of individual phases in a quenched and partitioned steel,” *Mater. Sci. Eng. A*, vol. 630, pp. 27–35, 2015, doi: 10.1016/j.msea.2015.01.077.

[77] M. Cheng, H. W. Song, X. Li, S. H. Zhang, M. Cheng, and T. Lin, “Effects of quenching and partitioning process on mechanical properties of a hot-stamping steel,” *Mater. Sci. Forum*, vol. 788, pp. 340–345, 2014, doi: 10.4028/www.scientific.net/MSF.788.340.

[78] H. Y. Li, X. W. Lu, W. J. Li, and X. J. Jin, “Microstructure and mechanical properties of an Ultrahigh-Strength 40SiMnNiCr steel during the one-step quenching and partitioning process,” *Metall. Mater. Trans. A Phys. Metall. Mater. Sci.*, vol. 41, no. 5, pp. 1284–1300, 2010, doi: 10.1007/s11661-010-0184-8.

[79] B. Chen *et al.*, “A study of the optimum quenching temperature of steels with various hot rolling microstructures after cold rolling, quenching and partitioning treatment,” *Metals (Basel).*, vol. 8, no. 8, 2018, doi: 10.3390/met8080579.

[80] L. Liu, B. B. He, G. J. Cheng, H. W. Yen, and M. X. Huang, “Optimum properties of quenching and partitioning steels achieved by balancing fraction and stability of retained austenite,” *Scr. Mater.*, vol. 150, pp. 1–6, 2018, doi: 10.1016/j.scriptamat.2018.02.035.

[81] E. J. Seo, L. Cho, J. K. Kim, J. Mola, L. Zhao, and B. C. De Cooman, “Constituent-specific properties in quenching and partitioning (Q&P) processed steel,” *Mater. Sci. Eng. A*, vol. 740–741, no. August 2018, pp. 439–444, 2019, doi: 10.1016/j.msea.2018.10.082.

[82] Z. Xiong, P. J. Jacques, A. Perlade, and T. Pardoen, “Ductile and intergranular brittle fracture in a two-step quenching and partitioning steel,” *Scr. Mater.*, vol. 157, pp. 6–9, 2018, doi: 10.1016/j.scriptamat.2018.07.030.

[83] H. Jirková, L. Kučerová, and B. Mašek, “The Effect of Chromium on Microstructure Development During Q-P Process,” *Mater. Today Proc.*, 2015, doi: 10.1016/j.matpr.2015.07.362.

[84] L. Kaufman and H. Nessor, “Coupled phase diagrams and thermochemical data for transition metal binary systems — V,” *Calphad Comput. Coupling Phase Diagrams Thermochem.*, vol. 2, no. 1, pp. 55–80, 1978, doi: doi.org/10.1016/0364-5916(78)90005-6.

[85] P. J. Spencer, “A brief history of CALPHAD,” *Calphad Comput. Coupling Phase Diagrams Thermochem.*, vol. 32, no. 1, pp. 1–8, 2008, doi: 10.1016/j.calphad.2007.10.001.

[86] S. N and A. . Miodownik, *CALPHAD - Calculation of Phase Diagrams*, vol. 1. Pergamon Materials, 1998. doi: 10.1016/s1470-1804(98)80034-5.

[87] A. Borgenstam, A. Engstro, L. Ho Lund, and J. A. Ren, “DICTRA, a Tool for Simulation of Diffusional Transformations in Alloys,” *J. phase equilibria*, vol. 21, no. 3, pp. 269–280, 2000, doi: doi.org/10.1361/105497100770340057.

[88] ThermoCalc, “Thermo-Calc,” 2014. https://thermocalc.com/wp-content/uploads/Brochures_and_Flyers/Current/thermo-calc-a4-web-1.pdf (accessed Sep. 04, 2022).

[89] ThermoCalc, “Diffusion Module (DICTRA),” *Thermo-Calc Software*, 2019. https://www.thermocalc.com/products-services/software/diffusion-module-(dictra)/ (accessed Sep. 04, 2022).

[90] D. Den Ouden, L. Zhao, C. Vuik, J. Sietsma, and F. J. Vermolen, “Modelling precipitate nucleation and growth with multiple precipitate species under isothermal conditions: Formulation and analysis,” *Comput. Mater. Sci.*, vol. 79, pp. 933–943, 2013, doi: 10.1016/j.commatsci.2013.07.047.

[91] J. . Langer, “Statistical theory of the decay of metastable states,” in *Annals of Physics*, vol. 54, no. 2, 1969, pp. 258–275. doi: doi.org/10.1016/0003-4916(69)90153-5.

[92] Q. Chen, K. Wu, G. Sterner, and P. Mason, “Modeling Precipitation Kinetics During Heat Treatment with Calphad-Based Tools,” *J. Mater. Eng. Perform.*, vol. 23, no. 12, pp. 4193–4196, 2014, doi: 10.1007/s11665-014-1255-6.

[93] O. Prat, J. García, D. Rojas, J. P. Sanhueza, and C. Camurri, “Study of nucleation, growth and coarsening of precipitates in a novel 9%Cr heat resistant steel: Experimental and modeling,” *Mater. Chem. Phys.*, vol. 143, no. 2, pp. 754–764, 2014, doi: 10.1016/j.matchemphys.2013.10.010.

[94] ThermoCalc, “TC PRISMA.” https://thermocalc.com/products/add-on-modules/precipitation-module-tc-prisma/ (accessed Sep. 04, 2022).

[95] Z. Guo *et al.*, “Introduction of materials modelling into processing simulation,” *Mater. Sci. Forum*, vol. 762, pp. 266–276, 2013, doi: 10.4028/www.scientific.net/MSF.762.266.

[96] N. Saunders, Z. Guo, X. Li, A. P. Miodownik, and J. P. Schillé, “Using JMatPro to model materials properties and behavior,” *Jom*, vol. 55, no. 12, pp. 60–65, 2003, doi: 10.1007/s11837-003-0013-2.

[97] W. Callister and D. Rethwisch, “Materials Science and Engineering,” 8th ed., John Wiley & Sons, 2011, pp. 356–370.

[98] A. Soult, “Spontaneous Reactions and Free Energy,” in *UK: CHE 103 - Chemistry for Allied Health*, vol. 2, University of Kentucky: CK-12 Foundation, 2019, pp. 1–3.

[99] M. J. Moran, H. N. Shapiro, D. D. Boettner, and M. B. Bailey, “Fundamentals of Engineering Thermodynamics,” in *Wiley*, 8th ed., vol. 8, no. 1, L. Ratts, Ed. Don Fowley, 2014, pp. 716–717. doi: 10.7227/ijmee.29.1.2.

[100] Petrucci, “Spontaneous Change: Entropy and Gibbs Energy,” *General Chemistry*, 2021. https://chem.libretexts.org/Bookshelves/General_Chemistry/Map%3A_General_Chemistry_(Petrucci_et_al.) (accessed May 28, 2023).

[101] J. Ågren, *CALPHAD - An Approach to Predict Microstructural Stability*, vol. 4. Elsevier Ltd., 2021. doi: 10.1016/B978-0-12-819726-4.00042-9.

[102] G. . Dantzig, “Linear Programming,” *Oper. Res.*, vol. 50, no. 1, pp. 42–47, 2002, doi: 10.1201/9780429354649-7.

[103] G. . Gulliver, “The quantitative effect of rapid cooling upon the constitution of binary alloys,” *J Inst Met*, vol. 13, pp. 263–291, 1915.

[104] P. Schaffnit, C. Stallybrass, J. Konrad, F. Stein, and M. Weinberg, “A Scheil-Gulliver model dedicated to the solidification of steel,” *Calphad Comput. Coupling Phase Diagrams Thermochem.*, vol. 48, pp. 184–188, 2015, doi: 10.1016/j.calphad.2015.01.002.

[105] E. Scheil, “Remarks on layer crystal formation,” *J. Mater. Res.*, pp. 70–72, 1942.

[106] T. Koshikawa, C. A. Gandin, M. Bellet, H. Yamamura, and M. Bobadilla, “Computation of phase transformation paths in steels by a combination of the partial- and para-equilibrium thermodynamic approximations,” *ISIJ Int.*, vol. 54, no. 6, pp. 1274–1282, 2014, doi: 10.2355/isijinternational.54.1274.

[107] N. Saunders and A. Midownik, “Chapter 11 Combining Thermodynamics and Kinetics,” in *CALPHAD - A Comprehensive Guide*, vol. 1, 1998, pp. 411–461. doi: 10.1016/S1470-1804(98)80031-X.

[108] Q. Chen and B. Sundman, “Computation of partial equilibrium solidification with complete interstitial and negligible substitutional solute back diffusion,” *Mater. Trans.*, vol. 43, no. 3, pp. 551–559, 2002, doi: 10.2320/matertrans.43.551.

[109] F. Mignard, “TATA UK CAPL Manual - Furnace Description Part 1.” p. 26, 1997.

[110] Q. Li, X. Huang, and W. Huang, “Microstructure and mechanical properties of a medium-carbon bainitic steel by a novel quenching and dynamic partitioning (Q-DP) process,” *Mater. Sci. Eng. A*, vol. 662, pp. 129–135, 2016,

doi: 10.1016/j.msea.2016.03.042.

[111] J. Speer, D. K. Matlock, B. C. De Cooman, and J. G. Schroth, “Carbon partitioning into austenite after martensite transformation,” *Acta Mater.*, vol. 51, pp. 2611–2622, 2003, doi: 10.1016/S1359-6454(03)00059-4.

[112] J. G. Speer, “Phase transformations in quenched and partitioned steels 8,” in *Phase transformations in steels: Volume 2: Diffusionless transformations, high strength steels, modelling and advanced analytical techniques*, 2012. doi: 10.1533/9780857096111.2.247.

[113] B. L. Ennis *et al.*, “Metastable austenite driven work-hardening behaviour in a TRIP-assisted dual phase steel,” *Int. J. Plast.*, vol. 88, pp. 126–139, 2017, doi: 10.1016/j.ijplas.2016.10.005.

[114] A. Borgenstam and M. Hillert, *Kinetics of bainite transformation in steels*. Woodhead Publishing Limited, 2012. doi: 10.1533/9780857096104.3.468.

[115] S. B. Singh, “Mechanisms of bainite transformation in steels 10,” in *Phase transformations in steels: Volume 1: Fundamentals and diffusion-controlled transformations*, 2012, pp. 385–416. doi: 10.1533/9780857096104.3.385.

[116] J. C. Zhang, H. S. Di, Y. G. Deng, S. C. Li, and R. D. K. Misra, “Microstructure and mechanical property relationship in an ultrahigh strength 980MPa grade high-Al low-Si dual phase steel,” *Mater. Sci. Eng. A*, vol. 645, pp. 232–240, 2015, doi: 10.1016/j.msea.2015.08.016.

[117] S. S. Babu, “Application of synchrotron and neutron scattering techniques for tracking phase transformations in steels 19,” in *Phase transformations in steels: Volume 2: Diffusionless transformations, high strength steels, modelling and advanced analytical techniques*, no. 2007, 2012, pp. 588–633. doi: 10.1533/9780857096111.4.588.

[118] F. . Cabellero, “Carbide-free bainite in steels 12,” in *Phase transformations in steels: Volume 1: Fundamentals and diffusion-controlled transformations*, 2012, pp. 436–467. doi: 10.1533/9780857096104.3.436.

[119] S. J. Kim, C. G. Lee, I. Choi, and S. Lee, “Effects of heat treatment and alloying elements on the microstructures and mechanical properties of 0.15 wt pct C transformation-induced plasticity-aided cold-rolled steel sheets,” *Metall. Mater. Trans. A Phys. Metall. Mater. Sci.*, vol. 32, no. 3, pp. 505–514, 2001, doi: 10.1007/s11661-001-0067-0.

[120] M. Zhou, G. Xu, J. Tian, H. Hu, and Q. Yuan, “Bainitic Transformation and Properties of Low Carbon Carbide-Free Bainitic Steels with Cr Addition,” *Metals (Basel).*, vol. 7, no. 7, p. 263, 2017, doi: 10.3390/met7070263.

[121] H. Mohrbacher, “Metallurgical optimization of martensitic steel sheet for automotive applications,” 2010, Accessed: May 29, 2019. [Online]. Available: https://www.niobelcon.com/NiobelCon/resources/Metallurgical-optimization-of-martensitic-steel-sheet-for-automotive-applications.pdf

[122] BSI, “BSI Standards Publication Metallic materials — Tensile testing Part 1 :

Method of test at room temperature (ISO 6892-1:2016)," 2016. doi: 10.3403/30268532.

[123] ASTM, "ASTM E8 / E8M-21 Standard Test Methods for Tension Testing of Metallic Materials," 2021. doi: 10.1520/E0008_E0008M-21.

[124] BSI, "BS ISO EN Metallic materials - Vickers hardness test - Part 1: Test method," 2018. doi: doi.org/10.3403/BSENISO6507.

[125] ISO, "BS EN ISO 14577-1-2015 - Metallic materials. Instrumented indentation test for hardness and materials parameters.," 2015. doi: doi.org/10.3403/BSENISO14577.

[126] BSI, "BS ISO 16630-2017 Metallic materials - Sheet and Strip - Hole expanding test," 2017.

[127] S. K. Paul, "A critical review on hole expansion ratio," *Materialia*, vol. 9, no. December 2019, p. 100566, 2020, doi: 10.1016/j.mtla.2019.100566.

[128] J. L. Dossett and H. E. Boyer, "Fundamentals of the Heat Treating of Steel," in *Practical Heat Treating*, 2nd ed., 2006, pp. 1–18. doi: 10.1361/pht2006p009.

[129] Y. Wen *et al.*, "Influences of manganese content and heat treatment on mechanical properties of precipitation-strengthened steels," *Mater. Sci. Eng. A*, vol. 837, no. October 2021, p. 142724, 2022, doi: 10.1016/j.msea.2022.142724.

[130] M. C. Pantilimon *et al.*, "Comparative Evaluation of the TRIP Effect in Steels with Different Contents of Mn and Al," *Metals (Basel).*, vol. 12, no. 3, 2022, doi: 10.3390/met12030443.

[131] A. Grajcar, R. Kuziak, and W. Zalecki, "Third generation of AHSS with increased fraction of retained austenite for the automotive industry," *Arch. Civ. Mech. Eng.*, vol. 12, no. 3, pp. 334–341, 2012, doi: 10.1016/j.acme.2012.06.011.

[132] X. Chen *et al.*, "Effects of niobium alloying on microstructure, toughness and wear resistance of austempered ductile iron," *Mater. Sci. Eng. A*, 2019, doi: 10.1016/j.msea.2019.05.100.

[133] K. Hausmann, D. Krizan, K. Spiradek-Hahn, A. Pichler, and E. Werner, "The influence of Nb on transformation behavior and mechanical properties of TRIP-assisted bainitic-ferritic sheet steels," *Mater. Sci. Eng. A*, vol. 588, pp. 142–150, 2013, doi: 10.1016/j.msea.2013.08.023.

[134] S. J. Lee, J. S. Park, and Y. K. Lee, "Effect of austenite grain size on the transformation kinetics of upper and lower bainite in a low-alloy steel," *Scr. Mater.*, vol. 59, no. 1, pp. 87–90, 2008, doi: 10.1016/j.scriptamat.2008.02.036.

[135] L. Ryde, O. Lyytinen, P. Peura, M. Titova, Y. Vilander Granbom, and T. Hebesberger, *Cold-rolled complex-phase (CP) steel grades with optimised bendability, stretch-flangeability and anisotropy (CP-Steels)*. European

Commission, 2012. doi: data.europa.eu/doi/10.2777/97678.

[136] J. Herrnring, B. Sundman, P. Staron, and B. Klusemann, “Modeling precipitation kinetics for multi-phase and multi-component systems using particle size distributions via a moving grid technique,” *Acta Mater.*, vol. 215, p. 117053, 2021, doi: 10.1016/j.actamat.2021.117053.

[137] N. Saunders, Z. Guo, A. P. Miodownik, and J.-P. Schillé, “The Calculation of TTT and CCT diagrams for General Steels,” *JMatPro Softw. Lit.*, pp. 1–12, 2004.

[138] British Iron and Steel Research Association, *Atlas of Isothermal Transformation Diagrams in B.S. En Steels*, 2nd ed. Iron and Steel Institute, London, 1956.

[139] American Society for Metals, *Atlas of Isothermal Transformation and Cooling Transformation Diagrams*. American Society for Metals, 1977.

[140] R. K. Evans, *Steel Transformation Diagrams: Atlas of Continuous Cooling Transformation Diagrams for Engineering Steels*, 12th ed. Metal Science, 1978.

[141] E. Kozeschnik and H. K. D. H. Bhadeshia, “Influence of silicon on cementite precipitation in steels,” vol. 24, no. 3, pp. 343–348, 2008, doi: 10.1179/174328408X275973.

[142] I. Miettunen, S. Ghosh, M. C. Somani, S. Pallaspuro, and J. Kömi, “Competitive mechanisms occurring during quenching and partitioning of three silicon variants of 0.4 wt.% carbon steels,” *Journal of Materials Research and Technology*, vol. 11. pp. 1045–1060, 2021. doi: 10.1016/j.jmrt.2021.01.085.

[143] S. Das and A. Haldar, “Continuously cooled ultrafine bainitic steel with excellent strength-elongation combination,” *Metall. Mater. Trans. A Phys. Metall. Mater. Sci.*, vol. 45, no. 4, pp. 1844–1854, 2014, doi: 10.1007/s11661-013-2173-1.

[144] Sente Software Ltd, “Tempered Hardness of Martensitic Steels,” *JMatPro Softw. Lit.*, vol. 1, pp. 7–9, [Online]. Available: https://www.sentesoftware.co.uk/site-media/temperedhardness

[145] Sente Software Ltd, “Tempering of Steels,” *JMatPro Softw. Lit.*, pp. 1–8, 2012, [Online]. Available: http://jmatpro.ru/artikles/Tempering of Steels.pdf

[146] J. M. Tartaglia, “The effects of martensite content on the mechanical properties of quenched and tempered 0.2%C-Ni-Cr-Mo steels,” *J. Mater. Eng. Perform.*, vol. 19, no. 4, pp. 572–584, 2010, doi: 10.1007/s11665-009-9503-x.

[147] D. Farrugia, S. Brown, N. P. Lavery, C. Pleydell-Pearce, and C. Davis, “Rapid Alloy Prototyping for a range of strip related advanced steel grades,” *Procedia Manuf.*, vol. 50, no. 2019, pp. 784–790, 2020, doi: 10.1016/j.promfg.2020.08.141.

[148] F. Huang, Q. Chen, H. Ding, Y. Wang, X. Mou, and J. Chen, “Automotive steel with a high product of strength and elongation used for cold and hot forming simultaneously,” *Materials (Basel).*, vol. 14, no. 5, pp. 1–12, 2021, doi: 10.3390/ma14051121.

[149] P. Landgraf, P. Birnbaum, E. Meza-García, T. Grund, V. Kräusel, and T. Lampke, “Jominy End Quench Test of Martensitic Stainless Steel X30Cr13,” *Metals (Basel).*, vol. 11, no. 7, p. 1071, 2021, doi: 10.3390/met11071071.

[150] E. Ahmad, F. Karim, K. Saeed, T. Manzoor, and G. H. Zahid, “Effect of cold rolling and annealing on the grain refinement of low alloy steel,” *IOP Conf. Ser. Mater. Sci. Eng.*, vol. 60, no. 1, pp. 0–8, 2014, doi: 10.1088/1757-899X/60/1/012029.

[151] Z. Yanushkevich, S. V. Dobatkin, A. Belyakov, and R. Kaibyshev, “Hall-Petch relationship for austenitic stainless steels processed by large strain warm rolling,” *Acta Mater.*, vol. 136, pp. 39–48, 2017, doi: 10.1016/j.actamat.2017.06.060.

[152] Tata Steel, “Cold-rolled DP800 Data Sheet,” 2016. www.tatasteeleurope.com/automotive (accessed May 25, 2023).

[153] Tata Steel, “Cold-rolled DP1000LY-UC High strength , high ductility , high formability,” 2016. www.tatasteeleurope.com/automotive (accessed May 25, 2023).

[154] Tata Steel, “Cold-rolled CP800-GI Highly bendable roll forming steel,” 2016. www.tatasteeleurope.com/automotive (accessed May 25, 2023).

[155] R. . Grange, C. . Hribal, and L. . Porter, “Hardness of tempered martensite in carbon and low-alloy steel,” *Metall. Trans. A*, vol. 8, pp. 1775–1785, 1977, doi: doi.org/10.1007/BF02646882.

[156] D. T. Pierce *et al.*, “Microstructural evolution during quenching and partitioning of 0.2C-1.5Mn-1.3Si steels with Cr or Ni additions,” *Acta Mater.*, vol. 151, pp. 454–469, 2018, doi: 10.1016/j.actamat.2018.03.007.

[157] J. G. Speer, F. C. Rizzo, D. K. Matlock, and D. V Edmonds, “The ‘ Quenching and Partitioning ’ Process : Background and Recent Progress 2 . Background and Q & P Fundamentals,” *Mater. Res.*, vol. 8, no. 4, pp. 417–423, 2005, doi: doi.org/10.1590/S1516-14392005000400010.

[158] E. De Moor, S. Lacroix, L. Samek, J. Penning, and J. G. Speer, “Dilatometric Study of the Quench and Partitioning Process,” in *Proceedings of the 3rd International Conference on Advanced Structural Steels.*, 2006, no. 1, pp. 73–83. doi: doi.org/1854/5301.

[159] R. R. de Avillez, A. L. V da Costa e Silva, A. R. F. Martins, and F. C. Rizzo Assuncao, “The effect of alloying elements on constrained carbon equilibrium due to a quench and partition process,” *Zeitschrift fuer Met. Res. Adv. Tech.*, vol. 99, no. 11, pp. 1280–1284, 2008, doi: doi.org/10.3139/146.101764.

[160] N. Pathak, C. Butcher, M. J. Worswick, E. Bellhouse, and J. Gao, “Damage evolution in complex-phase and dual-phase steels during edge stretching,” *Materials (Basel).*, vol. 10, no. 4, pp. 1–29, 2017, doi: 10.3390/ma10040346.

[161] N. Pathak, C. Butcher, and M. Worswick, “Assessment of the Critical Parameters Influencing the Edge Stretchability of Advanced High-Strength Steel Sheet,” *J. Mater. Eng. Perform.*, vol. 25, no. 11, pp. 4919–4932, 2016, doi: 10.1007/s11665-016-2316-9.

[162] Z. Guo, N. Saunders, P. Miodownik, and J. P. Schille, “Modelling the strain-life relationship of commercial alloys,” in *Proceedings of CREEP8 Eighth International Conference on Creep and Fatigue at Elevated Temperatures*, 2007, pp. 281–287. doi: 10.1115/CREEP2007-26074.

[163] TATA, “Cold-rolled DP1000-GI,” 2016. http://www.tatasteeleurope.com/static_files/Downloads/Automotive/Data Sheets/Tata Steel AM - CR DP1000-GI - data sheet.EN.pdf (accessed May 27, 2023).

[164] BAOSTEEL, “BaoSteel Automotive Advanced High Strength Steel,” 2015. http://esales.baosteel.com/portal/download/manual/AHSS-Automotive-En.pdf (accessed May 25, 2023).

[165] X. Wu and Y. Zhu, “Heterogeneous materials: a new class of materials with unprecedented mechanical properties,” *Mater. Res. Lett.*, vol. 5, no. 8, pp. 527–532, 2017, doi: 10.1080/21663831.2017.1343208.

[166] S. A. H. Motaman, F. Roters, and C. Haase, “Anisotropic polycrystal plasticity due to microstructural heterogeneity: A multi-scale experimental and numerical study on additively manufactured metallic materials,” *Acta Mater.*, vol. 185, pp. 340–369, 2020, doi: 10.1016/j.actamat.2019.12.003.

[167] Y. Chang *et al.*, “Compositional heterogeneity in multiphase steels: Characterization and influence on local properties,” *Mater. Sci. Eng. A*, vol. 827, no. September, p. 142078, 2021, doi: 10.1016/j.msea.2021.142078.

[168] B. B. He, M. Wang, L. Liu, and M. X. Huang, “High-strength medium Mn quenching and partitioning steel with low yield ratio,” *Mater. Sci. Technol. (United Kingdom)*, vol. 35, no. 17, pp. 2109–2114, 2019, doi: 10.1080/02670836.2019.1566046.

[169] Y. Chang *et al.*, “Compositional heterogeneity in multiphase steels: Characterization and influence on local properties,” *Mater. Sci. Eng. A*, vol. 827, no. September, p. 142078, 2021, doi: 10.1016/j.msea.2021.142078.

[170] E. A. Ariza-Echeverri, M. Masoumi, A. S. Nishikawa, D. H. Mesa, A. E. Marquez-Rossy, and A. P. Tschiptschin, “Development of a new generation of quench and partitioning steels: Influence of processing parameters on texture, nanoindentation, and mechanical properties,” *Mater. Des.*, vol. 186, p. 108329, 2020, doi: 10.1016/j.matdes.2019.108329.

[171] F. Ozkan and A. Bach, “Future trends and challenges in using AHSS in body

structure," 2019. [Online]. Available: https://www.worldautosteel.org/projects/future-steel-vehicle/steel-eliminates-the-weight-gap-with-aluminium-for-car-bodies/

Appendix 1: C-Mn-Si - Initial Composition Exploration

Table 23: C-Mn-Si - Transformation temperatures and times.

							Bainitic Transformation Time (s)	
Alloying Content (Wt.%)	Composition	A1 (°C)	A3 (°C)	Bs (°C)	Ms (°C)	M90% (°C)	Tip of C Curve	Low Temperature
3.75	0.15C-2.2Mn-1.4Si	701	835	524	357	242	30	94
3.85	0.15C-2.3Mn-1.4Si	699	831	520	352	237	34	100
3.95	0.15C-2.4Mn-1.4Si	697	828	517	348	233	38	133
4.05	0.15C-2.5Mn-1.4Si	694	824	513	344	228	42	141
4.15	0.15C-2.6Mn-1.4Si	692	821	510	340	224	48	191
3.8	0.15C-2.2Mn-1.45Si	702	837	523	356	241	32	95
3.9	0.15C-2.3Mn-1.45Si	700	833	519	352	237	35	101
4	0.15C-2.4Mn-1.45Si	698	830	516	348	232	40	135
4.1	0.15C-2.5Mn-1.45Si	695	826	512	343	227	44	143
4.2	0.15C-2.6Mn-1.45Si	693	822	509	339	223	49	194
3.8	0.2C-2.2Mn-1.4Si	708	821	516	338	221	42	187
3.9	0.2C-2.3Mn-1.4Si	706	818	513	333	217	47	198
4	0.2C-2.4Mn-1.4Si	704	814	509	329	212	53	271
4.1	0.2C-2.5Mn-1.4Si	702	811	506	325	207	59	286
4	0.2C-2.35Mn-1.45Si	706	818	510	331	213	51	207
4.05	0.2C-2.4Mn-1.45Si	705	816	508	329	211	55	275
4.1	0.2C-2.45Mn-1.45Si	704	814	506	326	209	58	284
4.15	0.2C-2.5Mn-1.45Si	703	813	505	324	207	63	291

Step 1 - To determine the appropriate processing windows on CAPL for C-Mn-Si alloys, a series of simulations were carried out. Firstly, transformation temperatures and times were extracted from repeated TTT and CCT simulations. Compositions marked in green were found to be suitable for fitting within these windows.

Table 24: CCT point information.

Composition	Phase Formation at CR 10°C per Second
0.15C-2.4Mn-1.4Si	F-8.1%, B-77.47%, P-1.42%, M-13.01%
0.15C-2.5Mn-1.4Si	F-5.11%, B-74.85%, P-1.17%, M-18.87%
0.15C-2.6Mn-1.4Si	F-3.3%, B-71.21%, P-0.97%, M-24.53%
0.15C-2.4Mn-1.45Si	F-8.07%, B-76.22%, P-1.53%, M-14.18%
0.15C-2.5Mn-1.45Si	F-5.12%, B-73.38%, P-1.23%, M-20.28%
0.2C-2.4Mn-1.4Si	F-3.13%, B-64.32%, P-2.61%, M-29.94%
0.2C-2.5Mn-1.4Si	F-1.91%, B-58.96%, P-2.15%, M-36.98%

Step 2 - The second step involved gathering JMatPro point information from CCT simulations, which predicts the formation phases for different rates of cooling. A rate of 10°C/s was used, and compositions highlighted in this step showed lower proportions of ferrite and pearlite, even with a slower rate than that which will be used during CAPL simulations.

Table 25: Ferrite transformation times.

	Ferrite Transformation Time at 700°C (s)	
Composition	**1% Transformed**	**10% Transformed**
0.15C-2.5Mn-1.4Si	16.03	47.34
0.15C-2.6Mn-1.4Si	20.65	61.16
0.15C-2.5Mn-1.45Si	15.79	46.6
0.2C-2.5Mn-1.4Si	29.45	89.61

Step 3 - Next, four highlighted compositions from the previous step were reduced to the two final compositions. These were selected as the ferrite transformation times were longer, providing greater confidence that no ferrite formation would occur during the slow cool section on CAPL (CGJC).

Finally, the two selected compositions underwent further simulations, see sections on Martensite tempering (5.4.1), Jominy hardenability (5.4.2), ThermoCalc validation of alloys (5.5.2), and JMatPro property simulations (5.5.3). By carefully analysing the results of these simulations, it was possible to determine the optimal processing windows for C-Mn-Si alloys on CAPL.

Appendix 2: C-Mn-Si-Cr - Initial Composition Exploration

Table 26: C-Mn-Si-Cr - Transformation temperatures and times.

		Transformation Temperatures (°C)					Bainitic Transformation Time (s)	
Alloying Content	**Composition**	**A1**	**A3**	**Bs**	**Ms**	**M90%**	**Tip of C Curve**	**Low Temperature**
3.95	0.15C-2Mn-1.4Si-0.4Cr	718	837	523	358	344	44	136
4.05	0.15C-2Mn-1.4Si-0.5Cr	721	835	522	357	242	51	152
4.15	0.15C-2Mn-1.5Si-0.5Cr	723	839	519	355	241	54	156
4.35	0.15C-2.2Mn-1.5Si-0.5Cr	718	832	512	347	231	67	221
4.25	0.15C-2.2Mn-1.5Si-0.4Cr	715	833	514	348	233	59	199
4.4	0.2C-2.2Mn-1.5Si-0.5Cr	723	818	505	328	210	90	432
4.3	0.2C-2.2Mn-1.5Si-0.4Cr	721	819	507	329	212	80	392
4.2	0.2C-2.2Mn-1.4Si-0.4Cr	719	816	509	331	214	75	293
4	0.2C-2Mn-1.4Si-0.4Cr	723	823	516	339	223	60	261
4.1	0.2C-2Mn-1.4Si-0.5Cr	726	821	514	338	221	68	291
3.95	0.15C-2.3Mn-1.4Si-0.1Cr	702	830	518	351	235	40	114
4.05	0.15C-2.3Mn-1.4Si-0.2Cr	705	828	517	349	234	47	162
4.15	0.15C-2.3Mn-1.5Si-0.2Cr	707	832	514	348	232	50	167
4.25	0.15C-2.5Mn-1.4Si-0.2Cr	701	821	510	341	224	58	182
4.15	0.15C-2.5Mn-1.4Si-0.1Cr	698	823	511	342	226	50	161
4.25	0.15C-2.5Mn-1.5Si-0.1Cr	699	826	509	341	225	53	165
4.4	0.2C-2.5Mn-1.5Si-0.2Cr	709	812	500	320	202	85	373
4.3	0.2C-2.5Mn-1.5Si-0.1Cr	706	813	502	322	204	73	333
4.2	0.2C-2.5Mn-1.4Si-0.1Cr	705	810	504	323	205	69	325
4.1	0.2C-2.3Mn-1.5Si-0.1Cr	711	820	509	330	213	59	229
4	0.2C-2.3Mn-1.4Si-0.1Cr	709	816	511	332	215	55	224
4.2	0.2C-2.3Mn-1.5Si-0.2Cr	713	817	507	329	211	68	333
4.1	0.2C-2.3Mn-1.4Si-0.2Cr	712	815	509	330	213	63	352
4.05	0.15C-2.4Mn-1.4Si-0.1Cr	700	826	515	347	231	45	152
4.1	0.15C-2.4Mn-1.4Si-0.15Cr	702	826	514	346	230	48	162
4.12	0.15C-2.4Mn-1.47Si-0.1Cr	701	829	513	346	230	47	155
4.17	0.15C-2.4Mn-1.47Si-0.15Cr	703	828	512	345	229	52	165
4.37	0.15C-2.6Mn-1.47Si-0.15Cr	698	821	505	336	220	64	236
4.3	0.15C-2.6Mn-1.4Si-0.15Cr	697	819	507	337	221	61	232
4.32	0.15C-2.6Mn-1.47Si-0.1Cr	697	822	506	337	221	59	222
4.4	0.18C-2.6Mn-1.47Si-0.15Cr	703	813	501	325	207	77	344
4.35	0.18C-2.6Mn-1.47Si-0.1Cr	701	814	502	326	208	71	323
4.28	0.18C-2.6Mn-1.4Si-0.1Cr	700	812	503	327	209	69	317
4.08	0.18C-2.4Mn-1.4Si-0.1Cr	704	818	510	335	218	54	219
4.15	0.18C-2.4Mn-1.47Si-0.1Cr	705	821	509	334	217	57	223
4.13	0.18C-2.4Mn-1.4Si-0.15Cr	706	818	510	334	217	59	233

Step 1 - A series of simulations were carried out to determine the appropriate processing windows to achieve the desired microstructural evolution on CAPL for C-Mn-Si-Cr alloys. Firstly, transformation temperatures and times were extracted from repeated TTT and CCT simulations. Compositions marked in yellow were found to be suitable for fitting within these windows. In total, eight compositions were put forward for further analysis. The levels set for each element are shown in Table 27.

Table 27: Element levels for repeated TTT and CCT simulations.

	Element	1	2
A	C	0.15	0.2
B	Mn	2	2.2
C	Si	1.4	1.5
D	Cr	0.4	0.5
🟩			
	Element	1	2
A	C	0.15	0.2
B	Mn	2.3	2.5
C	Si	1.4	1.5
D	Cr	0.1	0.2
🟧			
	Element	1	2
A	C	0.15	0.18
B	Mn	2.4	2.6
C	Si	1.4	1.47
D	Cr	0.1	0.15

Step 2 - This step involved looking at both point information from simulated CCT diagrams and ferritic transformation times at 700°C from simulated TTT diagrams. Table 28 illustrates the predicted formation of phases and ferritic transformation times. It can be noted the one selected composition shows little ferrite formation, largest martensite fraction, even with a slow cooling rate and the longest ferrite transformation times at 700°C.

Table 28: Point information and ferritic transformation times.

			Ferrite Transformation Time at 700°C (s)	
Alloying Content	Composition	Phase Formation at CR 10°C per Second	1% Transformed	10% Transformed
4.25	0.15C-2.5Mn-1.4Si-0.2Cr	F-3.01%, B-61.69%, P-0.28%, M-35.01%	21.29	62.8
4.15	0.15C-2.5Mn-1.4Si-0.1Cr	F-3.91%, B-68.76%, P-0.49%, M-26.83%	18.64	55
4.25	0.15C-2.5Mn-1.5Si-0.1Cr	F-4.07%, B-65.46%, P-0.51%, M-29.96%	17.87	52.65
4.05	0.15C-2.4Mn-1.4Si-0.1Cr	F-6.06%, B-72.78%, P-0.59%, M-20.57%	14.37	42.29
4.37	0.15C-2.6Mn-1.47Si-0.15Cr	F-2.45%, B-57.11%, P-0.3%, M-40.14%	23.83	70.43
4.3	0.15C-2.6Mn-1.4Si-0.15Cr	F-2.28%, B-60.07%, P-0.29%, M-37.36%	24.86	73.56
4.32	0.15C-2.6Mn-1.47Si-0.1Cr	F-2.65%, B-61.49%, P-0.41%, M-35.46%	22.56	66.66
4.28	0.18C-2.6Mn-1.4Si-0.1Cr	F-1.4%, B-51.79%, P-0.54%, M-46.26%	33.24	100.05

Finally, similarly to the C-Mn-Si alloy, the chosen C-Mn-Si-Cr alloy will go through further simulations.

Appendix 3: C-Mn-Si-Mo - Initial Composition Exploration

Table 29: Element levels for repeated TTT and CCT simulations.

	Element	1	2
A	C	0.15	0.18
B	Mn	2.3	2.4
C	Si	1.4	1.47
D	Mo	0.2	0.24
	Element	1	2
A	C	0.15	
B	Mn	2.5	2.6
C	Si	1.4	1.47
D	Mo	0.22	0.24

Table 30: C-Mn-Si-Mo - Transformation temperatures and times.

		Transformation Temperatures (°C)					**Bainitic Transformation Time**	
Alloying Content (Wt.%)	**Composition**	**A1**	**A3**	**Bs**	**Ms**	**M90%**	**Tip of C Curve**	**Low Temperature**
4.05	0.15C-2.3Mn-1.4Si-0.2Mo	701	836	519	350	235	73	261
4.09	0.15C-2.3Mn-1.4Si-0.24Mo	701	836	518	350	234	82	290
4.16	0.15C-2.3Mn-1.47Si-0.24Mo	703	839	517	349	233	86	296
4.12	0.15C-2.3Mn-1.47Si-0.2Mo	702	838	517	349	234	76	265
4.26	0.15C-2.4Mn-1.47Si-0.24Mo	700	836	513	344	229	95	251
4.19	0.15C-2.4Mn-1.4Si-0.24Mo	699	833	515	345	230	91	308
4.22	0.15C-2.4Mn-1.47Si-0.2Mo	700	835	513	345	229	85	282
4.15	0.15C-2.4Mn-1.4Si-0.2Mo	699	832	515	346	230	83	221
4.29	0.18C-2.4Mn-1.47Si-0.24Mo	705	827	509	333	216	112	438
4.25	0.18C-2.4Mn-1.47Si-0.2Mo	704	826	509	333	217	100	395
4.18	0.18C-2.4Mn-1.4Si-0.2Mo	703	823	511	334	218	96	387
4.22	0.18C-2.4Mn-1.4Si-0.24Mo	703	824	510	334	217	106	430
4.08	0.18C-2.3Mn-1.4Si-0.2Mo	705	827	514	339	222	85	366
4.15	0.18C-2.3Mn-1.47Si-0.2Mo	707	830	512	338	221	89	373
4.12	0.18C-2.3Mn-1.4Si-0.24Mo	706	828	514	338	222	97	406
4.19	0.18C-2.3Mn-1.47Si-0.24Mo	707	830	512	337	221	99	413
4.25	0.15C-2.5Mn-1.4Si-0.2Mo	696	828	512	342	226	91	293
4.27	0.15C-2.5Mn-1.4Si-0.22Mo	697	829	511	341	225	96	310
4.29	0.15C-2.5Mn-1.4Si-0.24Mo	697	829	511	341	225	103	327
4.36	0.15C-2.5Mn-1.47Si-0.24Mo	698	832	510	340	224	106	333
4.34	0.15C-2.5Mn-1.47Si-0.22Mo	698	831	510	340	224	101	316
4.46	0.15C-2.6Mn-1.47Si-0.24Mo	696	828	506	336	219	120	449
4.39	0.15C-2.6Mn-1.4Si-0.24Mo	695	825	508	337	221	114	441
4.44	0.15C-2.6Mn-1.47Si-0.22Mo	696	828	506	336	220	113	426
4.37	0.15C-2.6Mn-1.4Si-0.22Mo	694	825	508	337	221	109	418

Step 1 - All possible combinations of the set levels in Table 30 underwent simulations. Through repeated TTT and CCT simulations, transformation temperatures and times were extracted. For further analysis, compositions highlighted in green were selected.

Table 31: Point information and ferritic transformation times.

			Ferrite Transformation Time at 700°C (s)	
Alloying Content	**Composition**	**Phase Formation at CR 10°C per Second**	**1% Transformed**	**10% Transformed**
4.19	0.15C-2.4Mn-1.4Si-0.24Mo	B-31.62%, M-68.31%, P-0.0587%	659.52	1650.53
4.22	0.15C-2.4Mn-1.47Si-0.2Mo	F-0.01%, B-36.14%, M-63.77%, P-0.0816%	361.5	945.89
4.25	0.15C-2.5Mn-1.4Si-0.2Mo	B-39.33%, M-60.59%, P-0.0762%	543.99	1387.94
4.27	0.15C-2.5Mn-1.4Si-0.22Mo	B-27.38%, M-72.56%, P-0.0551%	730.33	1817.94
4.29	0.15C-2.5Mn-1.4Si-0.24Mo	B-24.38%, M-75.57%, P-0.047%	790.51	1953.07
4.36	0.15C-2.5Mn-1.47Si-0.24Mo	B-28.25%, M-71.69%, P-0.0626%	748.2	1859.78
4.34	0.15C-2.5Mn-1.47Si-0.22Mo	B-24.27%, M-75.67%, P-0.0569%	693.8	1735.6

Step 2 - In this step, the data from various sources was examined, including point information from simulated CCT diagrams, ferritic transformation times at 700°C from simulated TTT diagrams, and transformation temperatures from Table 31. Table 32 provided a prediction of the expected formation of phases and ferritic transformation times. After careful consideration, the chosen composition was opted for due to its lower A_r^1 and A_r^3 values compared to the highlighted compositions, extensive ferrite transformation times, and the fact that point information for a cooling rate of 10°C/s indicated no significant ferrite or pearlite formation.

Again, further simulations were completed to further validate this alloy.

Appendix 4: 1-Step Quenching and Partitioning Cycles

MnSiC$_{(0.15\%)}$

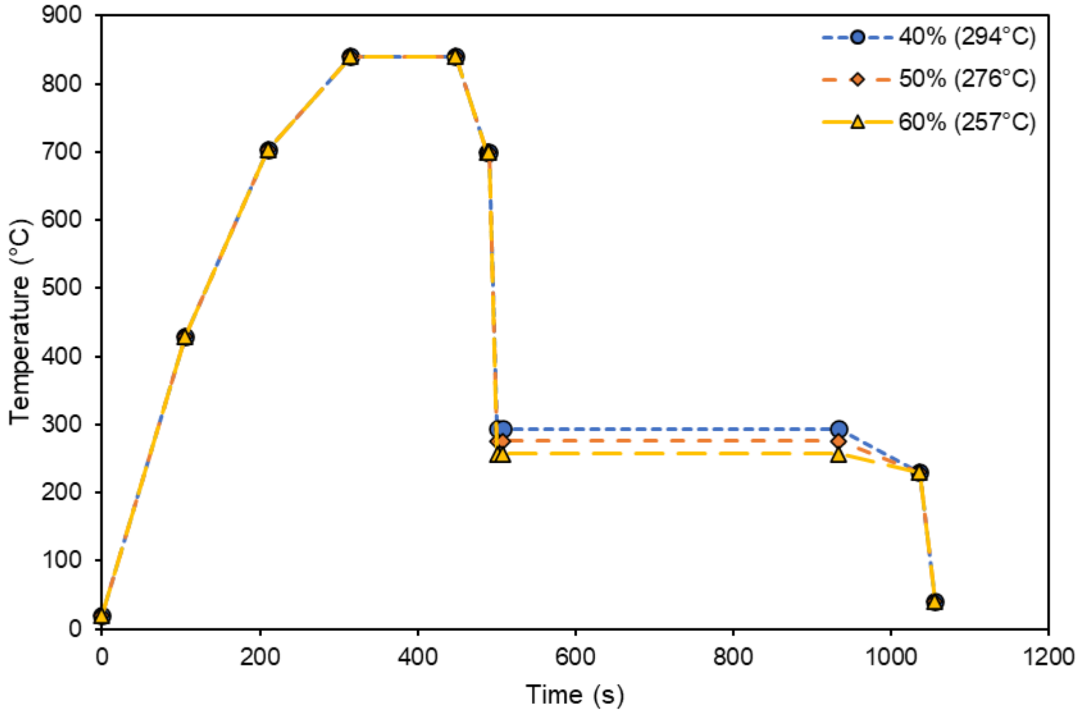

Figure 104: HT1 annealing cycles for MnSiC$_{(0.15\%)}$.

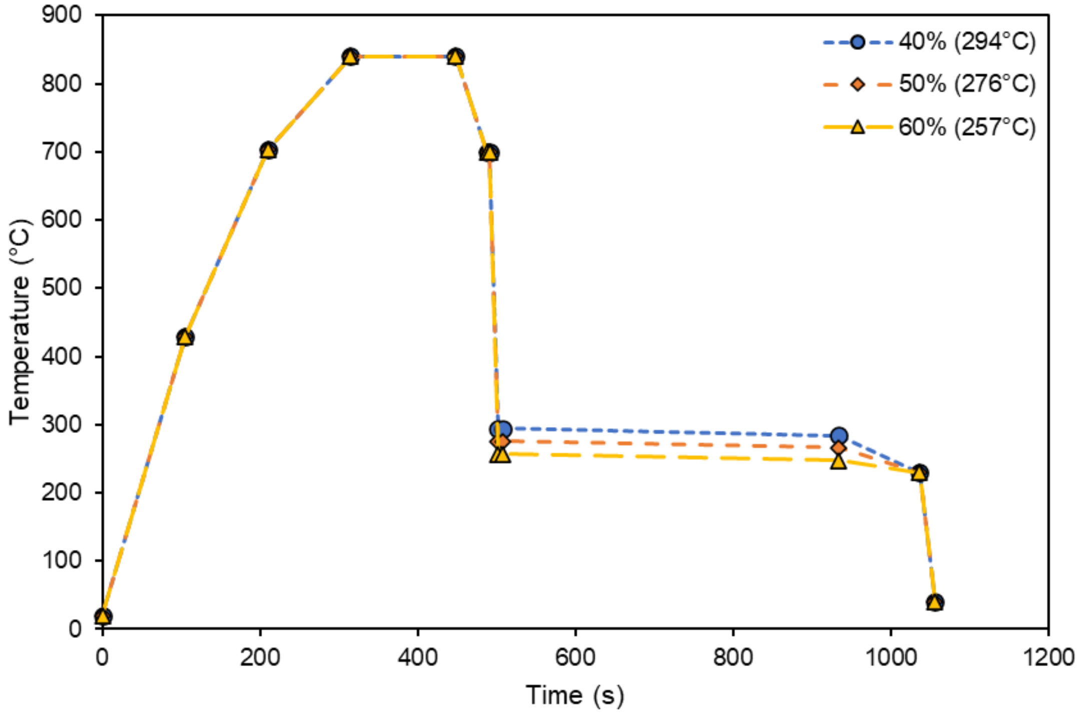

Figure 105: HT2 annealing cycles for MnSiC$_{(0.15\%)}$.

CMnSiCr

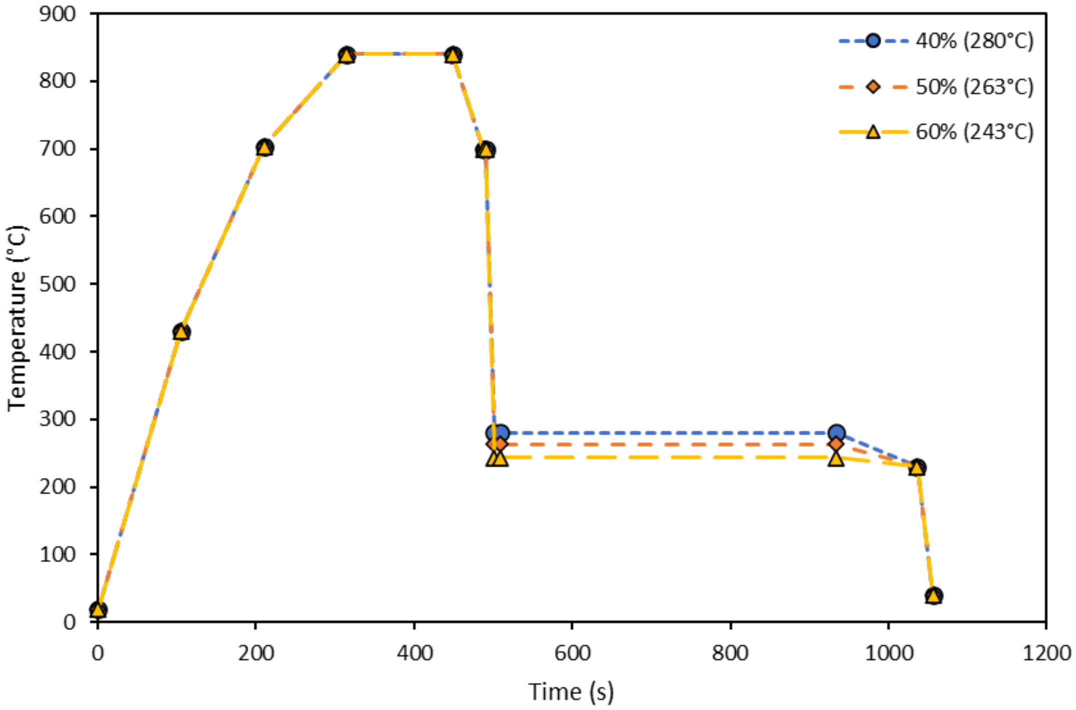

Figure 106: HT1 annealing cycles for CMnSiCr.

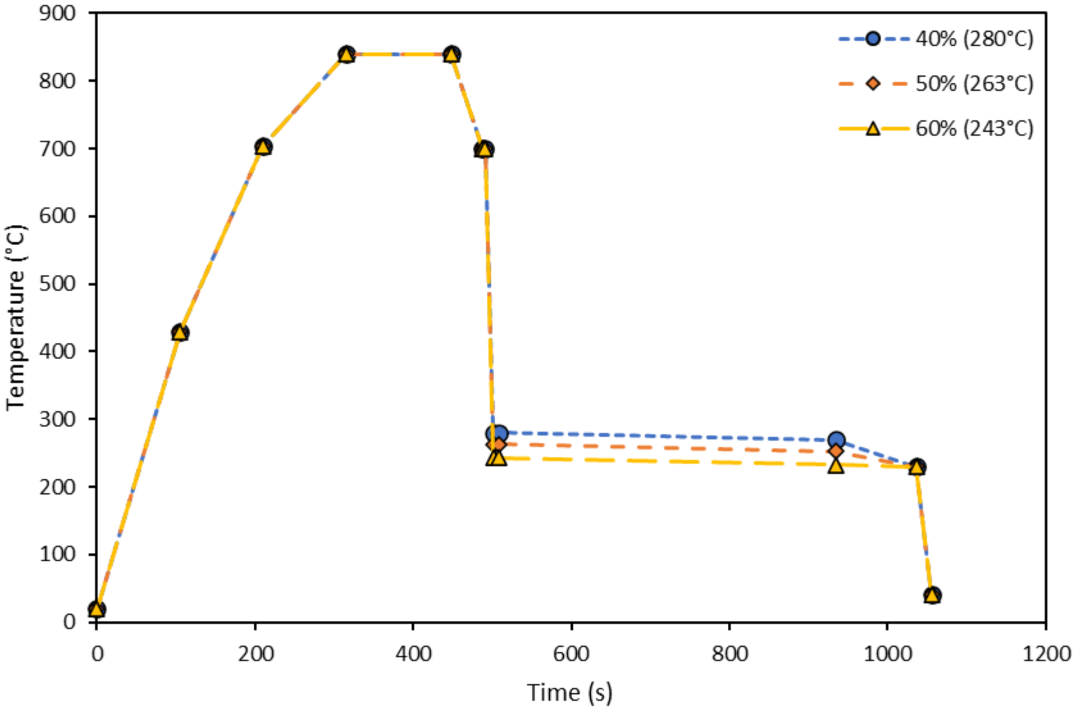

Figure 107: HT2 annealing cycles for CMnSiCr.

CMnSiMo

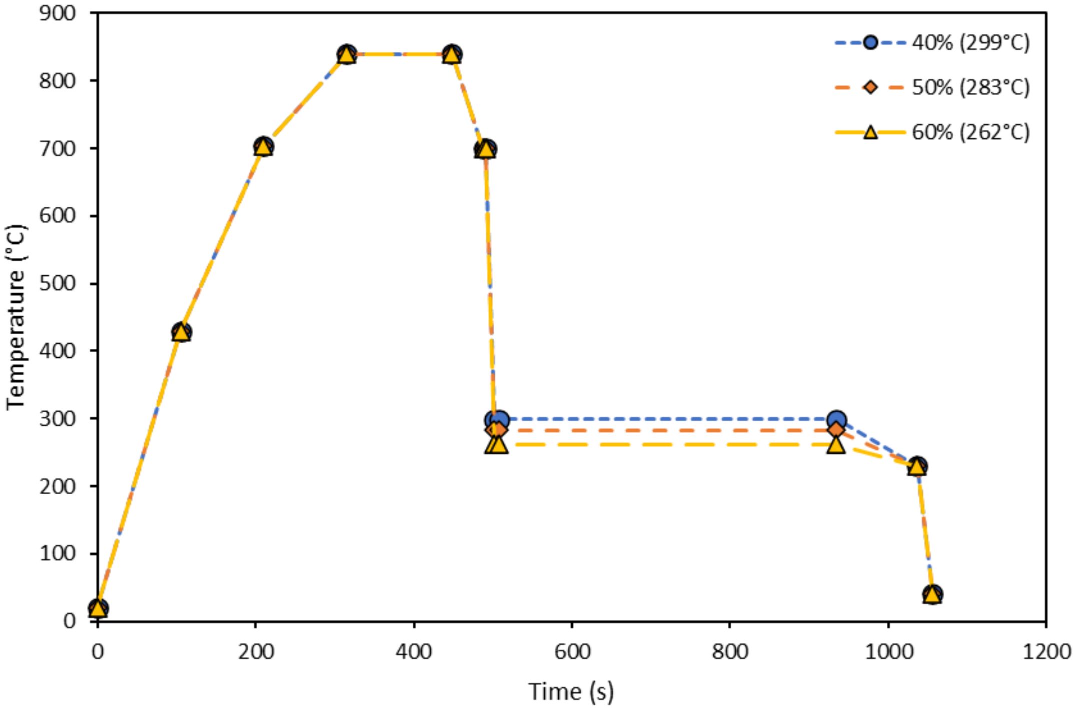

Figure 108: HT1 annealing cycles for CMnSiMo.

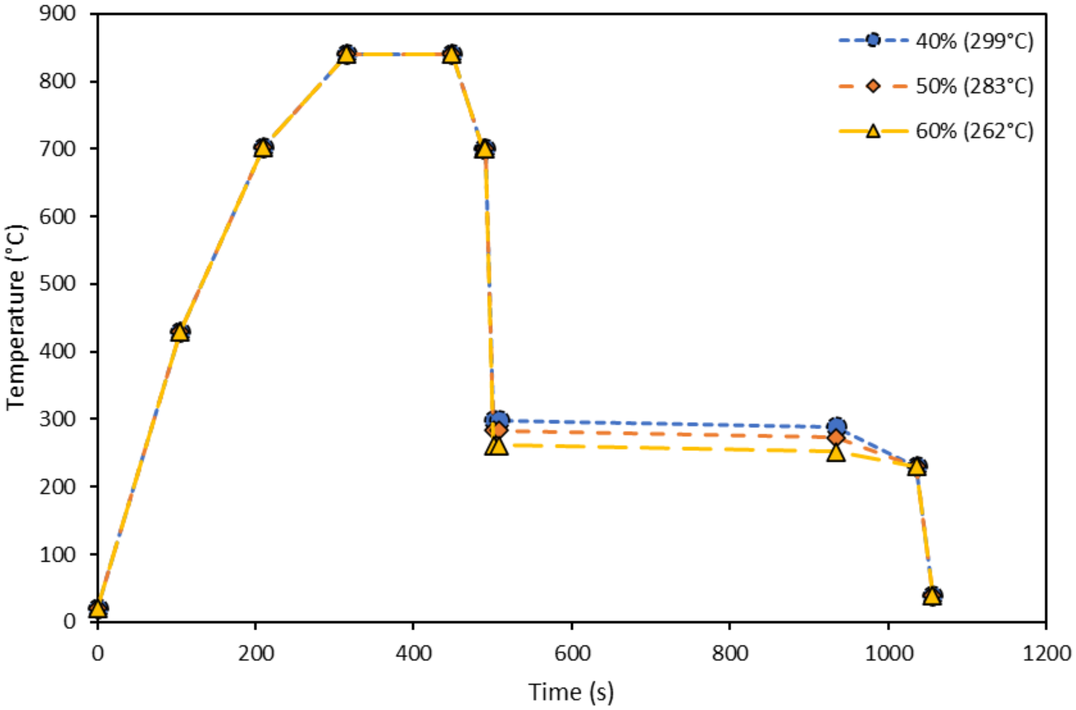

Figure 109: HT2 annealing cycles for CMnSiMo.

Appendix 5: HT1 and HT2 - Stress/Strain Curves

MnSiC(0.2%)

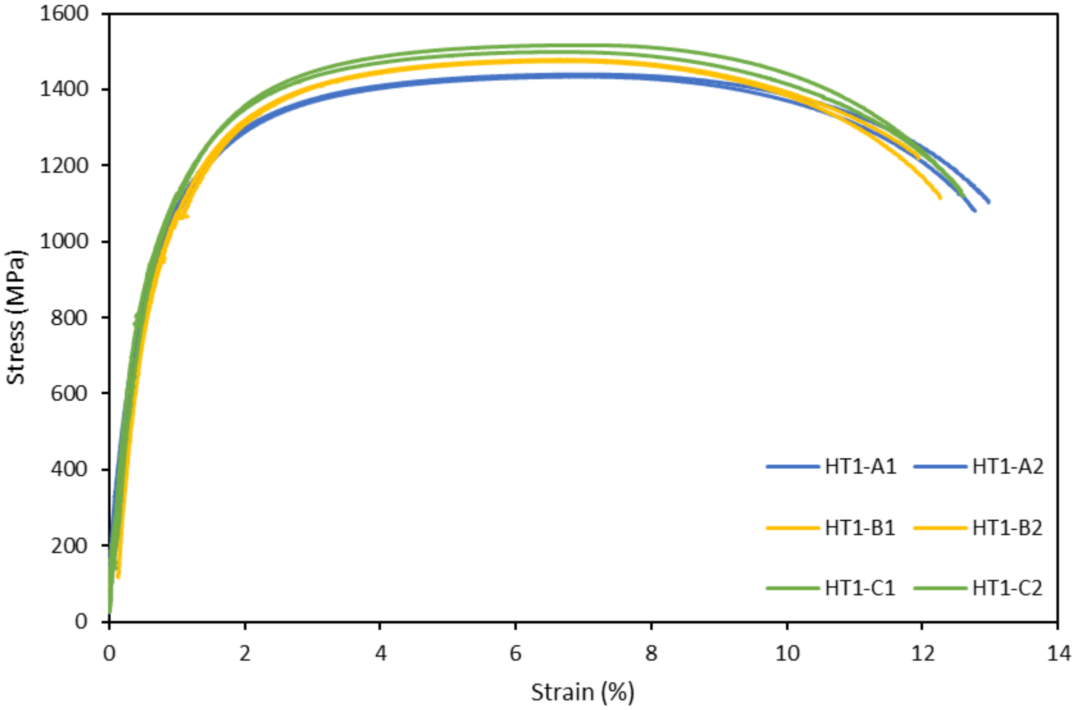

Figure 110: MnSiC(0.2%) - HT1 stress/strain curves.

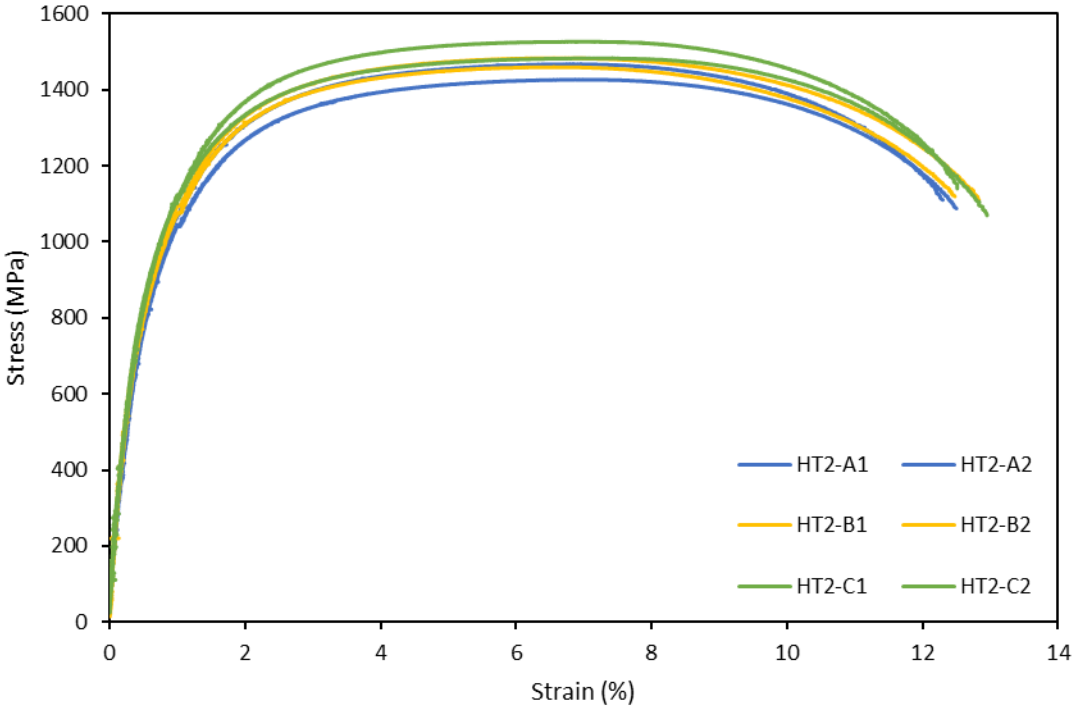

Figure 111: MnSiC(0.2%) - HT2 stress/strain curves.

MnSiC$_{(0.15\%)}$

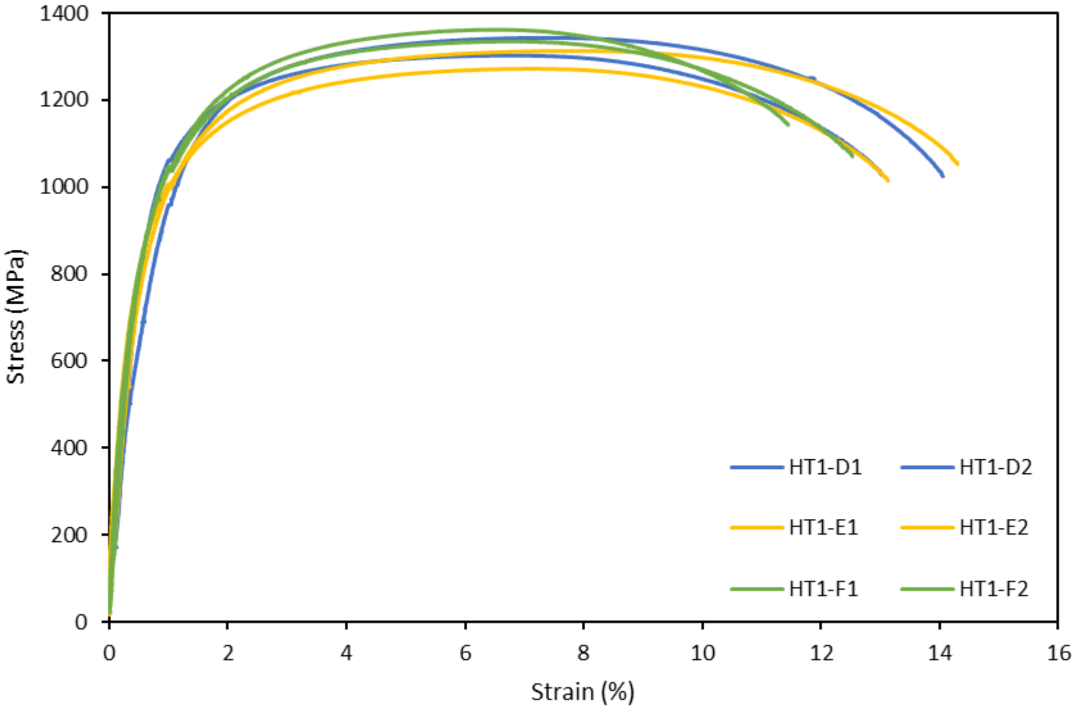

Figure 112: MnSiC$_{(0.15\%)}$ - HT1 stress/strain curves.

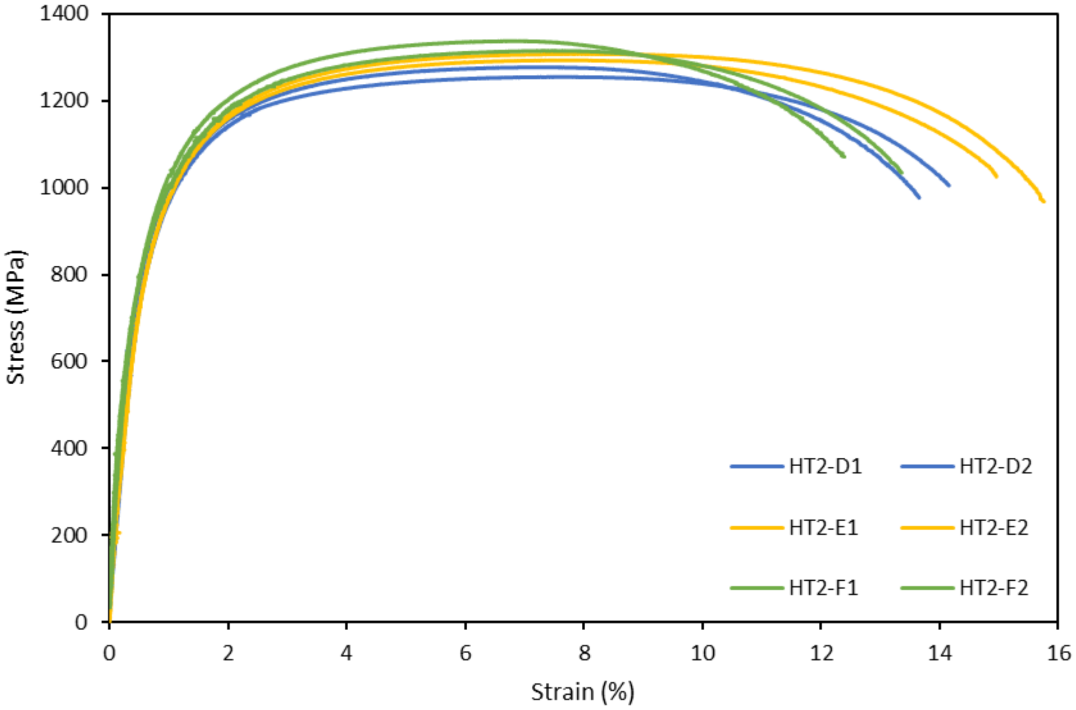

Figure 113: MnSiC$_{(0.15\%)}$ - HT2 stress/strain curves.

CMnSiCr

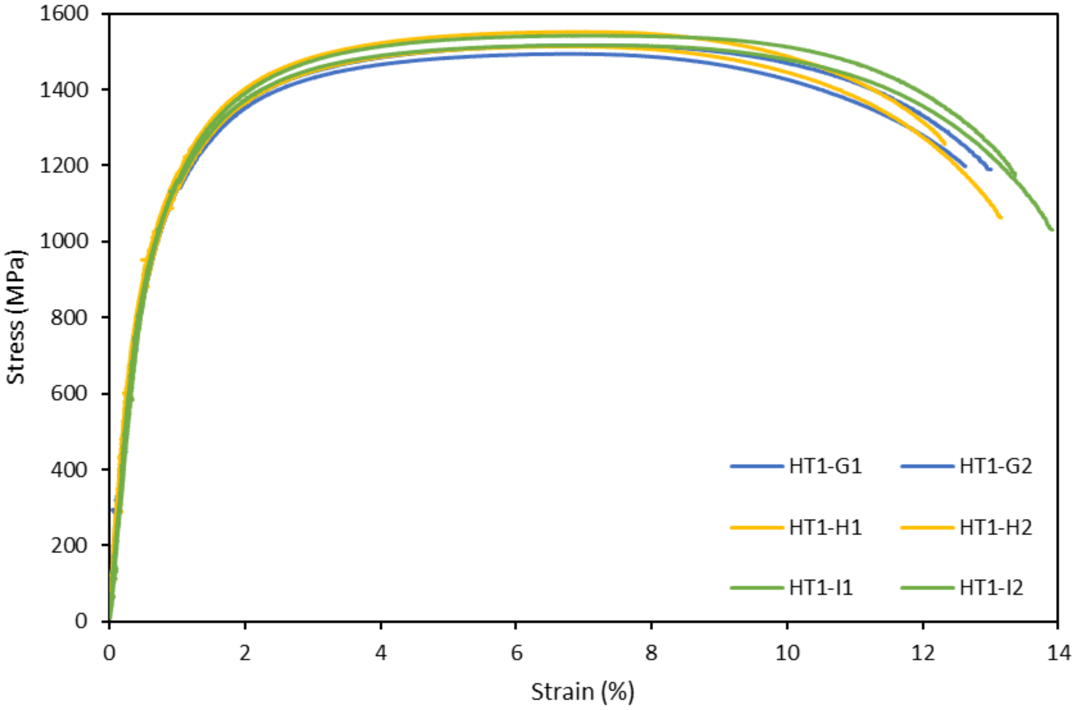

Figure 114: CMnSiCr - HT1 stress/strain curves.

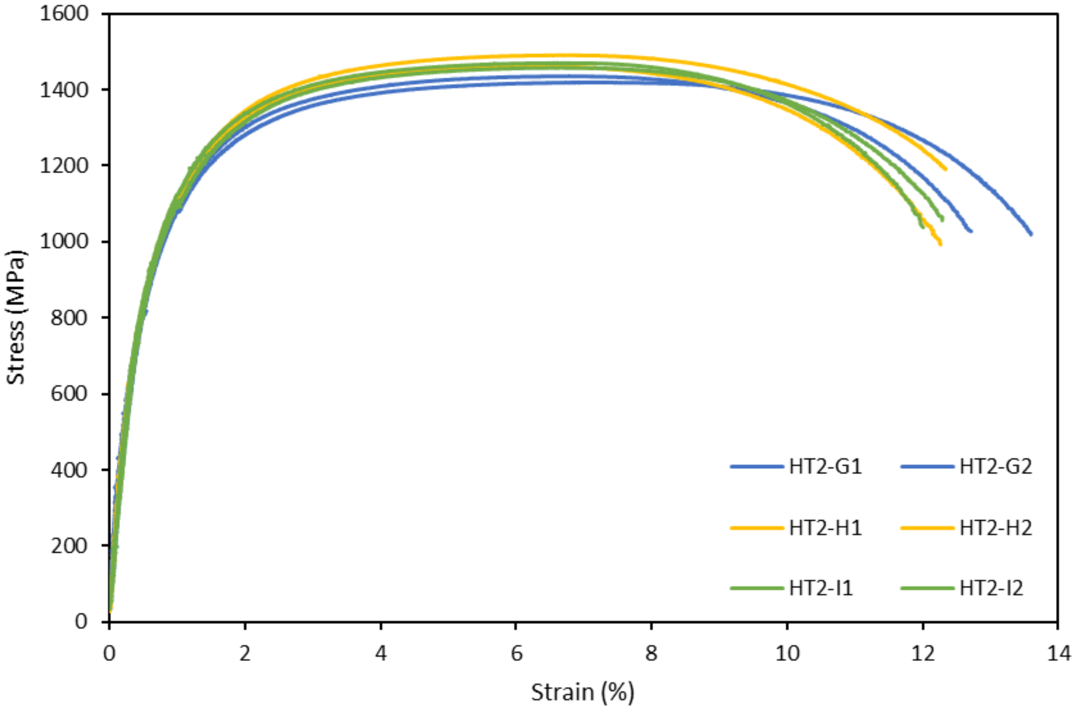

Figure 115: CMnSiCr - HT2 stress/strain curves.

CMnSiMo

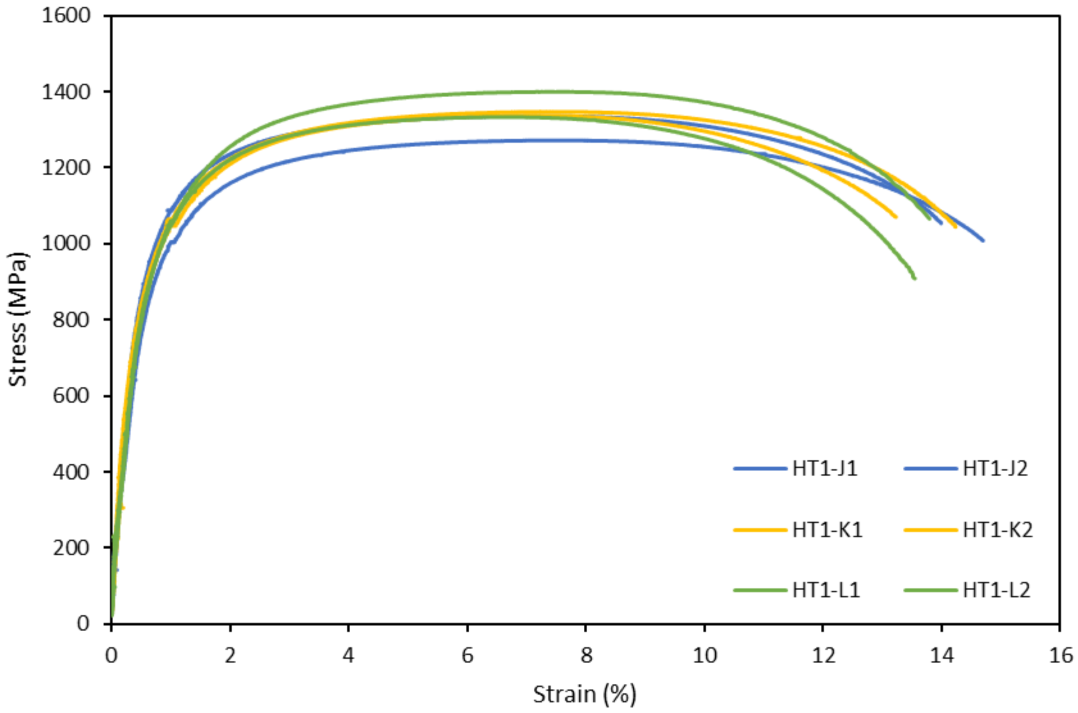

Figure 116: CMnSiMo - HT1 stress/strain curves.

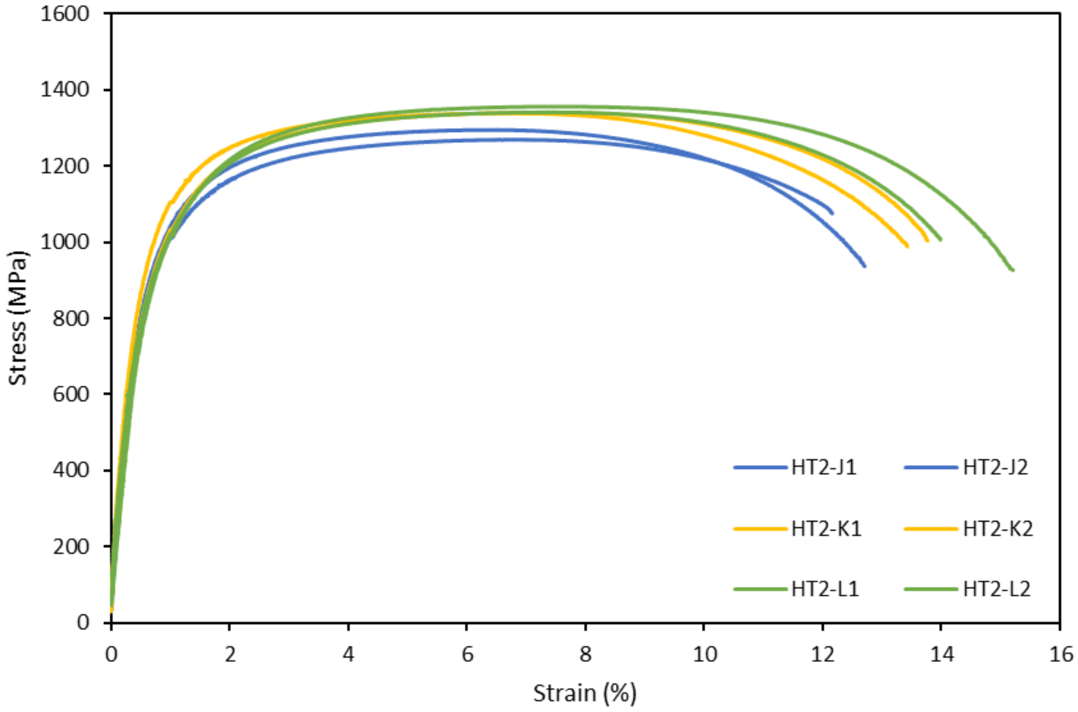

Figure 117: CMnSiMo - HT2 stress/strain curves.

Appendix 6: Gleeble 3500 - Isothermal Analysis

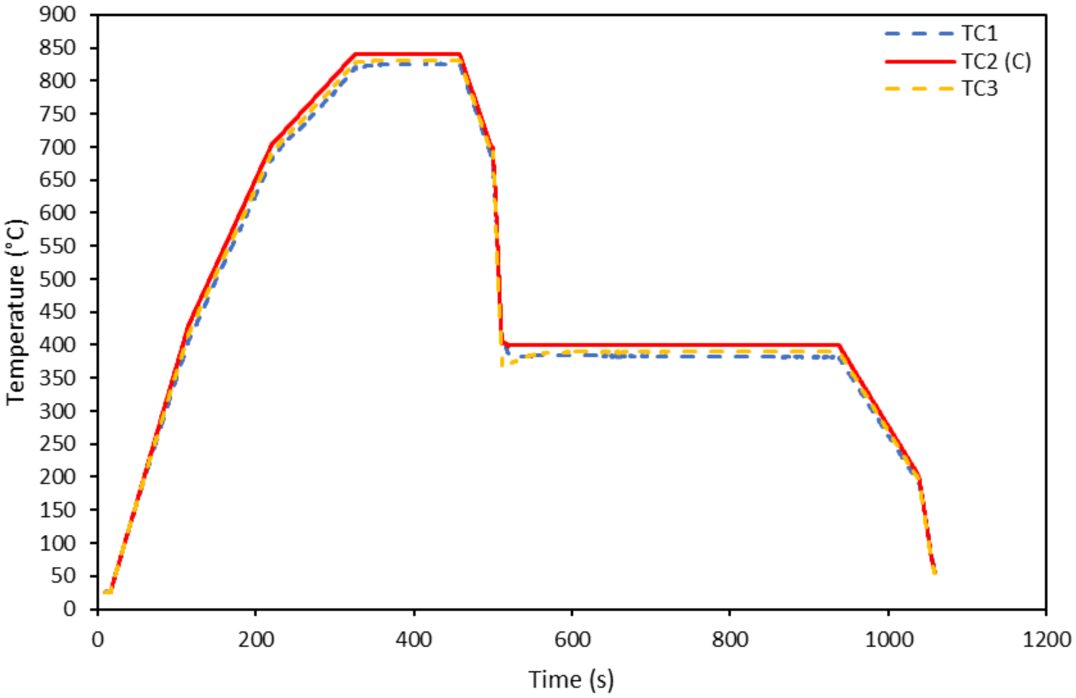

Figure 118: Temperature profile across the length, 32mm.

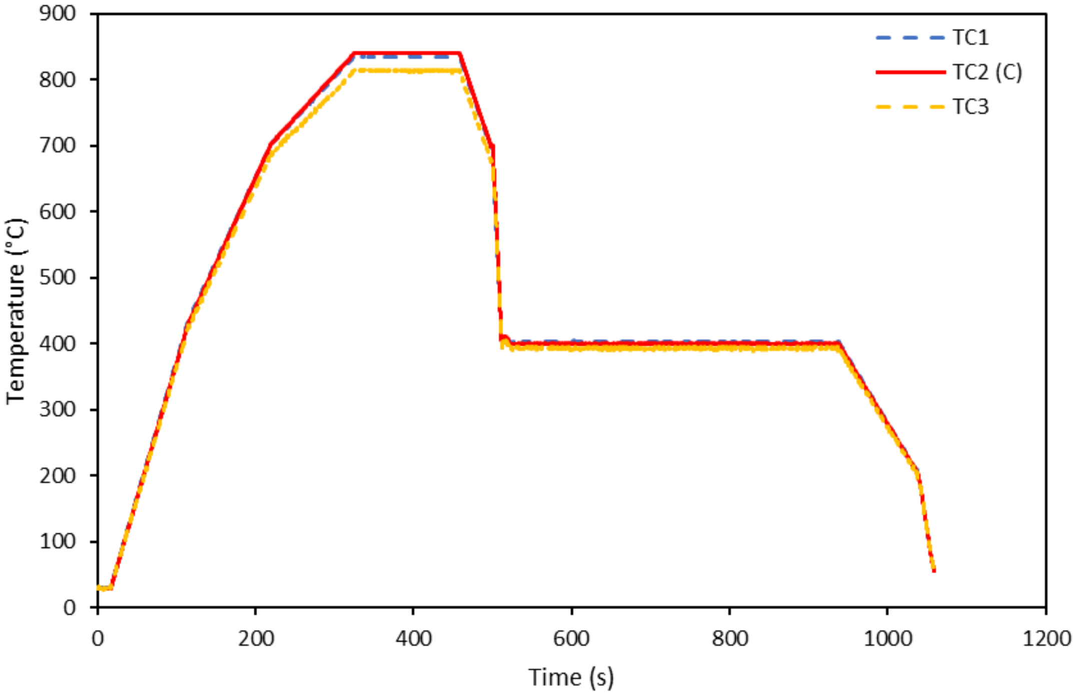

Figure 119: Temperature profile across the width, 16mm.

Table 32: Absolute average temperature difference across the length, 32mm.

Absolute Average Temperature Difference Across the Length, 32mm									
Average Difference (°C)	**Ramp 1**	**Ramp 2**	**Soak Start**	**Soak Hold**	**CGJC**	**HGJC**	**OA**	**2nd Cooling**	**Final Cooling**
TC1	8.0	23.4	21.7	15.2	13.5	6.8	16.9	14.5	3.3
TC3	4.2	13.3	12.8	9.4	8.1	25.8	11.6	8.0	5.9

Table 33: Absolute average temperature difference across the width, 16mm.

Absolute Average Temperature Difference Across the Width, 16mm									
Average Difference (°C)	**Ramp 1**	**Ramp 2**	**Soak Start**	**Soak Hold**	**CGJC**	**HGJC**	**OA**	**2nd Cooling**	**Final Cooling**
TC1	3.3	2.3	2.6	5	3.7	16.9	3.1	2.4	1.2
TC3	2.9	11.3	22	26.1	24.4	8	6.9	4.9	1.5